The Galaxy beyond TeV energies with H.E.S.S. and CTA

Luca Giunti

▶ **To cite this version:**

Luca Giunti. The Galaxy beyond TeV energies with H.E.S.S. and CTA. Astrophysics [astro-ph]. Université Paris Cité, 2021. English. NNT : 2021UNIP7096 . tel-03696526

HAL Id: tel-03696526

https://theses.hal.science/tel-03696526

Submitted on 16 Jun 2022

HAL is a multi-disciplinary open access archive for the deposit and dissemination of scientific research documents, whether they are published or not. The documents may come from teaching and research institutions in France or abroad, or from public or private research centers.

L'archive ouverte pluridisciplinaire **HAL**, est destinée au dépôt et à la diffusion de documents scientifiques de niveau recherche, publiés ou non, émanant des établissements d'enseignement et de recherche français ou étrangers, des laboratoires publics ou privés.

Université de Paris

Université de Paris

Ecole doctorale 560 STEP'UP

Laboratoires APC et IRFU

The Galaxy beyond TeV energies with

H.E.S.S. and CTA

Par Giunti Luca

Thèse de doctorat de **astrophysique**

Dirigée par Regis Terrier

Présentée et soutenue publiquement le 18/11/2021

Devant un jury composé de :

Anna Franckowiak, Prof., AIRUB-Bochum, Rapporteur
Stefan Funk, Prof., ECAP-Erlangen, Rapporteur
Hélène Sol, Prof., LUTh-Paris, Examinateur
Francois Brun, Dr., CEA-Saclay, Examinateur
Alessandra Tonazzo, Prof., APC-Paris, Examinateur
Regis Terrier, Prof., APC-Paris, Directeur de these
Bruno Khelifi, Dr., APC-Paris, Membre invité
Karl Kosack, Dr., CEA-Saclay, Membre invité

Except where otherwise noted, this work is licensed under
https://creativecommons.org/licenses/by-nd/3.0/fr/

Titre : La Galaxie au-delà du TeV avec HESS-2 et CTA

Court résumé :

L'origine des rayons cosmiques galactiques est un problème centenaire qui peut être abordé en étudiant les propriétés de l'émission de rayons provenant de sources astrophysiques. Les usines galactiques à rayons cosmiques, également connues sous le nom de PeVatrons, devrait accélérer les particules jusqu'à au moins quelques PeV (1 PeV = 10 15 eV). Ils peuvent donc être révélé au moyen d'observations de rayons à des énergies dépassant les dizaines et centaines de TeV, c'est-à-dire autour de la transition entre les très hautes énergies (VHE) et bandes de rayons à ultra haute énergie (UHE). Dans cette thèse, nous avons analysé les données du système stéréoscopique à haute énergie (H.E.S.S.), un réseau de télescopes à rayons γ VHE situé en Namibie, pour localiser le meilleur PeVatron candidats dans le ciel des rayons γ du Sud. Nous avons largement utilisé la technique d'analyse 3D, récemment adopté en astronomie des rayons γ VHE, pour obtenir des informations sur la physique propriétés des objets galactiques en utilisant des modèles paramétriques spatiaux et spectraux. Les les résultats présentés dans cette thèse ont été obtenus à l'aide de Gammapy, le logiciel officiel de l'observatoire Cherenkov Telescope Array (CTA). Dans un premier temps, nous avons réalisé une étude détaillée de la source non identifiée HESS J1702-420. Cette nous a conduit à conclure que, sous l'hypothèse que les collisions inélastiques entre les rayons cosmiques relativistes et les protons du gaz cible sont à l'origine de son émission de rayons , HESS J1702-420 abrite probablement des protons PeV. HESS J1702-420 devient donc un excellent candidat PeVatron, même si les scénarios d'émission leptonique n'ont pu être exclus. En prolongeant les mêmes techniques d'analyse, nous avons ensuite effectué une recherche à l'aveugle pour les sources de rayons détectées de manière significative par H.E.S.S. au-dessus de 20 TeV, ce qui a entraîné un nouveau catalogue de 14 objets appelé le H.E.S.S. high-Energy Galactic Plane Survey (HEGPS). Cela constituera un héritage précieux pour les futures expériences de pointage telles que en tant que CTA, soutenant potentiellement un choix raisonné dans la stratégie d'attribution du temps pour le projet scientifique clé PeVatron. Nous avons en outre réalisé des performances basées sur la simulation. mance des études pour le CTA, en se concentrant sur les capacités de détection et de modélisation de PeVatron du futur tableau.

Résumé substantiel:

La découverte des rayons cosmiques par Victor Hess remonte à 1912. Aujourd’hui, nous savons que les rayons cosmiques sont des particules chargées d’origine extra-terrestre, atteignant le sommet de l’atmosphère à une vitesse fixe (qui dépend de leur énergie) et générant des pluies importantes de particules ultra-relativistes dans l’atmosphère. En termes de de composition, ils sont majoritairement constitués de hadrons (98%), c’est-à-dire de nucléons et de noyaux dépouillés de leurs électrons, avec une

contribution sous-dominante (2%) d'électrons et des positrons.

Les PeVatrons dans notre Galaxie, capable de accélérer les protons (c'est-à-dire l'essentiel des particules cosmiques) jusqu'à des énergies d'au moins PeV, n'ont pas encore été découverts, principalement en raison de la présence de turbulences galactiques qui isotropisent les trajectoires des rayons cosmiques, éliminant ainsi toute information sur leurs trajectoires.

Cette situation appelle des stratégies de détection plus indirectes, basées par exemple sur la recherche de signaux de rayons gamma ou de neutrinos provenant des sources galactiques.

Dans cette thèse,ous avons décrit la recherche des usines de rayons cosmiques galactiques, appelés PeVatrons, en utilisant les données de H.E.S.S., un réseau de télescopes gamma-ray VHE situé en Namibie. Pour la première fois dans l'histoire de H.E.S.S., la technique d'analyse 3D a été utilisée pour dériver des informations sur les propriétés physiques des objets galactiques en utilisant des modèles paramétriques spatiaux et spectraux.

Nous avons également contribué au développement de Gammapy, l'outil logiciel officiel de l'Observatoire Cherenkov Telescope Array (CTA). En utilisant Gammapy, nous avons créé un pipeline d'analyse qui nous a permis d'identifier des candidats PeVatron prometteurs dans le sud de l'Europe, à observer en priorité par les instruments de la future génération tels que CTA et SWGO.

Nus nous sommes d'abord concentrés sur une source particulière appelée HESS J1702-420. Le site L'analyse 3D nous a permis de séparer de l'ensemble de HESS J1702-420 une nouvelle source de petite taille, appelée HESS J1702-420.

HESS J1702-420A, pour laquelle nous avons trouvé des preuves d'émission de rayons gamma jusqu'à 100 TeV. gamma jusqu'à 100 TeV. HESS J1702-420A a une forme symétrique, et un indice spectral de rayons gamma remarquablement dur de 1.53. Sur la base des données disponibles, il n'a pas été possible d'établir si ce nouvel objet est indépendant des autres objets. d'établir si ce nouvel objet est indépendant du reste de HESS J1702-420, ou s'il s'agit simplement d'une zone d'émission à haute énergie dans une source à la morphologie complexe. Dans l'un ou l'autre cas, notre étude nous a permis de conclure que, si elle est alimentée par des processus hadroniques, l'émission de rayons gamma de HESS J1702-420A est probablement associée à la présence de protons de PeV. Ce scénario n'a cependant pas pu être confirmé en raison de l'absence d'une corrélation claire corrélation entre la morphologie de HESS J1702-420A et les images de distribution du gaz, ce qui laisse une

interprétation leptonique pour cette nouvelle source de rayons gamma encore possible.

Le site nature de HESS J1702-420, et en particulier de HESS J1702-420A, reste insaisissable, mais notre analyse nous a permis de l'identifier comme un candidat au PeVatron et une cible de haute priorité pour les futures études VHE et UHE. pour les futures installations de rayons gamma VHE et UHE.

Après une étude aussi détaillée consacrée à HESS J1702-420, l'étape logique à suivre était l'application d'une approche d'analyse similaire. était l'application d'une approche d'analyse similaire à un ensemble plus large de sources.

Nous avons donc adopté les mêmes ingrédients de base (gammapie, IRFs optimisés à haute énergie et modélisation 3D) pour mettre en place une méthode d'analyse similaire. et modélisation 3D) pour mettre en place un pipeline d'analyse complet. Cet effort nous a conduit à la production de la version préliminaire d'un catalogue H.E.S.S. high-Energy Galactic Plane Survey (HEGPS).

Il s'agit d'une collection de 14 sources significativement détectées par H.E.S.S. au-dessus de 20 TeV. Les trois d'entre eux ayant la plus grande signification de détection sont HESS J1825-137, HESS J0835-455 (Vela X) et HESS J1702-420. Remarquablement, ces trois mêmes sources ont été confirmées comme étant les plus brillantes au-dessus de 20 TeV par une analyse croisée, et les trois seuls objets pour lesquels H.E.S.S. a détecté une émission significative de rayons gamma au-dessus de 50 TeV. au dessus de 50 TeV. Ils deviennent donc des cibles prioritaires pour les futurs télescopes VHE et les télescopes UHE.

Pour la première fois, la technique d'analyse 3D nous a permis de séparer l'émission de rayons gamma au-dessus de 20 TeV associée au PWN de PSR J0855-4644 de la coquille du SNR Vela Jr, qui est peu visible à des énergies aussi élevées. L'indice spectral du PWN, 1.75, est extrêmement dur et remarquablement similaire à celui de HESS J1702-420A, ce qui pourrait indiquer un mécanisme d'émission commun.

Une autre réalisation a été la détection de l'émission de rayons gamma au-dessus de 20 TeV du système binaire LS 5039, pour lequel toutes les mesures existantes s'arrêtent en dessous de 20 TeV. pour lequel toutes les mesures existantes s'arrêtent en dessous de 20 TeV.

Nous avons comparé le HEGPS avec les catalogues les plus récents de HAWC et LHAASO, dans la région d'observation qui se chevauche. la région d'observation qui se chevauche. Nous avons constaté que toutes les sources UHE détectées par les WCTs sont des sources VHE au-dessus de 20 TeV, alors que seulement la moitié des sources UHE détectées par les WCTs ont des contreparties VHE (H.E.S.S.) au-dessus de 20 TeV.

Nous avons également comparé la distribution spatiale des sources HEGPS avec celle des pulsars galactiques puissants connus. Sur les 25 objets H.E.S.S., 16 ont un pulsar à spin-down luminosity élevé à proximité (moin de 0.5 deg offset). Les 9 autres sources (plus 6 autres qui ont des pulsars puissants mais pas clairement associés à proximité) constituent naturellement une liste héritée de H.E.S.S. de candidats PeVatron hadroniques.

Dans le Dans le futur, le travail de HEGPS sera entièrement vérifié en utilisant une configuration d'analyse alternative. configuration. Cela nous permettra de valider les résultats de l'analyse, d'exporter les données DL4 (jeux de données) et DL5 (catalogue) au format FITS et de les publier dans l'esprit de l'approche scientifique open source.

Dans le dernier chapitre, nous avons discuté des perspectives d'identification du PeVatron pour la future réseau CTA. Tous les résultats sont préliminaires, puisque les IRFs du réseau final ne sont pas encore disponibles, et doivent être considérés comme une preuve de concept plutôt que comme une réelle estimation du le potentiel du CTA. Néanmoins, il est intéressant de voir que, sur la base de la version actuellement disponible des IRF de la CTA, les résultats sont les suivants actuellement disponible, le futur réseau sera capable de détecter et de modéliser correctement au moins les sources les plus brillantes ou à plus petite échelle jusqu'à 100 TeV, et de faire des prédictions sur la détectabilité des sources par les installations UHE.

la détectabilité des sources par les installations UHE telles que SWGO et LHAASO. Ce type d'interaction entre les télescopes Cherenkov à eau UHE, avec leur bonne sensibilité mais faible résolution angulaire au-dessus de 100 TeV, et CTA, avec son excellente sensibilité et PSF jusqu'à 100 TeV, sera l'un des nouveaux éléments les plus importants du domaine dans les années à venir.

En ces temps passionnants, nous sommes peut-être sur le point d'identifier, comme nous l'attendions depuis longtemps, les puissantes usines du cosmos. l'identification tant attendue des puissantes usines à rayons cosmiques de la Galaxie.

Mots clefs : rayons gamma, rayons cosmiques, gammapy, H.E.S.S., CTA, PeVatron

Title : The Galaxy beyond TeV energies with H.E.S.S. and CTA

Abstract :
The origin of Galactic cosmic rays is a century-old problem that can be tackled by studying the properties of the γ-ray emission from astrophysical sources in the Galactic plane. The Galactic cosmic ray factories, also known as PeVatrons, are expected to accelerate particles up to at least few PeV (1 PeV = 10 15 eV). They may therefore be revealed by means of γ-ray observations at energies exceeding tens and hundreds of TeV, i.e. around the transition between the very-high energy (VHE) and ultra-high-energy (UHE) γ-ray bands. In this thesis we analyzed data from the High-Energy Stereoscopic System (H.E.S.S.), a VHE γ-ray telescope array located in Namibia, to pinpoint the best PeVatron candidates in the Southern γ-ray sky. We made large use of the 3D analysis technique, recently adopted in VHE γ-ray astronomy, to derive information on the physical properties of Galactic objects using spatial and spectral parametric templates. The results presented in this thesis were obtained using Gammapy, the official software tool of the Cherenkov Telescope Array (CTA) Observatory. First, we performed a detailed study of the unidentified source HESS J1702-420. This led us to conclude that, under the assumption that inelastic collisions between ultra- relativistic cosmic rays and target gas protons are at the origin of its γ-ray emission, HESS J1702-420 likely harbors PeV protons. HESS J1702-420 therefore becomes an excellent PeVatron candidate, even if leptonic emission scenarios could not be ex- cluded. Extending the same analysis techniques, we then performed a blind search for γ-ray sources significantly detected by H.E.S.S. above 20 TeV, which resulted in a new catalog of 14 objects called the H.E.S.S. high-Energy Galactic Plane Survey (HEGPS). This will constitute a valuable legacy for future pointing experiments such as CTA, potentially supporting a reasoned choice in the time allocation strategy for the PeVatron key science project. We have additionally made simulation-based perfor- mance studies for CTA, focusing on the PeVatron detection and modeling capabilities of the future array.

Keywords : gamma rays, cosmic rays, gammapy, H.E.S.S., CTA, PeVatron

Contents

Part I

Motivations and scientific context

Chapter 1

Galactic cosmic rays and their sources

1.1 Introduction

The discovery of cosmic rays by Victor Hess dates back to 1912 [1]. With electroscope measurements carried out during high-altitude baloon rides, V. Hess measured a correlation between the height of flight and the level of ionization of air particles in the atmosphere. He correctly attributed this effect to a continuous flux of charged particles from outer space, penetrating the Earth's atmosphere with ionizing effects.

Today, we know that cosmic rays are charged particles with extra-terrestrial origin, reaching the top of the atmosphere at a fixed rate (that depends on their energy) and generating extensive showers of ultra-relativistic particles in the atmosphere. In terms of composition, they are mostly made of hadrons ($\approx 98\%$), i.e. nucleons and nuclei stripped of their electrons, with a subdominant ($\approx 2\%$) contribution from electrons and positrons. The hadronic component is dominated by ionized hydrogen nuclei (protons, $\approx 87\%$), while helium ($\approx 12\%$) and other heavier elements ($\approx 1\%$) account for the remaining hadronic flux [2]. The most energetic cosmic rays ever detected reach energies up to $10^{20}\,\mathrm{eV}$ ($\simeq 16\,J$), which is an amazing amount of energy for an elementary particle. For example, it corresponds to the kinetic energy of a 57 g tennis ball moving at the speed of 85 km/h. However, the majority of cosmic rays have energies much lower than that, and in fact the bulk of cosmic rays is made of GeV energy protons. Figure 1.1 shows the cosmic ray spectrum measured at Earth, which extends over more than ten orders of magnitude in energy and thirty in flux with a remarkably smooth profile. At PeV energies, the *knee* break in the cosmic rays flux marks a transition betweeen an extremely smooth *power law*[1] regime, with energy-dependence $\propto E^{-2.7}$, and a slightly steeper power law $\propto E^{-3}$. The knee takes place around $3-5\,\mathrm{PeV}$, as measured by the KASCADE-Grande collaboration [3][2]. The knee also marks a transition in terms of chemical composition, with a trend for cosmic rays to become more dominated by heavy nuclei beyond the knee. A natural

[1] Throughout this thesis, the term *power law* refers to the functional form $dN/dE(E) = \Phi_0 (E/E_0)^{-\Gamma}$, where Φ_0 is the spectral normalization at the reference energy E_0 and Γ is the spectral slope. The reference energy is often chosen to correspond with the so-called *pivot* energy, which minimizes the statistical uncertainties on the spectral parameters.

[2] We notice that this estimate refers to the all-particle cosmic ray spectrum. The PAMELA experiment has shown that below the knee the individual hydrogen and helium spectra experience a hardening break, and have slightly different slopes [4].

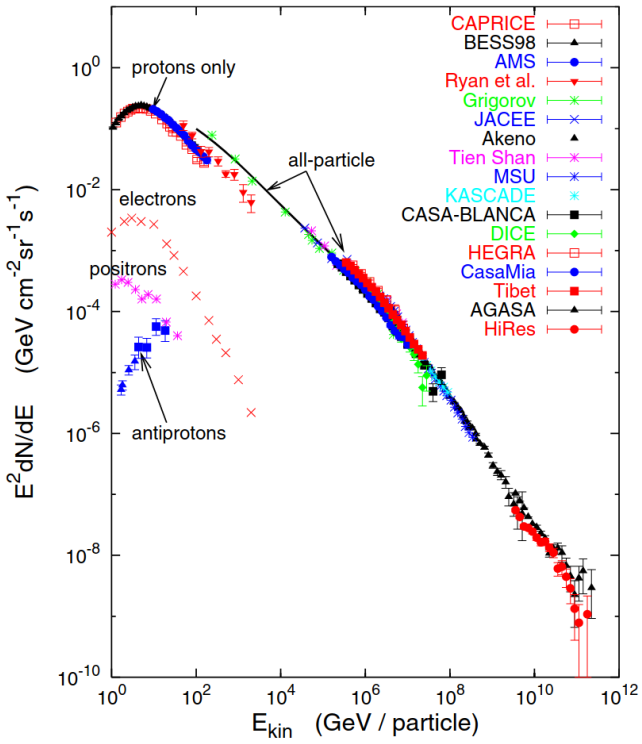

FIGURE 1.1: A compilation of local cosmic ray flux measurements, from various experiments. Image credit: [7]

explanation for this might involve a *rigidity-dependent* acceleration scenario[3]. If the maximum energy of the accelerated particles is inversly proportional to their rigidity, then the knee in the heavy element (charge Ze) spectra should be found at Z times the energy of the hydrogen knee. For example, the knee in the iron spectrum should occur at ≈ 26 times higher energy than the proton knee. The KASCADE-Grande collaboration measured the iron knee at 80 PeV, which is in the expected range for a proton knee at $3-5\,\text{PeV}$ [5][4].

More than a century has passed since cosmic rays were discovered, and yet there are some fundamental questions that still remain unanswered. Namely: *where do they come from*, and *how are they accelerated*? Possible answers to the second point will be discussed in section 1.2. Regarding the first question, today we know that the cosmic rays have extra-solar origin. This is proven by the fact that the measured cosmic ray flux is anti-correlated in time with the intensity of the Sun's activity, and drastically lowered below $\approx 1\,\text{GeV}$ by the interaction with the magnetized solar wind (*solar modulation*). We also know that the most energetic cosmic rays have extra-Galactic origin, while the bulk of lower-energy particles are accelerated inside the Galaxy. In particular, the transition is believed to take place somewhere around $10^{18}\,\text{eV}$, where the particle gyroradii in the typical interstellar medium (ISM) magnetic field ($\approx 3\,\mu G$) become comparable with the thickness of the Galactic disk ($\approx 360\,\text{pc}$), meaning that particles can no longer be confined within the Galaxy [8]. This implies

[3]The rigidity of an ultra-relativistic particle, usually measured in Volts, is defined as the ratio between its energy and charge. For example, a 10 TeV hydrogen (helium) nucleus has a rigidity of 10 TV (5 TV). The larger the rigidity (i.e. the larger the particle energy or the smaller its charge) the harder it is for the magnetic field to bend the particle trajectory.

[4]We note that these findings are in tension with other experiments, which in some cases even report a sub-PeV knee for both proton and helium spectra [6].

that the Galaxy should harbor the sources of all cosmic rays with energy $\ll 10^{18}\,\mathrm{eV}$. Such sources must in particular accelerate protons (i.e. the bulk of cosmic particles) up to *at least* PeV energies ($1\,\mathrm{PeV} = 10^{15}\,\mathrm{eV}$), hence they are called *PeVatrons*[5]. Whether the knee spectral feature at PeV energies is due to a change in the nature of the cosmic ray acceleration sites or a change in the propagation regime of cosmic rays, such as a break in the energy-dependent escape time [9, 10], remains an open question. The PeVatrons in our Galaxy have not yet been discovered, mainly due to the presence of turbulent Galactic magnetic fields which isotropize the cosmic ray trajectories washing out all information on their original acceleration sites. This calls for more indirect detection strategies, based for example on the search for γ-ray or neutrino signals from Galactic PeVatrons (see section 1.3).

The residence time of cosmic rays in the Galaxy depends on their energy as [11]:

$$\tau_{\mathrm{esc}}(E) \propto E^{-\delta}\,, \tag{1.1}$$

where the normalization constant has units of [time] and the slope $\delta = 0.3 \div 0.6$ can be obtained from measurements of the ratio between the fluxes of cosmic boron (synthesized in large amount by *spallation*) and carbon. Equation 1.1 modulates the injection spectrum ($Q_{\mathrm{CR}}(E) \propto E^{-\alpha}$, units of [energy^{-1} time^{-1}]) to the one that is measured at Earth ($F_{\mathrm{CR}}(E) \propto E^{-\Gamma}$, units of [energy^{-1}]) as:

$$F_{\mathrm{CR}}(E) = Q_{\mathrm{CR}}(E) \times \tau_{\mathrm{esc}}(E)\,. \tag{1.2}$$

Using $\Gamma = 2.7$ (valid below the knee), one obtains that the sources of cosmic rays up to the knee must accelerate a particle spectrum with slope of $\alpha = \Gamma - \delta = 2.1 \div 2.4$. Remarkably, this kind of injection spectrum is close to the prediction of the theory of particle acceleration at astrophysical shocks (see sections 1.2).

From measurements of the residence time of cosmic rays in the Galaxy, it is also possible to estimate that their sources must provide a power of $P_{\mathrm{CR}} \approx 10^{41}\,\mathrm{erg\,s^{-1}}$ to maintain the cosmic ray flux at the observed levels [12]. Due to the absence of pronounced features in the cosmic rays spectrum below the knee, it is generally believed that a single source (class) provides most of this power in our Galaxy. The main argument for this is that it seems unlikely (although not impossible) that the combined contribution of different source classes adds up to such a neat power law.

The rest of this chapter is dedicated to a brief overview of the physics of Galactic cosmic rays and their sources, which is meant to provide the broad context and motivations for the PeVatron quest. Section 1.2 describes the most important cosmic ray acceleration mechanisms, while section 1.3 discusses the link between cosmic ray and γ-ray physics. Finally, section 1.4 describes the main PeVatron candidates that have been proposed so far. The contents of this chapter were inspired by the books [2, 13, 14], along with the in-line references provided in the text.

1.2 Cosmic ray acceleration mechanisms

Given the extremely high conductivity of ionized plasmas, electric fields are quickly short-circuited by the motion of free charges. Therefore, the total net electric field is

[5] Throughout this thesis, unless otherwise specified, this term refers to *hadronic* particle accelerators only.

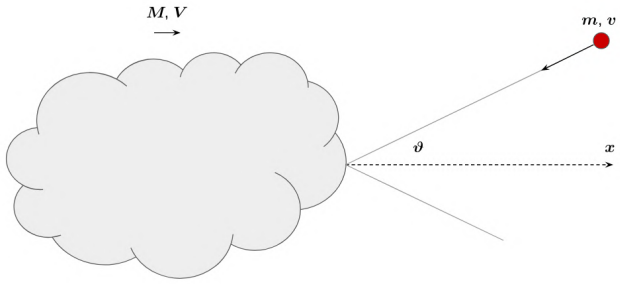

FIGURE 1.2: Geometry of the head-on collision ($\theta < 90^{o}$) between an ultra-relativistic particle and a slowly-drifting magnetized cloud.

always zero (in the plasma reference frame), which means that a simple electrostatic accelerator ($d\vec{p}/dt = Ze\vec{E}$) accelerate particles, and neither can static magnetic fields. But since we unambiguously observe non-thermal phenomena in the Universe, there must be some other way to accelerate particles. So far, two mechanisms have been proposed to solve this issue:

- the *Fermi processes*, based on the idea that particles are accelerated by the differential motion of highly magnetized plasmas;
- the sudden re-arrangement of magnetic field lines, called *magnetic reconnection*, which generates strong electric fields capable of efficiently transfering magnetic energy to charged particles.

In the following sections, these two acceleration mechanisms are briefly discussed.

1.2.1 Fermi-type acceleration

The foundations of the field were laid in 1949 by Enrico Fermi [15]. In his idea, purely based on relativistic kinematics, a charged particle interacting with a moving magnetized object experiences, in its own reference frame, an induced electric field. This theory, called *second order* Fermi acceleration, is summarized in the next section. Later on we will describe its modern reformulation known as *first order* Fermi acceleration or diffusive shock acceleration (DSA)[6].

Second order Fermi acceleration

Let's take a charged particle with initial energy E_i and momentum p_i (in the laboratory frame), which is already ultra-relativistic[7]. The particle scatters elastically on a magnetized *cloud*, slowly drifting in the laboratory frame at $V \ll c$, at an angle $\theta \in [0, \pi]$ (see figure 1.2). The cloud is assumed to be much more massive than the particle and to act as a perfect magnetic mirror, meaning that the exit angle of the particle from the cloud is the same as the entering one[8]. Then, the initial particle

[6] We will limit the discussion to the non-relativistic case.

[7] The particle extraction from a thermal distribution and boost up to relativistic speeds is still an open issue.

[8] If instead the cloud was considered as real scattering center, allowing for different exit angles, the conclusions of this section would be unchanged, modulo a factor 1/2 in eq. 1.7.

energy in the center of mass (or cloud) frame can be written as:

$$E_i^{\mathrm{CM}} = \gamma_V (E_i + V p_i \cos\theta) \tag{1.3}$$

Since the scattering is elastic, $E_i^{\mathrm{CM}} = E_f^{\mathrm{CM}}$. Moving back to the particle's frame:

$$E_f = \gamma_V (E_f^{\mathrm{CM}} - V p_f \cos\theta)\,. \tag{1.4}$$

Then, using $p_f \cos\theta = -p_i \cos\theta$, $p_i = v E_i/c^2$ and substituting 1.3 into 1.4 (with the approximations $\gamma_V \simeq 1 + 2V^2/c^2$ and $v \simeq c$), one obtains:

$$\frac{E_f - E_i}{E_i} \equiv \frac{\Delta E}{E} \approx 2\frac{V}{c}\left(\cos\theta + \frac{V}{c}\right)\,. \tag{1.5}$$

After each collision the particle may gain or lose energy, depending on whether the collision is head-on ($\cos\theta > 0$) or tail-on ($\cos\theta < 0$). This is a stochastic process, but it is possible to show that the net energy change resulting from a large number of subsequent collisions is non-null and in fact positive. The scattering probability along a given direction θ is proportional to the relative velocity in that direction:

$$P(\cos\theta) \propto (v + V\cos\theta) \propto (1 + \frac{V}{c}\cos\theta) \tag{1.6}$$

From the condition $\int_{-1}^{1} P(\cos\theta)\, d\cos\theta = 1$ one can obtain the normalization factor $1/2$, which means that (using 1.5)

$$\left\langle \frac{\Delta E}{E} \right\rangle_{\cos\theta} = \int_{-1}^{1} \frac{\Delta E}{E}(\cos\theta) P(\cos\theta)\, d\cos\theta = \frac{8}{3}\frac{V^2}{c^2}\,. \tag{1.7}$$

Equation 1.7 shows that the average energy change is positive, yielding a net particle acceleration. This is due to the fact that head-on collisions are favoured with respect to tail-on collisions, due to the cloud's motion. However, since $V \ll c$, this acceleration mechanism is not efficient, because at each collision the energy gain has a *second order* dependency on the cloud's speed. A modified version of this theory, called diffusive shock acceleration (DSA) or *first order* Fermi mechanism, is discussed in section 1.2.1.

As already noticed by Fermi, one of the most appealing features of this theory is that it naturally predicts a power law spectrum of accelerated cosmic rays. The main reason is that the ratio between the particle's pre and after-collision energy is independent of the particle energy (see equaton 1.7): $\langle \Delta E/E \rangle(E) = \beta$. If the initial distribution contains N_0 particles with the same energy E_0, and we define P as the probability that a given particle remains within the acceleration site after one collision, then after k collisions there will be $N = N_0 P^k$ particles with energy $E = E_0(1+\beta)^k$. Then, by comparing k from the last two equations, one can compute the number of particles with energy $\geq E$ after k collisions:

$$N = N_0 \left(\frac{E}{E_0}\right)^{\ln P/\ln(1+\beta)} \Rightarrow \frac{dN}{dE} \propto \left(\frac{E}{E_0}\right)^{\ln P/\ln(1+\beta)-1} \tag{1.8}$$

This theory, however, does not predict a spectral slope for the power law distribution of the accelerated particles.

First order Fermi acceleration

The inefficiency of the original Fermi mechanism is essentially due to the presence of tail-on collisions. If particles were somehow forced to bounce back and forth between two *converging* clouds, than all the collisions would be head-on. This configuration is actually realized across astrophysical shock waves, where particles are (partially) confined by the presence of magnetic turbulence on both sides of the shock. There, they repeatedly cross the shock with a net energy gain at each cycle, until eventually escaping in the interstellar medium when the shock is no longer able to confine them. By renormalizing the probability 1.6 and re-computing equation 1.7 between $\cos\theta = 0$ and 1, one obtains

$$\left\langle \frac{\Delta E}{E} \right\rangle_{\cos\theta} = \frac{2}{3}\frac{V}{c} \,. \tag{1.9}$$

This process, having now a *first order* dependency on the (small) cloud's velocity, can efficiently accelerate cosmic rays. In 1978, A. R. Bell computed the return probability to the shock in this *converging-walls* configuration [16]. This way, under the assumption of strong shocks, he found that the spectrum of accelerated particles has a *universal* (i.e. independent of the details of the acceleration process) power law index of:

$$\alpha = -2 \,. \tag{1.10}$$

The theory of first-order Fermi acceleration of cosmic ray particles can be treated in two ways:

- in the so-called *test particle* or linear approximation, the cosmic ray feedback on the shock is neglected. In this case, one can solve the coupled mass, momentum and energy conservation equations for particles across the shock surface, taking into account the presence of magnetic fields. Alternatively, with a more formal approach, one can solve the transport equation of cosmic rays across the shock surface. Either way, the main conclusions are that that the passage of a strong shock heats and compresses (by a factor ≈ 4) the swept-up ISM material, which is then towed along with the shock in the form of a thin radiative shell;
- in the *non-linear* theory, the dynamical reaction of cosmic rays on the acceleration process is also taken into consideration. The non-negligible pressure of ultra-relativistic particles slows down the upstream plasma (in the shock reference frame), creating a so-called *precursor*. The precursor decreases the *compression factor* of the swept-up gas, which in turn implies a steepening of the spectrum with respect to E^{-2}. This is true only for low and intermediate-energy particles, that do not *feel* the full velocity jump across the shock. High-energy particles instead have such large gyroradii that they can probe regions further upstream of the shock, thus experiencing larger compression factors. This leads to more efficient acceleration and harder spectra with respect to E^{-2}, at high energies. Therefore, the particle spectrum assumes a concave shape, ended by a high-energy cutoff at the maximum energy attainable by the system [17]. Another important effect caused by the particle feedback on the shock is the emergence of strongly amplified magnetic fields. This aspect will be further discussed in section 1.4.1.

1.2.2 Magnetic reconnection

The concept of magnetic reconnection was originally introduced to explain the fast energy outbursts observed during solar flares and in the Earth's magnetosphere [18, 19]. It consists of the acceleration of particles by an electric field induced by the spatial re-arrangement of magnetic field lines. Perhaps the simplest configuration associated with magnetic reconnection is the *X-point*, where the magnetic field lines of opposite orientantions meet in a X-shaped way, and then break and re-arrange with a different topology. This can efficiently dissipate magnetic energy into particle kinetic energy. Reconnection is more likely to occur in regions characterized by strong magnetic *shear*, i.e. where the magnetic field direction changes abruptly over short distances. In section 1.4.2, we will describe an application of this concept, together with the expected spectrum from simulations, to the case of highly magnetized winds of electron-positron particles surrounding rapidly spinning neuton stars.

1.3 Non-thermal radiation: from cosmic rays to γ-rays

Below the knee, the level of anisotropies in the arrival directions of cosmic rays is extremely low ($\approx$0.1% [20]). Indeed, being charged particles, during their journey toward the Earth cosmic rays interact with the turbulent Galactic magnetic field, which isotropizes their arrival directions washing out all information on their original acceleration sites. Therefore, in order to find the sources of Galactic cosmic rays, we have to rely on *secondary* non-charged messengers. These are produced by the interactions of cosmic rays with matter, radiation or magnetic fields, which can occur inside or nearby their accelerators. The most important examples of such messengers are *neutrinos* and *γ-rays*, which, being electrically neutral, point back directly to their production sites. This thesis is focused entirely on the γ-ray channel.

According to Plank's law, which governs the physics of thermal blackbody radiation, typical astrophysical objects with surface temperatures of $\approx 10^3 - 10^4\,\mathrm{K}$ mostly radiate in the visible energy band (see e.g. [2], figure 1.1). Instead, some of the hottest objects ever observed in the Universe, like the accretion discs around compact objects, $\approx 10^7\,\mathrm{K}$, can radiate up to the X-ray band ($\approx$ few keV). This means that any radiation observed in the γ-ray domain ($\gtrsim$ MeV) must have been produced by *non-thermal* radiative processes, based on the interaction of ultra-relativistic cosmic rays with diffuse matter or electromagnetic radiation. In particular, we will focus in this section on those proceses that can yield γ-ray emission in the very-high energy (VHE; $0.1\,\mathrm{TeV} \lesssim E_\gamma \lesssim 100\,\mathrm{TeV}$) band. Such processes are classified as *hadronic* (section 1.3.1) or *leptonic* (section 1.3.2), depending on the species of particles involved.

1.3.1 Hadronic processes

The inelastic scattering of cosmic ray hadrons off the ISM can explain most of the γ-ray emission observed from the Galactic disk. In the simplest case, an ultra-relativistic proton hits and disrupts an ISM proton. Subsequent QCD processes then lead to the production of charged and neutral pions, as in:

$$p + p \rightarrow p + p + \pi^0 \,. \tag{1.11}$$

Then, the pion decay leads (with $\approx 98.8\%$ branching ratio [21]) to the production of two photons:

$$\pi^0 \rightarrow 2\gamma \,, \tag{1.12}$$

both having the same energy $E_\gamma^{\rm CM} = m_{\pi^0}/2 \simeq 67.5\,{\rm MeV}$ in the center of mass (or pion) frame. In the laboratory frame, if the pion speed is v, the photon energies become

$$E_\gamma = \gamma_v (E_\gamma^{\rm CM} + v p_\gamma^{\rm CM} \cos\theta^{\rm CM}) \simeq \frac{m_{\pi^0}}{2} \gamma_v (1 + \frac{v^2}{c^2} \cos\theta^{\rm CM}) \,. \tag{1.13}$$

Assuming a mono-energetic distribution of pions, the resulting γ-ray spectrum in the laboratory frame is limited to the range $E_{\rm min} \leq E_\gamma \leq E_{\rm max}$, where

$$\begin{aligned} E_{\rm min} &= E_\gamma(\cos\theta^{\rm CM} = -1) = \frac{m_{\pi^0}}{2}\sqrt{\frac{1-v/c}{1+v/c}} \\ E_{\rm max} &= E_\gamma(\cos\theta^{\rm CM} = 1) = \frac{m_{\pi^0}}{2}\sqrt{\frac{1+v/c}{1-v/c}} \,. \end{aligned} \tag{1.14}$$

This interval is centered (in log-scale) around $\sqrt{E_{\rm min} E_{\rm max}} = m_{\pi^0}/2$. It can be shown that, between $E_{\rm min}$ and $E_{\rm min}$, the spectrum has a flat value $\propto 1/E_{\pi^0}$ [22]. Therefore, for an arbitrary distribution of pion energies, the resulting γ-ray spectrum takes the shape of a superposition of boxes, all centered around $m_{\pi^0}/2$ and having widths inversly proportional to their heights. This gives rise to the characteristic *pion bump* at 67.5 MeV.

To describe the shape of the hadronic γ-ray spectra, [23] developed an analytical approximation for the π^0 production cross section $\sigma_{\pi^0}(E_p)$ in a wide energy range, from the kinematic threshold (280 MeV) up to PeV energies. This was achieved by combining experimental data, for proton energies $E_p \leq 2\,{\rm GeV}$, with theory-driven Monte Carlo simulations, for $E_p > 2\,{\rm GeV}$. Then, the differential γ-ray production cross section $d\sigma_\gamma/dE_\gamma(E_p, E_\gamma)$ was parametrized as a function of $\sigma_{\pi^0}(E_p)$, for an arbitrary proton energy distribution of the form

$$\frac{dN_p}{dE_p}(E_p) \propto p_p^{-\alpha} \exp[-(E_p/E_p^{\rm cutoff})^\beta] \,. \tag{1.15}$$

The resulting γ-ray flux, produced by the interaction of the proton spectrum 1.15 with the ISM and measured at a distance d from the interaction point, is [23]:

$$\frac{dN_\gamma}{dE_\gamma}(E_\gamma) = \frac{n_H c}{d^2} \int_{E_p^{\rm min}}^{\infty} \frac{d\sigma_\gamma}{dE_\gamma}(E_p, E_\gamma) \frac{dN_p}{dE_p}(E_p) dE_p \,, \tag{1.16}$$

where n_H is the volume density of target protons. Figure 1.3 (left panel) shows an example γ-ray spectrum computed using equations 1.16 and 1.15 (black curve), assuming $\alpha = 2$, $\beta = 1$ and $E_p^{\rm cutoff} = 10\,{\rm TeV}$. The pion bump at $E_\gamma \simeq 67.5\,{\rm MeV}$, indicated by the dashed red line, is clearly visible in the γ-ray spectrum. The blue curve in the figure represents a simple γ-ray power law with exponential cutoff, of the form

$$\frac{dN_\gamma}{dE_\gamma}(E_\gamma) \propto E_\gamma^{-\alpha'} \exp[-(E_\gamma/E_\gamma^{\rm cutoff})^{\beta'}] \,. \tag{1.17}$$

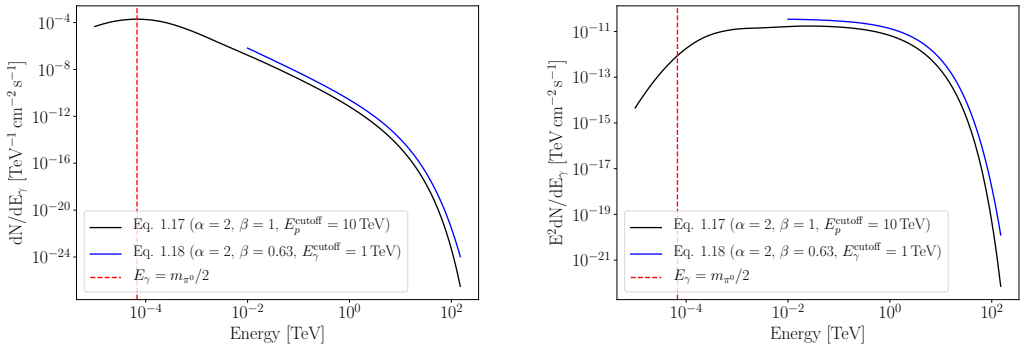

FIGURE 1.3: γ-ray spectrum (left) and SED (right) for hadronic interactions. The blue curves correspond to simple analytic approximations of the complete phenomenological model (black curves), while the vertical red line indicates the pion bump.

Away from the pion bump peak, equation 1.17 provides a good approximation of 1.16, assuming that:

$$\alpha' = 2.0 \ (= \alpha) \tag{1.18}$$

$$\beta' = 0.62 \ (< \beta) \tag{1.19}$$

$$E_\gamma^{\rm cutoff} = 1\,{\rm TeV} \ (= E_p^{\rm cutoff}/10) \tag{1.20}$$

Equation 1.18 tells us that the γ-ray spectral index closely mimics the one of the parent proton distribution, while equation 1.19 means that the spectrum of secondary γ-rays undergoes a slower cutoff with respect to the parent proton distribution. Finally, equation 1.20 tells us that the cutoff energy of the γ-ray distribution is 10 times lower than in the proton one. In fact, by means of numerical simulations, [24] proved the general validity of the rule of thumb $E_\gamma = E_p/10$.

When multiplied by E_γ^2, the γ-ray spectrum assumes the form shown in figure 1.3 (right panel). This is a common way to display spectra in γ-ray astronomy, not exclusive to hadronic spectra, because it enhances features with respect to the steep dN_γ/dE_γ plots. The quantity $E_\gamma^2 dN_\gamma/dE_\gamma$, equivalent to the νF_ν used in radio astronomy, is called the spectral energy distribution (SED). As the name suggests, the SED allows one to assess how the energy is distributed across the γ-ray spectrum. To see this, one can compute the total γ-ray energy carried in the spectrum:

$$W = \int_{E_{\rm min}}^{E_{\rm max}} E_\gamma \frac{dN_\gamma}{dE_\gamma} dE_\gamma \ . \tag{1.21}$$

Assuming, to simplify, that the γ-ray spectrum is a simple power law ($dN_\gamma/dE_\gamma \propto E^{-\Gamma}$), then 1.21 yields

$$W \propto \int_{E_{\rm min}}^{E_{\rm max}} E_\gamma^{1-\Gamma} dE_\gamma \propto \begin{cases} E_{\rm max}^{2-\Gamma} - E_{\rm min}^{2-\Gamma}, \ \Gamma \neq 2 \\ \ln(E_{\rm max}/E_{\rm min}), \ \Gamma = 2 \end{cases} \tag{1.22}$$

If $\Gamma < 2$ ($\Gamma > 2$), then $W \propto E_{\rm max}$ ($W \propto E_{\rm min}$), which means that most of the energy is carried by particles at the highest (lowest) end of the spectrum. In particular, for spectra much harder (steeper) than $\Gamma = 2$, the energy bulk is stored almost exclusively in the form of particles at the energy cutoff (threshold).

Another useful quantity is the particle cooling time due to inelastic $p-p$ interactions in the ISM [25]:

$$\tau_{pp} \simeq 6 \times 10^5 \left(\frac{n_h}{100\,\mathrm{cm}^{-3}} \right)^{-1} \mathrm{yr} \,. \tag{1.23}$$

Equation 1.23, which is valid for protons with energies between 1 GeV and few hundreds TeV, is energy-independent. This means that, for any given freshly-accelerated proton distribution, the shape of the resulting γ-ray spectrum is not modified with time (modulo a scaling factor) by energy-dependent proton losses. This is not true for leptons, as discussed in the next section.

Finally, we note that charged pions (π^+ and π^-) are also produced in inelastic $p-p$ interactions, with roughly equal probability to the π^0 channel:

$$\begin{aligned} p + p &\rightarrow p + p + \pi^+ + \pi^- \\ p + p &\rightarrow p + n + \pi^+ \,. \end{aligned} \tag{1.24}$$

They decay into muons and neutrinos [9], as in

$$\pi^\pm \rightarrow \mu^\pm + \nu_\mu / \bar{\nu}_\mu \,, \tag{1.25}$$

and muons decay in turn into electrons and neutrinos:

$$\mu^\pm \rightarrow e^\pm + \nu_e / \bar{\nu}_e + \nu_\mu / \bar{\nu}_\mu \,. \tag{1.26}$$

This establishes an important connection between hadronic γ-rays and neutrino astronomy. In particular, if a γ-ray source is accompanied by a neutrino signal, a hadronic interpretation for the origin of its γ-ray emission is considered strongly favored.

1.3.2 Leptonic processes

Relativistic electrons can produce VHE γ-rays through the *inverse-Compton* upscattering of diffuse low-energy photon fields:

$$e^\pm + \gamma_{\mathrm{CMB/ISRF}} \longrightarrow \; e^\pm + \gamma_{\mathrm{VHE}} \,. \tag{1.27}$$

Here, CMB indicates the *cosmic microwave background*, which can be treated as a black-body distribution with energy density of $\epsilon_{\mathrm{CMB}} = 0.261\,\mathrm{eV\,cm}^{-3}$ and temperature of $T_{\mathrm{CMB}} = 2.73\,\mathrm{K}$. The ISRF (short for *interstellar radiation field*) is instead a combination of starlight and dust re-emission, which permeates (with large energy density variations) the interstellar space. The starlight (dust) emission peaks in the near (far) infra-red, with a typical energy density $\epsilon_{\mathrm{stars}} \approx 1\,\mathrm{eV\,cm}^{-3}$ ($\epsilon_{\mathrm{dust}} \approx 0.5\,\mathrm{eV\,cm}^{-3}$) and temperature $T_{\mathrm{stars}} \approx 3000\,\mathrm{K}$ ($T_{\mathrm{dust}} \approx 30\,\mathrm{K}$). Thanks to [26, 27], the ISRF in the Galaxy has been mapped in a full 3D model, which has been made publicly available online. In addition to the CMB and ISRF, another possible target field for the inverse-Compton process is the lower energy radiation generated by the interaction of the same electron population with magnetic fields (synchrotron self-Compton, or SSC).

Depending on the electron energy, inverse-Compton scattering may occur in the non-relativistic (Thompson, $\sigma_{\mathrm{Th}} \approx 66.5\,\mathrm{fm}^2$) or ultra-relativistic (Klein-Nishina) regime.

[9] With $\approx 99.99\%$ branching ratio [21].

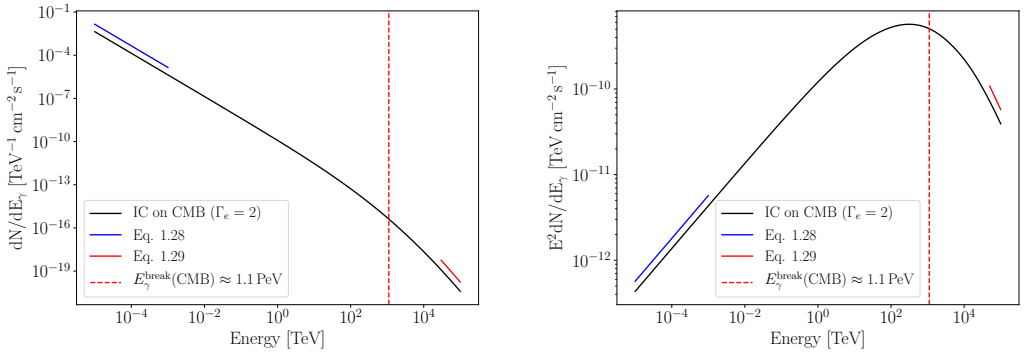

FIGURE 1.4: γ-ray spectrum (left) and SED (right) resulting from leptonic interactions. The blue and red curves correspond to simple analytic approximations of the complete phenomenological model (black curves), while the vertical red line indicates the Klein-Nishina break.

In the latter case, the scattering cross-section is suppressed as

$$\sigma_{\rm KN} \propto \frac{\ln 4k}{k} \ , \tag{1.28}$$

where $k = E_{\rm rad} \times E_e$ is the product of the photon and electron energies. The resulting energy spectrum of up-scattered γ-rays, assuming a power law electron distribution ($\Gamma_e = 2$), is shown by the black curve in figure 1.4, in terms of differential flux (left) or SED (right). The γ-ray spectrum has a clear high-energy break, from the relatively hard power law spectral slope

$$\Gamma_\gamma = \frac{\Gamma_e + 1}{2} \ (= 1.5) \ , \tag{1.29}$$

shown by the blue curve, to a steep power law

$$\Gamma_\gamma = \Gamma_e + 1 \ (= 3) \tag{1.30}$$

at the highest energies, shown by the red curve[10]. This break marks the transition between the Thomson and Klein-Nishina regimes, at $E_\gamma^{\rm break} \approx m_e^2 c^4 / E_{\rm rad}$. For the CMB, whith an energy of $E_{\rm rad} = kT \simeq 0.235\,{\rm meV}$, the break occurs at $E_\gamma^{\rm break}({\rm CMB}) \approx 1.1\,{\rm PeV}$ (see the red line in figure 1.4). In more realistic cases, one has also to consider the ISRF target photons, for which much lower break energies are found: $E_\gamma^{\rm break}({\rm stars}) \approx 1\,{\rm TeV}$, $E_\gamma^{\rm break}({\rm dust}) \approx 100\,{\rm TeV}$. We note that in real astrophysical applications it might sometimes be hard to distinguish between the Klein-Nishina spectral break and an intrinsic cutoff of the underlying electron distribution, due to a lack of statistics at high energy.

The spectra described until now are affected by the *energy-dependent* radiative losses of electrons, due to their interaction with the ambient radiation and magnetic fields. The electron cooling time due to synchrotron emission in a magnetic field B is

$$\tau_{\rm Syn} \approx 3 \times 10^5 \left(\frac{E_e}{1\,{\rm TeV}} \right)^{-1} \left(\frac{\epsilon_B}{1\,{\rm eV\,cm^{-3}}} \right)^{-1} \ {\rm yr} \ , \tag{1.31}$$

where $\epsilon_B \propto B^2$ is the energy density of the magnetic field [28]. This expression is valid

[10] In equation 1.30 we neglected a multiplicative ($\ln E_\gamma$ + constant) factor [14].

both in the Thomson and Klein-Nishina regimes, provided that the magnetic field value is not extreme ($B \ll 10^{12}\,G$) [29]. In the Thomson regime, the inverse-Compton up-scattering off a given seed photon field (e.g. the CMB, starlight or dust emission) results in an electron cooling time which does not depend on the spectral distribution of target photons but only on their total energy density. It can be expressed in the same form as equation 1.31, with the substitution $\epsilon_B \to \epsilon_{\rm rad}$ [28]:

$$\tau_{\rm IC}^{\rm Th} \approx 3 \times 10^5 \left(\frac{E_e}{1\,\mathrm{TeV}}\right)^{-1} \left(\frac{\epsilon_{\rm rad}}{1\,\mathrm{eV\,cm^{-3}}}\right)^{-1} \mathrm{yr}\,. \tag{1.32}$$

In the Klein-Nishina regime instead this is not the case, but for the standard scenario of a black-body target photon field one has [30] [11]:

$$\tau_{\rm IC}^{\rm KN} \approx 10^9 \left(\frac{E_e}{1\,\mathrm{TeV}}\right) \left(\frac{\epsilon_{\rm rad}}{1\,\mathrm{eV\,cm^{-3}}}\right)^{-1} \mathrm{yr}\,. \tag{1.33}$$

This cooling time-scale is significantly higher than the in the Thomson regime (see equation 1.32), due to the Klein-Nishina suppression of the Compton scattering cross-section (equation 1.28).

In steady state, radiative losses modify the electron spectrum as:

$$F_e(E_e) = Q_e(E_e) \times \tau_{\rm loss}(E_e)\,, \tag{1.34}$$

where Q_e and F_e respectively are the injected and cooled electron spectra (with units of [energy^{-1} time^{-1}] and [energy^{-1}]), while $\tau_{\rm loss}$ is combination of the synchrotron and inverse-Compton cooling times. To understand the impact of this modulation on the resulting γ-ray spectra, we can assume $Q_e(E_e) \propto E_e^{-\Gamma_e}$ and distinguish two extreme cases [28, 31, 32]:

- If $\epsilon_B \gg \epsilon_{\rm rad}$ (i.e. inverse-Compton losses are negligible), then $\tau_{\rm loss} = \tau_{\rm Syn}$ and equation 1.34 yields $F_e \propto E_e^{-(\Gamma_e+1)}$. Using 1.29 and 1.30, and assuming again $\Gamma_e = 2$, one obtains in this case a broken γ-ray power law with a low-energy part
$$\Gamma_\gamma = \frac{\Gamma_e + 2}{2}\ (=2) \tag{1.35}$$
and a high-energy end
$$\Gamma_\gamma = \Gamma_e + 2\ (=4)\,. \tag{1.36}$$
In both regimes, and in particular above the Klein-Nishina break, the spectrum is significantly steepened with respect to the un-cooled case;
- if instead $\epsilon_B \ll \epsilon_{\rm rad}$, the situation is a bit more complex [33]. Since the inverse-Compton losses in the Thomson regime have the same form as the synchrotron ones, at low energies the resulting γ-ray spectral slope is steepened as in equation 1.35. But in the Klein-Nishina regime, according to equation 1.33, the electron cooling time is directly proportional to the energy. Therefore, the electron spectrum hardens to $F_e \propto E_e^{-\Gamma_e+1}$, which in turn reflects into a hardening

[11] To obtain the formula 1.33, we converted the equation (13) from [30] to the same units as equation 1.31, and approximated $E_e^{0.7}$ with E_e.

of the γ-ray spectrum[12]:

$$\Gamma_\gamma = \Gamma_e \ (= 2) \ . \tag{1.37}$$

This effect can potentially compensate and wash out the Klein-Nishina break in the photon spectrum, leading to hard leptonic γ-ray spectra up to tens or hundreds of TeV [28].

1.4 The sources of Galactic cosmic rays

As discussed in section 1.3, there is a tight connection between cosmic ray physics and γ-ray astronomy. In particular, the powerful PeVatrons that are (or have been in the past) active in our Galaxy are also expected to be bright γ-ray sources. At TeV energies, the γ-ray sky is crowded with bright sources, such as supernova remnants (SNRs) and pulsar wind nebulae (PWNe), which are now established to be accelerators of non-thermal particles. However, their possible contribution up to the knee (i.e. their PeVatron nature) is still debated. A few γ-ray binaries have also been detected (≈ 5), but they generally have steep γ-ray spectra measured only up to few hundreds GeV [34–36], with the exception of LS 5039 that has been detected up to $\lesssim 20\,\mathrm{TeV}$ by H.E.S.S. [37].

The H.E.S.S. Galactic Plane Survey (HGPS) [38] is the most comprehensive scan of the Galactic plane from $l = 250^\mathrm{o}$ to 65^o, with data taking completed in 2013 and published in 2018 by the H.E.S.S. Collaboration (see section 2.3). It lists 78 VHE γ-ray sources, 31 of which were firmly identified with known SNRs, PWNe, plerions and γ-ray binaries. Other 36 objects, for which at least one possible counterpart was found, were classified as associated but not clearly identified sources. Finally, 4 objects were found to be spatially close with unidentified *Fermi*-LAT GeV sources, while for the remaining 7 no multiwavelength counterpart was found. They are HESS J1702-420, J1708-410, J1729-345, J1741-302, J1828-099, J1832-085 and J1457-593. These objects, that are bright only in the VHE γ-ray range, are called *dark* sources [39, 40]. Whether the physical processes powering their VHE γ-ray emission are hadronic or leptonic is unknown, and they still remain unidentified. It seems plausible that some of them are evolved PWNe, as in the case of other previously unassociated VHE sources. For example, the sources HESS J1303-631 and HESS J1825-137, detected in the early days of H.E.S.S. and originally unidentified [41, 42], were later associated with old PWNe based on the discovery of energy-dependent morphology and compact X-ray counterparts [43, 44]. There are also dark sources that may be associated with molecular clouds illuminated by nearby SNRs, for example HESS J1457-593 and HESS J1729-345 [38]. In the part II of this thesis, we will discuss in detail the case of one of the most puzzling dark TeV sources, HESS J1702-420. In particular, we will try to find out whether this source is a PeVatron.

In order to look for PeVatron candidates in the γ-ray sky, we may try to define a (tentative) list of their expected spectral characteristics:

- their γ-ray power law spectral index should be *hard*, i.e. not much steeper than $\propto E^{-2}$. Such spectrum, if produced via hadronic processes (section 1.3.1), has the same slope of the parent cosmic ray distribution. Therefore the modulation

[12] However, no matter how small the ratio $\epsilon_B / \sum_i \epsilon^i_{\mathrm{rad}}$, at sufficiently high energies the synchrotron losses will always dominate and rapidly cool down the electron spectrum inducing a high-energy cutoff in the final γ-ray spectrum.

by the energy-dependent escape from the Galaxy (equation 1.2) would allow to reproduce the measured cosmic ray slope $\propto E^{-2.7}$ at Earth;

- the γ-ray spectrum has to extend at least up to several tens of TeV, without a sharp high-energy cutoff. Ideally, hadronic γ-ray emission detected up to $E_\gamma \approx 100\,\mathrm{TeV}$ would imply the presence of $E_p = 10 \times E_\gamma \approx 1\,\mathrm{PeV}$ protons (see section 1.3.1);

We note however that such requirements are in most cases not sufficient to prove the PeVatron nature of an object, because leptonic processes can also produce similar spectra. Until recently one could often hear the argument that γ-ray emission above few tens of TeV must be hadronic, due to the Klein-Nishina suppression of the inverse-Compton cross section at high energies (see e.g. [45]). However, it is becoming increasingly clear that this is a crude simplification that does not hold in many situations. For example, as already discussed in section 1.3.2, [28] have pointed out that hard high-energy electron spectra yielding 100 TeV γ-rays are possible, if the inverse-Compton electron cooling dominates over synchrotron losses. Also, recent observations have shown that γ-ray emission above 100 TeV is often associated with powerful pulsars, which are mostly leptonic accelerators, rather than SNRs (see [46, 47] and also the discussion in section 8.4).

The rest of this chapter is dedicated to a brief description of all the sources that have been proposed, throughout the years, as PeVatron candidates.

1.4.1 Supernova remnants

In 1934 Baade and Zwicky introduced the concept of super-novae (SNe) and advanced the hypothesis that they could be the sources of cosmic rays [48, 49]. This posed the bases for the so-called *SNR hypothesis*, which has been until recent years the standard paradygm for the origin of Galactic cosmic rays. The main supporting arguments are two:

- energetically, SNe (of any type) exploding in our Galaxy at a rate ν_{SN} of ≈ 3 per century and liberating a kinetic energy (in the form of ejecta bulk motion) of $E_{\mathrm{SN}} \approx 10^{51}\,\mathrm{erg}$[13] can provide the power necessary to support the observed cosmic ray flux, $P_{\mathrm{CR}} \approx 10^{41}\,\mathrm{erg\,s^{-1}}$. Namely, if each SN uses a $\approx 10\%$ fraction of its kinetic energy to accelerate particles, the total power transferred by SNe to cosmic rays is

$$P_{\mathrm{SN}\to\mathrm{CR}} = 10\%\, E_{\mathrm{SN}}\, \nu_{\mathrm{SN}} \approx 10^{41}\,\mathrm{erg\,s^{-1}} = P_{\mathrm{CR}}\ . \tag{1.38}$$

- the previous argument is strengthened by the fact that the SN remnants are associated with strong collisionless[14] shock waves propagating through the ISM ahead of the expanding ejecta. This, together with the presence of magnetic turbulences clearly seen in the X-ray images of SNRs, make them the perfect places for the emergence of first-order Fermi acceleration (see section 1.2.1).

[13] Here, it is implicitly assumed that all SNe transfer a fraction 1% of their total gravitational energy ($\approx 10^{53}\,\mathrm{erg}$) into kinetic energy of the ejecta, while the rest is released in the form of neutrinos.

[14] SNR shocks are not mediated by particle collisions (as for the shocks created by supersonic aeroplanes in the atmosphere) but rather by electromagnetic interactions.

The SNR shock expands in the ISM as

$$R_{\rm shock} \propto t^{\alpha},\ v_{\rm shock} \propto t^{\alpha-1}\ . \tag{1.39}$$

This allows to divide the SNR lifetime into three phases:

Free expansion (ejecta-dominated) phase: at first the blast wave of SN ejecta expands unhindered into the surrounding ISM, traveling at supersonic speed ($v_{\rm shock} \approx 10^4\,{\rm km\,s^{-1}} \gg c_s^{\rm ISM}$, where $c_s^{\rm ISM} \lesssim 10^2\,{\rm km\,s^{-1}}$). It is a case of ballistic expansion, with $\alpha = 1$. This phase lasts until the mass of swept-up ISM material (heated, compressed and towed behind the shock) becomes comparable with the ejecta mass. This occurs a few centuries after the SN explosion when the shock radius is of the order of few pc, with the precise values depending on the (typically asymmetric) ISM density profile. At this point, the swept-up material accumulated behind the shock increases the shock inertia and starts decelerating its expansion;

Sedov-Taylor (adiabatic) phase: the shock slows down, $\alpha < 1$. For example, a uniform ISM density profile yields $\alpha = 2/5$ (the original solution found by Sedov and Taylor in the late '40s and '50s for the case of bombs). Instead, a stellar wind density profile decreasing quadratically from the star position yields a less pronounced deceleration: $\alpha = 2/3$. In this phase the expansion is adiabatic, meaning that total energy is still roughly conserved. The kinetic energy of the ejecta is stored as internal energy of the shocked ISM and used to accelerate particles at the shock, and all radiative energy dissipations are still negligible compared with the bulk inertia of the ejecta. But since the temperature drops with time ($T \propto t^{-6/5}$), at some point the shocked ISM nuclei start emitting a significant amount of thermal X-ray emission [50];

Radiative (snow plough) phase: eventually ($\approx 10^5\,{\rm yr}$ after the explosion), the plasma temperature becomes low enough ($\lesssim 10^4\,{\rm K}$) to allow the recombination of atoms. This becomes now the dominant process of energy dissipation, which makes the shell glow from the ultra-violet to the near infra-red bands and slows down the shock to $\alpha = 1/4$. After $\lesssim 10^6\,{\rm yr}$, the ejecta speed eventually reaches the speed of sound in the ISM. At this point, the shock disappears and the SNR finally merges with the ISM.

Throughout the SNR lifetime, particles from the swept-up ISM interact with the magnetic field turbulence around the shock and are accelerated via DSA (see section 1.2.1). Part of these particles are continuously advected toward downtream infinity, while those that remain tied to the shock are released into the ISM as a non-thermal spectrum when the shock ultimately dissipates. However since the highest energy particles may escape upstream of the shock at earlier times, at $t = \infty$ the SNR spectra can be steeper than the standard DSA prediction (equation 1.10). Significant particle escape starts taking place during the Sedov-Taylor phase, when the shock slows down and is no longer able to confine (and therefore also accelerate) the highest-energy particles. This means that the maximum particle energy $E_{\rm CR}^{\rm max}$ is reached at the beginning of the Sedov-Taylor phase.

The $E_{\rm CR}^{\rm max}$ can be determined in varous ways [51, 52]. In all cases, for a shock size $R_{\rm shock}$ and velocity $v_{\rm shock}$ one finds

$$E_{\rm CR}^{\rm max} \propto R_{\rm shock} v_{\rm shock}^2 BZ\ , \tag{1.40}$$

where $B \approx 3\,\mu G$ is the typical ISM magnetic field strength upstream of the shock and Z is the cosmic ray charge. Under realistic conditions, equation 1.40 yields $E_{\rm CR}^{\rm max} \lesssim 10^{13}\,{\rm eV}$ for protons, which is clearly insufficient to explain the cosmic ray spectrum up to the knee. However, if one considers also the non-linear DSA effects, plasma instabilities driven by the cosmic rays themselves can arise, leading to dynamo effects which efficiently ($\approx \times 100$) amplify the magnetic field ahead of the shock (see e.g. [53]). According to equation 1.40, this could bring the maximum proton energy up to the knee. X-ray observations of young SNRs provide indirect evidence of strong magnetic field amplification with resopect to the typical $B \approx 3\,\mu G$ ISM value. For example, well-known SNRs like Tycho and Cassiopea A exhibit narrow X-ray filaments that clearly outline the shock profile. Assuming that they result from the sudden synchrotron cool down of electrons in the strongly amplified magnetic field near the shock, one can estimate a $B \approx 100\,\mu G$ (see e.g. [54]) [15]. Also, the observation of fast time variability (on a yearly time scale) of synchrotron X-ray hot spots in the shells of young SNRs seems to confirm the presence of strong (altough in this case localized) magnetic fields, reaching $B \approx 1\,mG$ [56, 57].

Today, γ-ray observations have established that SNRs actually operate as cosmic ray accelerators. For example, the remnant W28 (G6.4-0.1) is firmly associated with γ-rays emitted by a nearby molecular cloud. However, there is no known SNR that unambiguously accelerates protons up to the knee. In most cases, a possible leptonic contribution to the γ-ray emission cannot be ruled out (e.g. [58]). Moreover, all known TeV-bright SNRs have steep spectra with maximum γ-ray energies around 10-20 TeV [59]. This poses the question whether SNRs can actually operate as PeVatrons, and casts a doubt on the standard SNR hypothesis for the origin of Galactic cosmic rays. It might be argued that, since the acceleration of particles at $E_{\rm CR}^{\rm max} \approx 1\,{\rm PeV}$ occurs in a very limited period of the SNR lifetime (at the beginning of the Sedov-Taylor phase), we are just not looking at the right time to see a PeVatron SNR. However, recent studies have showed that only SNRs resulting from exceptionally powerful ($E_{\rm SN} \gtrsim 4 \times 10^{51}\,{\rm erg}$) and rare ($\nu_{\rm SN} \approx 1/10^4\,{\rm yr}$) core-collapse SNe, for which low ejecta mass $\lesssim {\rm few} M_\odot$ and dense progenitor winds anticipate the beginning of the Sedov-Taylor phase to few years after the explosion, may accelerate light nuclei such as hydrogen and helium up to the knee [60]. In this scenario, the chances of ever detecting SNR PeVatrons are extremely faint.

1.4.2 Pulsar wind nebulae

Pulsars are rapidly-spinning (period of $P \approx 10^{-3} - 10^{1}\,{\rm s}$) and highly magnetized ($B_{\rm surface} \approx 10^{7} - 10^{15}\,{\rm G}$) neutron stars, with masses similar to the Sun but packed into $\approx 10\,{\rm km}$ radius compact objects. Their total spin-down luminosity is emitted in the form of pulsed electromagnetic radiation ($\approx 1\%$) and a magnetized wind of electron-positron pairs created by electromagnetic cascades in the pulsar *magnetosphere*. The pulsar slow-down from the initial period P_0 is characterised by the braking index n (for ideal magnetic dipole emission, $n = 3$):

$$\dot{\Omega} = -k\Omega^n \,, \tag{1.41}$$

where $\Omega(t) = 2\pi/P(t)$. Assuming $P_0 \gg P(t)$, one can use equation 1.41 to derive the so-called *spind-down age* of the pulsar, which provides a rough estimate for its true

[15] We note that other interpretations for these X-ray filaments are possible (see e.g. [55]).

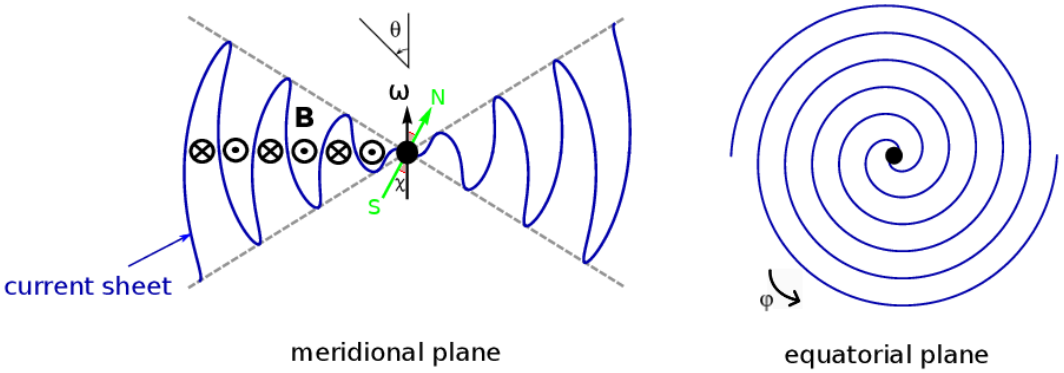

FIGURE 1.5: Diagram of the pulsar's current sheet geometry, at $r \gg r_{\rm LC}$. Adapted from [61].

age:

$$\tau_{\text{spin-down}} = \frac{P}{2\dot{P}} \,. \tag{1.42}$$

The magnetic field lines co-rotate rigidly with the pulsar, up to the distance at which they would reach the speed of light (*light cylinder*):

$$r_{\rm LC} = \frac{Pc}{2\pi} \,. \tag{1.43}$$

For millisecond (typical $P \approx 1\,$s) pulsars, the light cylinder has a radius of $r_{\rm LC} \approx 50\,$km (5000 km).

Beyond the light cylinder, the magnetic field lines open and the field topology smoothly changes from a dipolar geometry ($r \ll r_{\rm LC}$) to a monopolar (radial) one ($r \gg r_{\rm LC}$), giving rise to the so-called pulsar *striped-wind* [62, 63] (see figure 1.5). In this region, the wind assumes a split-monopole geometry in the equatorial (rotation) plane, in which two archimedean spirals $r(\phi) \propto \phi$ of magnetic field lines with opposite polarity alternate, separated by a *current sheet* in which $B = 0$. The current sheet is confined to a wedge $\pi/2 - \chi \leq \theta \leq \pi/2 + \chi$, where χ is the angle between the rotation and magnetic field axes of the pulsar, and carries away the pulsar's wind in the form of particles and Poynting flux. The wind *magnetization* σ_w is defined as the ratio between the magnetic energy and particle energy:

$$\sigma_w = \frac{B^2}{n_w \gamma_w m_e c^2} \,. \tag{1.44}$$

Eventually, the particle density n_w ($\propto r^{-2}$) drops to a level which is insufficent to maintain the current sheet, at which point the magnetic field lines reconnect and the wind terminates. There, a roughly standing termination shock (TS) is created ($R_{\rm TS} \approx 10^{19}\,$cm for the Crab pulsar) [64]. At the TS, the wind ram pressure is balanced by the confining external (shocked) medium, and the isotropized plasma is dispersed outward leading to the formation of a PWN, which usually evolves inside a SNR (*plerion*, or *composite* SNR). PWNe can be crushed by the SNR *reverse* shock, or sometimes (in cases of high pulsar kick velocity) be left to fade away without a central engine. The sizes of PWNe, determined by the length scale of the region in which electrons accelerated at the TS are advected outwards by the wind flow, strongly depend on their age, but typically are of the order of few pc. Outside the nebula, leptons propagate diffusively into the ISM and can create diffuse *halos* which

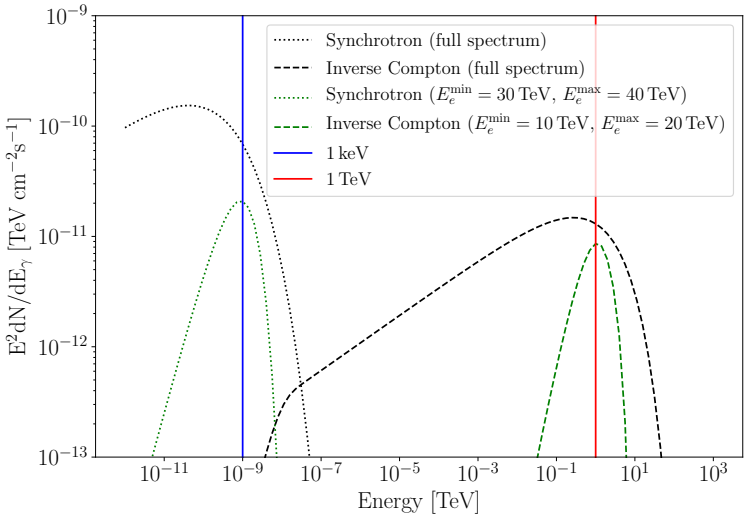

FIGURE 1.6: Synchrotron (inverse-Compton) emission from electrons with energy $30 \leq E_e \leq 40\,\text{TeV}$ ($10 \leq E_e \leq 20\,\text{TeV}$), shown by the green dotted (dashed) curves. The black curves indicate instead the full spectra obtained from a power law electron spectrum $\propto E_e^{-2.5}$.

have been recently discovered as a new source class in TeV γ-ray astronomy [65].

Pulsed emission from pulsars, attributed to synchrotron-curvature radiation in their magnetospheres [66], is generally detected only up to few tens of GeV [16]. At TeV energies, the detected γ-ray emission is instead non-pulsed and due to particles (mainly leptons) in the PWN region. Particles can be accelerated in different ways by pulsars, essentially depending on their (upstream) wind magnetization level [69, 70]. Multi-dimensional particle-in-cell (PIC) simulations have shown that, for an upstream wind magnetization $\sigma_w \gg 1$, most of the magnetic field energy is transferred to particles via magnetic reconnection (see section 1.2.2) upstream of the TS. Reconnection is triggered by the formation of X-points at the boundaries of isolated *plasmoids*, or magnetic islands, that rapidly grow and coalesce until the striped structure of the wind is disrupted at the TS. This process yields the formation of hard downstream electron spectra, $\Gamma_e \approx 1.2-1.5$. The highest-energy particles from reconnection populate a steep high-energy tail with slope $\Gamma_e \approx 2.5$, created by relativistic [17] first order Fermi acceleration at the TS. Instead, for moderately magnetized winds ($\sigma \approx$ few) the reconnection spectra are somewhat steeper, $\Gamma_e \approx 2.0-2.5$. We also notice that, based on recent simulation studies, millisecond pulars might be capable of accelerating ions (e.g. protons) in the magnetosphere up to PeV energies and beyond (see [71] and references thereis). This means that such objects might operate as PeVatrons, and also be responsible for part of the diffuse TeV emission (of hadronic origin) measured around the Galactic center region [72].

The non-thermal electrons accelerated by reconnection and/or shock acceleration at the TS can radiate via synchrotron emission (mainly in the X-ray, typically up to

[16] With remarkable exceptions such as the Crab pulsar, for which pulsed emission up to TeV energies has been detected by MAGIC [67]. H.E.S.S. has also detected, thanks to its largest telescope called CT5 (see section 2.3.1), pulsed emission from the Vela pulsar in the $20-100\,\text{GeV}$ range [68]. A follow-up H.E.S.S. Collaboration paper on Vela, announcing the detection of pulsed emission up to $\approx 40\,\text{TeV}$ with a remarkably hard power law spectrum ($\Gamma \approx 1.3$), is currently in preparation.

[17] Due to the high bulk speed of the wind.

tens of MeV) and inverse-Compton scattering off ambient photon fields in the multi-GeV and TeV γ-ray bands. The type and amount of radiation emitted by PWNe, together with their spatial dimensions, depends strongly on their age [73]. Figure 1.6 illustrates that, assuming a typical magnetic field $B \approx 10\,\mu G$ and CMB up-scattering, the electrons that are responsible for synchrotron X-ray emission at 1 keV (green dotted curve) are more energetic than those emitting inverse-Compton γ-rays at 1 TeV (green dashed curve). This, together with the fact that radiative losses scale like $\propto E_e^{-1}$ (see section 1.3.2), implies that electrons emitting in the X-ray band are cooled down faster than those emitting in the TeV range. Therefore, for old PWNe, the emission near (far away from) the pulsar is mainly found in the X-ray (TeV γ-ray) band. At the same time, the γ-ray spectrum is expected to steepen as a function of the distance from the pulsar's position, because only the lowest-energy particles can travel large distances without being quickly cooled down. This means that PWNe are typically characterized by energy-dependent morphologies, which is one of the arguments that have been used in the past to associate *dark* TeV sources (see the introduction of section 1.4) with evolved PWNe.

1.4.3 Diffuse emission around the Galactic center

The H.E.S.S. Collaboration (see chapter 2) has found evidence for the acceleration of PeV protons in the central molecular zone (CMZ) within ≈ 200 pc from the supermassive black hole at the center of our Galaxy, Sgr A* [74, 75].

The central γ-ray source HESS J1745-290, positionally coincident with Sgr A*, has a γ-ray spectral cutoff around ≈ 10 TeV. It is still unclear whether it is actually associated with Sgr A* or with a PWN on the same line of sight [76]. Searches for the variability of this source, that would constrain the PWN scenario, have been performed without leading to a detection by VERITAS [77], and are currently underway in H.E.S.S..

The γ-ray spectrum of the CMZ around Sgr A*, measured by H.E.S.S. up to ≈ 40 TeV, is compatible with hadronic emission from a cosmic ray proton distribution with a cutoff at $E_p^{\mathrm{cutoff}} \approx 1$ PeV [75]. Also, the estimated $\propto r^{-1}$ spatial distribution of cosmic rays in the CMZ is consistent with continuous particle injection in the region [74]. However, the level of this emission is too low to sustain the flux of PeV cosmic rays observed at Earth. This means that if sources in the CMZ (e.g. Sgr A*, star clusters, supernova remnants, millisecond pulsars) are responsible for the acceleration of all cosmic rays up to the knee, then the past activity in the region must have been much higher than today. Recent searches for a high-energy cutoff in the γ-ray spectrum of the diffuse emission around Sgr A* have led to unclear conclusions, with MAGIC reporting a 2σ hint for a spectral turnover around ≈ 20 TeV and VERITAS measuring a straight power law up to 40 TeV [77, 78].

1.4.4 Young massive stellar clusters

Young ($\lesssim 100$ Myr) and massive ($\gtrsim 10^4\,M_\odot$) stellar clusters (YMSCs) harbor plenty of powerful stars, whose interacting winds and SNR shocks can carve superbubbles in the ISM and produce efficient particle acceleration [79–81]. This is confirmed by the detected γ-ray emission from several such systems, such as the Cygnus OB2 and Westerlund 1 cocoons [82, 83]. For these two systems, the γ-ray spectrum and radial

cosmic ray profile are similar to the CMZ [83]. This can be seen as evidence that the YMSCs can operate as PeVatrons, and also that the diffuse emission from the CMZ might result from a superposition of unresolved clusters of powerful stars.

Recently, strong evidence of VHE and UHE γ-ray emission from the Cygnus cocoon region (near the Galactic longitude $l \approx 81^{\circ}$) has been reported by multiple experiments. HAWC has detected it up to 100 TeV, with a spectrum that is significantly better described by hadronic than leptonic emission models [84], while LHAASO has detected it with photons up to 1.4 PeV [47]. Also, the Tibet AS+MD experiment has detected four photons with energy > 398 TeV within 4° from the center of the Cygnus cocoon[18] [86]. All of these independent measurement concur in making the Cygnus cocoon one of the most compelling PeVatron candidates observed in the γ-ray sky.

1.4.5 Other PeVatron candidates

Beside the previously mentioned source classes, a few individual sources have also been proposed as PeVatron candidates. For example, it has been suggested that the *whole* cosmic ray spectrum between 200 GeV and the knee might be explained by the combination of fluxes from just two nearby sources [87]:

- between 200 GeV and 200 TeV, cosmic rays could be attributed to a 2-3 Myr old SN, for which independent evidence was found in ocean and lunar sediments;
- all the rest, from 200 TeV up to the knee, could be due to the 11 kyr old Vela SNR[19], located a the distance 270 pc (nearby, but outside the local superbubble).

In this scenario, the Vela SNR would be a proton PeVatron.

Another source that has been proposed as a PeVatron candidate is the remnant SNR G106.3+2.7, for which γ-ray emission up to 100 TeV has been detected by the HAWC and Tibet ASγ collaborations in good coincidence with a nearby molecular cloud [88, 89]. The emission is well described by hadronic models, but a leptonic origin associated with the Boomerang PWN, contained in the SNR and powered by the pulsar PSR J2229+6114, cannot be presently ruled out[20]. Finally, in part II of this thesis we will describe the case of the TeV source HESS J1702-420, which has also been proposed as a promising PeVatron candidate.

[18] Tibet AS+MD has also discovered two 100 TeV γ-ray sources positionally coincident with PWNe in the Cygnus OB1 and OB2 associations [85].

[19] Also known as Vela XYZ, or SNR G263.9-03.3, and associated with the TeV-bright Vela X PWN powered by the Vela pulsar (PSR B0833-45).

[20] Although recent observation by MAGIC might difavour this scenario [90].

Chapter 2

VHE γ-ray astronomy with H.E.S.S. and CTA

2.1 Introduction

The Earth's atmosphere is opaque to photons in the γ-ray energy band. Different experimental strategies are adopted, depending on the photon energy:

- in the high energy (HE) γ-ray domain, $0.1\,\mathrm{GeV} \lesssim E_\gamma \lesssim 100\,\mathrm{GeV}$, photons are directly measured by space-based experiments, such as the *Fermi* Large Area Telescope [91];
- at higher energies, $0.1\,\mathrm{TeV} \lesssim E_\gamma \lesssim 100\,\mathrm{TeV}$, we enter the so-called very high energy (VHE) range. Due to the steep decline of the typical source spectra with energy, photon fluxes in the VHE range are extremely low. For example, for a spectrum $\propto E_\gamma^{-2}$, the flux drops by six orders of magnitudes between 1 GeV and 1 TeV. Therefore, a $1\,\mathrm{m}^2$ collection area such as the one of the *Fermi*-LAT would be insufficient to detect VHE γ-rays at a reasonable rate. For this reason, VHE γ-ray astronomy relies on *ground-based* telescopes. A successful experimental concept is the imaging atmospheric Cherenkov telescope (IACT), examples of which are MAGIC, VERITAS and H.E.S.S.. Such instruments are able to detect the Cherenkov light created by the passage of ultra-relativistic particle showers, initiated by γ-rays and cosmic rays from space, through the atmosphere (see section 2.2). The images are recorded by fast and sensitive cameras, placed on the focal plane of a spherical or parabolic mirror. Camera images of γ-rays typically consist of two-dimensional Gaussians, resulting from the projection of the three-dimensional shower into the two-dimensional camera plane, while for background cosmic rays the images are more enlarged and irregular due to the presence of hadronic interactions and multiple sub-showers. Further details on the detection technique of IACTs may be found e.g. in [92, 93];
- at even higher energies, $100\,\mathrm{TeV} \lesssim E_\gamma \lesssim \mathrm{few\,PeV}$, one enters the ultra high energy (UHE) band. In this regime the experimental technique is that of water Cherenkov telescopes (WCTs). These experiments, such as HAWC, LHAASO and Tibet ASγ, directly detect particles from the air shower at ground level as they pass through tanks of water and emit Cherenkov light, rather than the Cherenkov light emitted while they are still in the air (as for IACTs).

A comparison of the sensitivities of the main currently operating and future γ-ray experiments can be found e.g. in [94].

In this chapter, we focus in particular on the IACT technique. First, section 2.2 provides a brief overview of the history and future of VHE γ-ray astronomy. Then, section 2.3 describes the H.E.S.S. experiment, used in this thesis, and section 2.4 briefly discusses CTA, the main project for the next generation of IACTs.

2.2 Brief history and perspectives

VHE γ-ray astronomy is based on two main physical ingredients: Cherenkov radiation and extensive air shower (EAS) physics. The former, discovered in 1934 by Pavel A. Cherenkov[1], consists of a form of ultraviolet and visible radiation, produced by particles moving faster than light through a medium (for example, the atmosphere). EASs are instead cascades of secondary particles initiated by the interaction of γ-rays and cosmic rays with the atmosphere, that were first described by Pierre Auger in 1939 [95]. Further details on these topics may be found for example in [93]. In 1953, W. Galbraith and J. V. Jelley proved that VHE γ-ray astronomy was possible, by building a pioneering detector made of a single photo-multiplier tube (PMT)[2] illuminated by a small mirror [96]. During clear dark nights, they observed the first flashes of Cherenkov light associated with EASs (mostly from cosmic ray events).

In 1968, at the Fred Lawrence Whipple Observatory in Arizona (USA), the construction of the first IACT with a 10 m diameter dish was completed. The Whipple telescope originally had a single PMT, but in 1983 it was equipped with a 37 pixel imaging camera, with multiple PMTs inside each pixel. The main challenge for this kind of telescope was the presence of cosmic ray (background) showers, with a rate as high as $10^4 - 10^5$ times above the the γ-ray (signal) count rate. The first background rejection methods were introduced in 1977, by T.C. Weekes and K.E. Turver [97]. Later, in 1985, A.M. Hillas introduced the *Hillas parameters* method for the analysis of EAS images (see section 2.3.2), that greatly improved the level of background rejection and the precision of the event reconstruction. Thanks to this technique, in 1989, the Whipple Collaboration detected for the first time the Crab nebula above 0.7 TeV, at 9σ confidence level [98]. In 1996, after a camera upgrade to 109 pixels, Whipple announced the discovery of a second source, this time extra-Galactic: the blazar Markarian (Mkn) 421 [99]. This discovery confirmed that the Universe contained extreme and violent objects, that can be discovered and studied using VHE γ-ray telescopes.

In 1992, on the occasion of an international workshop at Palaiseau (Île-de-France), the VHE astronomy community gathered together with the aim of designing a new *Major Atmospheric Cherenkov Detector* [100]. This ambitious project did not take off at the time, and instead the growing ideas and excitement of the community led to the parallel development of several new IACTs, each one exploring different design solutions, which started coming online already in the '90s. Among them were the CAT (Cherenkov Array at Themis) telescope [101], which was equipped with an unprecedently fast and fine-grained camera consisting of 546 pixels with an angular size of 0.12° each. HEGRA (High-Energy-Gamma-Ray Astronomy) was the

[1] Nobel prize in 1958, shared with Ilya Frank and Igor Tamm who developed the mathematical theory in 1937.

[2] A PMT is a device able to convert the faintest incident light (in the ultra-violet, visible and near infra-red bands) to an electric current (in units of *photo-electrons*, or p.e.) through a photoelectric effect on a photocatode (efficiency of $\approx 10\%$), and amplify it by a large factor ($\gtrsim 10^5$ in number of p.e.) via a series of dynodes contained in a vacuum tube to yield a measurable signal.

first experiment which combined together multiple telescopes in a IACT array, thus demonstrating the benefits of *stereoscopy* [102]. In 1997, HEGRA confirmed the detection of Mkn 421 [103], boosting confidence in the field. In the late '90s and early '2000s, the construction of the current-generation IACTs began. The main idea was to combine together the best aspects and all the practical knowledge accumulated thanks to the previous generation facilities: large mirror dishes (from Whipple) to lower the energy threshold, fast and finely-grained cameras (from CAT) to efficiently record the EAS images, and multiple telescopes (from HEGRA) to achieve a better event reconstruction and background rejection. In this context, the present-day major IACT facilities were developed: MAGIC [104], VERITAS [105] and H.E.S.S. (see section 2.3). It is also worth mentioning the ASGAT, THEMISTOCLE and CELESTE experiments, all built on the same decommissioned solar farm (Themis) in the French Pyrénée. ASGAT and THEMISTOCLE used an approach similar to IACTs, while CELESTE featured a $100\,m$ high tower equipped with PMTs where the Cherenkov light from EASs (reflected by mirrors on the ground) was collected and focused on a fast camera, the same technique later used by STACEE [106]. Between the '90s and early '2000s, these experiments confirmed the Crab Nebula emission at VHE energies [107–109].

IACTs have two main weaknesses: first of all, they have relatively small *field of views* (FoVs)[3], with tipical radii of a few degrees. Also, IACTs have short duty cycles (maximum $\approx 20\%$). Indeed, to detect the pool of Cherenkov light emitted by EASs, the level of background light has to be very low, limiting the operational time of IACTs to clear and (at least partially) moonless nights. To overcome these limitation, other experimental designs have been explored. The most successful so far is the WCT technique, which consists in building vast arrays of water tanks at high-altitude locations, and to detect particles of the EAS using PMTs directly in the tanks. Instead of pointing to a given sky location, these experiments can detect events from nearly the whole visible sky at the same time, which makes them perfect to perform survey studies. However, the WCT technique also has its own drawbacks. In particular, since the EASs from low-energy γ-rays are more likely to be absorbed by the atmosphere before reaching the ground, the detection energy thresholds is much higher for WCTs than IACTs. In fact, WCTs reach their best sensitivities at UHE energies, 1–2 order of magnitudes higher than IACTs. Also, their design implies a significantly poorer angular and energy resolution than the IACTs. For all these reasons, the WCT and IACT techniques are considered complementary.

Examples of WCTs include MILAGRO [110], operated from 1999 to 2008 at an altitude of 2630 m in the Jemez mountains near Los Alamos (New Mexico), and the more recent High Altitude Water Cherenkov (HAWC) observatory [111], completed in 2015 at 4100 m above sea level on the volcano Sierra Negra (Mexico). With an instantaneous FoV covering 15% of the sky, HAWC is able to observe two-thirds of the sky in 24 hours. Another example is the Tibet ASγ array [112], which has been recently upgraded with the addition of a muon detector to better reject hadronic showers (Tibet AS+MD [113]). This experiment has already reported the first detection of γ-rays beyond 100 TeV from an astrophysical source (the Crab nebula) [114], and the measurement of diffuse γ-ray emission up to PeV energies from the Galactic disk [86]. Finally the LHAASO experiment, located at an altitude of 4,410 m in the

[3] The term FoV indicates the angular aperture (sometimes also the solid angle) on the sky that is visible by a telescope with a single pointing. We notice that the typical IACT FoVs are small only compared to all sky facilities such as the WCTs and solar farm experiments, but they are large compared for example to X-ray telescopes (e.g. XMM-Newton has a FoV radius of $\approx 0.25^{\circ}$ only).

Sichuan province of China, has very recently (late 2019) come online and already made history, with the first detection of UHE γ-rays (with a maximum energy of 1.4 PeV) from 12 astrophysical sources [47].

The future of the IACT thechnique is represented by the Cherenkov Telescope Array (CTA, section 2.4), that will gather scientists and engineers from multiple countries in a worldwide effort to further explore the high-energy Universe. This is the result of a series of seven international workshops held between 1992 and 2005 at Palaiseau (France), Padova (Italy) and Snowbird (USA). The next generation of WCTs is instead represented by the Southern Wide-field Gamma-ray Observatory (SWGO), that will be the first such instrument to be located in the Southern emisphere and will observe for the first time the Galactic plane and Galactic center region in the UHE band.

2.3 H.E.S.S.

The High Energy Stereoscopic System (H.E.S.S.) is an array of five IACTs located in the Khomas Highland of Namibia, 1800 m above sea level[4]. The site is in a remote location, far away from human settlements, with very limited light and air pollution. The semi-desert climate favors clear cloudless skies, and the proximity with the Tropic of Capricorn makes it a perfect location to observe the Galactic disk. The design of the original array (H.E.S.S. I), operating since 2003, involved four 12 m diameter telescopes (CT1–4) at the corners of a 120 m $\times$ 120 m square. This design configuration allows to achieve a good stereoscopic view of the Cherenkov light pool (with diameter $\approx$ 250 m) of EASs with multiple telescopes.

The trigger system of the CT1–4 array is a three-steps process [115] based on successive pixel, telescope and array trigger criteria. First, a pixel trigger threshold $n_{\text{p.e.}}$ is defined, corresponding to the minimum number photons that produced photoelectrons via photoelectric effect within a pixel during a $\approx$ 1.5 ns integration time. Then, a telescope is considered triggered if at least n_{pix} exceed the $n_{\text{p.e.}}$ threshold in a given time window ($\approx$ 13 ns). Standard choices for $n_{\text{p.e.}}$ and n_{pix} are 4 and 3, respectively. Finally, the simultaneous (within $\approx$ 80 ns) trigger of $n_{\text{tel}} \geq 2$ cameras is required to initialize the data-readout from the central data acquisition (DAQ) system. The DAQ serves the purpose of collecting data and storing them on local servers, before they are dispatched to Europe[5]. The H.E.S.S. operation schedule consists of successive *observations* (also called *runs*) of 28 min, a nominal time that can occasionally be shortened by worsening weather or Sun/Moon rising phases. This short pointing strategy helps to avoid variations of the observation conditions within a run. During data taking, a *real-time analysis* is run, to inspect the data quality and identify possible issues. In 2012, a second phase began (H.E.S.S. II) with the addition of a 28 m diameter telescope (CT5) at the centre of the grid, which reduced the detection energy threshold from $\approx$ 100 to $\approx$ 30 GeV.

In the following sections, we will briefly describe the technical design of the H.E.S.S. telescopes (section 2.3.1) and the analysis of H.E.S.S. data (section 2.3.2).

[4] This altitude represents a good compromise, between the increase in atmosphere transparency to Cherenkov light at higher altitudes and the better calorimetric measurement of the shower energy at lower altitudes, given by the higher probability that showers have completely faded before reaching the ground.

[5] Traditionally in the form of magnetic tapes [116], now via optical fibers.

2.3.1 Characteristics of the H.E.S.S. array

The CT1–4 array

Each of the CT1–4 telescopes is equipped with a 12 m diameter mirror dish with a focal length f of 15 m, and a $r = 65$ cm radius camera placed at the focal point. This means that the single-telescope FoV is a circle with radius $\arctan(r/f) \approx 2.5^{\circ}$.

The mirrors are segmented into 382 circular facets of radius 30 cm, following a Davies-Cotton optical design [117]. In order to align the mirror facets, a star on the focal axis is observed by a CCD camera placed at the center of the dish, then each facet generates a light spot which is matched with the star image. Each telescope is mounted on a mechanic support that allows a relatively rapid (maximum $100^{\circ}\,\mathrm{min}^{-1}$) repointing of the telescopes, by rotating the base support and/or the mirror dish in an altitude-azimuth reference frame.

The telescope cameras follow a modular design, to ease their maintenance. Each camera is made of 60 *drawers*, each one grouping 16 PMTs and related electronics and representing a camera pixel. In front of each drawer there is a funnel plate, equipped with Winston cones to reduce the light loss in the gaps between pixels [118]. In 2017, the CT1–4 cameras were upgraded (entering a phase called H.E.S.S. IU [119]) to a design similar to the NectarCAM concept, developed as the a prototype for the CTA medium-sized telescope cameras (see section 2.4). The camera replacement was made necessary by the significant aging and performance degradation of the old cameras. Also, it allowed for the CT1–4 energy threshold and trigger deadtime to be reduced, thus increasing the overlap with the CT5 energy range and improving the stereoscopy capabilites of the array.

CT5

The fifth telescope of the H.E.S.S. array, inaugurated in september 2012, is currently the largest IACT in the world. The mirror dish, made of 875 hexagonal facets of 45 cm radius, has a diameter of 28 m. The CT5 camera, containing 2048 PMTs grouped by 16 into 128 drawers, is much larger and finer-grained than those of CT1–4. In 2019 the camera was upgraded to the FlashCam design, developed for CTA (see section 2.4). Since the ratio between the camera radius ($r = 100$ cm) and the focal length ($f = 36$ m) is smaller than for CT1–4, the FoV of CT5 is also smaller: $\arctan(r/f) \approx 1.6^{\circ}$ in radius.

We will not go into further details on CT5, because all the results presented in this thesis were obtained using CT1–4 data only. The reasons for this are twofold: first of all, the main interest of CT5 resides in the possibility of lowering the analysis energy threshold, which, although potentially useful, is not a primary necessity for PeVatron studies. Secondly, the analysis configuration used in this thesis was optimized to collect a large number of high-energy events (see section 2.3.3). Those typically create large shower images in the telescope's cameras, that the smaller CT5 FoV would likely truncate thus complicating the data analysis.

Complementary instruments for atmospheric monitoring

A permanent monitoring of the atmospheric conditions is crucial to assess the data quality on a run-by-run basis. For this purpose, several instruments are present on site. Among them:

- each telescope is equipped with an *infrared radiometer*, used to monitor the presence of clouds in the FoV of the telescope;
- a *ceilometer*, i.e. a laser beam scanning the sky and detecting light back-scattered by clouds and aerosols;
- an *optical telescope* observing the night sky stars, to measure atmospheric transmission;
- a *weather station*, to constantly monitor the temperature, velocity and direction of winds and the level of air humidity.

2.3.2 Low-level data analysis in H.E.S.S.

The analysis of IACT data consists of several steps. In preparation for the future analysis of CTA data, the concept of data levels (DLs) has been introduced, with each DL corresponding to a different stage of data processing [120]. In this section we present an overview of the data analysis pipeline from the lowest (DL0) to the third (DL3) stage. This is called the *low-level* analysis, whereas the steps $\geq$ DL3, on which this thesis is mainly focused, are considered *high-level* analysis and will be described in chapter 3. Often, throughout this section, examples of algorithms and terminology unique to H.E.S.S. will be made, even if the presented concepts are in general valid for any IACT.

The DL0 stage corresponds to the *raw* camera data. In order to correct the signal charge of each pixel for instrumental effects, a first step called *calibration* is performed [121]. In this process, one corrects the signal within each pixel for the expected *pedestal*, i.e. the background counts due to electronic/thermic noise and the night sky background (NSB) light[6]. A *flat-fielding* factor, which takes into account the relative difference in optical and quantum efficiencies between pixels, is also applied. At this stage, one may also discard broken pixels and correct for imperfections of the pointing direction or for variations of the instrument's *optical efficiency*[7].

After calibration, the data are at the DL1 stage. To pass to the DL2, two analysis processes are performed: *image cleaning* and *event reconstruction*. The first consists of removing as much as possible of the NSB from the camera images. This is usually done with a double-threshold algorithm, that masks off pixels containing pure noise. The event reconstruction then consists of determining the physical properties of the air shower, that are linked with the energy and direction of the primary particle. In H.E.S.S., one can choose among several different reconstruction methods [93]:

[6] The NSB is a combination of starlight, diffuse luminosity from the Galaxy, the Earth's turbulent atmosphere, moonlight albedo and light reflection on the telescope structures.

[7] This is a combination of several hardware-related parameters, such as the efficiency of the photocatodes in the PMTs, the mirror reflectivity level and the status of the funnel plate. The optical efficiency is expected to degrade on a timescale of years, leading to a reduction in the image intensities compared to ones expected from simulations, which causes a bias in the reconstructed event energy. Being calibrated using muons rings, it is also known as *muon efficiency*.

Hillas parameters [122]: This method is essentially a principal component analysis (PCA), which decomposes the camera image into its moments. The images of γ-ray showers are assumed to be ellipses, whose properties are linked with the direction and energy of the events. Examples of Hillas parameters include the the distance between the camera center and the image center of gravity, the ellipse height, width and inclination angle, and the total charge (in units of photo-electrons) deposited in the cameras. The latter, together with the altitude of maximum development of the shower, determines (by means of Monte Carlo simulations) the reconstructed energy of the event. Stereoscopy is used to reconstruct the event direction by intersecting the major axes of the shower images in the camera plane and on the ground;

Maximum likelihood methods: This is a class of methods that are all based on the assumption of a three-dimensional shower model, whose parameters (related with the event's properties) are adjusted by means of a maximum likelihood fit to the pixel-by-pixel amplitudes in the telescope's cameras. The only difference between them is in the kind of models that are adopted. They are:

Model 3D [123]: In this case the points of Cherenkov light emission from EASs (also called the Cherenkov *photosphere*) are modeled in a fully analytical way, as three-dimensional symmetric Gaussians;

Model ++ [124]: Here the Model 3D concept is brought one step forward by introducing semi-analytic shower models generated from simulations;

ImPACT [125]: In this method, Monte Carlo simulations of air showers are used to build a lookup table of camera image templates, for each realization of air shower parameters. This way, the templates can be matched with the measured images, allowing to efficiently reconstruct the event properties.

After reconstruction, the data are not anymore stored "by camera" but "by event" in the data level 2 (DL2). Each event has been assigned own characteristics, like reconstructed energy, direction and time of arrival, but no distinction has yet been made between photons (signal) and cosmic rays (background). For this, dedicated γ/hadron separation techniques are now applied, which classify events as *γ-like* or *hadron-like* depending on a certain number of parameters such as the shower lateral development and its irregolarities (both enhanced in hadronic with respect to γ-ray induced showers). This step drastically reduces the hadronic background, but inevitably leaves a number of *residual* backround events due to the presence of hadronic showers with a roughly γ-like shape. This residual hadronic background has to be properly estimated or modeled, during the high-level analysis, in order to measure the γ-ray signal (see chapter 3). The strictness of the hadron rejection is defined by the prechosen cut configurations, which for H.E.S.S. are standardized into few cathegories such as *standard*, *hard* or *loose*, that are optimal for different science cases [115]. In H.E.S.S., several γ/hadron separation methods are used:

Hillas [115] Based on the same Hillas parameters used for the event reconstruction, this method separates γ-like from hadron-like events based on the length (L) and width (W) of their shower images. Monte Carlo simulations of γ-ray events are run to compute the expected quantities $\langle L \rangle$ and $\langle W \rangle$ and dispersions σ_L and σ_W, as a function of the image amplitude in the cameras, impact parameter and pointing zenith angles. Then, for each camera i and parameter P ($P = L$

or W), a *scaled* quantity is built as:

$$P^i_{\text{scaled}} = \frac{P^i - \langle P \rangle}{\sigma^i_P} \tag{2.1}$$

Finally, the *mean reduced scaled* length (MRSL) and width (MRSW) are computed, by averaging over all cameras (after cleaning):

$$\text{MRSP} = \frac{\sum_{\text{i=1}}^{N_{\text{tel}}} P^{\text{i}}_{\text{scaled}}}{N_{\text{tel}}} \tag{2.2}$$

The expected distributions of MRSL and MRSW for γ-rays (from simulations) and hadrons (from real data) are significantly different, but partially overlap (see e.g. figure 7 of [115]). This confirms that the rejection of a certain number γ-rays and the approval of γ-like hadronic events are inevitable.

Model 3D / Model ++ In this case, the discrimination technique relies on the goodness of fit of an analytic (Model 3D) or semi-analytic (Model ++) three-dimensional EAS model to the camera images.

Muli-Variate Analysis (MVA) This technique relies on the use of boosted decision trees (BDTs) [126]. In a decision tree, each event is defined by a finite set of parameters, which are tested one by one to determine if they are more γ-like or hadron-like. Each test represents a binary *branching* of the tree, which moves the event toward the signal or background *leaf*. The tree is trained on a sample of simulated γ-ray and real cosmic ray events, to *learn* the proper pass/fail criteria. Since the outcome of a single tree might be affected by statistical fluctuations, usually many trees are combined together in a *forest*. During the training procedure of the forest, a *boost weight* is assigned to events that got misclassified in the building of the previous tree, which improves the convergence efficiency of the forest toward the correct outcome (*AdaBoost* [127]). After the training, each tree can be fed the characteristics of a real event to which it assignes a signal ($+1$) or background (-1) label. Then, by computing a weighted mean over the whole forest, an overall label $\in [-1, 1]$ is obtained, which meaures the *gammaness* of an event. Finally, the event is kept or rejected, depending on the chosen gammaness cut. In H.E.S.S., at least two such schemes have been proposed, both based on the TMVA package [128]:

- one, called Paris-MVA [129–132], uses a set of 8 parameters: the scaled Hillas height and width, three parameters inherited from the Model 3D reconstruction scheme, and 3 more that were expressly developed for Paris-MVA [129];
- another called *Zeta MVA* uses a set of 6 parameters: two are the scaled Hillas height and witdth, and 4 are derived from the ImPACT event reconstruction [133].

The γ/hadron discrimination step gets the data to the DL3 level, where the remaining events are all γ-like. The *high-level* analysis is then performed on DL3 data to extract physical quantities and high-level information on the observed phenomena. More details on this are provided in the next chapter.

2.3.3 The HAP-Fr analysis chain

With the term *analysis chains* we refer here to the possible pipelines that can be used to perform the low-level data analysis. Each chain adopts a different combination of (i) EAS simulations, (ii) detector simulation, (iii) calibration, (iv) reconstruction and (v) γ/hadron discrimination methods, as well as different software frameworks and code languages. The three main analysis chains used in H.E.S.S. are *Paris Analysis* (PA), *HAP-Hd* (for HAP-Heidelberg) and *HAP-Fr* (for HAP-France), where HAP stands for H.E.S.S. Analysis Package. In this thesis, all results were obtained using the HAP-Fr chain [131].

In HAP-Fr, the event reconstruction can be done either with the Hillas or Model 3D methods, while the γ/hadron discrimination is performed with Paris-MVA. HAP-Fr is built on the Storage and Analysis Software at H.E.S.S. (SASH) framework [134] and written in C++ (using ROOT). The Monte Carlo simulations of air showers and telescope response functions are respectively based on the KASCADE [135] and SMASH [136] packages. KASCADE simulates the development of EASs from the first interaction point in the atmosphere to their complete absorption. Several processes are taken into account: pair production, bremsstrahlung, Compton scattering, ionization of air molecules by electrons and annihilation of e^+/e^- pairs. The Cherenkov light yield of each particle in the shower is computed individually, and then summed with the other particles' contributions. From these simulations, only the Cherenkov photons that are intercepted by the telescope's mirrors are retained. Each photon is followed individually along its path to the detector, whose geometry and electronic components are simulated by the SMASH software.

The HAP-Fr chain comes in three possible *configurations*, called *elm*, *ash* and *he*. The *he* (for *high-energy*) configuration, used in this thesis, was developed to fully exploit the H.E.S.S. potential in the search of PeVatrons, by maximizing the number of events detected at high energy. This was achieved by relaxing the event selection cut on a parameter called *LocalDistance*, which measures the distance between the center of gravity of a shower and the camera center. A hard *LocalDistance* rejects events with truncated images and achieves better event reconstruction performance. Instead, in the *he* configuration, a loose *LocalDistance* cut was used to achieve a significant improvement of the telescope's *effective area* (see section 3.2.1, $\approx \times 2$) and sensitivity ($\approx \times 1.5 - 2$) at high energies, at the expense of a modest degradation of the angular resolution ($\approx +25\%$). In the *he* onfiguration, the event reconstruction is made with Model 3D, except for the cases of non-convergence of the likelihood fit, in which case the standard Hillas method is used. The γ/hadron discrimination is made with Paris-MVA, optimized to maximize the signal/background ratio for a source with 10% of the Crab nebula flux above 1 TeV and power law index $\Gamma = 2.3$. This analysis configuration for the moment has been tested and validated only for high-energy ($E \gtrsim 1\,\mathrm{TeV}$) analyses, while at lower energies the degradation of the angular resolution might lead to systematic effects.

2.4 CTA

The Cherenkov Telescope Array (CTA) represents the future of IACT γ-ray astronomy. It is a worldwide project, involving a Consortium of more than 200 institutes from 31 countries. CTA will provide unprecedented sensitivity, energy and angular

resolution for γ-rays in the energy range $20\,\mathrm{GeV} \lesssim E_\gamma \lesssim 300\,\mathrm{TeV}$. It will be operated (for the first time in the field of VHE γ-ray astronomy) as a proposal-driven and open *observatory*, called CTAO. This means that a certain time fraction will be dedicated to guest scientists, who will propose observations and obtain (pre-processed) DL3 data to be analyzed with the official high-level software (called Gammapy, see section 3.4.1). Then, after a limited proprietary period (1 year), data will be made openly available through the CTA data archive (similarly e.g. to the Fermi-LAT Data Server).

CTA will consist of two arrays, one in the Northern and one in the Southern hemisphere. The Northern array is under construction at the MAGIC site at La Palma (Canary islands, Spain), while Southern array will be deployed at the ESO site at Cerro Paranal in the Atacama desert (Chile), after the necessary infrastructure (including roads) will be in place. To achive a good sensitivity over three orders of magnitude in γ-ray energies, CTA will feature three classes of telescopes:

Large-size telescope (LST): Below $\approx 150\,\mathrm{GeV}$, the Cherenkov light pools generated by EASs are dim, yielding at most few Cherenkov photons per m^2 at the shower core at ground level [137]. A large mirror surface ($23\,m$ in diameter) is thus needed, to distinguish EAS signals from the NSB and achieve a correct event reconstruction. The Northern CTA site will host four closely ($\approx 100\,m$) spaced LSTs, with parabolic mirror design and focal length of $28\,m$, while none will be deployed at the Southern site. At La Palma, a first prototype LST, called LST-1, was completed in October 2018. The LST-1 is currently undergoing calibration (also cross-calibration with MAGIC [138]) phases, and has already detected photons from the Crab nebula [139–141]. The camera of the other LSTs will likely follow the design of the LST-1 camera, yielding a FoV radius of 2.25°. More details (updated to 2019) may be found e.g. in [142].

Medium-size telescope (MST): Between $\approx 150\,\mathrm{GeV}$ and $\approx 5\,\mathrm{TeV}$, which is the core energy range of CTA, the Cherenkov light pools produced by EASs are bright enough to allow the use of smaller mirror dishes ($11.5\,m$ in diameter). Also, increasing the number of telescopes enhances the effective area of the array and allows to make an optimal use of stereoscopy. For these reasons, the Northern (Southern) CTA site will be equipped with 9 (14) MSTs, with numbers that may increase based on the amounts of available funds. There are two camera concepts currently under development for the MST: the NectarCAM [143] (similar to the LST-1 camera and already tested with the CT1–4 H.E.S.S. telescopes [144]) for the Northern array, and the FlashCAM [145] (tested on the large H.E.S.S. II telescope) in the South. The MSTs will have a large FoV diameter of $\approx 8°$. A first complete MST prototype (mounting a NectarCAM) has been deployed in Berlin in 2012, and is currently undergoing performance testing and structure monitoring operations [146].

Small-size telescope (SST): Between $\approx 5\,\mathrm{TeV}$ and $\approx 300\,\mathrm{TeV}$, γ-rays create bright images which are easily separated from the inconspicuous NSB and cosmic ray backgrounds. However, at the such high energies the flux of photons reaching the Earth is very small. This means that to detect a sufficient number of γ-rays in a reasonable amount of time, arrays with huge collection areas are needed. One way to achieve this is spreading a large number of small-sized (to reduce costs) telescopes across a vast area on the ground. Therefore, the Southern CTA site will host 37 SSTs. At the Northern site instead no SST will be built, because of the lack of physical space at the Roque de los Muchachos site and

the fact that the Galactic center region (expected to host the largest number of PeVatrons) is not observable from there[8]. The SST construction will likely be based on the ASTRI (Astrofisica con Specchi a Tecnologia Replicante Italiana) [147] design with CHEC (Compact High Energy Camera) cameras [148], yielding a single-telescope FoV diameter of 10.5°.

[8] Altough we note that there are promising PeVatron candidates, such as the Cygnus cocoon ($l \approx 81^{\circ}$), which would be observable only from the Northern CTA site.

Chapter 3

Advanced high-level analysis of VHE γ-ray data

3.1 Introduction

The high-level analysis of IACT data consists of all those operations $\geq$ DL3 that produce physical results such as maps, spectra, lightcurves[1] and catalogs (see figure 3.1). It may be either conducted using private instrument-specific software tools (e.g. HAP in H.E.S.S.), or via open-source analysis packages like Gammapy (section 3.4.1) and ctools [149]. The latter option potentially offers more code flexibility and verification, as a result of an open developer base and the public availability of the source code. In this thesis, HAP was used only as a low-level analysis tool, while the high-level analysis was performed with Gammapy.

To perform the high-level analysis with open tools, the DL3 data need first to be exported from their instrument-specific storage format (e.g. ROOT for H.E.S.S.) to a common one, agreed upon by the scientific community. The format that is currently under development for the future CTA observatory relies on the flexible image transport system (FITS) [150], which allows one to serialize event lists, meta data (e.g. the observation target) and run-specific instrument response functions (IRFs) into flexible storage bundles called header-data units (HDUs). The DL3 FITS files are the entry point for the high-level analysis with open source tools. The high-level analysis can then be further divided into two steps. The transition from DL3 to DL4 corresponds to the *data reduction* step from event lists to high-level analysis containers (called `Datasets` in Gammapy), while at the highest level (DL5) one finds data products such as maps, spectra, lightcurves, sky surveys, source catalogs and population studies.

This chapter is structured as follows. In section 3.2 and 3.3 we describe some of the building blocks of the high-level analysis, such as the IRFs and the counts statistics. In section 3.4 instead we provide an overview of the main high-level analysis techniques in VHE γ-ray astronomy, with a special attention to their implementation in Gammapy.

[1] In this thesis the temporal evolution of sources was not studied, which is why the construction of lightcurves will not be treated in this chapter.

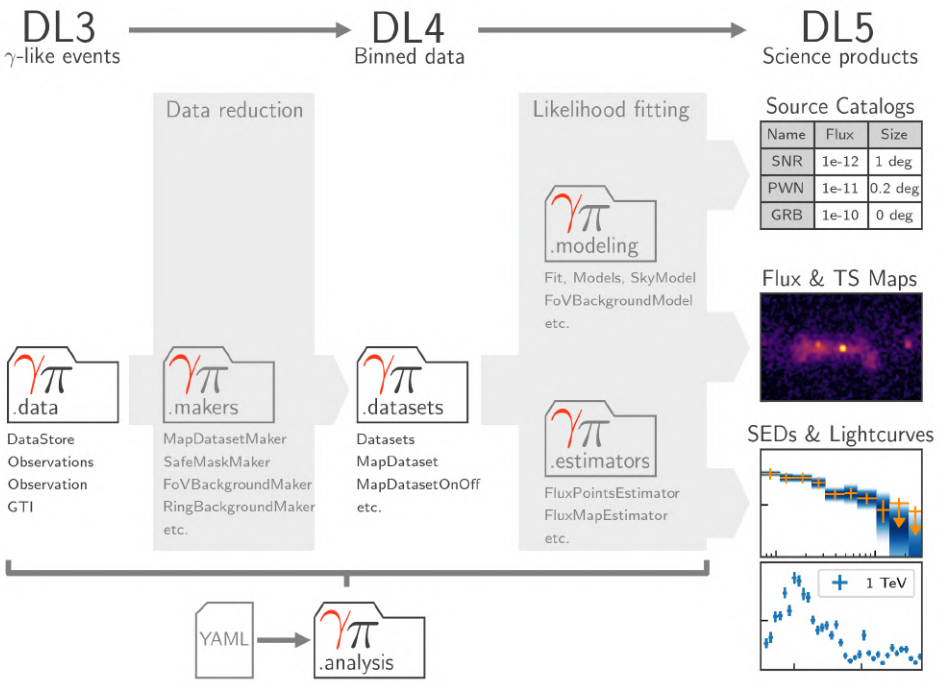

FIGURE 3.1: High-level γ-ray data analysis workflow from DL3 to DL5, and its structure in the Gammapy package. The folder icons represent the corresponding Gammapy sub-packages. From the Gammapy documentation.

3.2 Instrument Response Functions

The IRFs encode our knowledge of the instrument performance and reconstruction error, obtained either by means of Monte Carlo simulations or using dedicated observations. They are the *effective area*, *energy dispersion* and *point spread function* of the instrument (see sections 3.2.1- 3.2.3). Their purpose is to link together the *true* and *reconstructed* event parameters, such as their energy and arrival direction. There is also a fourth IRF, called the *FoV background model* (section 3.2.4), which has been recently introduced to carry out three-dimensional analyses.

In practice, all IRFs are strongly dependent on observation conditions such as the pointing zenith angle and the instrument optical efficiency. That is why they are usually computed in the form of multidimensional lookup tables, that can be interpolated to assign tailored IRFs to each individual observation. An important assumption, which is made whenever computing the predicted number of photons from an astrophysical source, is that the IRFs are independent from each other and can be factorized as separate functions (see e.g. equations 3.27 and 3.31). In cases where such hypothesis does not hold, systematic effects may arise.

3.2.1 Effective area

The effective (or *collection*) area, A_{eff}, represents the effective detection surface of the array (units of m^2). It results from a combination of the geometric area of the Cherenkov light pools intersecting at least 1 telescope (A_{geom}), the array detection

efficiency (η) and the chosen analysis cuts:

$$A_{\rm eff}(E_{\rm true}, \mathbf{x}_{\rm true}, \xi) \propto A_{\rm geom} \times \eta(E_{\rm true}, \mathbf{x}_{\rm true}, \xi) \,, \tag{3.1}$$

where $E_{\rm true}$ is the true event energy, $\mathbf{x}_{\rm true}$ the true FoV position and ξ defines the observation conditions such as pointing zenith angle and optical efficiency. Clearly, the higher the number of telescopes the larger is the $A_{\rm geom}$ factor of the array, which is why the Southern CTA site will host a large number of SSTs to be able to detect rare high-energy events with good effective area. The detection efficiency η can be determined by computing, for each possible $(E_{\rm true}, \mathbf{x}_{\rm true}, \xi)$ set, the fraction of simulated γ-ray events passing the γ/hadron separation test.

3.2.2 Energy dispersion

The energy dispersion (EDisp) represents the probability density function (PDF) for the reconstruction of an energy $E_{\rm reco}$ when the true event's energy and direction are $E_{\rm true}$ and $\mathbf{x}_{\rm true}$:

$$\text{EDisp} = \text{EDisp}(E_{\rm reco} | E_{\rm true}, \mathbf{x}_{\rm true}, \xi) \,. \tag{3.2}$$

The EDisp is a normalized PDF, with units of TeV^{-1}:

$$\int_0^\infty \text{EDisp}(E_{\rm reco} | E_{\rm true}, \mathbf{x}_{\rm true}, \dots)\, d(E_{\rm reco}) = 1 \,. \tag{3.3}$$

The quantity $E_{\rm reco}/E_{\rm true}$ is also called *migration* (μ), and the EDisp *energy migration matrix*. For each $E_{\rm true}$ and $\mathbf{x}_{\rm true}$, the EDisp is approximately a one-dimensional Gaussian along the $E_{\rm reco}$ axis, which means that its characteristics can be defined by two quantities: the Gaussian center (*energy bias*) and width (*energy resolution*). If the Gaussian peaks at $E_{\rm reco} > E_{\rm true}$ ($< E_{\rm true}$), which means $\mu > 1$ (< 1), the reconstructed event energies are biased toward too high (low) values. The energy resolution which is often quoted in publications corresponds to a given (e.g. 68%) containment interval of the Gaussian. It is a representative number, which should be taken with a grain of salt since it depends on the true event parameters and also on the observation conditions, and is based on a Gaussian approximation that may not always be accurate.

3.2.3 Point Spread Function

The Point Spread Function (PSF) measures the error made on the event direction reconstruction[2], which corresponds to the smearing of a point-like source in the array FoV. Usually, the PSF is derived from Monte Carlo simulations, but it may also be checked using bright and isolated (extra-Galactic) point sources like active Galactic nuclei (AGNs). The PSF is also a normalized PDF (units of sr^{-1}):

$$\text{PSF} = \text{PSF}(\mathbf{x}_{\rm reco} | E_{\rm true}, \mathbf{x}_{\rm true}, \xi) \tag{3.4}$$

$$\iint_{\rm FOV} \text{PSF}(\mathbf{x}_{\rm reco} | E_{\rm true}, \mathbf{x}_{\rm true}, \xi)\, d(\mathbf{x}_{\rm reco}) = 1 \,. \tag{3.5}$$

[2] Due to optical effects that degrade the shape of the Cherenkov images in the camera, pointing error of individual telescope, limited accuracy in the positionnement of the pixels, fluctuations of the Cherenkov images and limits of the reconstruction algorithms.

For each true energy, the H.E.S.S. PSF is a two-dimensional distribution which, at first order, can be considered radially symmetric around $\mathbf{x}_{\rm true}$:

$$\mathrm{PSF} = \frac{dP}{\pi d\theta^2}(\theta) \,, \tag{3.6}$$

where dP is the probability of reconstructing an event within an annulus of solid angle $\pi d\theta^2$ at an offset θ from $\mathbf{x}_{\rm true}$. More realistically, the PSF can be described by a linear combination of (up to) three two-dimensional Gaussians, as in

$$\mathrm{PSF} \propto \sum_{i=1}^{3} A_i \exp\left(-\frac{\theta^2}{2\sigma_i^2}\right) \,, \tag{3.7}$$

or using a two-parameter King function. Underlying this is the implicit assumption that the PSF and EDisp are independent, which is not always the case and can lead to systematic errors.

3.2.4 FoV background model

As mentioned in section 2.3.2, after the γ/hadron separation step a residual background of γ-like hadrons is always present. There are two possible approaches to deal with it: one may either try to estimate it from the data themselves (see sections 3.4.2 and 3.4.3), or build a background model and treat it as an IRF (altough a peculiar one, being defined as a function of reconstructed quantities). In this section we describe the latter option.

The probability that a hadronic event passes the γ/hadron discrimination cuts, which is a function of the reconstructed energy, FoV position and zenith angle, is called (hadron) *acceptance*: $\mathscr{A}(E_{\rm reco}, \mathbf{x}_{\rm reco}, Z)$ [151]. At first order, the H.E.S.S. acceptance can be considered a radially symmetric function around the FoV center. It can be determined either from simulations[3], or from real empty-field observations. In the latter case, under the assumption of radial symmetry of the hadronic acceptance, a simple *FoV background model* can be obtained by "rotating" the radial acceptance curve along the FoV center axis. In more detail, for the HAP-Fr analysis chain used in this thesis, the FoV background model was produced (before the start of this thesis) as follows:

- first, a sufficiently large sample of empty-field[4] observations was selected, avoiding the Galactic plane region: $|b| > 5^{\rm o}$, $|l| > 60^{\rm o}$. Additionally, an exclusion mask was applied to exclude γ-ray sources, based on the TeVCat catalog [152];
- observations were then grouped into 10 zenith angle (Z) bins, linearly spaced in in $\cos Z$ ($Z \in [0, 70]\,\mathrm{deg}$);
- under the assumption of radial symmetry, the runwise background events (passing the γ/hadron discrimination) were accumulated into two-dimensional histograms based on their $E_{\rm reco}$ and offset from the camera center. The histograms were divided by the runwise *exposure*[5], to get the correct units for a background rate ($\mathrm{s}^{-1}\,\mathrm{TeV}^{-1}\,\mathrm{sr}^{-1}$);

[3] A method called *runwise simulations* in H.E.S.S., in which hadronic acceptance maps (supposed to be identical to the γ-ray acceptance after cuts) are created by means of γ-ray simulations.

[4] E.g. AGN observations with an exclusion mask at the AGN position.

[5] The exposure is obtained multiplying the effective area by the observation livetime.

- within each $\cos Z$ bin, the histograms were stacked together, to increase photon statistics and reduce fluctuations. This way, a *general* radial FoV background model was obtained, as a function of the zenith angle of observation;
- at this point, a background re-scaling outside the exclusion mask was performed, for each run. Finally the predicted background rate was linearly interpolated between adjacent $\cos Z$ bins, to smooth out the background model normalization at the boundaries between different $\cos Z$ bins [153]. This allowed to assign a more adapted FoV background model to any new observation.

The background model used in this thesis was produced only for observations in which all four CT1–4 telescopes of the H.E.S.S. array were functioning[6]. This allowed us to avoid runs with asymmetric background model, which cannot be handled by the current background model production pipeline[7]. A known limitation of the HAP-Fr background model is in the fact that it is based entirely on H.E.S.S. I runs, because the available H.E.S.S. IU runs are still too few for a statistically robust study. This most likely introduces systematic effects, especially when the model is applied to the H.E.S.S. IU runs. Finally, the model is only a function of the $\cos Z$ variable, while other important (altough at second order) parameters such as the instrument's optical efficiency and the atmosphere transparency coefficient are not considered. For all these reasons it is absolutely necessary to properly adjust the background model to the observed (off-source) data at the moment of the actual analysis, as described in section 3.4.4.

3.2.5 IRF export in the HAP-Fr FITS release

The γ-ray astronomy community is currently preparing the ground for CTA (see section 2.4), which, for the first time in the era of Cherenkov astronomy, will be operated as an open observatory. For this reason well-defined, flexible and robust formats to store the telescope's data and IRF files have to be adopted. This unification effort represents a huge improvement with respect to the status quo, in which a variety of data formats and proprietary software (with plenty of code duplication) are used. However it also implies that difficult choices have to be made, for example on the default storage formats, names and units of columns in the event list, metadata and IRF structures.

For the moment, the CTA Consortium has not yet defined a preferred format, however it seems likely that the adopted one will be based on the experience accumulated in recent years thanks to the gamma astro data format (GADF) project [154, 155]. The GADF is an open-source repository born in 2015, describing the format specifications currently in use and/or under development by the main present-day IACTs and open tools communities. The GADF has already been tested in several occasions: for the first CTA data challenge (CTA DC1)[8], for the 2018 H.E.S.S. first public test data release (H.E.S.S. DR1) [156], as well as in a number journal publications (e.g. [153, 157, 158]).

[6] For such runs, the number of telescopes triggered by the same event can be 2, 3 and 4, the median multiplicity being around $2.6 - 2.8$.

[7] Alternatively, one could think of modifying the four-telescope model using spatial gradients. The same would in principle be required also for 4-telescope runs, since the zenith angle (and with it the background) is not constant within the FoV. This would be a significant improvement on the current background model design, but the required studies are beyond the scope of this thesis.

[8] Organized in 2017 to perform a preliminary validation of the CTA science tools and data formats.

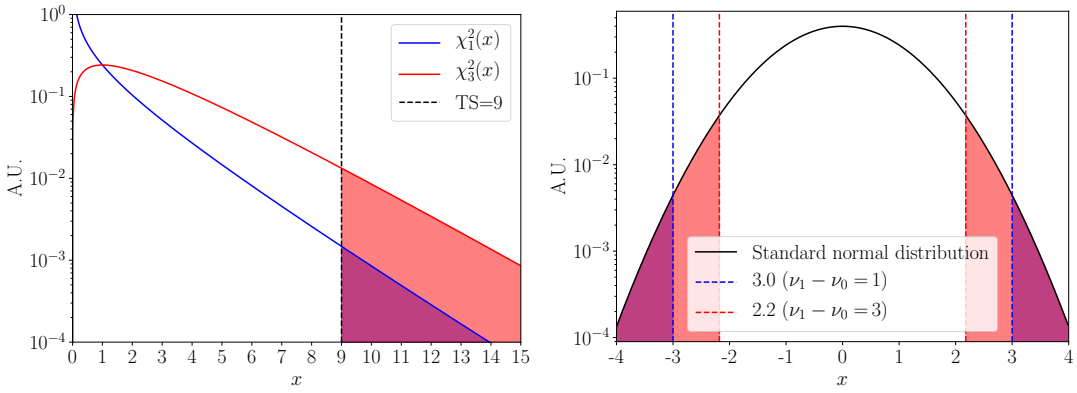

FIGURE 3.2: Left Distributions of $\chi^2_{\nu_1-\nu_2}$ with $\nu_1 - \nu_2 = 1$ (blue curve) and 3 (red curve). The red and blue areas represent the right-tail p-values of the two distributions, corresponding to a measured TS value of 9. Clearly, the p-value for χ^2_1 is lower than for χ^2_3, meaning that the probability of getting a higher TS value in case the null hypothesis was correct is lower (i.e. the significance of the alternative hypothesis is higher) for $\nu_1 - \nu_2 = 1$ than 3. Right: The p-values shown in the left panel are converted to statistical significance in units of Gaussian sigmas, by computing the corresponding two-tails p-value of a standard normal Gaussian distribution.

In H.E.S.S., DL3 data from the three main analysis chains (see section 2.3.2) are currently being exported to FITS productions for internal use. In the context of the HAP-Fr chain, DL3 IRFs are first produced using Monte Carlo simulations and stored in ROOT format, with HAP. Then, they are exported to FITS format on a runwise basis after a multi-dimenstional interpolation of a global IRF lookup table. The FoV background model is the only IRF to be produced directly in FITS format.

3.3 Basics of statistics for the high-level γ-ray analysis

3.3.1 TS-based statistical significance

A common problem in γ-ray astronomy is the one of *hypothesis testing*. For example, one may be interested in understanding whether a source has been detected in the FoV or not, or whether a source spectrum has a given shape or another one. All such cases can be tackled using the Wilk's theorem [159] (also called *likelihood ratio test*), which provides a way to estimate the relative significance of *nested* hypotheses by means of the test statistic:

$$\mathrm{TS} = -2\ln\left(\frac{\mathscr{L}_0^{\max}}{\mathscr{L}_1^{\max}}\right). \tag{3.8}$$

Here, $\mathscr{L}_0^{\max}$ ($\mathscr{L}_1^{\max}$) represents the maximum likelihood of the model under the null (alternative) hypothesis, e.g. the absence (presence) of a source in the FoV. The hypotheses are said to be nested if the parameters defining the null hypothesis form a subset (of length ν_0) of the $\nu_1 > \nu_0$ parameters defining the alternative hypothesis. If this is the case, according to Wilks' theorem, the TS defined in equation 3.8 is distributed as a $\chi^2_{\nu_1-\nu_0}$, in the asympthotic limit of high statistics. Thanks to

this theorem, the statistical significance of the alternative hypothesis relative to the null one can be estimated from the measured TS value, by simply determining the corresponding right-tail p-value of a $\chi^2_{\nu_1-\nu_0}$ distribution:

$$p(\mathrm{TS}) = \int_{\mathrm{TS}}^{\infty} \chi^2_{\nu_1-\nu_0}(x)\,dx\,, \tag{3.9}$$

where

$$\chi^2_r(x) = \frac{1}{2^{r/2}\Gamma(r/2)} x^{r/2-1} e^{-x/2} \quad (x>0)\,. \tag{3.10}$$

A small value of $p(\mathrm{TS})$ (for example 0.1%) indicates that the probability of obtaining such a high TS value, if the null hypothesis was correct, is very small. Therefore, the alternative hypothesis is preferred to the null one at a confidence level $1-p$ (for example 99.9%).

For convenience, one can convert the significance value to units of Gaussian standard deviations (σ), by computing the inverse of the two-tails[9] cumulative distribution function (CDF) of a standard normal Gaussian distribution corresponding to the given p-value. Figure 3.2 illustrates this operation, showing how a $\mathrm{TS}=9$ leads to a 3.0σ (2.2σ) confidence level significance for the alternative hypothesis in the case $\nu_1-\nu_2=1$ ($\nu_1-\nu_2=3$). In the special case in which the alternative hypothesis features just one parameter more than the null hypothesis ($\nu_1-\nu_0=1$), all this operation reduces to simply taking the $\sqrt{TS}$. This can be shown by setting $r=1$ in equations 3.9 and 3.10:

$$p(\mathrm{TS}) = \int_{\mathrm{TS}}^{\infty} \frac{1}{\sqrt{2\pi x}} e^{-x/2}\,dx\,. \tag{3.11}$$

Making the substitution $y=\sqrt{x}$, eq. (3.11) can be re-written as

$$p(\mathrm{TS}) = \left(\int_{-\infty}^{-\sqrt{\mathrm{TS}}} + \int_{\sqrt{\mathrm{TS}}}^{\infty}\right) \frac{1}{\sqrt{2\pi}} e^{-y^2/2}\,dy\,, \tag{3.12}$$

which means that (for $r=1$) the right-tail χ^2 p-value for a given measured TS also corresponds to the two-tails p-value of a standard normal Gaussian for the value $\sqrt{TS}$.

We note that this (fully analytical) recipe for the significance computation may lead to biased estimates in some extreme cases, especially when a model parameter is at the borders of its physically meaningful interval. For example, one may want to compute the significance of an elliptical source morphology (alternative hypothesis, eccentricity $e\in[0,1]$) against a circular model (null hypothesis, $e=0$). Since the eccentricity is at its physical minimum in the null hypothesis, the rotation angle becomes a degenerate parameter, that, if counted as a degree of freedom, can lead to an over-estimation of the significance of the alternative hypothesis. In the future, more sophisticated (simulation-based) approaches will hopefully allow to convert the TS values into statistical significance in a more rigorous way.

[9] Since the background can fluctuate in both directions.

3.3.2 Counts statistics

The γ-ray signal (also called *excess*) within an ON sky region[10] is defined as the number of photon counts exceeding the residual hadronic background. The background can be obtained in two ways: either *estimated* by means of OFF control regions (assumed to be signal-free), or *modeled* as described in section 3.2.4. In the former case, the signal in the ON region is computed as [160]

$$N_\gamma = N_{\rm ON} - \alpha N_{\rm OFF} \,, \tag{3.13}$$

where

$$\alpha = \frac{t_{\rm ON} \int_{\rm ON} \mathscr{A}_{\rm ON}(E_{\rm reco}, \mathbf{x}_{\rm reco}, Z)\, d\mathbf{x}_{\rm reco}}{t_{\rm OFF} \int_{\rm OFF} \mathscr{A}_{\rm OFF}(E_{\rm reco}, \mathbf{x}_{\rm reco}, Z)\, d\mathbf{x}_{\rm reco}} \tag{3.14}$$

corrects for possible differencies in the ON and OFF observation livetimes, solid angles and hadronic acceptances. In general, to limit systematics, the OFF measurement should be made not too far (in time and space) from the ON region. Also, the smaller the α factor, i.e. the larger the OFF acceptance, solid angle or livetime, the higher is the statistical significance of the γ-ray signal, because background fluctuations are reduced[11]. Alternatively, if an estimate $\mu_{\rm bkg}$ of the background rate in the ON region based on a FoV background model is available, the signal can be obtained as

$$N_\gamma = N_{\rm ON} - \mu_{\rm bkg} \,. \tag{3.15}$$

We note that the γ-ray signal defined in equations 3.13 and 3.15 can also be negative, for example as a result of positive statistical fluctuations of the background rate in the OFF region, a contamination of the OFF region by real γ-ray emission or an over-estimated background model.

The definitions 3.13 and 3.15 are not exactly equivalent, since the first can be affected by statistical fluctuations in the OFF region while the second is not. This means that the two cases correspond to different *counts statistics*:

wstat: This is the case of Poissonian data with Poissonian background estimation, corresponding to equation 3.13. If the expected value for $N_{\rm ON}$ ($N_{\rm OFF}$) is $\mu_{\rm sig} + \mu_{\rm bkg}$ ($\mu_{\rm bkg}/\alpha$), then the combined likelihood for the ON and OFF measurements is:

$$\begin{aligned} \mathscr{L} &= \mathcal{P}(N_{\rm ON}|\mu_{\rm sig}+\mu_{\rm bkg}) \times \mathcal{P}(N_{\rm OFF}|\mu_{\rm bkg}/\alpha) \\ &= \frac{(\mu_{\rm sig}+\mu_{\rm bkg})^{N_{\rm ON}}}{N_{\rm ON}!} e^{-(\mu_{\rm sig}+\mu_{\rm bkg})} \times \frac{(\mu_{\rm bkg}/\alpha)^{N_{\rm OFF}}}{N_{\rm OFF}!} e^{-\mu_{\rm bkg}/\alpha} \end{aligned} \tag{3.16}$$

where $\mathcal{P}$ denotes the poisson distribution. By taking twice the negative logarithm of the previous equation and neglecting constant terms, one obtains the definition of *wstat*:

$$W = 2[\mu_{\rm sig} + (1+1/\alpha)\mu_{\rm bkg} - N_{\rm ON} \ln(\mu_{\rm sig}+\mu_{\rm bkg}) - N_{\rm OFF} \ln(\mu_{\rm bkg}/\alpha)] \,. \tag{3.17}$$

[10] The ON could also be, for example in the case of pulsed emission studies, a temporal integration interval.

[11] However this may also lead to increased systematic errors in some cases, for example when the OFF region is contaminated by γ-ray signal.

Using the likelihood ratio test (see section 3.3.1), the γ-ray signal significance is then simply computed as $\sqrt{\mathrm{TS}} = \sqrt{W_0 - W_1}$[12]. Here, W_0 and W_1 are computed following equation 3.17, under the following assumptions:

$$W_0 \ \text{(null hypothesis)}: \quad \mu_{\mathrm{sig}} = 0, \quad \mu_{\mathrm{bkg}} = \frac{\alpha}{1+\alpha}(N_{\mathrm{ON}} + N_{\mathrm{OFF}})^{[13]}, \tag{3.18}$$

$$W_1 \ \text{(alternative hypothesis)}: \quad \mu_{\mathrm{sig}} = N_{\mathrm{ON}} - \alpha N_{\mathrm{OFF}}, \quad \mu_{\mathrm{bkg}} = \alpha N_{\mathrm{OFF}} \,. \tag{3.19}$$

Using equations 3.17-3.19, one can retrieve the formula (17) from the 1983 Li and Ma paper [160], which is (hystorically) the standard method for the significance calculation in TeV astronomy.

Cash [161]: This counts statictic applies to the case of Poissonian data with perfectly known background model (equation 3.15). If the expected values for N_{ON} and for the background in the ON region are respectively $\mu_{\mathrm{sig}} + \mu_{\mathrm{bkg}}$ and μ_{bkg}, then the likelihood is written

$$\begin{aligned} \mathscr{L} &= \mathcal{P}(N_{\mathrm{ON}} | \mu_{\mathrm{sig}} + \mu_{\mathrm{bkg}}) \\ &= \frac{(\mu_{\mathrm{sig}} + \mu_{\mathrm{bkg}})^{N_{\mathrm{ON}}}}{N_{\mathrm{ON}}!} e^{-(\mu_{\mathrm{sig}} + \mu_{\mathrm{bkg}})} \,. \end{aligned} \tag{3.20}$$

The *Cash* counts statistic is then obtained by taking twice the negative logarithm of the above formula, which yields:

$$\mathcal{C} = 2[\mu_{\mathrm{sig}} + \mu_{\mathrm{bkg}} - N_{\mathrm{ON}} \ln(\mu_{\mathrm{sig}} + \mu_{\mathrm{bkg}})] \,. \tag{3.21}$$

Similarly to the *wstat* case, the γ-ray signal significance is then computed as $\sqrt{\mathcal{C}_0 - \mathcal{C}_1}$, where $\mathcal{C}_0$ and $\mathcal{C}_1$ are obtained from equation 3.21 under the assumptions:

$$\mathcal{C}_0 \ \text{(null hypothesis)}: \quad \mu_{\mathrm{sig}} = 0 \,, \tag{3.22}$$

$$\mathcal{C}_1 \ \text{(alternative hypothesis)}: \quad \mu_{\mathrm{sig}} = N_{\mathrm{ON}} - \mu_{\mathrm{bkg}} \,. \tag{3.23}$$

In this case, using equations 3.21-3.23, the signal significance becomes

$$S = \sqrt{2}\left[\mu_{\mathrm{bkg}} + N_{\mathrm{ON}}\left(\ln\frac{N_{\mathrm{ON}}}{\mu_{\mathrm{bkg}}} - 1\right)\right]^{1/2} \,. \tag{3.24}$$

We note that this expression can also be seen as a special case of the classic Li and Ma formula 17, in the limit of perfecly known background model.

3.4 High-level analysis with Gammapy

In this section we provide an overview of some of the main high-level analysis techniques used in VHE γ-ray astronomy, with particular focus on their implementation in Gammapy.

[12] The $\sqrt{\mathrm{TS}}$ rule applies in this case because the alternative hypothesis has only 1 degree of freedom more (the number of signal counts) than the null one (0 signal counts).

[13] This expression is derived in [160].

3.4.1 Gammapy

Gammapy (γ_π) is an open source python library for γ-ray[14] astronomy [157, 162, 163]. Historically, a first version of the package (today completely superseded by new code) was implemented in the context of the HGPS campaign, starting from 2013. Since then, the package has been continuously developed as an open-source and community-based package, stored in the public https://github.com/gammapy/gammapy repository on GitHub. More detailed informations, including a history log of the main code changes and a description on the Gammapy project and team, are available at the website https://gammapy.org/team.html. Gammapy has been recently (1 June 2021) selected as the official science tool supported by the CTA observatory, which means that a basic knowledge of its interface and implementation will be required to perform most standard CTA analysis tasks. To produce all the results of this thesis, different versions of Gammapy were used: 0.17 for the whole part II and the more recent 0.18.2 for the part III (apart for the section 9.2.1 in which the version 0.15 was used).

Some of the most important building blocks of Gammapy are:

`gammapy.models`: in this sub-module a toolkit of spatial, spectral and temporal models is provided, that can be used to fit and simulate the γ-ray emission from astrophysical sources. Examples of spectral models, expressing the number of counts per true energy bin (differential flux), are the γ-ray power law and the power law with exponential cutoff. Spectral models can be multiplied by spatial models, such as point-like or two-dimensional Gaussian morphologies, and temporal models, such as the constant or exponential decay models, to obtain *spectro-morphological* (3D) models that in Gammapy are called `SkyModels`[15]. A `SkyModel` is an object that allows to compute the γ-ray emission from a source at each true energy, position and time. All models are parametric, which implies that they can be adjusted to the data by means of a maximum likelihood technique. For the model fitting, Gammapy relies on a choice of external backends, among which we chose to use `iminuit` [164], being for the moment the only one that is fully tested and supported by Gammapy;

`gammapy.datasets`: the `Dataset` class, bundling together data, IRFs, model and fit statistic computation, is arguably the cornerstone of the Gammapy code. This class corresponds to the implementation of the DL4 level in Gammapy. It allows to compute the (IRF-folded) model-predicted counts in each reconstructed energy bin and/or spatial pixel, which can then be adjusted to the measured data using a maximum likelihood technique. Different `Dataset` objects are available, each one corresponding to a particular analysis task: the 1D analysis (see section 3.4.2) relies on the `SpectrumDataset` and `SpectrumDatasetOnOff`, while the 2D and 3D analyses (section 3.4.3 and 3.4.4) are based on the `MapDataset` and `MapDatasetOnOff` classes[16]. Typically, after the data reduction step (handled by `Makers`, see below), the array's observations are stored each one in a different `Dataset` instance, with its own IRFs. Then, one may proceed in two ways: either keeping each `Dataset` separate (*joint-likelihood* analysis), or

[14] An effort for the inclusion of multi-wavelength (X-ray) and multi-messenger (neutrino) funtionalities is currently underway.

[15] If one counts also the additional temporal templates, `SkyModels` can actually be seen as 4D models. In this thesis we always assumed temporally constant models.

[16] A `FluxPointsDataset` class is also available for spectral points storage and fitting.

combining them all together into one single `Dataset` instance (*stacked* analysis). The latter option has a computational advantage, since the number of background model parameters scales with the number of `Dataset` instances, but also leads to a deterioration of the instrument response knowledge, due to the approximations that are made when the IRFs are combined. In the current Gammapy implementation, the *stacked* PSF and EDisp values in a given energy bin i and spatial pixel j are computed as the average values from two parent observations (a and b), weighted by the run-wise exposure values ϵ:

$$\mathrm{PSF}_{i,j} = \frac{\mathrm{PSF}^a_{i,j} \times \epsilon^a_{i,j} + \mathrm{PSF}^b_{i,j} \times \epsilon^b_{i,j}}{\epsilon^a_{i,j} + \epsilon^b_{i,j}} \tag{3.25}$$

$$\mathrm{EDisp}_{i,j} = \frac{\mathrm{EDisp}^a_{i,j} \times \epsilon^a_{i,j} + \mathrm{EDisp}^b_{i,j} \times \epsilon^b_{i,j}}{\epsilon^a_{i,j} + \epsilon^b_{i,j}} \,. \tag{3.26}$$

This means that, for observations with significantly different response (either due to different observation conditions or telescope aging levels) the stacking procedure leads to intermediate IRFs that are not really adapted to the analysis of events from any of the two stacked observations, which potentially increases the analysis systematics. Also, the good instrument response of a small number of high-quality runs can be completely washed out by a larger number of observations with worse response. For this reason, as better described with a practical example in section 4.4.1, dedicated strategies for a reasoned run stacking have to be used.

`gammapy.makers`: this submodule contains a collection of `Maker` objects, designed to carry out data reduction tasks from DL3 data to DL4. First of all, they perform the binning of the event lists in terms of energy and/or direction according to the user's choices, and interpolate the IRFs on the chosen analysis bins. Additionally they are also used to determine the hadronic background at each energy and/or FoV position, and to compute the safe spatial and/or energy ranges (called the *safe mask*) in which the data can be analyzed (see e.g. equation 4.3). In Gammapy the basic logic of the data reduction for a stacked analysis is the following:

```
stacked = Dataset.create()                          #Create empty dataset
for obs in observations:                            #For each run
    dataset = DatasetMaker.run(obs)                 #Bin data and IRFs
    dataset = SafeMaskMaker.run(dataset, obs)       #Compute safe range
    dataset = BackgroundMaker.run(dataset)          #Compute background
    stacked.stack(dataset)                          #Stack
```

For a joint analysis, the logic is the same, except that at the end of the loop the reduced datasets are appended to a `Datasets` container instead of being stacked.

`gammapy.estimators`: this submodule contains `Estimator` objects to carry out high-level analysis tasks such as flux points, flux maps, flux profiles, light curves and significance maps computation.

During the PhD, I contributed to Gammapy by means of GitHub interactions such as issues and pull requests (PRs). Examples of such contributions are[17]:

[17] The complete record of my contributions to the Gammapy code can be found here (PRs) and here (issues). Additional pull requests addressing the validation of the Gammapy analysis pipeline can instead be found here.

2034, **2046**, **2313**, **2371**: in this series of PRs symmetric and asymmetric spatial models (Gaussian and elliptical) were implemented. Using `astropy` utilities for spherical distance calculations, they were defined and normalized on the celestial sphere[18];

2124: with this PR the `NaimaSpectralModel` class, a *wrapper*[19] around the physically-motivated radiative models defined in the Naima package [165], was added to the `gammapy.models` module. The Naima models allow to compute the non-thermal emission from populations of relativistic electrons or protons via hadronic and leptonic processes (see sections 1.3.1 and 1.3.2). The main advantage of using the `NaimaSpectralModel` class of Gammapy, instead of plain Naima, is given by the possibility of adjusting the cosmic ray spectral parameters directly on γ-ray data. This represents a significant improvement with respect to the adjustment radiative models to precomputed flux points, which is the more traditional way in which Naima models can be fitted[20]. Indeed, in the latter case one must first compute the spectral points by assuming a given γ-ray spectral descripion (e.g. a γ-ray power law), which then inevitably biases by the radiative model results. The use of Naima presents however some drawbacks. Namely, Naima does not allow to take into account the effects of time and energy-dependent cooling of (leptonic) cosmic rays on the γ-ray spectra. For this reason, and also since Naima is no longer developed and mostly unmaitained, it seems likely that in the future more up-to-date and integrated solutions will be adopted in Gammapy;

2481, **2520**, **2525**: In the first of these PRs a new `Dataset` type was introduced, called the `MapDatasetOnOff`. This is essentially a container used for two-dimensional ON-OFF analyses, in which the background model is estimated by means of a measurement from control regions. Together with the two other PRs of this series, this allowed to restructure the logic of two-dimensional analysis following the `Maker` concept. In practice, before 2520 the ring background analysis (see section 3.4.3) was handled by an `Estimator` object, called the `RingBackgroundEstimator`. Now instead, thanks to these PRs, a dedicated `RingBackgroundMaker` class is available, which converts `MapDataset` objects into `MapDatasetOnOff` by adding the information on the estimated OFF background;

3038, **3065**: In these PRs a method called `Fit.stat_surface()` was added, which can be used to compute two-dimensional likelihood surfaces by fitting a model on a grid of trial parameter values. This is useful to estimate confidence contours and assess the level of correlation between the model's parameters, but can also be slow in case of finely binned parameter spaces.

3.4.2 One-dimensional (1D) binned analysis

The 1D analysis technique (also known as *aperture photometry*) is used to obtain information on the γ-ray source spectra, while all the information on their morphology

[18] This is desirable because the planar approximation yields imprecise results for models larger than few degrees. This is also true for small size models that are defined in regions of strong geometrical distortion, such as at the poles in case of a tangential (at the equator) sky projection.

[19] The term wrapper in this case means that the `NaimaSpectralModel` takes care of translating the `naima` model parameters in a format that can be directly used for simulation and fitting in Gammapy.

[20] See e.g. https://naima.readthedocs.io/en/latest/mcmc.html.

is washed out by a 2D spatial (and temporal) integration within a ON region. For point-like sources, the spectral extraction (ON) region is typically chosen to correspond with a given (e.g. 68%) containment fraction of the PSF, which maximizes the signal to noise ratio. Then, the wrong flux estimate resulting from the PSF leakage outside the spectral extraction region is corrected by applying a muliplicative factor to the effective area. Removing events from the tail of the PSF, where the signal to background ratio is low, is also a way to select events with good γ/hadron separation power leading to an increased detection significance. Instead for extended sources larger integration regions are used, typically encompassing the full γ-ray emission, and no containment correction is required.

To extract the γ-ray spectrum in the ON region, which is usually (but not necessarily) circular and encompassing a γ-ray source, one has to subtract the hadronic background from the total number of events detected in the region. The most common way of doing this involves the *reflected regions background estimation* method [151], which uses *wstat*[21]. If (like in H.E.S.S.) the hadronic acceptance of the system is assumed to be radially symmetric, to simplify the acceptance correction (see equation 3.14) usually the array is pointed at a certain offset ($\approx 0.5°$) from its real scientific target (*wobble* mode [166]). Then, by "reflecting" the ON region with respect to the FoV center, one can define a number of OFF regions located at the same angular offset (which means same acceptance) from the FoV center as the ON region. Therefore the correction factor simply becomes $\alpha = 1/n_{\mathrm{OFF}}$, where n_{OFF} is the number of OFF regions. In Gammapy, observations with this kind of background estimate are stored in `SpectrumDatasetOnOff` instances.

For each observation, the largest possible number of OFF regions is used, in order to limit the impact of background fluctuations. However, the number of reflected regions is sometimes limited by the presence of nearby (resolved or diffuse) γ-ray sources, which may lead to background over-estimations and therefore biased spectral measurements. For this reason all known or expected γ-ray emission needs to be ignored by means of an *exclusion mask*, typically based on γ-ray source catalogs or computed by iteratively enlarging first-guess exclusion regions until all γ-ray emission has been excluded. In some cases, for extremely crowded sky regions (e.g. the Galactic center), it might even become impossible to find enough reflected regions to achieve a reliable background estimation. This can be seen as an argument in favor of telescopes with larger FoVs than the existing ones. In any case this situation is deemed to become more and more frequent, due to the increasing exposure of the current generation of IACTs and the upcoming transition to new arrays with unprecedented sensitivity. For example, simulation studies show that CTA may detect up to ≈ 500 γ-ray sources in the Galactic plane [167], making it impossible to disentangle their emission and find enough background control regions with classical 1D analyses. For this reason, in the future this technique will likely remain in use only for certain use cases such as extra-Galactic source studies.

After the background estimation step, the γ-ray spectrum in the ON region is obtained by means of a maximum-likelihood fit, in which a parametric spectral model (e.g. a power law) is convolved with the instrument's IRFs to determine the model-predicted

[21] Gammapy also provides the possibility of performing a more unusual kind of 1D analysis, based on the FoV background model (section 3.2.4) and the `SpectrumDataset` class. In this case, the background model is integrated within the ON region, and the relevant counts statistic is *Cash*.

counts in each reconstructed energy bin i:

$$N_i = \int_{E_i}^{E_{i+1}} dE_{\rm reco} \int_0^{\infty} dE_{\rm true} \frac{dN}{dE_{\rm true}}(E_{\rm true}, \Theta) \times A_{\rm eff}(E_{\rm true}) \times {\rm EDisp}(E_{\rm reco}|E_{\rm true}) \times t \, . \tag{3.27}$$

This way, one can fine-tune the model parameters Θ so that N_i mimics as closely as possible the measured data ($\tilde{N}_i$) in all energy bins, which is equivalent to maximizing the likelihood

$$\mathscr{L}(\Theta) = \prod_i \mathcal{P}(\tilde{N}_i \mid N_i(\Theta)) \tag{3.28}$$

or minimizing a *wstat* fit statistic. This approach is known as *forward-folding* [168]. Finally, after the best-fit spectral model has been determined, one may re-scale it independently inside each reconstructed energy bin, to obtain the ON region's flux points.

3.4.3 Two-dimensional (2D) binned analysis

The 2D analysis has the opposite purpose of the 1D case, in the sense that it studies the γ-ray signal morphology by integrating over the spectral energy dimension. It therefore relies on 2D data arrays, carrying information on the number of photon and background events observed within a discrete grid of sky pixels. In this case, the hadronic background is typically determined using the *ring background estimation* method [151]. In this algorithm, the background within each pixel is estimated by means of a measurement made in a ring-shaped OFF region, concentric around the target pixel and parametrized either by an inner and outer radius or by an inner radius and a width. Unlike the 1D case, here the ON and OFF acceptances are not the same, and are not even constant within the OFF ring, which implies that the acceptance correction factor has to be computed using the full formula 3.14. This method is therefore limited by systematics arising from our imperfect knowledge of the instrument's acceptance. Since the latter varies with energy, this kind of background estimation technique is inefficient for spectral analyses. In Gammapy, the ring background estimation is performed by the `RingBackgroundMaker`, which dispaches the measured data and background into `MapDatasetOnOff` instances.

Similarly to the 1D case, this method assumes that the OFF regions are signal-free. For this reason, exclusion regions have to be defined, which may overlap with portions of the ring leading to an increase of the α correction factor. In some cases, it may even become impossible to define a unique ring size to achieve a correct background estimate for all sky pixels. An evolution of the original method, called the *adaptive* ring background estimation technique [38, 151, 169], can address such cases. The idea is that the ring inner radius (or its width) are adaptively enlarged to avoid excluded regions, in such a way that an optimal α estimation is achieved everywhere in the analysis region.

The most common products of this type of analysis are sky maps, which display the distribution of *wstat* significance[22] or signal counts within a given sky region. Counts maps can be corrected by the instrument's exposure (for the assumed signal spectral

[22] The use of *wstat* here is an approximation. Indeed, the OFF pixels forming the rings are used to estimate the background for multiple ON pixels, which means that the background estimates (and the resulting maps) are correlated.

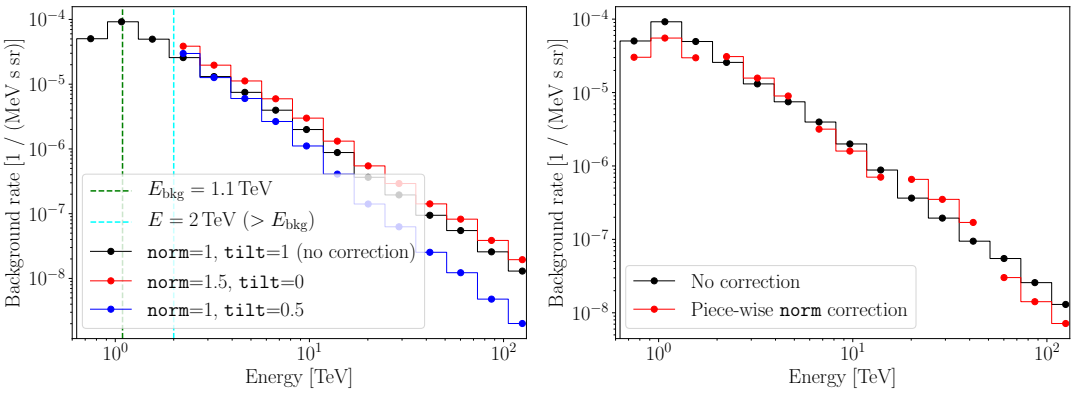

FIGURE 3.3: Left: Energy spectrum of the background model in the pointing direction of one randomly picked observations (in black), corrected with the `norm` (red) and `tilt` (blue) parameters defined in the text (equation 3.29). The spectral corrections are applied only above 2 TeV (cyan line), which is sufficiently above the background peak energy E_{bkg} (green line). Right: Piece-wise `norm` correction to the original background model, shown in black, using the formula 3.30. The normalization factors have been chosen to provide a visually clear illustration, and do not correspond to a real analysis case.

shape) to obtain flux maps, which provide the best way to assess the morphology of sources since they are unbiased by the often uneven observation exposure. Flux maps can then be modeled using 2D analytical templates such as Gaussians and ellipses, to derive physical information on the intrinsic (i.e. PSF-corrected) size and asymmetry level of γ-ray sources.

We finally mention that there is another way of estimating the background in the 2D case, called in H.E.S.S. the *ON-OFF* background estimation method. This consists of using an independent empty-field observation, with similar zenith angle and atmospheric parameters as the on-source one, to subtract the hadronic background bin-by-bin in the whole FoV. If not correctly renormalized, this background estimate may however be affected by systematic errors, due to background fluctuations or γ-ray pollution in the OFF observations. This can be partially avoided if dedicated off-source observations are made following each on-source pointing, which however is rarely done since it doubles the observation time. Finally, one can also use the FoV background model, after a re-normalization outside the exclusion regions, to obtain γ-ray flux and significance maps. This method suffers from systematics due to background model imperfections and is based on the *Cash* counts statistic.

3.4.4 Three-dimensional (3D) binned analysis

The 3D (or *cube*) analysis, routinely used in the HE γ-ray domain [170, 171], has been only recently adopted in VHE γ-ray astronomy [153, 172]. In its *binned* version, this technique allows the adjustment of a spectro-morphological model to a data cube, that carries information on the number of reconstructed events within 3D bins. The term 3D refers to the fact that the data are distributed along 2 spatial dimensions (e.g. Galactic longitude and latitude) plus 1 energy dimension. The model can be seen as a collection of spectral and spatial parametric shapes that are assumed to describe

γ-ray sources (source model), plus the residual hadronic background of γ-like events (FoV background model).

The 3D modeling technique is especially useful to extract information from non-trivial sky regions, crowded with multiple overlapping sources and large-scale *diffuse emission*[23]. In such cases the classic analysis techniques described in sections 3.4.3 and 3.4.4, based on the background estimation from the data themselves, become inefficient, due to the impossibility of finding enough background control regions. Another important 3D analysis use case comes from the recent discovery of very extended sources such as TeV halos [65]. These objects, whose apparent size is comparable with the telescope's FoV, are by construction washed out by traditional background estimation methods like the ring.

The typical 3D analysis workflow is the following.

Data reduction:

- first, a binned spatial *region of interest* (RoI)[24] and spectral (both true and reconstructed) energy axes are defined. In Gammapy, those are said to define the analysis *geometry*;
- then, after loading a certain number of observations in DL3 format, they are reduced (i.e. binned in space and energy) to separate `MapDataset` instances by the `MapDatasetMaker`. For each run, the safe data range is computed by the `SafeMaskMaker` based on criteria that may vary depending on the use-case;
- at this point the runwise FoV background is adjusted to the counts measured outside the exclusion regions[25]. This is an important step, because it corrects for effects that are not taken into account during the FoV background model construction (see section 3.2.4), such as variations of the level of NSB and atmosphere transparency. In this work, following the example of [153], we applied a purely spectral correction to the FoV background model, based on two free parameters called `norm` and `tilt`:

$$\mathcal{B}(E) \longrightarrow \mathcal{B}(E) \times \texttt{norm} \times \left(\frac{E}{1\,\mathrm{TeV}}\right)^{-\texttt{tilt}} , \tag{3.29}$$

  where $\mathcal{B}(E)$ is the predicted background rate at a given reconstructed energy E. The `norm` is a unitless normalization factor with expected value of 1, used to re-scale the background flux without changing its spectral shape. Since the number of the detected events decreases with energy as a power-law, this kind of correction is statistically dominated by the lowest energy bins (close to the energy threshold). Therefore, fitting only the `norm` parameter would lead to a wrong background estimation at the highest energies, except for the special case in which the background spectrum maintains the same spectral index across the whole energy range. The `tilt` correction (with e xpected

[23] With this term we refer to a combination of truly diffuse γ-rays, produced by cosmic ray hadronic and leptonic interactions in the interstellar space, and unresolved γ-ray sources, too faint or extended to be clearly detected.

[24] Not to be confused with the FoV, which refers to the solid angle that is visible by the telescope during one single pointing.

[25] We note that this can create problems for large-scale and diffuse sources, since the needed exclusion regions may often leave little un-masked space for a robust background model adjustment.

value of 0) to the background spectral slope is therefore necessary, to limit high-energy misestimations induced by the `norm` fit. However, this kind of slope correction can only be applied in a meaningful way in the energy range in which the background model follows a simple power law function. This is the case only above the reconstructed energy at which the background rate peaks, which means that the `tilt` fit forces the choice of a higher analysis energy threshold with respect to other more traditional (1D and 2D) analysis techniques. An example of this kind of correction, following equation 3.29 above the background peak energy, is shown in figure 3.3 (left panel). More elaborate solutions are currently under study to avoid the energy threshold issue. For example, one may adjust a piece-wise `norm` factor independently in a certain number n of energy ranges (see figure 3.3, right panel):

$$\mathcal{B}(E) \longrightarrow \mathcal{B}(E) \times \sum_{i=1}^{n} \texttt{norm}_i \times \tau_i \ , \tag{3.30}$$

where τ_i is a top-hat function which is equal to 1 in the energy range i and equal to zero outside. This kind of correction would avoid the necessity of introducing a background `tilt`, but possibly lead to the introduction of too many free background parameters. Alternatively, one may apply a sort of intermediate solution, by correcting with piece-wise `norm` factors (equation 3.30) up until a sufficiently high (above the background peak) energy, and at higher energies apply a single `norm` and `tilt` correction as in equation 3.29. In the future, some kind of background correction along these lines will hopefully achieve a lower energy threshold for the 3D analysis;

- finally, the `MapDataset` instances for each telescope's observation are either stacked on one another to obtain a single `MapDataset`, or stored together separately into a `Datasets` container.

Model fitting:

- up to this point, the only model component that has been attached to the observations is their FoV background model. Now a source model can be added, based on a guess[26] of the properties of all sources in the RoI. Each source is described by a separate `SkyModel`, which provides a parametric description of its morphology, spectrum and temporal evolution;
- the assumed model is completely defined by a set Θ of parameters for which the 3D analysis determines the best possible estimates, i.e. those for which the cube of *model-predicted* counts mimics as closely as possible the *measured* one. The number of predicted counts within the reconstructed energy bin i and spatial pixel j is given by:

$$N_{i,j} = t \times \int_{E_i}^{E_{i+1}} dE_{\rm reco} \int_j d\mathbf{x}_{\rm reco} \left\{ \mathcal{B}(E_{\rm reco}, \mathbf{x}_{\rm reco}, \Theta_{\mathcal{B}}) + \mathcal{M}^*(E_{\rm reco}, \mathbf{x}_{\rm reco}, \Theta) \right\} \ . \tag{3.31}$$

Here, $\mathcal{B}$ is the background model (already built in reconstructed parameter space, i.e. IRF-convolved) dependent on a set of parameters $\Theta_{\mathcal{B}}$, namely a `norm`

[26] Informed by the inspection of flux maps and/or 1D spectra.

and `tilt`, while $\mathcal{M}^*$ represents the convolution of the 3D source model $\mathcal{M}$ with the IRFs:

$$\mathcal{M}^*(E_{\rm reco}, \mathbf{x}_{\rm reco}, \Theta) = \int_0^\infty dE_{\rm true} \int_{\rm FoV} d\mathbf{x}_{\rm true}\, \mathcal{M}(E_{\rm true}, \mathbf{x}_{\rm true}, \Theta) \\ \times A_{\rm eff}(E_{\rm true}, \mathbf{x}_{\rm true})\, {\rm PSF}(\mathbf{x}_{\rm reco}|E_{\rm true}, \mathbf{x}_{\rm true})\, {\rm EDisp}(E_{\rm reco}|E_{\rm true}, \mathbf{x}_{\rm true})\ . \tag{3.32}$$

The best-fit estimates for the model parameters are found by maximizing (by means of numerical strategies such as the ones provided by the `iminuit` [164]) the binned likelihood

$$\mathscr{L}(\Theta) = \prod_{i,j} P(\tilde{N}_{i,j} \mid N_{i,j}(\Theta))\ , \tag{3.33}$$

where $\tilde{N}_{i,j}$ ($N_{i,j}$) is the number of measured (model-predicted) counts in each reconstructed energy bin i and pixel j. Since the 3D analysis relies on a background model, the relevant *fit statistic* is the *Cash* one, $\mathcal{C}(\Theta) = -2\ln\mathscr{L}(\Theta)$. In case of a joint-likelihood analysis, the source model parameters are *linked* across all `Dataset` instances. This means that the model applied to each `Dataset` k (as in equation 3.31) is

$$\mathcal{B}_k + \mathcal{M}^*\ , \tag{3.34}$$

where $\mathcal{M}^*$ is the IRF-folded source model (the same for all `Dataset` instances) and $\mathcal{B}_k$ is the background model for the `Dataset` k. In this case, the `Dataset`-specific values of the fit statistic are simply summed together, $\mathcal{C} = \sum_k \mathcal{C}_k$, and the minimization can essentially proceed as in the stacked case.

Another important aspect of the 3D analysis is the choice of an *exclusion mask*, which is a list of RoI portions that are ignored during the fit statistic computation. For example, it is generally a good practice to mask away the borders of the RoI, in order to limit possible edge effects such as background contaminations due to non-modeled sources leaking in from outside the RoI. Also, when there are multiple sources of γ-ray emission in the RoI, one as to make a choice on whether to model them all or mask some of them[27]. On one hand, modeling all the γ-ray emission in the FoV is desirable as it provides more physical information, together with a coherent description of the whole RoI. On the other hand, it may in some cases lead to the introduction of an excessive number of degrees of freedom, preventing a meaningful fit convergence for little gain in terms of physical knowledge. Therefore opting for a compromise solution, in which only the most relevant sources in the RoI are modeled, is often the best option.

Finally, we note that the 3D analysis allows to determine the best-fit parameters under any given model assumption, but it does not provide by itself a recipe to determine the best possible model choice. For example, it may happen that the 3D fit converges equally well when a γ-ray source is described by a symmetric morphology and a slightly elongated one. This is an hypothesis testing (or *goodness of fit*) problem, that can be tackled (for nested models) using the likelihood ratio test described in section 3.3.1.

[27] We note that if a region containing significant γ-ray emission is neither modeled nor masked, it inevitably contaminates the background model or the other model components.

Part II

Discovery of a PeVatron candidate in HESS J1702-420

Chapter 4

Updated H.E.S.S. observations and analysis of HESS J1702-420

4.1 Introduction

HESS J1702-420 is an extreme particle accelerator in the Galactic plane, discovered in the early days of H.E.S.S. operations near $l \approx 344.30^{o}$ [42]. With its bright and hard γ-ray spectrum, HESS J1702-420 is generally considered a promising PeVatron candidate, but its physical nature is still unclear due to the complete lack of associated objects at other wavelength, which make it a *dark* TeV source [40]. In an effort dedicated to the identification of HESS J1702-420, H.E.S.S. has recently carried out deep re-observations of the source region. The resulting data were processed according to the *he* configuration of the HAP-Fr analysis chain, dedicated to the study of potential PeVatron candidates (see section 2.3.3). This chapter presents the high-level analysis results obtained using Gammapy[1] version 0.17 [163], that were recently published in the H.E.S.S. Collaboration paper [158]. This is the first H.E.S.S. paper which makes use of open-source tools and the 3D analysis techniques.

The chapter is structured as follows: first, we summarize the history of TeV observations of HESS J1702-420 since its discovery to the present day (section 4.2). Then, in section 4.3 we describe the update H.E.S.S. observations of HESS J1702-420 that were processed with the 3D likelihood technique (section 4.4). The main analysis results consist in the derivation of a spectro-morphological source model that provides a coherent description of the HESS J1702-420 region (section 4.4.4), with the separation of HESS J1702-420 into two model components based on their significantly different morphologies and spectra (section 4.4.5). Finally, section 4.5 focuses on the morphology of HESS J1702-420 in different energy bands, as measured using the classical ring background estimation technique.

4.2 VHE γ-ray observations of HESS J1702-420

Discovered 15 years ago [42], HESS J1702-420 is a bright VHE γ-ray source whose physical nature is still unknown. So far, it was detected only by H.E.S.S., due to its location in the Southern equatorial sky that hides it from the other currently operating VHE γ-ray telescopes. To illustrate this fact, table 4.1 shows the difference between

[1] The high-level analysis with Gammapy has been validated against the standard H.E.S.S. software (HAP) and other open-source tools (ctool) in [153], allowing as to use it as the main analysis tool for our study.

Experiment	Location	Geographic latitude	$\tilde{Z}$
H.E.S.S.	Namibia	$-23°16'$	$18°44'$
Magic	Spain (La Palma)	$28°45'$	$70°46'$
VERITAS	USA (Arizona)	$31°40'$	$73°41'$
FACT	Spain (La Palma)	$28°45'$	$70°46'$
Tibet AS+MD	Tibet	$\approx 30°$	$\approx 72°00'$
HAWC	Mexico	$18°59'$	$61°00'$
LHAASO	China (Sichuan)	$29°21'$	$\approx 71°22'$
CTA North	Spain (La Palma)	$28°45'$	$70°46'$
CTA South	Chile	$-24°37'$	$17°23'$
SWGO	TBD [173]	$\approx -20° (\pm 10°)$	$\approx 22° (\pm 10°)$

TABLE 4.1: Location and geographical latitude of the main currently operating (future) VHE experiments, above (below) the horizontal line. The quantity $\tilde{Z}$, related with the visibity of HESS J1702-420 as a function of the telescope's location latitude, is defined in the text.

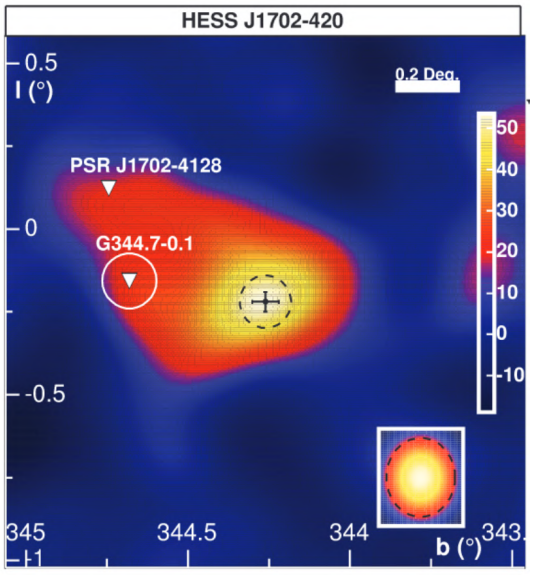

FIGURE 4.1: Excess map (smoothed with a 0.1°-radius Gaussian filter) of the HESS J1702-420 region, from [42]. The colorbar is in units of excess counts per smoothing radius.

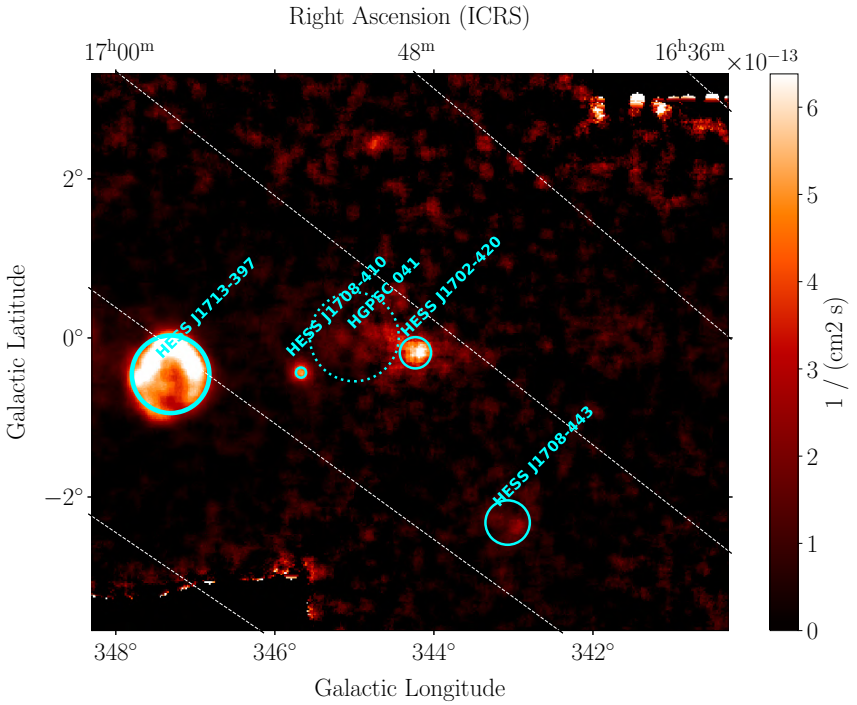

FIGURE 4.2: Map of the integral γ-ray flux above 1 TeV detected by H.E.S.S. in a portion of the Galactic plane centered on HESS J1702-420. The image was smoothed using a correlation radius $R_c = 0.1^o$. The data used to produce the image correspond to the publicly available material (`hgps_map_flux_0.1deg_v1.fits.gz`) from the HGPS [38].

the geographic latitude of the main VHE γ-ray observatories (present and future) and the equatorial declination of HESS J1702-420, $-42^{\circ}00'57''$. This quantity, indicated as $\tilde{Z}$, represents the smallest zenith angle at which the source is observable by a given telescope. As a rule of thumb, it can be assumed that the source is not well visible by an obervatory if $\tilde{Z} \gtrsim 60^{\circ}$. Table 4.1 shows that, among all currently operating telescopes, only H.E.S.S. can easily detect and study HESS J1702-420 ($\tilde{Z} \ll 60^{\circ}$). In the future instead CTA South and SWGO will be able to further observe it under favourable conditions.

The first (marginal) evidence for a detection of HESS J1702-420 was reported during the first Galactic plane survey campaign of H.E.S.S., published in 2006 [42], when the source was separated from the hadronic background with a post-trial significance of 4σ, based on a 5.7 h observation livetime and computed using the Li&Ma formula [174]. An indication of large-scale emission encompassing the astronomical objects PSR J1702-4128 and SNR G344.7-0.1 was also found (see figure 4.1), with an insufficient significance to classify HESS J1702-420 as an extended source. In July 2006, HESS J1702-420 was featured as source of the month on the H.E.S.S. website, in an article by the evocative title "HESS J1702-420 — Mystery Source or Pulsar Wind?". There, a possible association with the nearby pulsar PSR J1702-4128 was discussed. In [40], the detection of HESS J1702-420 was confirmed with a post-trial significance of 12.8σ (based on 9 h livetime), and the source was tagged as a *dark* object due to its non-detection at other wavelengths. At the time, a dedicated analysis revealed a hard power law spectral slope of $\Gamma = 2.07 \pm 0.08_{\mathrm{stat}} \pm 0.20_{\mathrm{sys}}$ with no sign of cutoff, an integrated flux above 1 TeV corresponding to 0.37 C.U.[2] and a significantly extended morphology, well described by a $0.30^{\circ} \times 0.15^{\circ}$ elongated Gaussian template.

In 2018, with better reconstruction and data selection algorithms, the HGPS catalog [38] confirmed the spectral hardness of the source ($\Gamma = 2.09 \pm 0.07_{\mathrm{stat}} \pm 0.20_{\mathrm{sys}}$), and estimated a TS-based source significance of 15σ based on 9.5 h of observations. The source extension was also confirmed, but its shape was simplified to a 0.2° symmetric Gaussian, due to the non-inclusion of elongated shapes in the semi-automated survey analysis chain. As a reference, figure 4.2 shows a map of the γ-ray flux in the source region, based on the HGPS published online material, together with the shapes and names of all catalog sources, including, in dotted lines, the components that were discarded by the HGPS crosscheck analysis. The closest neighbors of HESS J1702-420 in the TeV γ-ray sky are HESS J1708-410, which is also a dark TeV source [38], and HESS J1708-443. The latter is an extended source encompassing the astronomical objects SNR G343.1-2 and PSR B1706-44, with which it is likely associated via either leptonic or hadronic emission scenarios [38]. The HGPS catalog, which is exclusively based on data recorded until January 2013, represents the latest H.E.S.S. publication featuring HESS J1702-420. Since 2013, the source has been re-observed leading to the accumulation of a considerable amount of new on-source data ($\approx \times 4$, see section 4.3). In particular, a 2017 campaign of deep re-observations of HESS J1702-420, with the goal of probing its PeVatron nature, provided new high-quality data with the recently updated CT1-4 cameras [144]. In this chapter we present the analysis of the complete set of H.E.S.S. observations of HESS J1702-420 from 2004 up to 2019, which updates the previous H.E.S.S. publications on this source.

[2] Throughout this chapter, we adopt the convention of defining 1 Crab Unit (C.U.) as $8.36 \times 10^{-12}\,\mathrm{cm}^{-2}\,\mathrm{s}^{-1}$. This value corresponds to the integrated Crab nebula flux above 1 TeV, as measured in [115].

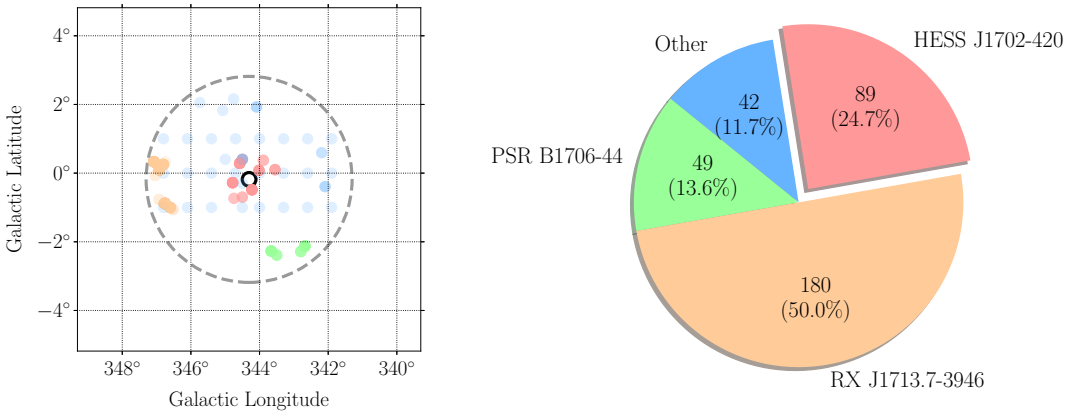

FIGURE 4.3: Left: The image shows the pointing directions of all the selected runs, with the the same color scheme as the right panel and opacity levels proportional to the number of overlapping pointings. The black solid circle represents the 1σ size of the HESS J1702-420, from [38], while the 3°-radius gray dashed circle indicates the maximum allowed offset (see main text) between the pointings of the selected runs and HESS J1702-420. Right: Pie chart showing the absolute (fractional) number of observations aiming at HESS J1702-420 and other targets in the region.

4.3 Updated H.E.S.S. data set

All results presented in this chapter make use of H.E.S.S. data that were collected between 2004 and 2019. During this time, H.E.S.S. observations of the HESS J1702-420 region were carried out in multiple contexts: deep pointings on HESS J1702-420, observations of other nearby objects (mainly RX J1713-3946 and PSR B1706-44) and Galactic plane scan observations taken in survey mode during the HGPS campaign. As a run selection criterion, we picked all 4-telescope high-quality observations with pointing direction within 3° from the HGPS position of HESS J1702-420:

$$(\tilde{l}, \tilde{b}) = (344.30^{\circ}, -0.18^{\circ}) \,. \tag{4.1}$$

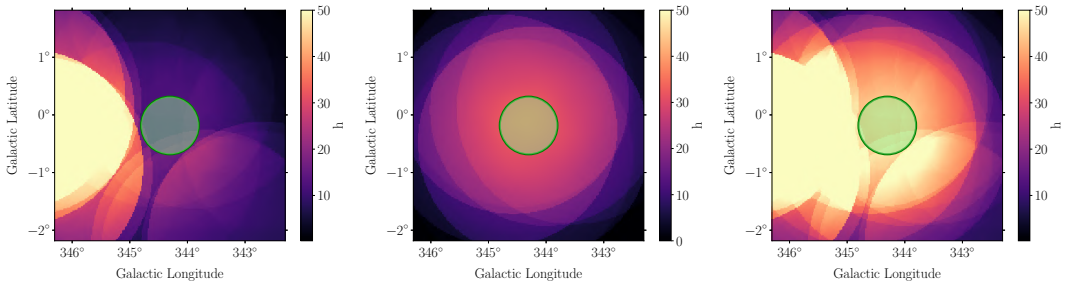

FIGURE 4.4: Acceptance-corrected livetime maps of the HESS J1702-420 region, computed using equation 4.2, obtained from the selection of all 4-telescope high-quality runs pointing within 3° from HESS J1702-420. The left (center, middle) panel refers to observation taken with the H.E.S.S. I (H.E.S.S. IU, both) cameras. The green 0.5°-radius circle denotes the area that was used to compute the (averaged) on-source livetime.

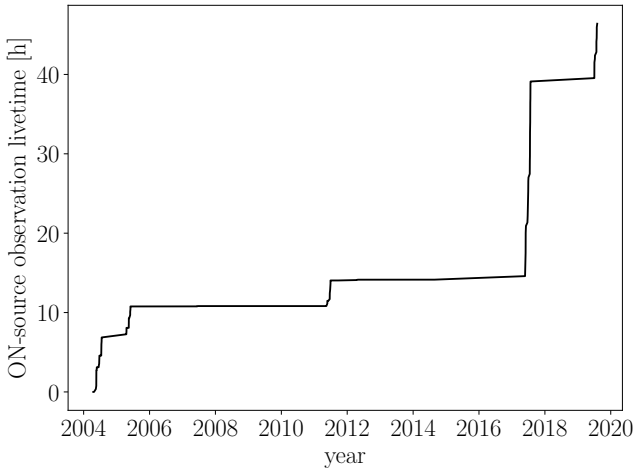

FIGURE 4.5: Growth of the observation livetime accumulated on HESS J1702-420, from 2004 to 2019. The livetime is obtained by averaging over the same circular region as in figure 4.4.

This resulted in the selection of 360 observations, whose pointing directions are shown in figure 4.3, left panel. The right panel of the same figure contains instead a pie chart, showing the fraction of runs whose primary target was HESS J1702-420 (about one quarter of the total) and the other nearby objects. The majority of the selected runs were not directly pointing on HESS J1702-420, but were analyzed to accurately measure the source morphology, which is known to be significantly extended. They also played an important role in constraining the background model in the region, which is essential to provide a coherent description of HESS J1702-420 and it surroundings.

As a safety measure, all events having reconstructed direction further away than `offset_max` $= 2^{\circ}$ from the run-wise pointing position were rejected. Indeed, between 2° and 2.5° (which corresponds to the CT1-4 array FoV radius) the knowledge of the instrument response is affected high systematics[3].

The *effective livetime* of observation at a given sky position (l, b) can be defined as

$$\sum_{i=1}^{N_{\text{runs}}} \tau_i \times \frac{A^i_{\text{eff}}(l,b)}{\max\{A^i_{\text{eff}}(l,b)\}} \ , \tag{4.2}$$

where τ_i is the run-wise livetime of observation (usually $\tau_i \approx 28\,\text{min}$), A^i_{eff} is the position-dependent effective area of the array and $\max\{A^i_{\text{eff}}\}$ is its peak value. This quantity measures the amount of time that was spent observing a given sky position, weighted by the telescope's collection area in the same direction. Figure 4.4 contains a map of the effective livetime accumulated in the HESS J1702-420 region, by the H.E.S.S. I (left), H.E.S.S. IU (center) and both (right) arrays. Clearly, the 15 years long observation history of the region led to a high degree of exposure inhomogeneity. The total acceptance-corrected livetime on HESS J1702-420, obtained by averaging over the 0.5°-radius circle shown in green in figure 4.4, is 44.9 h. H.E.S.S. I runs contribute 11.5 h on the source, while the largest fraction of the on-source livetime (33.4 h) was obtained from 2017 on, with the updated H.E.S.S. IU cameras. This is

[3]For example, PSF asymmetries are known to arise at offsets $\gtrsim 2^{\circ}$. This contrasts with the assumption of radial symmetry, currently made in the internal handling of the PSF by Gammapy and the other H.E.S.S. analysis software, which would potentially lead to biased fit results.

Name	Runs	Zenith [deg]	Offset [deg]	On-source time [h]	Period
A	166	16.3 - 35.9	1.6 - 2.8	1.8	2004 - 2014
B	88	36.1 - 62.4	2.2 - 2.8	0.0	2004 - 2014
C	26	17.8 - 35.1	0.2 - 1.4	9.7	2004 - 2011
D	80	37.5 - 59.1	0.3 - 0.8	33.4	2017 - 2019

TABLE 4.2: The 360 selected H.E.S.S. observations were sorted into four groups (named A-B-C-D as in figure 4.6, lower panel) based on their zenith angles and source offsets from the pointing direction. The on-source livetime column was obtained as explained in the caption of figure 4.4. Runs belonging to the groups A-B-C, that do not substantially increase the exposure on HESS J1702-420 due to the large pointing offset, were included in the analysis to better contrain the background level, while also providing a coherent description of source surroundings. The fourth group contains all (and only) H.E.S.S. IU observations, for which different IRFs have been used.

also illustrated in figure 4.5, which shows the growth of the on-source observation livetime (averaged on the same circle as in figure 4.4) from 2004 to 2019.

4.4 Three-dimensional likelihood analysis

4.4.1 Analysis setup

Performing a 3D *joint* likelihood analysis (see section 3.4.4) for all the 360 selected runs would be a computationally expensive and inefficient task. Indeed, each run carries at least one free model parameter, its FoV background normalization, which would add up to ≥ 360 degrees of freedom. In the future, Gammapy will possibly allow to distribute such a complicated fit among multiple machine cores, thus reducing the computation time by orders of magnitude. With the version 0.17 of Gammapy however, the 3D likelihood scan proceeds on a single CPU, which renders such jobs unmanageable. That is why, before moving on with the actual analysis, a few data inspection and preparation steps were performed, to optimize both computation time and systematic uncertainties. First, for each observation i we extracted the values of two parameters that are known to strongly affect the recorded data and IRFs:

- the pointing zenith angle Z_i, which influences the number of detected γ-like events. The higher is the zenith angle (i.e. the lower toward the horizon is the observation pointing), the more air mass has to be traversed by a shower before reaching the telescope, which implies more scattering and absorption of the Cherenkov light from the shower. This leads to an increase of the analysis energy threshold with the zenith angle, since the Cherenkov light from the lowest energy showers becomes too dim to be detected due to geometric spreading and atmospheric absorption. On the other hand, the effective area at high energies is expected to increase with the zenith angle, bringing a higher number of detected γ-like events. Indeed the highest energy showers are so bright that they can still trigger the array, even after traversing a long path in the Earth atmosphere. Also, they are less likely to saturate the camera as at low zenith, which often leads to event rejection;

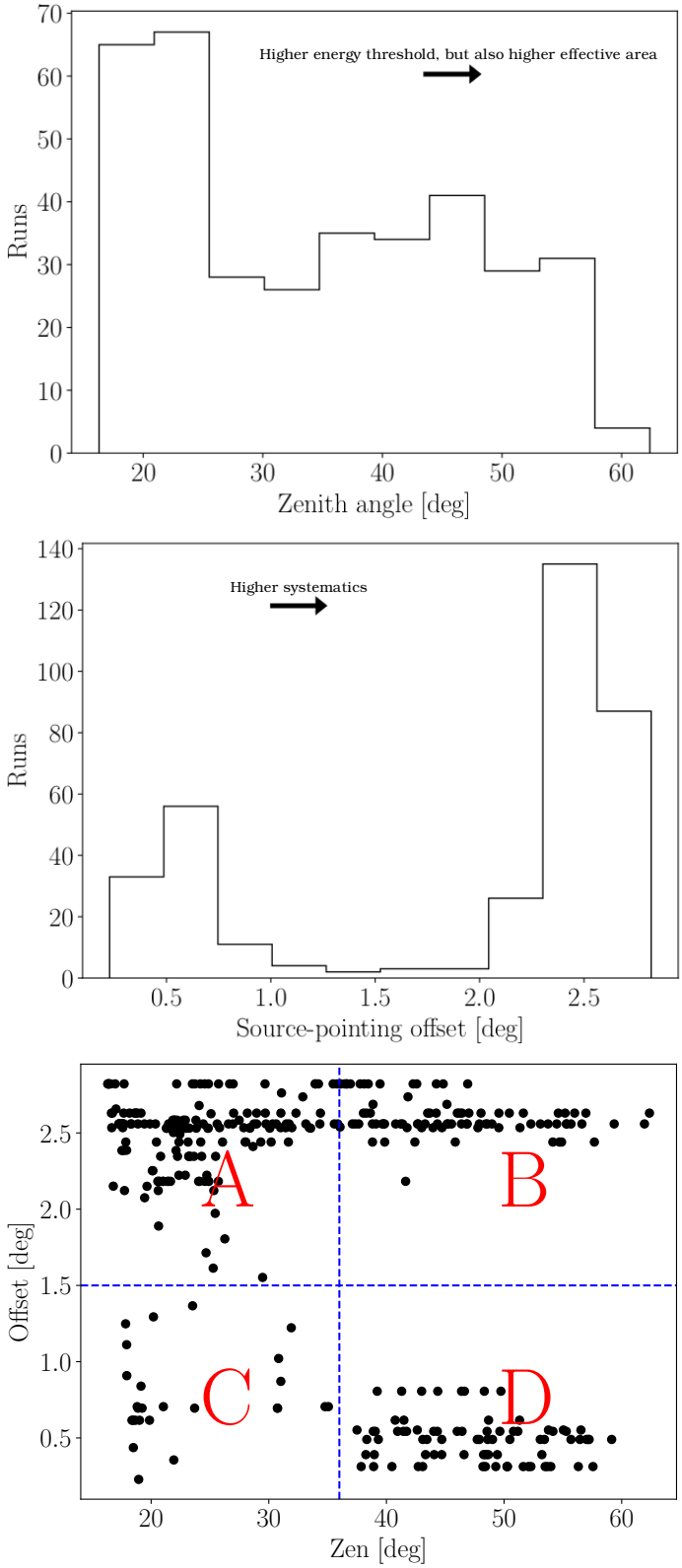

FIGURE 4.6: Top: Distribution of run-wise pointing zenith angles Z_i. Center: Distribution of offsets Θ_i between the nominal position of HESS J1702-420 (equation 4.1) and the run-wise pointing directions. Bottom: Division of the total 360 runs into four groups, named A-B-C-D, based on their offsets and zenith angle values.

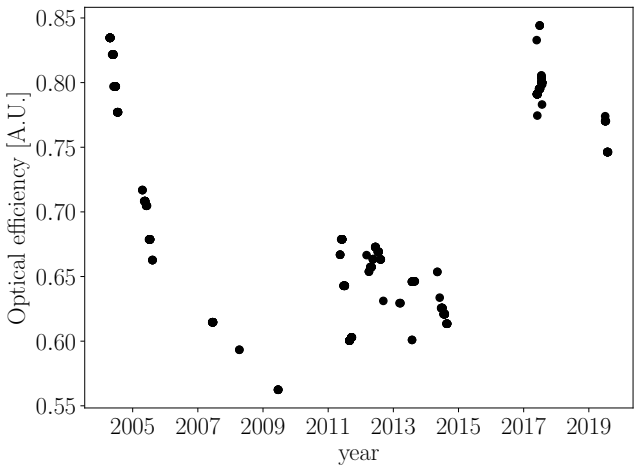

FIGURE 4.7: The image illustrates the variations of the *relative optical efficiency* (see main text) of the H.E.S.S. telescope array, from 2004 to 2019, for the observations that were used in the 3D likelihood analysis of HESS J1702-420. The optical efficiency steadily dropped until 2011, due to the aging of the hardware, then it slightly increased back as a result of maintenance operations such as mirror refurbishment and PMT funnel cleaning. Finally, the 2017 camera upgrade (H.E.S.S. I → H.E.S.S. IU, [144]) drastically improved again the instrument's optical efficiency.

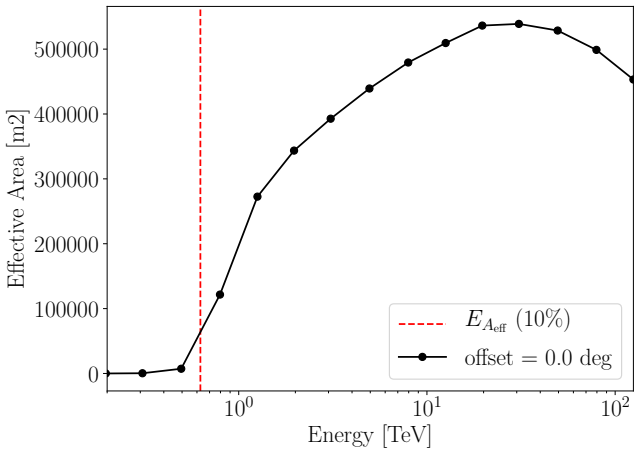

FIGURE 4.8: Effective area as a function of the true incident photon energy, extracted from the pointing direction (i.e. offset = 0°) of one randomly picked H.E.S.S. observation (zenith angle 17.7°) of HESS J1702-420. The red vertical line indicates the threshold energy at which the effective area curve drops to 10% of its maximum. We note that during the analysis this criterium was applied to the effective area as measured at the sky position of HESS J1702-420, defined in equation 4.1.

- the offset Θ_i between the pointing position and the location of HESS J1702-420 (see equation 4.1). The knowledge of the telescope's response gets worse at large offsets from the pointing direction, which is also why we rejected all events failing the `offset_max` cut at 2° (see section 4.3). This means that runs pointing far away from HESS J1702-420 (for example $\gtrsim 1.5°$) contribute with lower-quality data on the source than runs pointing directly on top of it. In other words, depending on the value of Θ_i, the on-source data are affected by different levels of systematic uncertainties.

The distribution of Z_i (Θ_i) values, for all the 360 analysis runs, is shown in the top (center) panel of figure 4.6. The figure illustrates the heterogeneity of the run list, with zenith angles and offsets in the wide ranges $18.7° \lesssim Z_i \lesssim 62.4°$ and $0.2° \lesssim \Theta_i \lesssim 2.8°$. This fact calls for a dedicated strategy to properly combine together observations while minimizing systematic effects. Ideally, if all observations were recorded under the same conditions, they could be *stacked* all together. However, stacking observations that were taken under significantly different conditions leads to the use of averaged IRFs that may increase the level of the analysis systematics (see section 3.4.1). Therefore we adopted compromise solution: by approximately splitting in half the Z_i and Θ_i distributions, at the intermediate values $Z^* = 36°$ and $\Theta^* = 1.5°$, we defined four groups of runs with similar observational conditions, that we named A-B-C-D (figure 4.6, lower panel). Then, we stacked together all observations within each group, ending up with four independent data sets to be used in a 3D joint-likelihood analysis. A third relevant factor that affects the data quality is the year of observation, which is connected with different hardware versions and aging conditions. In our scheme, the group D contains all (and only) H.E.S.S. IU runs, recorded after the 2017 camera upgrade [119], for which dedicated Monte Carlo IRF simulations are used, while the groups A-B-C contain exclusively pre-2017 data. Further details on the four groups of observations are reported in table 4.2.

In order to perform a *binned* 3D likelihood analysis, the γ-like events have to be filled into three-dimensional data structures called *cubes* (see section 3.4.4). For each of the four observation groups, the list of reconstructed events was reduced to a binned cube defined by:

- an analysis region of interest (RoI) with size of $4° \times 4°$. This choice represents a compromise between two factors: the necessity of a sufficiently large RoI to fully enclose the source and get enough off-source regions for a correct background estimation, and a sufficiently small RoI to minimize the number of nearby sources that have to be modeled. The RoI was centered at the HGPS position of HESS J1702-420, defined in equation 4.1;
- a spatial pixel size of $0.02° \times 0.02°$, which ensures sufficient per-pixel statistic while still providing good spatial resolution. We remember that for the chosen analysis configuration (see section 2.3.3) the PSF size (68% containment) is $\approx 0.12°$;
- the third axis of the cube, encoding the reconstructed energy of the incident photons, was divided into 20 equally-spaced (in logarithmic scale) bins between 0.5 and 150 TeV.

In order to reject poorly reconstructed data, for each observation i we discarded all events with reconstructed energy below the safe threshold

$$E^i_{\rm safe} = \max\{E^i_{\rm bkg}, E_{A^i_{\rm eff}}\}\,, \tag{4.3}$$

where:

- $E^i_{\rm bkg}$ represents the peak energy of the hadronic background model, i.e. the energy at which the maximum rate of hadronic background events is supposed to be detected. This choice was dictated by the fact that the adjustment of the run-wise background model to the off-source data (described in section 4.4.2) currently proceeds under the assumption that the background spectrum is approximately a pure power law, which is verified only below $E^i_{\rm bkg}$ (see section 3.4.4). Another perhaps more fundamental reason is that the run list contains observations that were recorded early in the history of H.E.S.S., at a time when the optical efficiency of the telescope was at its best. This can be seen in figure 4.7, where the *relative* (to a reference value measured during the construction phase) optical efficiency is shown. Instead, the background model was built from runs accumulated over the whole H.E.S.S. I period, that have on average a lower optical efficiency, potentially leading to systematic effects below the background peak energy [153];
- $E^i_{A_{\rm eff}}$ is the energy at which the effective area at $(\tilde{l}, \tilde{b})$ drops to 10% of its maximal value, for a given run. This criterion is meant to reject events for which the uncertainty on the effective area of the array is too large. Indeed, at low energies, the $A^i_{\rm eff}$ is a steeply rising function of the true photon energy (see figure 4.8), which means that even a small energy reconstruction error (due to e.g. atmospheric light absorption) potentially leads to a large error on the value of the effective area. We notice that the particular choice of 10% of the peak value, often adopted in H.E.S.S. and applied by default in Gammapy, is arbitrary, since it's hard to define a priori at which point the effective area becomes *sufficiently* flat.

After grouping together observations taken under similar conditions, binning the data cubes and rejecting events with reconstructed energy $< E^i_{\rm safe}$, the last data preparation step needed before the 3D analysis is the adjustment of the FoV background model, described in the next section.

4.4.2 FoV background model adjustment

The construction of a FoV background model in the form of a lookup table, and the assignment of a *tailored* background model to each H.E.S.S. observation are discussed in section 3.2.4. Here we describe the corrections to the FoV background model, made on a run-by-run basis, that were necessary to account for possible differences between the analyzed runs and those that were used to build the background model. The general notions behind this procedure are reported in section 3.4.4.

In order to exclude sky regions containing known (resolved and diffuse) γ-ray emission, we used the exclusion mask shown in figure 4.9. The mask was generated by iteratively adapting a first-guess list of exclusion regions, and excluding step-by-step all sky positions containing significant γ-ray emission[4].

For each run, we adjusted the background model to the off-source data (obtained after applying the exclusion mask) using a power law correction based on two free

[4]This algorithm, described in detail in section 4.5, made use of the *wstat* statistic, instead of the *Cash* statistic that applies for the 3D analysis. We verified a posteriori, from the inspection of the final *Cash* significance maps and the overall success of the 3D analysis, that this fact did not significantly affect the background model fit quality.

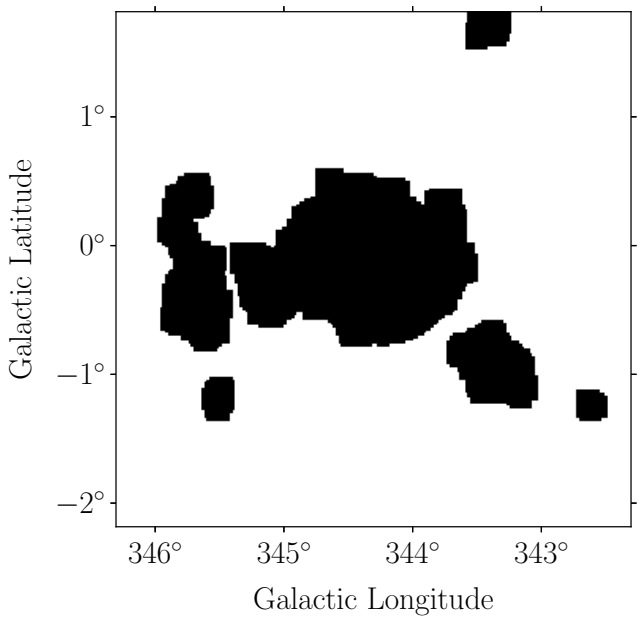

FIGURE 4.9: Exclusion mask used of the FoV background correction (see section 4.4.2). It was obtained by conservatively multiplying together the exclusion masks computed in section 4.5, for the energy thresholds of 2 and 5 TeV. This ensures the exclusion of all significant γ-ray emission in the RoI, and the achivement of an unbiased background model adjustment.

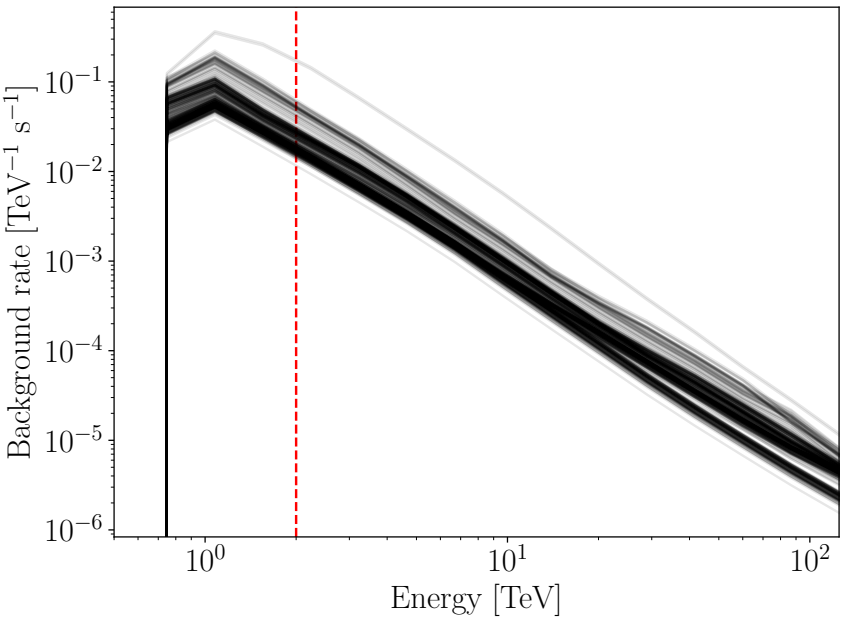

FIGURE 4.10: Energy spectra of the background models for the 360 runs used in the 3D analysis of HESS J1702-420. The spectra were obtained by integrating the background models over the FoV solid angle. The red dashed line indicate the $E_\gamma = 2\,\mathrm{TeV}$, chosen as E_{fit} in equation 4.4.

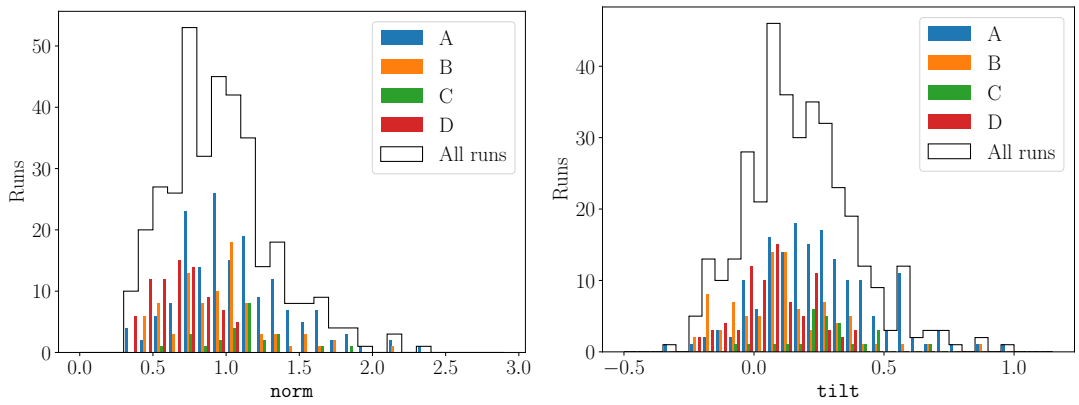

FIGURE 4.11: Distribution of the background model `norm` (left panel) and `tilt` (right panel) parameters, obtained by correcting the background spectrum for each run as described in formula 3.29. The separate distributions for each of the four observation groups (with the same naming scheme as the lower panel of figure 4.6 or table 4.2) are shown as colored histograms, while the total distributions for all runs are shown in black.

parameters, the spectral `norm` and `tilt` (see equation 3.29). Currently the `tilt` correction to the background spectrum is necessary to achieve a correct background estimation at the highest energies. Unfortunately, as explained in section 3.4.4, this implies an increase of the analysis energy threshold to $\approx few \times E_{\rm bkg}$, in order to entirely avoid the energy range close to the background peak during the fit. As visible from figure 4.10, above $E = 2\,\text{TeV}$ the background spectra of all the analyzed runs are (approximately) pure power laws. For this reason, we added the fit threshold condition

$$E_{\rm fit} = 2\,\text{TeV} \tag{4.4}$$

on top of the safe energy threshold definition (equation 4.3). We then adjusted the background model to the masked counts for each run i above the energy

$$E^i_{\rm threshold} = \max\{E^i_{\rm safe}, E_{\rm fit}\}\,. \tag{4.5}$$

The final distributions of fitted `norm` and `tilt` values are shown in figure 4.11. Clearly, neither of the two distributions resembles a Gaussian with $\sigma = 1$, which means that in this case the systematic uncertainties dominate over the statistical ones. The `tilt` distribution is reasonably symmetric, but its mean value is higher than the expectation (0). According to equation 3.29, this means that on average the measured bkg spectrum is steeper than the model prediction. The `norm` distribution instead is approximately centered on the expected value of 1, but it is clearly asymmetric, with a larger number of runs having a normalization smaller than 1. The precise origin of these effects is far from being obvious. They could be due to a difference between the time in which the runs used to build the background model and the analyzed runs were taken. What is sure is that they reveal the insufficient accuracy of the current background model, that can provide a good description of the off-source data in the whole energy range only after important spectral corrections. This is not ideal, but, given the known limitations of the current background model construction algorithm (section 3.2.4), it can't surprise either. Indeed, the exact purpose of the

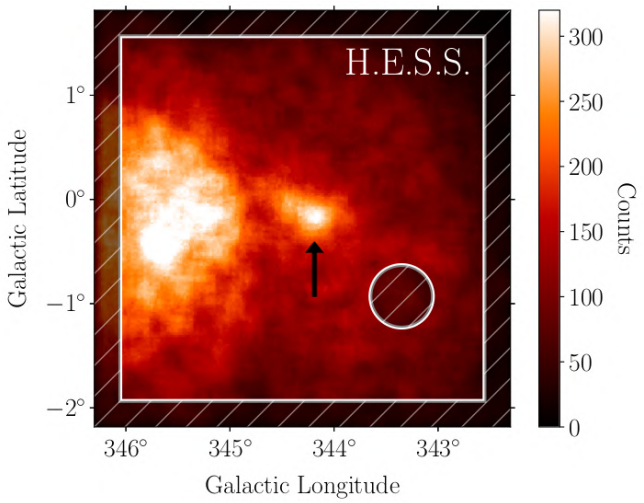

FIGURE 4.12: Map of H.E.S.S. counts in the HESS J1702-420 region. The emission of HESS J1702-420 is indicated by the black arrow.

FoV background correction procedure is to compensate for the background model imperfections, thus ensuring that the model can be safely applied to the 3D analysis of γ-ray sources.

After this step, the background models were stacked together by summing up the run-wise model-predicted counts within the four independent groups of observations A-B-C-D (defined in section 4.4.1). This way, a single background model was assigned to each group. Later on, during the 3D model fitting procedure, for each of the four background models a spectral `norm` parameter was again introduced as a free parameter, to be adjusted together with the models of all γ-ray sources in the region.

4.4.3 The updated H.E.S.S. counts map

Before proceeding with the 3D analysis, we inspected the H.E.S.S. data to visually assess the brightness and extension of HESS J1702-420. A map of the H.E.S.S. measured counts, centered on the source, is shown in figure 4.12. The image was obtained by stacking the four individual data sets, integrating the binned data cube over the reconstructed energy axis ($E > 2\,\mathrm{TeV}$) and correlating the data with a 0.1°-radius top-hat kernel. HESS J1702-420 is clearly visible at the center of the RoI, with its distinct *teardrop* shape elongating toward PSR J1702-4128 (as in figure 4.1). Since the counts map was not corrected by the observation exposure, the bright area at $l \gtrsim 345^\circ$ is explained as the result of deep observations of RXJ 1713-3946 (see figure 4.3).

In the figure, the hatched regions represent portions of the RoI that were masked during the 3D analysis (i.e. ignored for the fit statistic computation). The importance and the criteria for the choice of the exclusion mask for a 3D analysis are described in section 3.4.4. In our case, we chose to mask a 0.3°-radius circular region centered at $l = 343.35^\circ$ and $b = -0.93^\circ$, containing a $\approx 3\sigma$ significance hotspot. The presence of this hotspot was noticed during preliminary 3D analysis tests, and the choice of excluding it, instead of modeling it, was justified by its marginal significance and high angular offset from HESS J1702-420. All the rest of the γ-ray emission in the region was modeled, with the exception of a 0.25° frame around the borders of the RoI, also visible in figure 4.12. This region was additionally excluded from the analysis,

to limit possible contaminations due to unmodeled sources just outside the analysis RoI.

4.4.4 Source model derivation and results

We performed a 3D *joint-likelihood* analysis of four independent datasets (see section 3.4.4), obtained by stacking observations within each of the four groups defined in section 4.4.1. Each `Dataset` was assigned its own FoV background model, but all shared the same source model. The analysis was performed above the energy threshold defined in equation 4.5. The 3D analysis, with the *forward-folding* technique, allows one to determine the best set of parameter values to describe the measured data, given an underlying model assumption. However, the problem is how to assess the quality of the model assumption itself, or equivalently how to find the model that best describes the data based on a minimal set of parameters. For this, an additional statistical method, built on top of the 3D analysis technique, has to be adopted. For the case of HESS J1702-420 we used a strategy based on the *likelihood-ratio test* (see section 3.3.1). We developed a semi-automatic routine achieving the improvement of a first-guess model with the iterative addition of new components described by a symmetric Gaussian morphology and power law spectrum or the test of different spectral and spatial assumptions for the already existing components. Step-by-step, the statistical significance for the model improvement was assessed using two indicators:

- the likelihood-based *test statistic* (TS, see equation 3.8), which takes into account the number of degrees of freedom added at each step;
- the flattening of spatial and spectral residuals toward zero, assessed by visual inspection, as a result of the addition of new model components.

The gradual improvement of the source model is illustrated in figure 4.13, where only the statistically significant iteration steps are reported. The figure contains five sub-figures, ordered from (a) to (e), each one comprising three panels:

- left: a map of model-predicted counts, obtained by applying the formula 3.31 to all model components (background included). The energy range, smoothing filter and color bar normalization are the same as in figure 4.12, which should look identical (modulo the Poisson data fluctuations) if the source model provides a good description of the data. The sizes and names of all model components are also indicated;
- center: the spatial distribution of model residuals, showing the *Cash* significance (in units of Gaussian standard deviations) of the *data - model* residuals, given the fluctuations of the data;
- right: an histogram containing the number of occurrences of each singificance value from the center panel. The fit of a Gaussian function to the histogram is shown, together with a reference standard normal distribution. The two distributions should coincide, in case the model residuals were exclusively due to statistical Poisson fluctuations.

Now we can summarize the modeling process (in a simplified way, since all non-significant trials are omitted), by describing figure 4.13 panel-by-panel:

(a) this is the first analysis step, in which we only modeled the hadronic background and looked at the resulting distribution of model residuals. The measured data

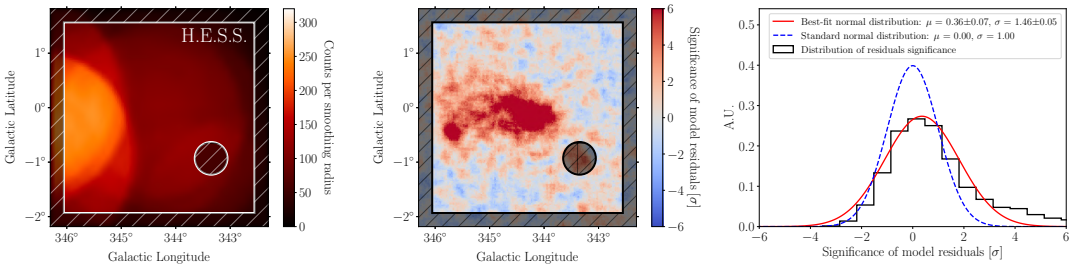

(a)

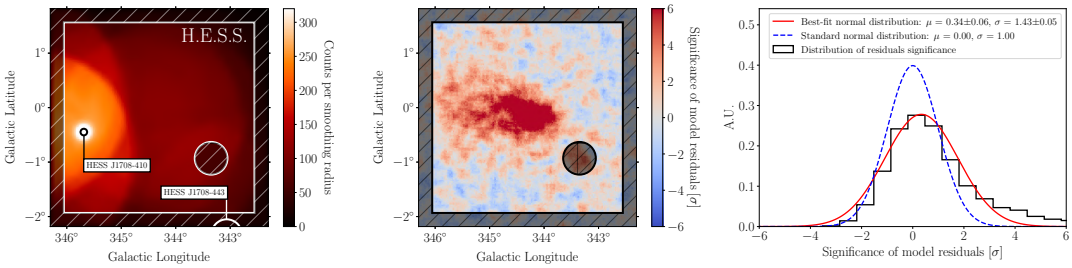

(b)

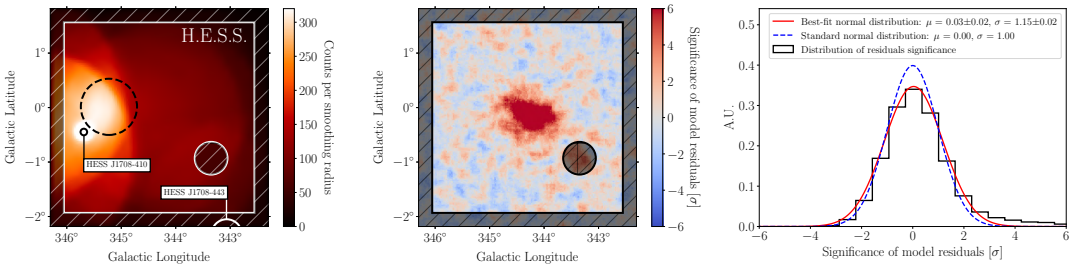

(c)

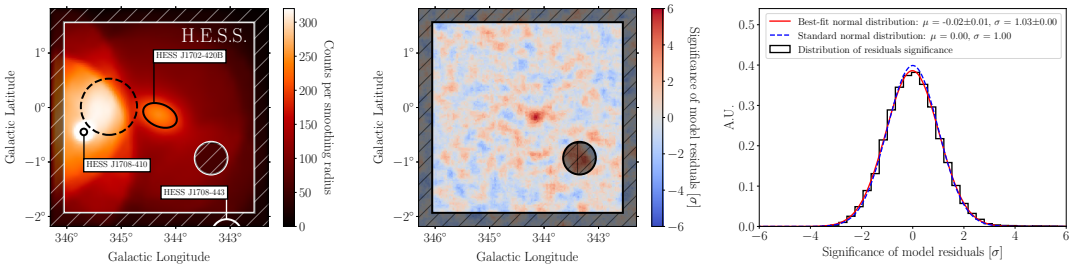

(d)

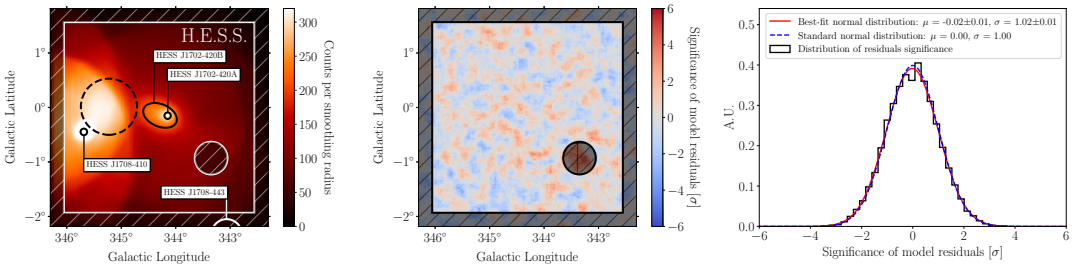

(e)

FIGURE 4.13: Iterative improvement of the source model for the HESS J1702-420 region. More details are provided in the main text (section 4.4.4).

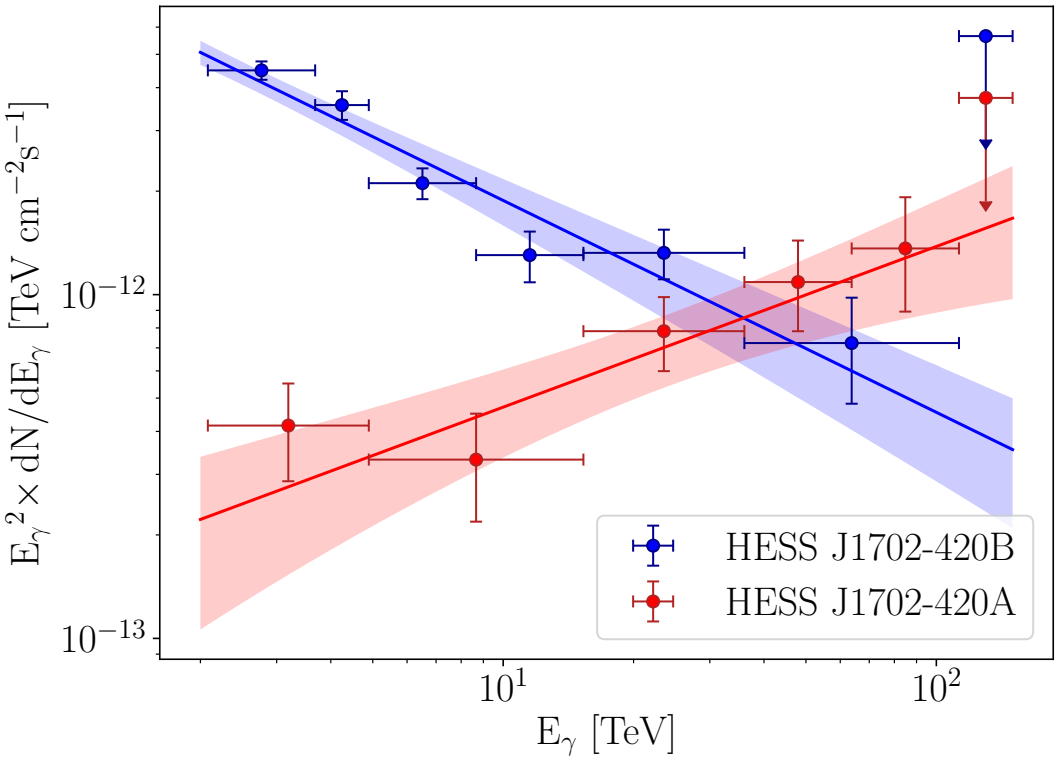

FIGURE 4.14: Power law spectra of HESS J1702-420A (red solid line) and HESS J1702-420B (blue solid line), as a function of the incident photon energy E_γ. The butterfly envelopes indicate the 1σ statistical uncertainty on the spectral shape. They have been obtained from a 3D fit of the H.E.S.S. data with Gammapy (more details in the main text). The spectral points, shown for reference purpose only, have been obtained by re-scaling the amplitude of the reference spectral model within each energy bin, re-optimizing at the same time all free nuisance parameters of the model. In the energy bins with less than 3σ excess significance, the 3σ confidence level upper limits are shown.

are not well reproduced by a background-only model, since strong features appear in the spatial model residuals, calling for the addition of source components;

(b) as a first-guess source model, we included all known TeV objects (from the HGPS) contained within the analysis RoI, with the exception of HESS J1702-420. They are the sources HESS J1708-410 and HESS J1708-443. The latter is actually not fully contained in the RoI, but it is a significantly extended source whose emission likely leaks into the analysis region, thus requiring to be modeled. Due to their large angular distance relative to the center of the RoI, these two sources do not have a strong influence on HESS J1702-420. We therefore decided to fix most of their model parameters to the values reported in the HGPS, and verified a posteriori that the spatial and spectral residuals in theirs surroundings did not exhibit significant features. For HESS J1708-410, the only parameters that we left free to vary are the spectral normalization and index, while HESS J1708-443 was completely fixed to the catalog description. The addition and modeling of HESS J1708-410 and HESS J1708-443 led to a significant improvement of the spatial residuals around their positions;

(c) we then included a large-scale source component, with free power law spectrum and Gaussian morphology, whose fitted location converged halfway between HESS J1708-410 and HESS J1702-420, leading to a significant improvement of the model residuals in the RoI. The shape of this extended component is indicated with a dashed line in the figure, because its presence was not confirmed by the crosscheck analysis (more details are provided in section 5.3.1). The only remaining excess in the RoI corresponds to HESS J1702-420;

(d) we injected a Gaussian component near the location of HESS J1702-420, leaving the spatial elongation, rotation angle and position free to vary together with the power law spectral parameters. This way we determined the presence (at TS=606, which corresponds to 23.9σ given the 7 fitted degrees of freedom) of an elongated component that we named HESS J1702-420B. The model residuals look compatible with statistical fluctuations, apart for a $\gtrsim 5\sigma$ excess hotspot at the center of the RoI;

(e) we finally added a spatially symmetric Gaussian source, called HESS J1702-420A, whose presence turned out to be significant at 5.4σ confidence level. This represents the last step of the modeling, because it achieved a the flat spatial distribution of the significance of model residuals. The histogram of significance values closely resembles a standard normal distribution, as expected for discrepancies that are only due to statistical Poisson fluctuations.

The 3D analysis allowed for the first time for HESS J1702-420 to be separated into two overlapping objects, called HESS J1702-420A and HESS J1702-420B, both detected at $> 5\sigma$ confidence level. For neither of the two sources did an exponential cutoff function statistically improve the fit with respect to a simple power law (cutoff significance $\ll 1\sigma$). The test of a point-source hypothesis for HESS J1702-420A resulted in a non-convergence of the fit, meaning that an extended source is needed to describe its emission. The γ-ray spectra of both components are shown in figure 4.14, together with spectral points computed under a power law assumption and re-optimizing all the nuisance parameters of the model (see table 4.3 at the end of the chapter for details). HESS J1702-420B is the brightest component up to roughly 40 TeV, where HESS J1702-420A eventually starts dominating with its $\Gamma < 2$ power law spectrum up to 100 TeV. The penultimate spectral point of HESS J1702-420A

(HESS J1702-420B), covering the reconstructed energy range $64-113\,\mathrm{TeV}$ ($36-113\,\mathrm{TeV}$), is significant at 4.0σ (3.2σ) confidence level. More details on the morphologies and spectra of HESS J1702-420A and HESS J1702-420B are provided in the next section.

4.4.5 HESS J1702-420A and HESS J1702-420B

The most relevant result of the 3D likelihood analysis, for the identification of proton Pevatrons in the Galaxy, is the discovery (with a TS-based confidence level of 5.4σ) of a new source component, HESS J1702-420A, hidden under the bulk emission formerly associated with HESS J1702-420. This object has a spectral index of $\Gamma = 1.53 \pm 0.19_{\mathrm{stat}} \pm 0.20_{\mathrm{sys}}$ and a γ-ray spectrum that, extending with no sign of curvature up to $100\,\mathrm{TeV}$, makes it a compelling candidate site for the presence of extremely high energy cosmic rays. With a flux above $2\,\mathrm{TeV}$ of

$$\int_{2\,\mathrm{TeV}}^{\infty} \frac{dN}{dE_\gamma}\, dE_\gamma = (2.08 \pm 0.49_{\mathrm{stat}} \pm 0.62_{\mathrm{sys}}) \times 10^{-13}\,\mathrm{cm}^{-2}\,\mathrm{s}^{-1} \tag{4.6}$$

and a 1σ radius of $(0.06 \pm 0.02_{\mathrm{stat}} \pm 0.03_{\mathrm{sys}})^{\circ}$, HESS J1702-420A is a weak source that is largely outshone below $\approx 40\,\mathrm{TeV}$ by the companion HESS J1702-420B. The latter has a steep spectral index of $\Gamma = 2.62 \pm 0.10_{\mathrm{stat}} \pm 0.20_{\mathrm{sys}}$, elongated shape and a flux above $2\,\mathrm{TeV}$ of $(1.57 \pm 0.12_{\mathrm{stat}} \pm 0.47_{\mathrm{sys}})\,10^{-12}\,\mathrm{cm}^{-2}\,\mathrm{s}^{-1}$ that accounts for most of the HESS J1702-420 emission at low energies.

The best-fit spectral and spatial parameters for both components are reported in table 4.4 at the end of the chapter. The systematic errors on the fitted parameters were estimated following the HGPS paper [38]:

- 0.01° systematic uncertainty on the source positions;
- 30% uncertainty on the source flux estimates;
- 0.2 error on the spectral indices.

We note that the HGPS analysis was not identical to the one performed in this work. At the time the 3D technique and the use of a FoV background model had not been introduced yet, which means that the source morphologies and spectra had to be measured in two separate steps. However, to properly estimate the level of systematics associated with the 3D analysis technique is a complex task that goes beyond this analysis and would require an extensive simulation approach. In our case, we simply performed an analysis crosscheck (see section 5.3.1) and verified that all discrepancies were consistent with the expected level of H.E.S.S. systematic uncertainties, as estimated in the HGPS paper. In the future, with more and more 3D analyses being performed and published in the VHE γ-ray astronomy field, dedicated studies will be needed to properly understand the systematics that are related with this new technique. For the sake of completeness, we also report the parameter correlation matrix for HESS J1702-420A and HESS J1702-420B, in figure 4.18.

Based on our results, it is impossible to tell whether HESS J1702-420A and J1702-420B describe two separate sources superimposed on the same line of sight, or different emission zones belonging to a single complex object. With the advent of the 3D analysis technique, the very notion of γ-ray *source* will probably need to be re-thought, since a single TeV-bright region may be described by a combination of multiple model components that may or may not be connected, i.e. belong to a single object or

not. Moreover, any morphology assumption based on exact geometric shapes (in this case two overlapping Gaussian components) represents an idealization that might differ from the underlying astrophysical reality. In particular, a model assumption based on the *energy-dependent morphology* of a single source, i.e. one source with a given energy spectrum and a morphology that varies as a function of the energy, might also well describe HESS J1702-420. From a physical point of view, the size of a γ-ray source is expected to increase with energy if the dominant process is the escape of high-energy particles, and to shrink if instead the energy-dependent radiative losses (e.g. syncrotron cooling) dominate. The latter scenario, common for PWNe, might apply also for HESS J1702-420, for which a physically-motivated energy-dependent model, encoding a smooth transition between HESS J1702-420B and HESS J1702-420A, could perhaps provide a good description of the data with a common γ-ray spectrum describing both components at once. However, such model would need to contain a information on the energy-dependent spatial elongation, size and center position of a two-dimensional Gaussian, based on physical prescriptions such as particle transport and radiative losses. Far from being obvious to implement, it would also be more dependent on physical assumptions than our simple and data-driven two-component approach. It is therefore left to future studies to accurately explore this (intriguing) possibility. In the next chapter, several simple tests are presented, that all agree in confirming our two-component approach. However, a model describing HESS J1702-420 with a single energy-dependent component cannot be considered definitively ruled out.

4.5 γ-ray flux maps and source morphology

As a complement to the 3D analysis approach, we performed a 2D analysis of the energy-integrated morphology of HESS J1702-420 in different energy bands. This technique is useful to assess the overall source morphology and verify the persistence of the TeV emission up to the highest energies, even if it does not allow us to disentangle HESS J1702-420A from HESS J1702-420B. The level of cosmic ray background in the region was estimated using the adaptive ring background (ARB) estimation method [151, 169] implemented in Gammapy (see section 3.4.3). The spatial geometry of the RoI is the same as for the 3D analysis.

In order to perform an un-biased background estimation, it is necessary to *mask* all regions containing γ-ray emission, both from known sources and from the diffuse Galactic emission. However, determining the regions containing significant γ-ray emission is the objective of the background estimation itself, which leads to an apparent contradiction. The issue is resolved by adopting an iterative approach, based on the gradual enlargement of a given set of initial exclusion regions. We adopted the following recipe:

i first, we added a circular exclusion region for each HGPS source with position contained inside the RoI. The radii of the exclusion regions were conservatively chosen to be 3 times larger than the 1σ source extensions;

ii for every individual H.E.S.S. observation, we estimated the hadronic background at each position using the ARB method and created a corresponding data set containing the observation counts and estimated background;

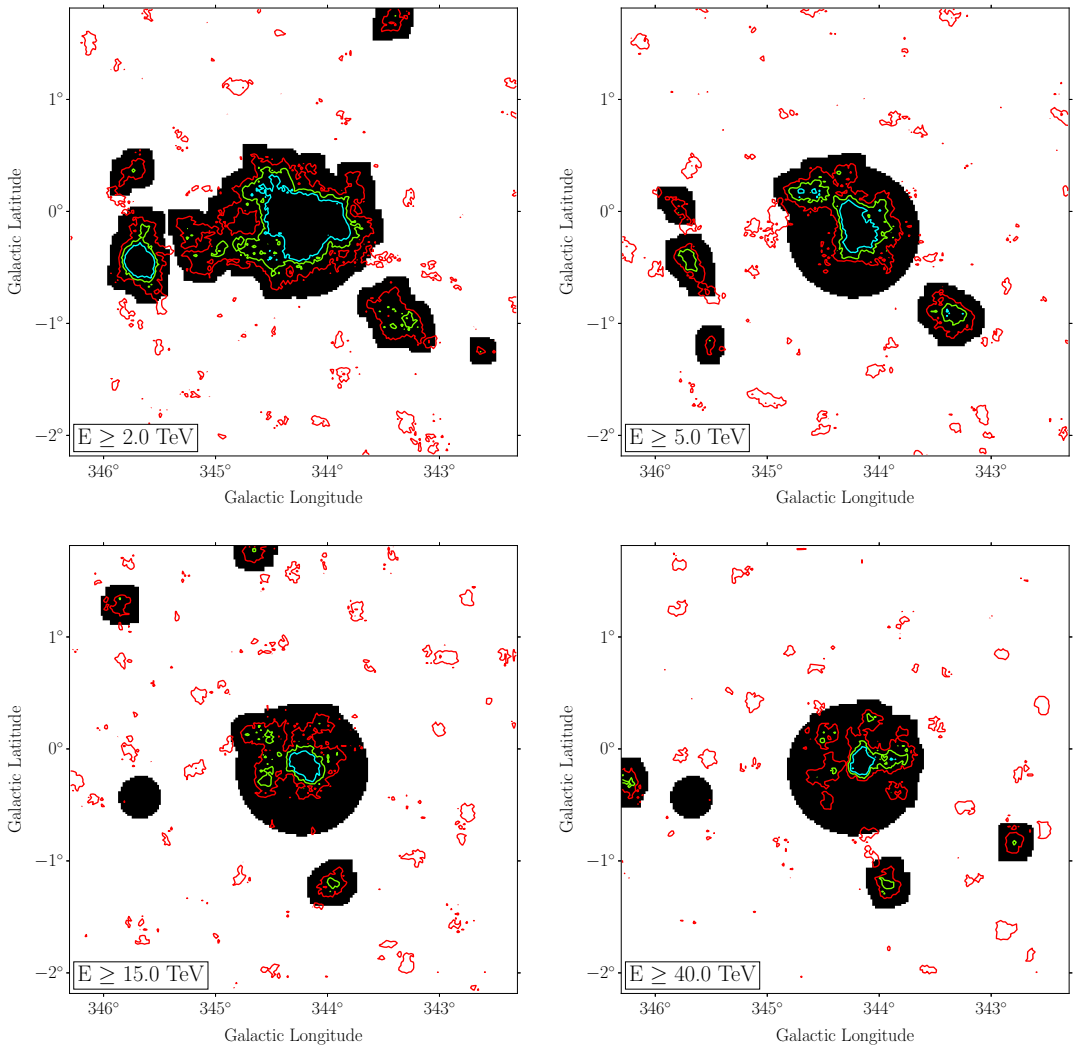

FIGURE 4.15: Exclusion masks used to compute the hadronic background with the adaptive ring background method, as described in section 4.5. The white regions, containing `True` (or 1) entries, were considered devoid of significant γ-ray emission, while the black regions, containing `False` (or 0) values, were excluded. The red (green, cyan) contours represent the 2σ (3.5σ, 5σ) signal significance levels, computed following [160].

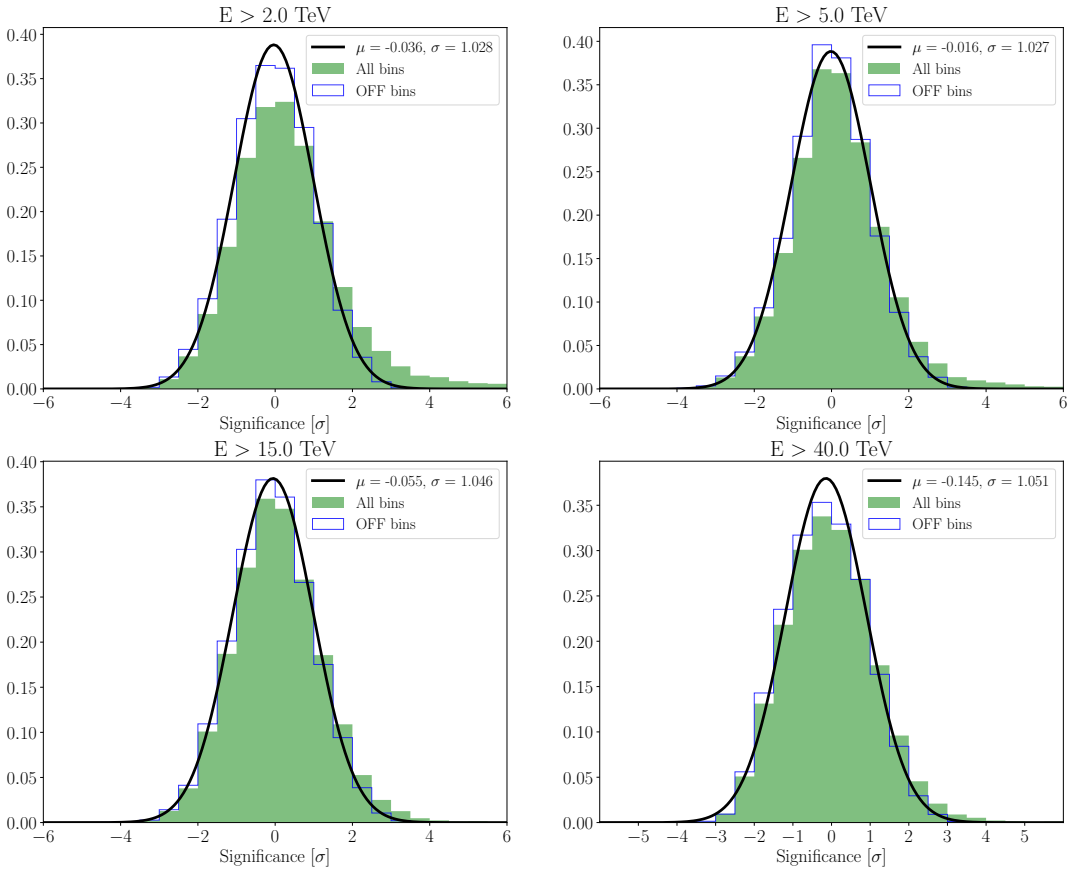

FIGURE 4.16: Normalized distributions of statistical significance (Li&Ma [160]) of the γ-ray emission in the HESS J1702-420 region, in the whole RoI (green histogram) and in the excluded regions (blue histogram). For the latter case, a Gaussian function was adjusted to check the compatibility with a standard normal distribution.

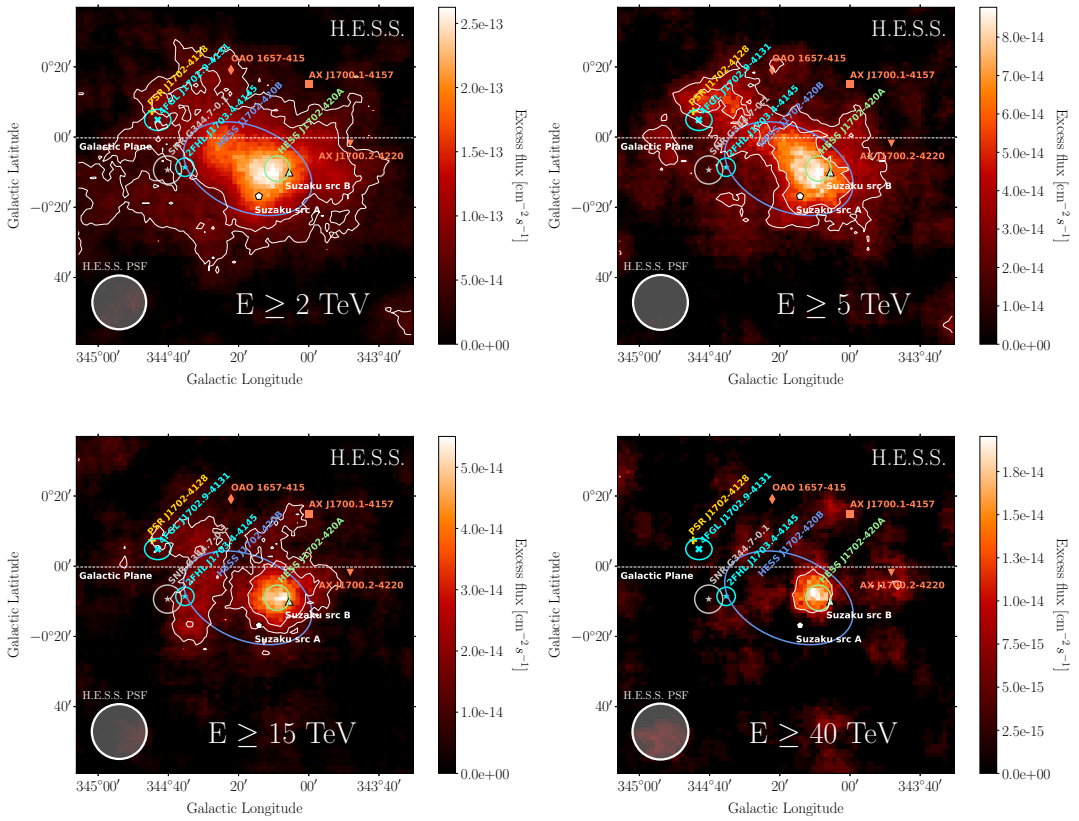

FIGURE 4.17: γ-ray flux maps of the HESS J1702-420 region, computed with the Ring Background Method, above 2 (top left), 5 (top right), 15 (bottom left) and 40 (bottom right) TeV. All maps are correlated with a 0.1°-radius top-hat kernel, and the color code is in unit of γ-ray flux (cm^{-2}s^{-1}) per smoothing area. The white contours indicate the 3σ and 5σ H.E.S.S. significance levels [174]. The cyan markers indicate the position (surrounded by uncertainty ellipses) of the *Fermi*-LAT sources 4FGL J1702.9-4131 and 2FHL J1703.4-4145. The former is associated with the PSR J1702-4128 (in yellow), the latter with the SNR G344.7-0.1 (in grey). The circle around the SNR represents its angular extension [175]. The white pentagon and upward-pointing triangle represent unidentified X-ray *Suzaku* sources. The orange markers show the positions of nearby X-ray binaries. Finally, the center and 1σ extension of HESS J1702-420A (HESS J1702-420B) are indicated in green (blue). In the bottom-left corner of each panel the 68% containment radius of the H.E.S.S. PSF is shown, which for the chosen analysis configuration does not have a strong dependency on the energy.

iii we stacked together all individual data sets, by summing up their counts and background maps;

iv for the resulting stacked dataset, we computed an excess significance map based on the *wstat* statistic (see section 3.3.2);

v we then applied an *hysteresis thresholding* algorithm to enlarge the original exclusion regions. Such algorithm, implemented in the `apply_hysteresis_threshold()` function of the `scikit-image` python library, identifies all pixels of an input image containing data higher than a certain `high` threshold, or above a lower `low` threshold but neighbouring with at least one pixel exceeding the `high` level. For our study, we tested different sets of `high-low` double-thresholds, finally settling for a `high` $= 3.5\sigma$, `low` $= 2\sigma$ definition. We found this to be a good compromise, as it ensured that most of the significant γ-ray emission in the region could be masked, at the same time avoiding the emergence of excluded regions containing only a 1 or few pixels scattered over the whole RoI;

vi We multiplied the previous exclusion mask with the one obtained from the hysteresis threshold method;

vii we repeated the steps ii-vi until a stable exclusion mask was obtained. This means until the step v did not result in any further enlargement of the exclusion regions.

Following this procedure, we produced exclusion masks above the four energy threshlds 2, 5, 15 and 40 TeV. The number of iterations that was necessary to obtain them are respectively 4, 3, 3 and 2. The masks are shown in figure 4.15, together with the 2σ, 3.5σ and 5σ excess significance contours (obtained after a 0.1°-radius top-hat smoothing). The figure shows that there is no significant γ-ray emission leaking outside the exclusion masks. This fact can also be assessed by looking at the one-dimensional (integrated over the two spatial dimensions) distributions of excess significance reported in figure 4.16. For each energy threshold, the significance distribution for the OFF pixels (i.e. those removed by the exclusion mask) closely resembles a standard normal distribution, as expected in case of pure Poissonian noise. The only visible distorsion occurs in the $E > 40\,\mathrm{TeV}$ distribution, for which the mean of the Gaussian fit is slightly shifted toward negative significance values. This is most likely attributable to low count statistics at such high energies.

The measured γ-ray fluxes on top of the γ-like hadronic background above 2, 5, 15 and 40 TeV, computed using the masks shown in figure 4.15 and assuming a γ-ray spectral index of 2 to convert the exposure from true to reconstructed energy, are reported in Figure 4.17. In order to provide a clear view of HESS J1702-420, the images focus on a $1.6^{\circ} \times 1.6^{\circ}$ zoomed region encompassing the source. The positions of nearby astronomical objects are also indicated. The figure suggests a shrinking of the VHE emission at high energy, with a shift of the γ-ray peak toward the position of the unidentified source *Suzaku* src B. Based on the 3D analysis results (section 4.4.5), this effect is understood as the transition between a low energy regime, dominated by the steep spectrum of HESS J1702-420B, to a high energy one, in which HESS J1702-420A stands out due to its exceptionally hard power law spectrum. Quantitatively, the distance between the low and high energy emission peaks, estimated from the distance between the centroids of HESS J1702-420A and HESS J1702-420B, amounts to $\approx 0.14^{\circ}$.

e_ref	e_min	e_max	sqrt_ts	counts	dnde	dnde_ul	dnde_errp	dnde_errn
[TeV]	[TeV]	[TeV]			$[\mathrm{TeV^{-1}\,cm^{-2}\,s^{-1}}]$			
3.19	2.08	4.90	3.36	40973	4.08e-14	8.35e-14	1.33e-14	1.27e-14
8.66	4.90	15.32	3.15	15812	4.42e-15	7.01e-15	1.59e-15	1.50e-15
23.50	15.32	36.04	5.29	3363	1.42e-15	2.00e-15	3.64e-16	3.33e-16
47.94	36.04	63.76	4.83	835	4.73e-16	1.02e-15	1.52e-16	1.33e-16
84.80	63.76	112.78	4.00	454	1.89e-16	4.91e-16	7.76e-17	6.54e-17
130.07	112.78	150.00	0.00	145	1.20e-23	2.21e-16	2.48e-17	1.20e-23

(A) Spectral points of HESS J1702-420A.

e_ref	e_min	e_max	sqrt_ts	counts	dnde	dnde_ul	dnde_errp	dnde_errn
[TeV]	[TeV]	[TeV]			$[\mathrm{TeV^{-1}\,cm^{-2}\,s^{-1}}]$			
2.77	2.08	3.68	18.62	31603	5.86e-13	7.16e-13	3.62e-14	3.58e-14
4.25	3.68	4.90	12.13	9370	1.98e-13	2.36e-13	1.92e-14	1.87e-14
6.51	4.90	8.66	11.01	10687	4.98e-14	5.78e-14	5.18e-15	5.06e-15
11.52	8.66	15.32	6.60	5125	9.82e-15	1.14e-14	1.68e-15	1.64e-15
23.50	15.32	36.04	6.89	3363	2.40e-15	3.44e-15	4.02e-16	3.89e-16
63.76	36.04	112.78	3.20	1289	1.78e-16	3.74e-16	6.31e-17	5.94e-17
130.07	112.78	150.00	0.49	145	2.48e-17	3.34e-16	5.62e-17	2.48e-17

(B) Spectral points of HESS J1702-420B.

TABLE 4.3: Spectral points obtained from the 3D analysis with Gammapy. The points were obtained by re-scaling the amplitude of the reference spectral model within each energy bin, re-optimizing at the same time all free nuisance parameters of the model. The quoted errors (dnde_errp and dnde_errn) represent the 1σ positive and negative statistical uncertainties on the measured flux in each bin, while the column dnde_ul reports the 3σ flux upper limit. The column names follow the convensions defined by the open-source *Data formats for gamma-ray astronomy* community (`https://gamma-astro-data-formats.readthedocs.io/en/latest/`).

Component name	Galactic longitude	Galactic latitude	Major 1σ semi-axis	Minor 1σ semi-axis	Rotation angle
	[deg]	[deg]	[deg]	[deg]	[deg]
HESS J1702-420A	$344.15 \pm 0.02_{\mathrm{stat}} \pm 0.01_{\mathrm{sys}}$	$-0.15 \pm 0.02_{\mathrm{stat}} \pm 0.01_{\mathrm{sys}}$	$0.06 \pm 0.02_{\mathrm{stat}} \pm 0.03_{\mathrm{sys}}$		—
HESS J1702-420B	$344.29 \pm 0.03_{\mathrm{stat}} \pm 0.01_{\mathrm{sys}}$	$-0.15 \pm 0.02_{\mathrm{stat}} \pm 0.01_{\mathrm{sys}}$	$0.32 \pm 0.02_{\mathrm{stat}} \pm 0.08_{\mathrm{sys}}$	$0.20 \pm 0.02_{\mathrm{stat}} \pm 0.07_{\mathrm{sys}}$	$67.0 \pm 5.4_{\mathrm{stat}} \pm 9.7_{\mathrm{sys}}$

(A) Best-fit morphology parameters of HESS J1702-420A and HESS J1702-420B. The rotation angle is measured counterclockwise starting from the $l = 0$, $b > 0$ axis.

Component name	Spectral index	Decorrelation energy	$\mathrm{dN/dE(E = E_{decorr})}$	$\mathrm{F(E > 2\,TeV)}$
		[TeV]	$[\mathrm{TeV^{-1}\,cm^{-2}\,s^{-1}}]$	$[\mathrm{cm^{-2}\,s^{-1}}]$
HESS J1702-420A	$1.53 \pm 0.19_{\mathrm{stat}} \pm 0.20_{\mathrm{sys}}$	24.53	$(1.19 \pm 0.28_{\mathrm{stat}} \pm 0.34_{\mathrm{sys}})\,10^{-15}$	$(2.08 \pm 0.49_{\mathrm{stat}} \pm 0.62_{\mathrm{sys}}) \times 10^{-13}$
HESS J1702-420B	$2.62 \pm 0.10_{\mathrm{stat}} \pm 0.20_{\mathrm{sys}}$	2.67	$(5.93 \pm 0.46_{\mathrm{stat}} \pm 1.78_{\mathrm{sys}})\,10^{-13}$	$(1.57 \pm 0.12_{\mathrm{stat}} \pm 0.47_{\mathrm{sys}}) \times 10^{-12}$

(B) Best-fit spectral parameters of HESS J1702-420A and HESS J1702-420B.

Component name	Surface brightness above 2 TeV	Test statistic (TS)	Number of d.o.f.	Significance
	$[\mathrm{cm^{-2}\,s^{-1}\,sr^{-1}}]$			$[\sigma]$
HESS J1702-420A	$(6.2 \pm 2.6_{\mathrm{stat}}) \times 10^{-8}$	42	5	5.4
HESS J1702-420B	$(2.5 \pm 0.4_{\mathrm{stat}}) \times 10^{-8}$	606	7	23.9

(C) Surface brightness and detection significance of HESS J1702-420A and HESS J1702-420B.

TABLE 4.4: Modeling results for HESS J1702-420A and HESS J1702-420B, obtained with a 3D maximum-likelihood analysis of H.E.S.S. data.

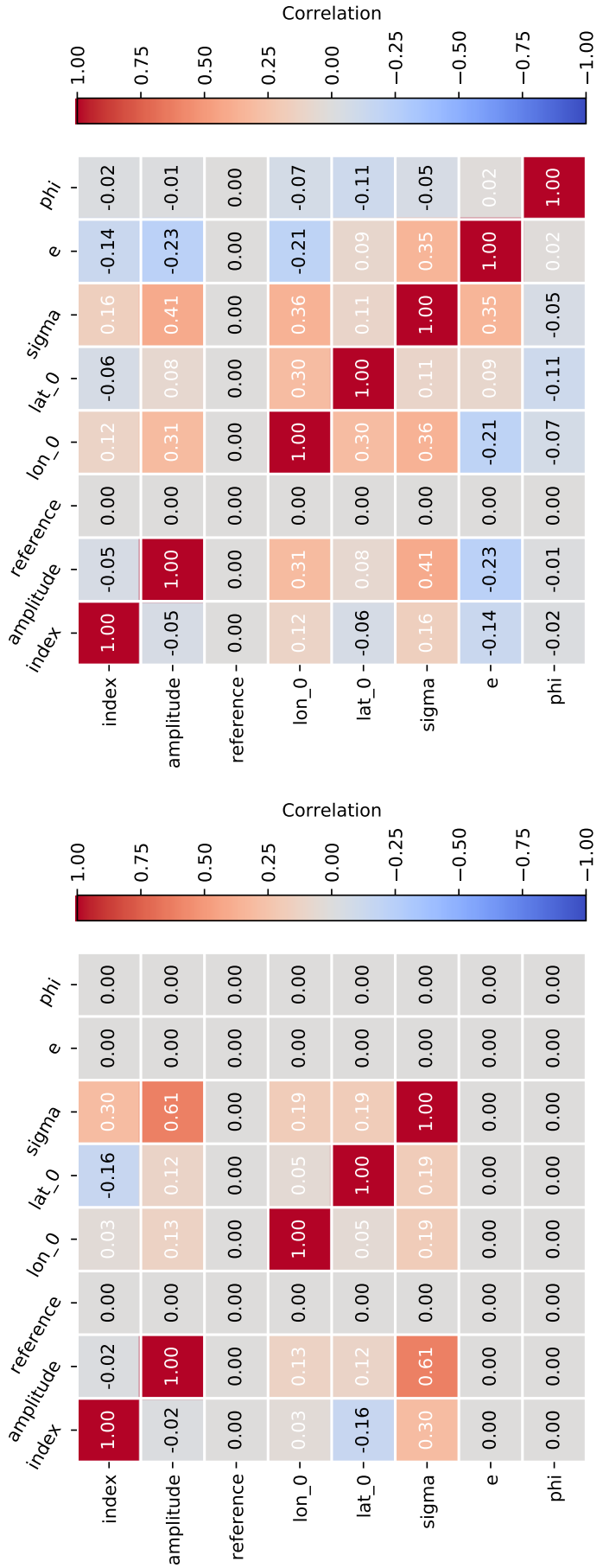

FIGURE 4.18: Parameter correlation matrix for the spatial and spectral models of HESS J1702-420A (left) and HESS J1702-420B (right). The correlation C is related to the covariance Σ via $C_{ij} = \Sigma_{ij}/\sqrt{\Sigma_{ii}\Sigma_{jj}}$. The first three columns and rows contain the spectral model parameters (spectral index, amplitude and reference energy), while the others refer to the spatial model (center longitude and latitude, radius, eccentricity and position angle).

Chapter 5

H.E.S.S. analysis cross-checks

5.1 Introduction

In the previous chapter, we presented a 3D likelihood analysis of the sky region around HESS J1702-420, which led to a simple parametric description of the source based on the superposition of two model components. It is the first time, for the H.E.S.S. collaboration, that the 3D analysis technique is used to derive and publish physics results. For this reason, a series of tests had to be performed, to assess the robustness of the analysis and validate it using other more classical background and flux estimation techniques. This chapter is devoted to the description of those tests.

First, section 5.2 describes a number of studies that were performed using the same high-energy oriented analysis configuration of the previous chapter. Namely, we assessed the level of spectral and spatial variations of our 3D model, as a function of the photon energy (section 5.2.1). We also applied the *reflected region background* estimation technique [151] to assess the level of spectral variations as a function of the distance from HESS J1702-420A, where the γ-ray emission is attributed to HESS J1702-420B (section 5.2.2). This kind of spectral analysis is not as sensitive or adapted to overlapping sources as the 3D technique, but is also less dependent on model assumptions. Then, in section 5.3 we present the tests that were made to validate the results using a different choice of low-level analysis configuration. In particular, section 5.3.1 contains the details of the 3D analysis crosscheck, while section 5.3.2 presents the comparison of the energy-integrated images obtained with the ring background estimation method.

5.2 Tests made with the main analysis configuration

5.2.1 3D analysis of H.E.S.S. data in independent energy bands

In order to measure possible variations of the 3D model as a function of the energy, we repeated the 3D analysis within three independent non-overlapping energy bands defined by the edges $2.0, 3.7, 15.3$ and $150\,\mathrm{TeV}$. These were chosen to ensure a roughly similar level of γ-ray excess on the source. During the fit, due to the limited lever arm and insufficient number of photons reconstructed within each individual energy band, we fixed all spectral indices to the values obtained in chapter 4. The spectral amplitudes and spatial parameters were instead left free to vary for all model components, together with the four background model normalizations. For each energy

E_{min} TeV	E_{max} TeV	Significance of H_1 vs. H_0 $[\sigma]$	Significance of H_2 vs. H_1 $[\sigma]$
2.0	3.7	19.0	2.4
3.7	15	20.2	2.0
15	150	12.1	5.0

TABLE 5.1: Significance for the presence of zero (H_0), one (H_1) or two (H_2) model components in each independent energy band, as described in the text (section 5.2.1). The significance was obtained by converting a log-likelihood ratio (see eq. 3.8) to a confidence levels in units of Gaussian standard deviations, taking into account the number of additional degrees of freedom corresponding to each new hypothesis.

band, we used the likelihood ratio test (see equation 3.8) to compare the statistical significance of three nested hypotheses:

H_0: Null hypothesis, with no model component describing HESS J1702-420;

H_1: HESS J1702-420 is described by one Gaussian component, with the spectral index of HESS J1702-420B. For this component, we left the spatial eccentricity and rotation angle free to vary, for a total of six[1] free model parameters;

H_2: HESS J1702-420 is described by two Gaussian components, with the spectral indices of HESS J1702-420B and HESS J1702-420A. For the latter, we considered a strictly symmetric Gaussian morphology, for a total of four[2] free model parameters.

The statistical comparison of these hypotheses in all energy bands is reported in Table 5.1.

HESS J1702-420B is significantly detected in all energy bands, while HESS J1702-420A is detected only in the $15-150\,\mathrm{TeV}$ band, as expected due its hard spectral index. The spatial and spectral shapes of the two components within each energy band are shown in figure 5.1, where the reference results from the whole $2-150\,\mathrm{TeV}$ fit range are reported in black. The top panel shows the best-fit morphologies of HESS J1702-420B and HESS J1702-420A. The latter is not drawn for the two lowest energy bands (i.e. $E \leq 15\,\mathrm{TeV}$), because it was not significantly detected. Neither of the two components have a clear energy-dependent morphology. The bottom panel of the figure compares the reference spectra of HESS J1702-420A and HESS J1702-420B (in black) with the spectra obtained in different energy bands. The energy-resolved spectra and morphologies are well connected and in agreement with the reference ones. Additionally, we summed the log-likelihood values obtained in each independent energy band, and estimated that globally a two-component model is better than a one-component model with a confidence level of 5.3σ. This value is consistent with the 5.4σ detection of HESS J1702-420A reported in the previous chapter.

From this study, we conclude that in each independent energy band HESS J1702-420 is well described by a simple model, based on either one or two components with Gaussian morphologies and power law spectra. This is precisely what is expected if the emission is really due to two separate model components, instead of a single energy-dependent one.

[1] One spectral normalization, plus five spatial parameters.
[2] One spectral normalization, plus three spatial parameters.

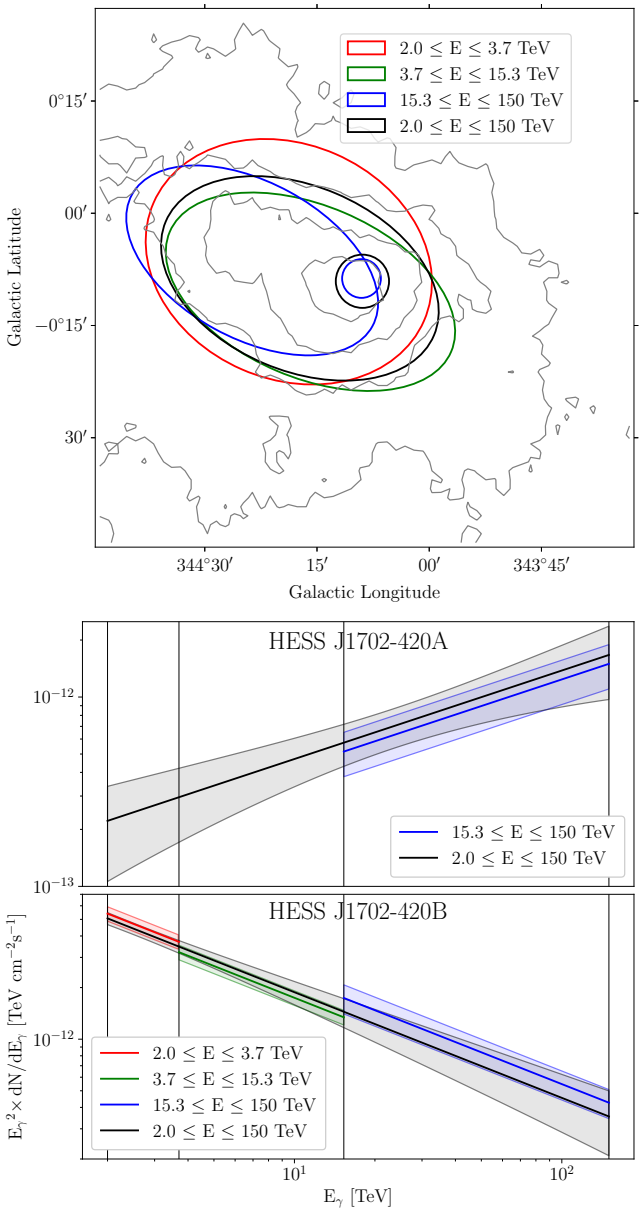

FIGURE 5.1: Upper panel: The figure, centered on the approximate position of HESS J1702-420, shows contours corresponding to 150, 200, 250 and 300 counts detected by H.E.S.S. above 2 TeV per smoothing area. Overlaid on the map are the 1σ extension contours of the components HESS J1702-420A and HESS J1702-420B, as obtained from the 3D fit in separate energy bands. Lower panel: spectral results of the 3D analysis in energy bands, for HESS J1702-420A and HESS J1702-420B. Vertical lines separate the energy bands that were independently used to perform the source modeling. In both panels, the reference results obtained over the full energy range (see section 4.4.5) are indicated in black.

#	Index	E_{decorr} [TeV]	$F(E>1\,TeV)$ [$cm^{-2}s^{-1}$]	Time [h]	Area [sr]	Excess [counts]	Significance [σ]
1	2.15 ± 0.05	2.6	$(9.47\pm3.59)\,10^{-13}$	32.7	$2.2\,10^{-5}$	499	18.8
2	2.36 ± 0.07	2.2	$(2.23\pm1.19)\,10^{-12}$	24.8	$10.0\,10^{-5}$	857	17.8
3	2.17 ± 0.09	3.1	$(2.48\pm1.51)\,10^{-12}$	15.4	$1.7\,10^{-4}$	552	10.5
4	2.46 ± 0.31	2.0	$(1.42\pm3.22)\,10^{-12}$	7.3	$2.5\,10^{-4}$	135	3.9

TABLE 5.2: Spectral results for the four extraction regions of Figure 5.2, under the assumption of power law γ-ray emission.

5.2.2 Spatially-resolved spectral analysis of H.E.S.S. data

With the benefit of an unprecedented level of statistics in the HESS J1702-420 region, we estimated the level of spectral variations around the source using a spatially-resolved spectral analysis. As spectral extraction regions, we defined three non-overlapping 0.2°-width annuli (numbered as 2, 3 and 4 in figure 5.2) concentric with the position of HESS J1702-420A, with a minimum inner radius of 0.15° which is sufficiently large to ensure that the contribution from HESS J1702-420A in the annuli is negligible. Using each annulus, we measured the variations of the spectrum of HESS J1702-420B as a function of the distance from HESS J1702-420A. If our two-component model were valid, those variations should be insignificant. Additionally, we extracted the γ-ray spectrum from a 0.15°-radius circle corresponding to the $\approx 3\sigma$ containment of HESS J1702-420A, concentric with the annuli and marked as region 1 in figure 5.2, where a mixture of the HESS J1702-420A and HESS J1702-420B spectra is expected to be observed. We note that the choice of such large extraction regions, instead of finer ones, was aimed at limiting the level of PSF-induced spillovers between them. The level of cosmic ray background within the extraction regions was computed with the *reflected region background* estimation technique [151]. We used a forward-folding approach [168] to determine the maximum-likelihood estimates for the spectral slope and flux in each region, under a power-law assumption. The safe energy threshold for the runwise event rejection was determined as

$$E^i_{\rm safe} = E^i_{A_{\rm eff}}\,, \tag{5.1}$$

where $E_{A_{\rm eff}}$ is the effective area of the observation i.

Figure 5.2 (top panel) shows the four non-overlapping spectral extraction regions, overlaid on a map of the excess significance above 2 TeV. The spectral variations as a function of the distance from HESS J1702-420A are shown in the bottom panel of the figure, while the detailed analysis results are reported in table 5.2. The errors reported in the table represent the statistical uncertainties on the fitted parameters. The results of this study show that there is no evidence of spectral variations for HESS J1702-420B, which confirms the validity of the model used in the 3D analysis.

5.2.3 Spectral distribution of the model residuals

The figure 4.13e, from the previous chapter, was used to prove that the 3D model provides a good description of the H.E.S.S. data in the whole analysis RoI. However, being integrated above 2 TeV, the image did not provide any information on the quality of the *spectral* modeling of the RoI. To address this point, we proceeded in two ways:

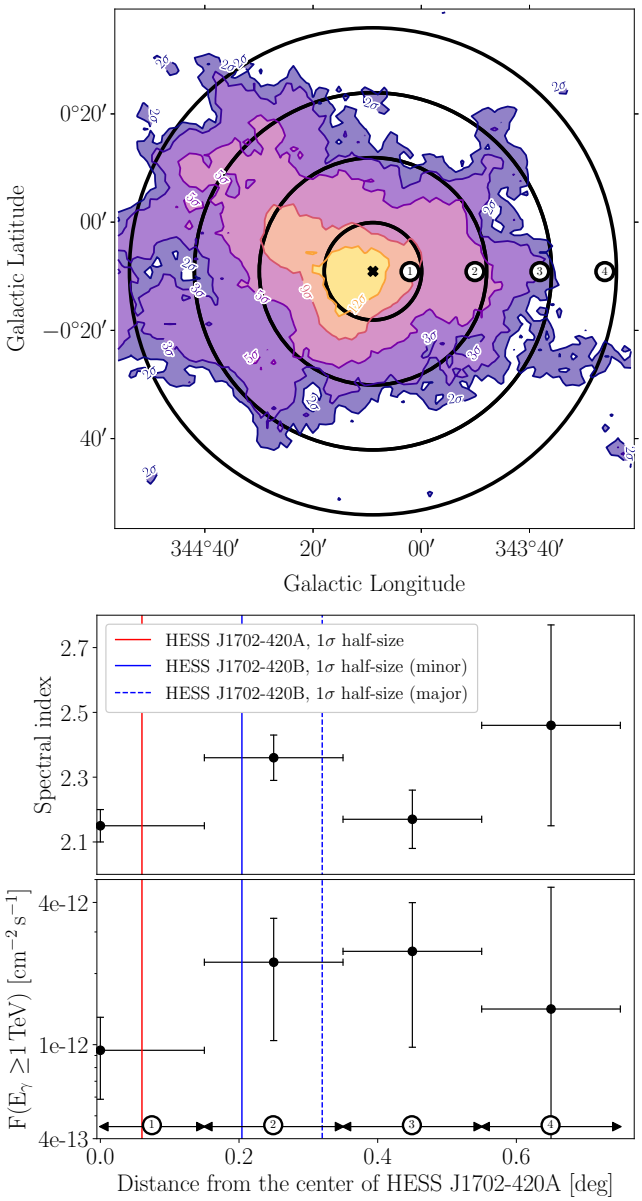

FIGURE 5.2: Upper panel: Map of the H.E.S.S. excess significance above 2 TeV, with contours corresponding to 2σ, 3σ, 5σ, 9σ and 12σ significance levels [174]. The map has been obtained with the Adaptive Ring Background estimation method, and centered on the position of HESS J1702-420A. Overlaid on the map are the concentric regions, one circle and three annuli, that were used to extract the source spectrum. Lower panel: Results of the spatially-resolved spectral analysis, showing the spectral index and flux as a function of the distance from HESS J1702-420A.

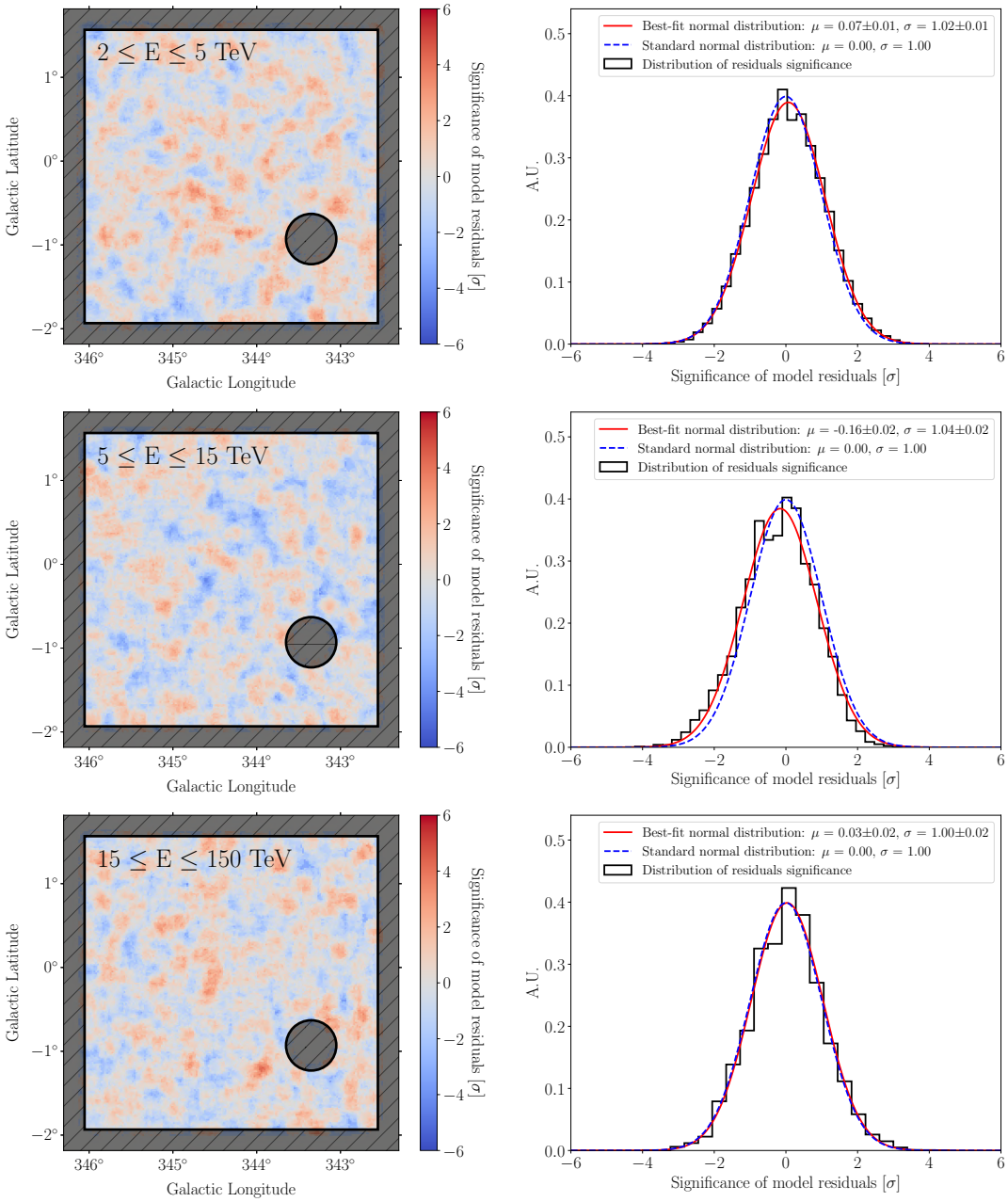

FIGURE 5.3: Spatial distributions of the significance of model residuals (left column) and histograms of significance values (right column), computed in the energy bands $2.0-5.0\,\mathrm{TeV}$ (top), $5.0-15.0\,\mathrm{TeV}$ (center) and $15.0-150\,\mathrm{TeV}$ (bottom).

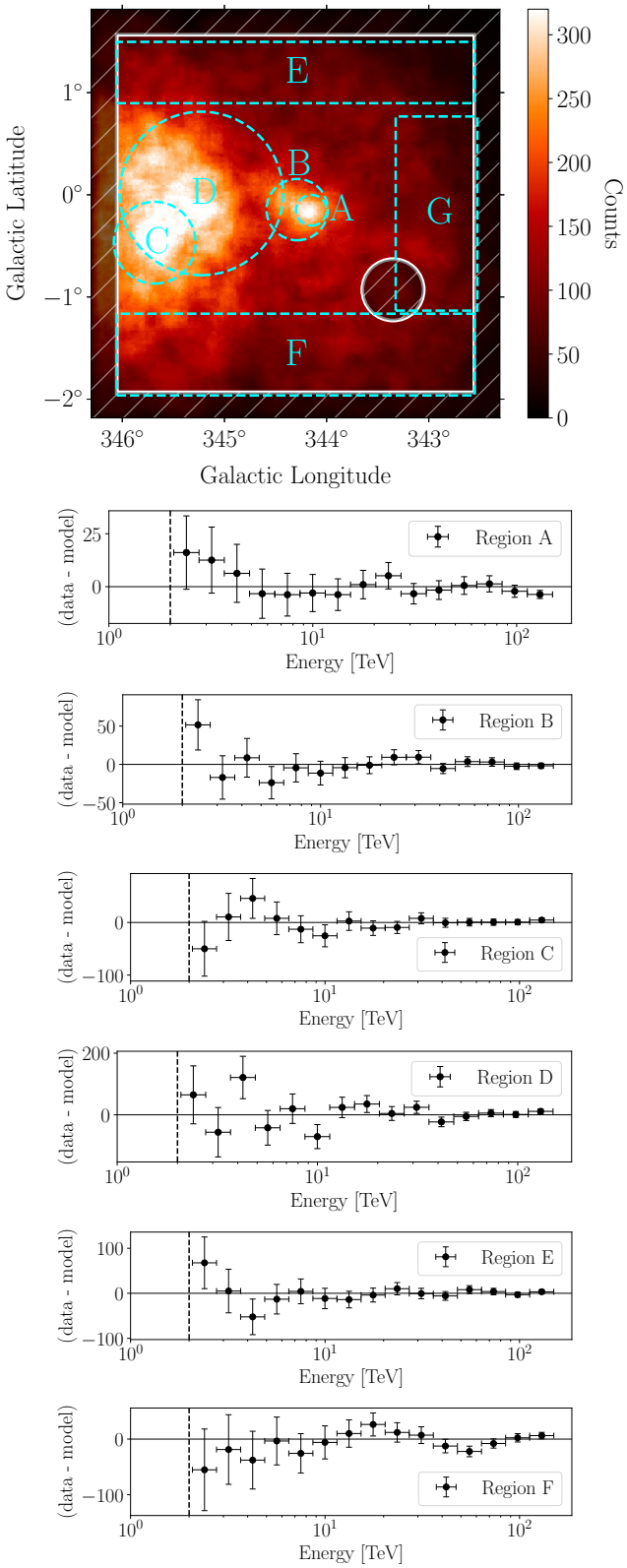

FIGURE 5.4: Top: Spectral extraction regions (from A to F) overlaid on a H.E.S.S. counts map (the same as in figure 4.12). *Other* panels: Energy distribution of model residuals (computed subtracting the model predicted counts from the measured data) inside each region shown in the top panel.

Background estimation	Fit statistic	Spectral index	dN/dE(1 TeV) $[\mathrm{TeV^{-1}\,cm^{-2}\,s^{-1}}]$
FoV	*Cash*	$2.009 \pm 0.091_{\mathrm{stat}}$	$(4.27 \pm 0.74_{\mathrm{stat}})\,10^{-13}$
Reflected	*wstat*	$2.013 \pm 0.082_{\mathrm{stat}}$	$(5.53 \pm 0.75_{\mathrm{stat}})\,10^{-13}$

TABLE 5.3: Spectral results obtained using different background estimation methods, under a power law assumption, for a $0.2^{\mathrm{o}} \times 0.2^{\mathrm{o}}$ square region centered on the position of HESS J1702-420A. More details are provided in the main text.

- we computed the spatial distribution of model residuals in three independent energy bands (see figure 5.3). The absence of anomalous spatial structures (left column of the figure) and the fact that the residuals are compatible with Poissonian noise (right column) indicates that the 3D model provides a satisfactory description of the ROI at all energies;
- we extracted the spectral distributions of model residuals inside six regions defined by the letters A to G, in alphabetical order. They are shown in figure 5.4 (top panel), together with their respective residual counts spectra (*other* panels). The regions A to D are circles, centered on the main 3D model components. The regions E to G instead are rectangles, chosen to encompass large-scale off-source portions of the RoI. The figure shows that the spectral residuals are compatible with statistical fluctuations around zero in all regions. This confirms once again that our RoI description does not suffer from relevant high energies systematics or large-scale background model issues.

5.2.4 Comparison of different background estimation techniques

In the previous chapter we presented both a 3D analysis and a 2D (energy-integrated) study of the HESS J1702-420 region. In principle, both methods can be used to measure the γ-ray excess in the RoI. Therefore, a comparison can be useful to assess the level of analysis-driven systematics. In practice, this means verifying that consistent excess counts maps are obtained using the *field of view* and *ring* background estimation methods (see sections 3.4.3 and 3.4.4). The comparison, shown in figure 5.5, clearly favors the compatibility of the two analysis approaches. The morphologies of the γ-ray emission obtained using the two techniques are compatible above each energy thresholds, confirming the low level of analysis-driven systematic uncertainties.

Additionally, we performed a 1D spectral analysis using the *reflected regions* background method (see section 3.4.2). This is useful to further ensure that the FoV background technique did not lead to biased results, due to a poor background model description. In particular, we focused on the source HESS J1702-420A, whose detection is perhaps the most remarkable result of the 3D analysis. As a spectral extraction region, we defined a $0.2^{\mathrm{o}} \times 0.2^{\mathrm{o}}$ square region aligned with the Galactic coordinates system and centered at the position of HESS J1702-420A. After estimating the level of hadronic background inside the region, by "reflecting" it around the pointing position of each run, we adjusted a power law spectrum to the 1D ON-OFF data. Then, we performed the same exercise using the FoV background model. To do so, we converted the 3D data set to a 1D spectral one, by integrating the measured counts and the model-predicted background over the two spatial dimensions inside

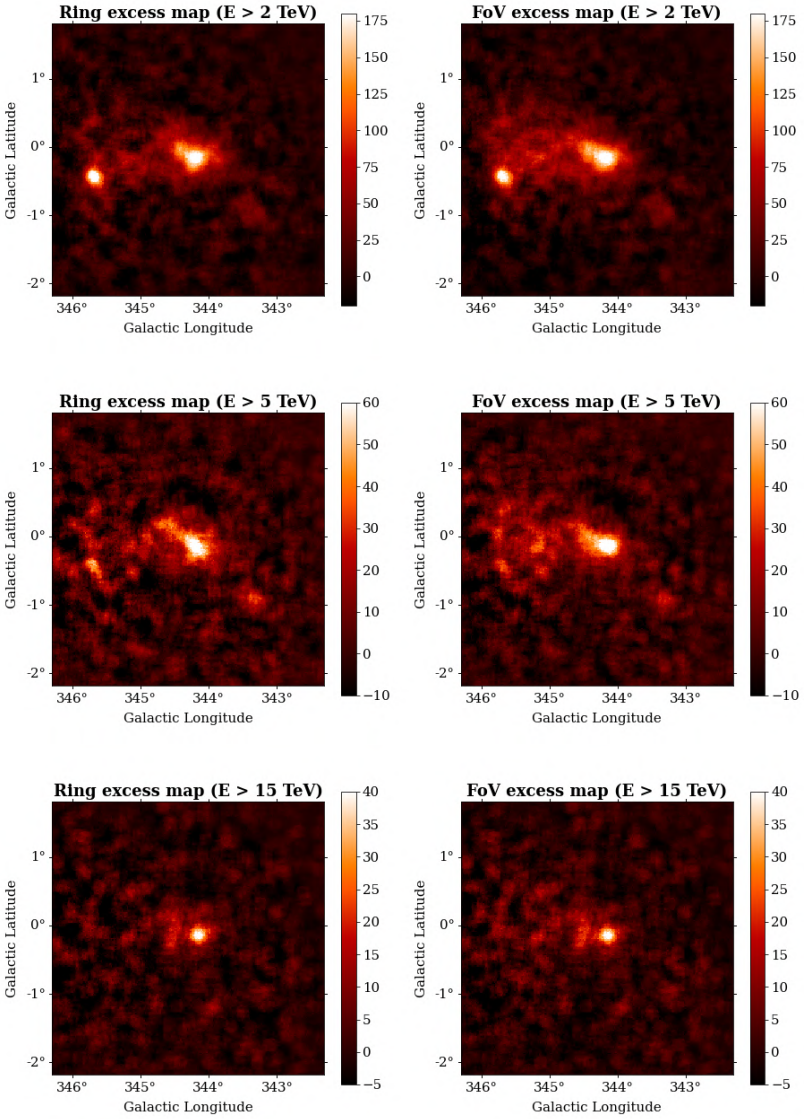

FIGURE 5.5: Comparison between the γ-ray excess maps computed with the ring (left) and FoV (right) background estimation techniques, above three increasing energy thresholds.

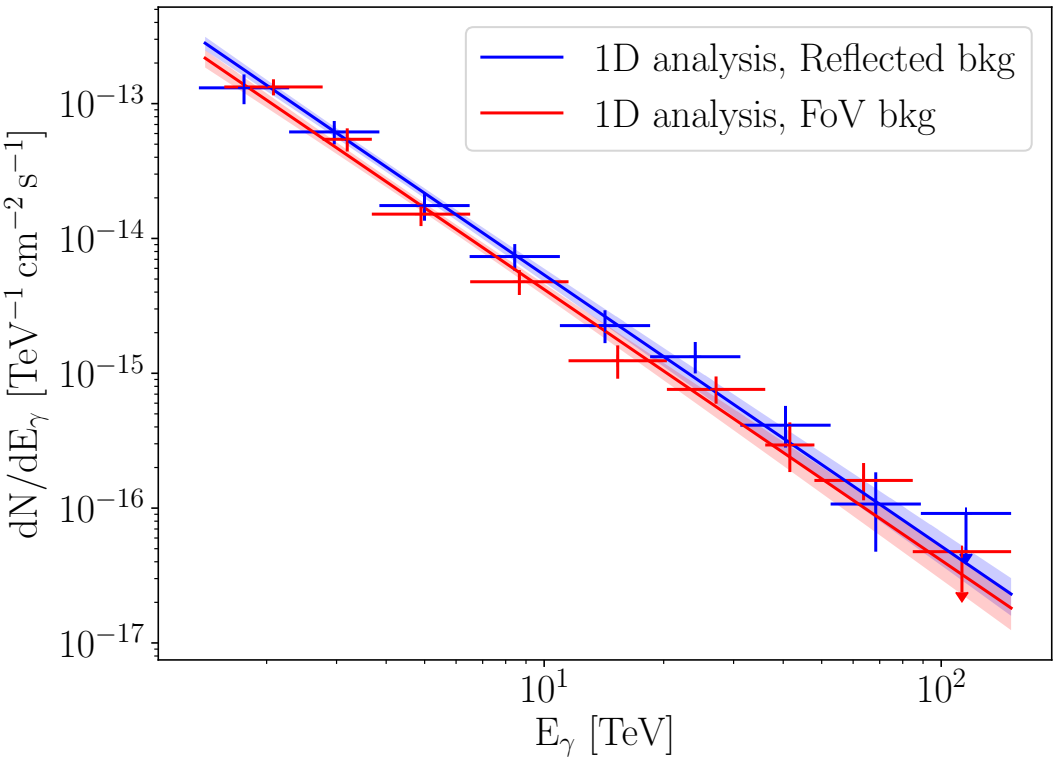

FIGURE 5.6: Comparison between the spectra obtained with the FoV (red) and reflected (blue) background estimaton techniques, using a $0.2^o \times 0.2^o$ square extraction region aligned with the Galactic coordinates system and centered at the position of HESS J1702-420A.

the square extraction region. The effective area was estimated from the average exposure inside the region, divided by the livetime, given in this case by the sum of the GTIs. The energy dispersion was instead taken from the region center. This way, we built a spectral data set with a background estimate based on the FoV background model prediction. The fit statistic applied to this data set is therefore *Cash* (see section 3.3.2). We adjusted a power law spectrum to the 1D-reduced 3D data set, and compared the result with the native 1D method (based on the *wstat* statistic). The comparison details are reported in table 5.3, and are shown in figure 5.6. The results obtained from the two different background estimation techniques are consistent. The agreement of the spectral index values is excellent, within 0.1%. The spectral amplitudes are compatible within the statistical error, and the difference between the best fit values (of the order of 25%) is within the expected level of systematics for the H.E.S.S. experiment [38]. This study confirms that the background model nearby HESS J1702-420A is not affected by strong systematic effects, thus further validating the 3D analysis results presented in the previous chapter.

5.3 Cross-check made with an alternative analysis configuration

A cross-check analysis on data performed with a different low-level analysis chain is another way to assess the systematics and robustness of a result. In fact, it is the policy of the H.E.S.S. Collaboration that all results obtained with a given main analysis (MA) configuration must be verified with an independent cross-check analysis (CA) configuration. This gives confidence that all results are stable, in the sense that they are not strongly dependent on the calibration, event reconstruction, γ/hadron discrimination, background model and Monte Carlo simulation techniques. In our case, the CA was performed using an analysis configuration called *std_zeta_FullEnclosure*, from a simulation and calibration chain developed by the Heidelberg H.E.S.S. group.

In the past both the MA and CA were performed with H.E.S.S. proprietary software, designed to process the telescope's data from the DL0 up to DL5. Due to the differences between the chain-specific codes, this often resulted in limited possibilities of inspection and comparison of all the intermediate analysis steps. The discrepancies in the final results inevitably resulted from both low-level ($<$ DL3) and high-level ($>$ DL3) analysis systematics, sometimes complicating the crosscheck interpretation. Now, for the first time we performed the exact same high-level steps in the MA and CA, by applying the same Gammapy analysis notebooks on the DL3 data produced with the different analysis chains. This means that all the differences in the analysis results must be due to the low-level analysis steps.

5.3.1 Cross-check of the 3D analysis

Different analysis chains can lead to differences in the overall exposure levels, since the definition of data quality[3], used to select or reject observations, is generally part of the low-level analysis. In our case, the same run selection criteria (applied at high level on the DL3 data) that led to 360 runs for the MA resulted in 332 runs in the case of the CA. These numbers are relatively similar, but the run lists are actually quite

[3] E.g. the accepted level of noisy/broken pixels, or the definition of functioning telescope.

Name	Runs	Zenith [deg]	Offset [deg]	Period
A	94	16.6 - 36.0	1.6 - 2.8	2004 - 2013
B	63	36.9 - 59.5	2.4 - 2.7	2004 - 2012
C	20	17.9 - 35.5	0.2 - 1.4	2004 - 2011
D	155	31.2 - 58.3	0.3 - 0.8	2017 - 2019

TABLE 5.4: Division of the 332 selected H.E.S.S. observations into four groups, based on the same criteria as in table 4.2.

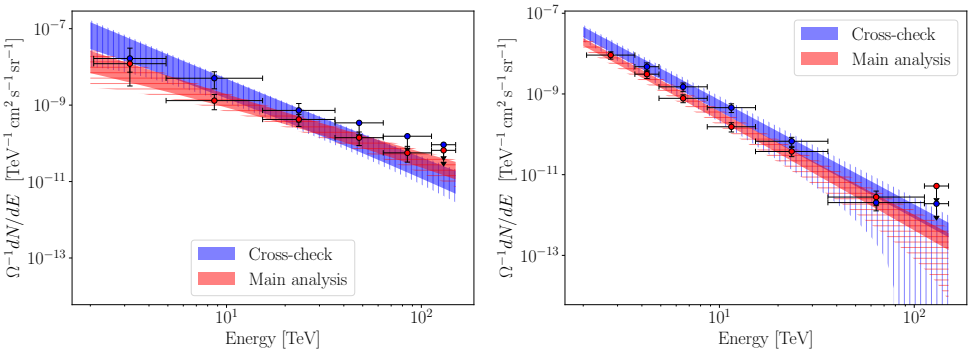

FIGURE 5.7: Comparison of the spectra obtained with the 3D modeling technique for HESS J1702-420A (left) and HESS J1702-420B (right), using the MA (red) and CA (blue) configuration. The vertical axis, normally measured in flux units, has been converted to surface brightness following equation 5.2. The filled (hatched) envelopes represent the statistical ($\sqrt{\text{statistical}^2 + \text{systematic}^2}$) error on the fitted spectra.

different, particularly in terms of the repartition between H.E.S.S. I and H.E.S.S. IU runs. The four observation groups defined for the CA, reported in table 5.4, can be compared to table 4.2. Thanks to the forward-folding method, the 3D analysis should lead to compatible results regardless of the exposure differences between the MA and CA. However, a lower exposure of the CA is expected to lead to larger uncertainties and lower statistical significance at the highest energies, compared to the MA.

Using the CA configuration, with the same setup as described in the previous chapter, the 3D technique confirmed the detection of HESS J1702-420A and HESS J1702-420B[4]. The comparison of the MA and CA spectra is shown in figure 5.7, respectively in red and blue. The filled (hatched) butterfly envelopes indicate the 1σ statistical ($\sqrt{\text{statistical}^2 + \text{systematic}^2}$) uncertainties. In the figure, the spectra of both sources were converted to surface brightness units, dividing their spectral normalizations by the respective 1σ solid angles:

$$\frac{dN}{dE} \rightarrow \frac{1}{\Omega}\frac{dN}{dE}\,, \tag{5.2}$$

where

$$\Omega = \pi \times \texttt{major\_semiaxis} \times \texttt{minor\_semiaxis}\,. \tag{5.3}$$

This allowed us to achieve a fair spectral comparison, un-biased by the different intrinsic source sizes that were obtained during the 3D fit. The spectral index of

[4]HESS J1702-420A (HESS J1702-420B) was detected with a (TS = 74) TS = 1722. We note that these values are not directly comparable with those obtained in the MA, due to the different exclusion regions used in the two cases (which have an impact on the number of bins considered for the likelihood computation).

HESS J1702-420A, obtained from the CA, is slightly steeper than the MA, due to the low sensitivity of the CA configuration at the highest energies. Accordingly, the last three flux points of HESS J1702-420A in the CA are upper limits (significance $< 3\sigma$). HESS J1702-420B instead is slightly brighter in the CA (with a similar spectral index), but still compatible with the MA results within the estimated uncertainties. For both sources, the flux points are compatible within the errors. Figure 5.8 (5.9) shows a parameter-by-parameter cross-check of the best fit model for HESS J1702-420A (HESS J1702-420B). In both figures, thick (thin) error bars indicate the statistical ($\sqrt{\text{statistical}^2 + \text{systematic}^2}$) uncertainties on the parameter values. From these tests, we concluded that, within the H.E.S.S. analysis uncertainties, the results are consistent between the MA and the CA. Further details on the CA fit are provided in the table 5.5 at the end of the chapter.

In the MA a large-scale ($\approx 0.5^\circ$ in radius) model component was also detected around $l = 345.23^\circ$ and $b = -0.01^\circ$ (see figure 4.13c). At that position, in the MA the borders of several runs partially overlap, resulting in a boosted exposure level but also strong systematics due to edge effects. In the crosscheck analysis, due to differences in the run lists, the exposure level at the position of the large-scale component is lower, resulting in a decreased sensitivity. Accordingly, we verified that its inclusion or exclusion in the source model of the crosscheck analysis did not have any relevant impact on the predicted number of counts at its position. We therefore could not confirm the detection of this new large-scale emission component nearby HESS J1702-420. However, we notice that (as visible in figure 5.10) in the CA the spatial model of HESS J1702-420B seems to extend further east from the source, as in an attempt to cover some emission that in the MA is attributed to the large-scale source. Also, the HGPS already reported the presence of a large-scale component with similar position and size, called HGPSG 041, that was similarly discarded due to a non-detection in the crosscheck analysis (see again figure 5.10). These facts tend to support the interpretation of this large-scale component as a real γ-ray emission source, which, being very faint and diffuse, can be detected only using certain analysis configurations that guarantee a good sensitivity in the region. However, a purely artifact origin of this component from systematic (e.g. background model) uncertainties cannot be ruled out at the moment. In the future new observations of the region with more uniform exposure will ultimately probe its presence and nature.

5.3.2 Cross-check of the ring background analysis

We repeated the same study presented in section 4.5 using the data obtained from the CA calibration. This way, we computed the resulting γ-ray flux maps above 2 and 40 TeV. They are shown in figure 5.12, together with the γ-ray flux contours obtained with the MA (in white, see figure 4.17). The comparison shows that, despite the different exposure levels in the region, the flux maps are reasonably similar both at low and high energies. Above 40 TeV, the MA configuration clearly allowed to detect more events than the CA. However, also with the latter a small-scale emission hotspot close to the position of HESS J1702-420A is found. Finally, figure 5.11 compares the exclusion mask computed with the alternative analysis configuration (black areas) with the one from the main configuration (red contours). They are compatible, apart for small discrepancies (especially, as expected, at the highest energies).

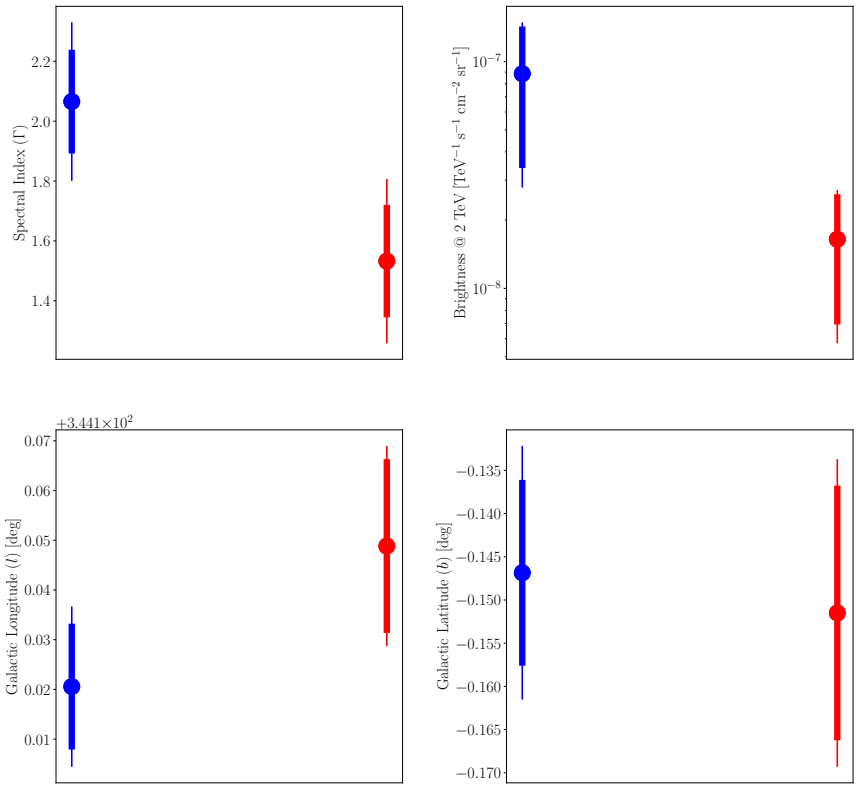

FIGURE 5.8: Best-fit values of the HESS J1702-420A parameters, with their statistical (statistical + systematic) errors shown by the thick (thin) error bars. The blue points correspond to the CA, while the red ones to the MA.

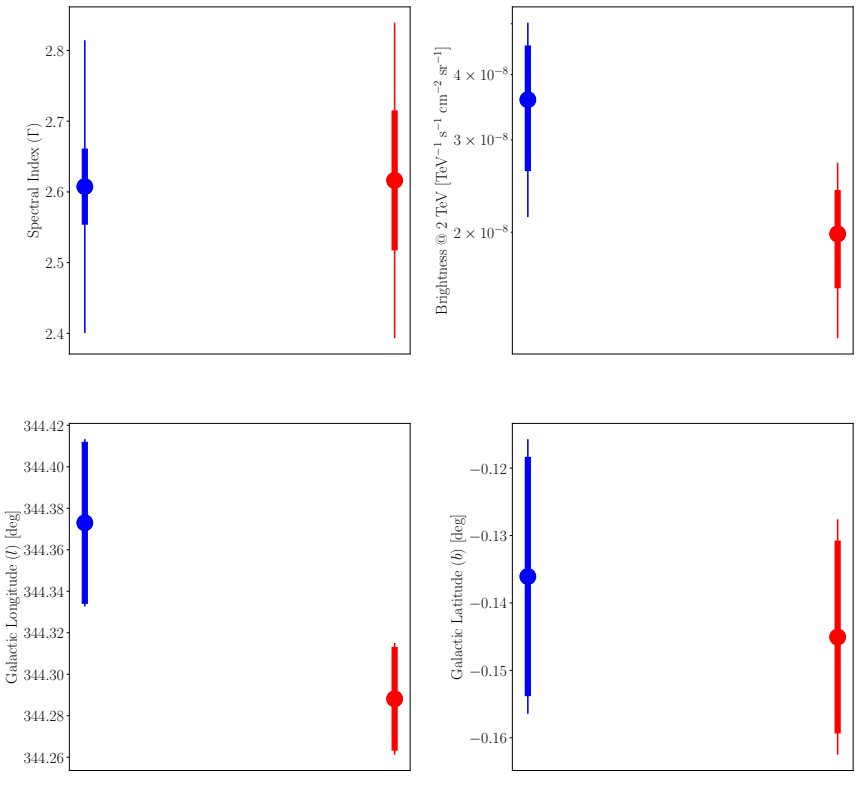

FIGURE 5.9: Same as in figure 5.8, for HESS J1702-420B.

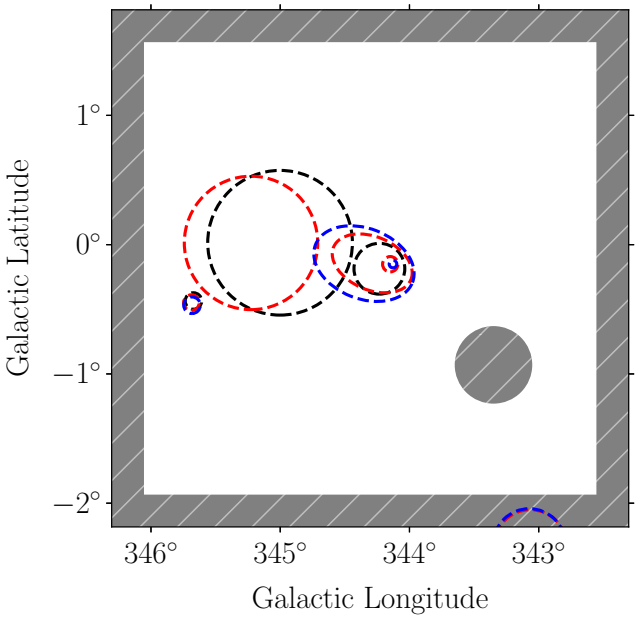

FIGURE 5.10: Comparison of the source models obtained from the MA (red), CA (blue) and the reference HGPS catalog (black). The large-scale component is visible for the MA and HGPS, but was not detected in the CA. More details are provided in the main text.

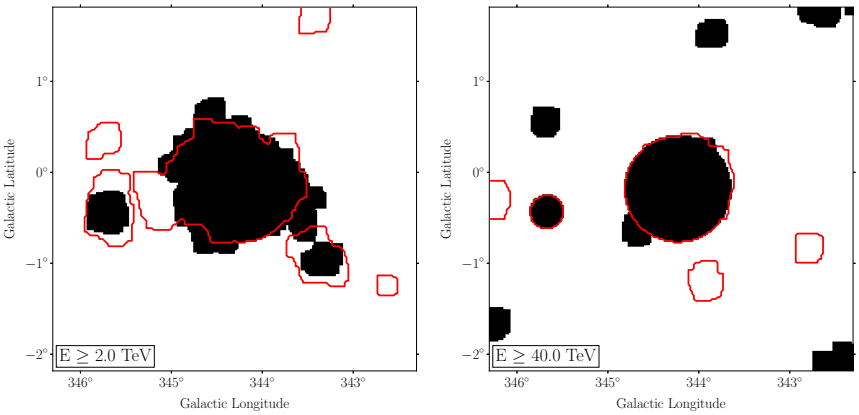

FIGURE 5.11: Exclusion masks used to estimate the hadronic background with the adaptive ring method, for $E > 2\,\mathrm{TeV}$ (left) and $E > 40\,\mathrm{TeV}$ (right). The black (red) regions correspond to the CA (MA) configuration.

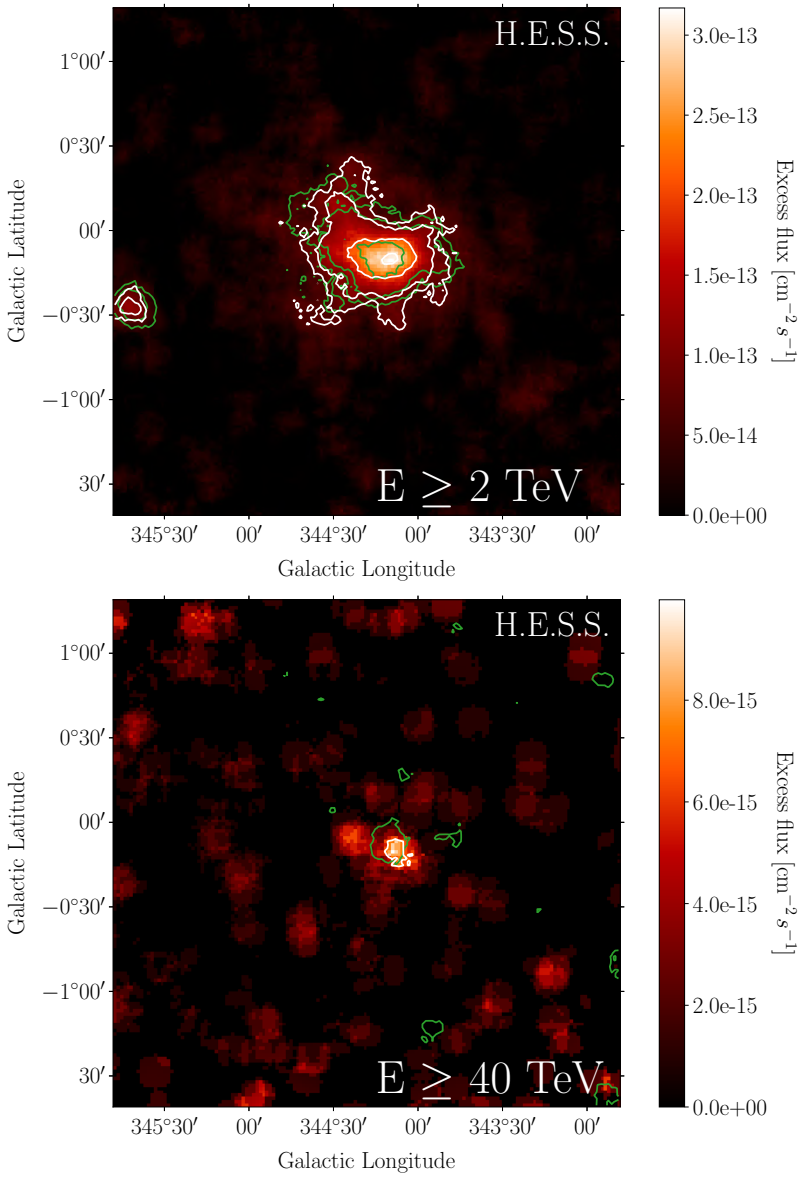

FIGURE 5.12: γ-ray flux maps of the HESS J1702-420 region, computed with the ring background method, above 2 (left) and 40 (right) TeV. The color map and the white contour correspond to the flux maps obtained from the CA, while the green contours were obtained from the MA (see section 4.5). Both maps are correlated with a 0.1°-radius top-hat kernel, and the color code is in unit of γ-ray flux (cm^{-2}s^{-1}) per smoothing area.

Component name	Galactic longitude	Galactic latitude	Major 1σ semi-axis	Minor 1σ semi-axis	Rotation angle
	[deg]	[deg]	[deg]	[deg]	[deg]
HESS J1702-420A	$344.13 \pm 0.01_{\mathrm{stat}} \pm 0.01_{\mathrm{sys}}$	$-0.15 \pm 0.01_{\mathrm{stat}} \pm 0.01_{\mathrm{sys}}$	$0.04 \pm 0.02_{\mathrm{stat}} \pm 0.03_{\mathrm{sys}}$		—
HESS J1702-420B	$344.40 \pm 0.04_{\mathrm{stat}} \pm 0.01_{\mathrm{sys}}$	$-0.14 \pm 0.02_{\mathrm{stat}} \pm 0.01_{\mathrm{sys}}$	$0.44 \pm 0.05_{\mathrm{stat}} \pm 0.12_{\mathrm{sys}}$	$0.27 \pm 0.04_{\mathrm{stat}} \pm 0.07_{\mathrm{sys}}$	$61.2 \pm 4.9_{\mathrm{stat}} \pm 6_{\mathrm{sys}}$

(A) Best-fit morphology parameters of HESS J1702-420A and HESS J1702-420B, obtained from the CA. The rotation angle is measured counterclockwise starting from the $l = 0$, $b > 0$ axis.

Component name	Spectral index	Reference energy	$\mathbf{dN/dE(E = E_{ref})}$	$\mathbf{F(E > 2\,TeV)}$
		[TeV]	$[\mathbf{TeV^{-1}\,cm^{-2}\,s^{-1}}]$	$[\mathbf{cm^{-2}\,s^{-1}}]$
HESS J1702-420A	$2.06 \pm 0.17_{\mathrm{sys}}$	24.53	$(6.03 \pm 1.63_{\mathrm{stat}} \pm 1.81_{\mathrm{sys}}) \times 10^{-16}$	$(2.00 \pm 0.54\mathrm{stat} \pm 0.60_{\mathrm{sys}}) \times 10^{-13}$
HESS J1702-420B	$2.61 \pm 0.05_{\mathrm{stat}} \pm 0.20_{\mathrm{sys}}$	1	$(2.43 \pm 0.97_{\mathrm{stat}} \pm 0.73_{\mathrm{sys}}) \times 10^{-11}$	$(2.97 \pm 1.11_{\mathrm{stat}} \pm 0.89_{\mathrm{sys}}) \times 10^{-12}$

(B) Best-fit spectral parameters of HESS J1702-420A and HESS J1702-420B, obtained from the CA.

Component name	Surface brightness above 2 TeV	Test statistic (TS)	Number of d.o.f.	Significance
	$[\mathbf{cm^{-2}\,s^{-1}\,sr^{-1}}]$			$[\sigma]$
HESS J1702-420A	$(1.7 \pm 1.1_{\mathrm{stat}}) \times 10^{-7}$	74	5	7.7
HESS J1702-420B	$(4.5 \pm 1.1_{\mathrm{stat}}) \times 10^{-8}$	1722	7	$\gg 5$

(C) Detection significance of HESS J1702-420A and HESS J1702-420B, obtained from the CA.

TABLE 5.5: Modeling results for HESS J1702-420A and HESS J1702-420B, obtained with a 3D maximum-likelihood analysis of H.E.S.S. data, using the cross-check analysis configuration.

Chapter 6

Multi-wavelength observations of HESS J1702-420

6.1 Introduction

In order to understand the nature of astrophysical sources, it is often useful to observe them with multiple types of instruments. This allows to build *multi-wavelength* (MW)[1] images, model broad-band energy spectra and achieve a coherent physical interpretation across several energy decades. In the case of HESS J1702-420, several attempts have been made to understand the origin of its TeV emission based on MW observations of its surroundings, all leading to the conclusion that no clear counterpart could be found. However, even in the absence of a MW detection, low-energy observations can be useful to constrain the TeV emission scenarios.

Historically, the two astrophysical objects on which the attention has been focused the most are the remnant SNR G344.7-0.1 and the pulsar PSR J1702-4128, both found $\lesssim 0.5^{\circ}$ from the centroid of the TeV emission (see figures 4.1 or 4.17):

SNR G344.7-0.1: this is a 3 kyr old [175] and small-sized (8 arcmin in diameter) SNR, whose centrally-peaked radio shell [175–177] is also emitting thermal X-rays [178, 179], with the brightest X-ray and radio features close to each other [175]. Recently, the *Fermi*-LAT association 2FHL J1703.4-4145, with the hard spectral index $\Gamma \approx 1.2$, was discovered on the western edge of the SNR [180]. The core-collapse origin of the supernova is debated, due to the absence of a compact remnant. Indeed, the X-ray point source at the center of the SNR [179] has optical and infrared spectra that fit better with a dwarf star in the foreground than with a pulsar. Also controversial is the SNR distance: [175] reported a HI absorption-based distance of 6.3 kpc, while [178] and [181] estimated the more reliable limit $d_{\mathrm{SNR}} \gtrsim 8$ kpc, motivated by the high value of X-ray absorbing hydrogen column density in the direction of the SNR. The cosmic ray diffusion time from the SNR to the VHE peak is compatible with the remnant age [180], which suggests that both 2FHL J1703.4-4145 and HESS J1702-420 may be associated with molecular clouds illuminated (via hadronic interactions) by SNR G344.7-0.1. However, the detection of an extended and bright TeV source such as HESS J1702-420 at $d \gtrsim 8$ kpc in the Galactic plane is unlikely, given the H.E.S.S. sensitivity [38]. Moreover, the surrounding ISM does not exhibit any clear morphological association with the VHE γ-ray source (see below), a fact that challenges a hadronic interpretation of the TeV emission;

[1] Sometimes even *multi-messenger*.

PSR J1702-4128: this pulsar has a large angular separation ($\approx 0.5^{o}$) from the TeV peak, corresponding to $\approx 50\,\mathrm{pc}$ at the estimated 5.2 kpc pulsar's distance [182]. It was estimated by [183] that it would require a conversion efficiency of its spin-down luminosity ($\dot{E} = 3.4 \times 10^{35}\,\mathrm{erg\,s^{-1}}$) into γ-rays $> 10\%$ in order to power the whole HESS J1702-420, higher than all other PWNe identified by H.E.S.S. [184]. This fact, together with the unconclusive searches for an asymmetric X-ray PWN around the pulsar [185], tend to disfavor an association of PSR J1702-4128 with (the whole) HESS J1702-420. Still, it remains possible (and even plausible) that PSR J1702-4128 powers at least part of HESS J1702-420. Further comments on this topic will be provided in chapter 7.

This discussion remains, to this date, inconclusive, since both SNR G344.7-0.1 and PSR J1702-4128 present arguments both in favor and against an association with HESS J1702-420.

Since the γ-ray flux from hadronic interactions scales linearly with the amounts of target gas and cosmic rays (see equation 1.16), measurements of the gas distribution around a γ-ray source can be used to constrain hadronic emission scenarios. In [181] it was shown that dense target material, although present at various distances along the line of sight of HESS J1702-420 in the form of molecular and atomic hydrogen clouds[2], does not exhibit any obvious correlation with the VHE γ-ray maps. In the X-ray domain instead, deep *Suzaku* observations revealed the presence of two extremely faint point-like objects (src A and src B, indicated in figure 4.17) and the absence of diffuse X-ray emission in the *Suzaku* FoV, whose dimensions were however insufficient to cover the whole TeV source [186].

In this chapter we report on the analysis of MW observations of HESS J1702-420, that were motivated by the updated source morphology and the discovery of the new TeV component HESS J1702-420A. They are presented in order of increasing photon energy, from radio (section 6.2) to X-rays (section 6.3) to HE γ-rays (section 6.4).

6.2 Morphology of the ISM near HESS J1702-420

About 70% of the ISM is made of hydrogen, in various forms:

- neutral hydrogen athoms (HI) are observed via the $\lambda = 21\,\mathrm{cm}$ (1.42 GHz, 5.9 μeV) hyperfine spectral line due to a spin-flip transition of the hydrogen's electron. This is a forbidden (i.e. low probability) transition, with an extremely long lifetime of the excited state ($\approx 10\,\mathrm{Myr}$). This means that HI observations are affected by a detection bias, for which only regions hosting large amounts of HI can be seen. This line appears in the radio spectrum, and has been the target of extensive campaigns such as the Southern Galactic Plane Survey (SGPS), which combined observations from the Australia Telescope Compact Array (ATCA) and Parkes Radio Telescope [187]. In that survey, the HI line was observed as an emission feature, which typically traces warm ($T \approx 500 - 5000\,K$) and diffuse ($n_H \lesssim 10^2\,\mathrm{cm^{-3}}$) gas phases [187, 188][3]. The combined ATCA and Parkes datasets have an angular resolution of $2'$, a spectral resolution of $0.8\,\mathrm{km\,s^{-1}}$ and a line sensitivity of $\approx 1.6\,K$ [187];

[2] With estimated average densities in the range $30 - 830\,\mathrm{cm^{-3}}$.

[3] When observed in absorption, it traces instead cold ($T \lesssim 100\,K$) and dense ($n_H \approx 10^2\,\mathrm{cm^{-3}}$) gas.

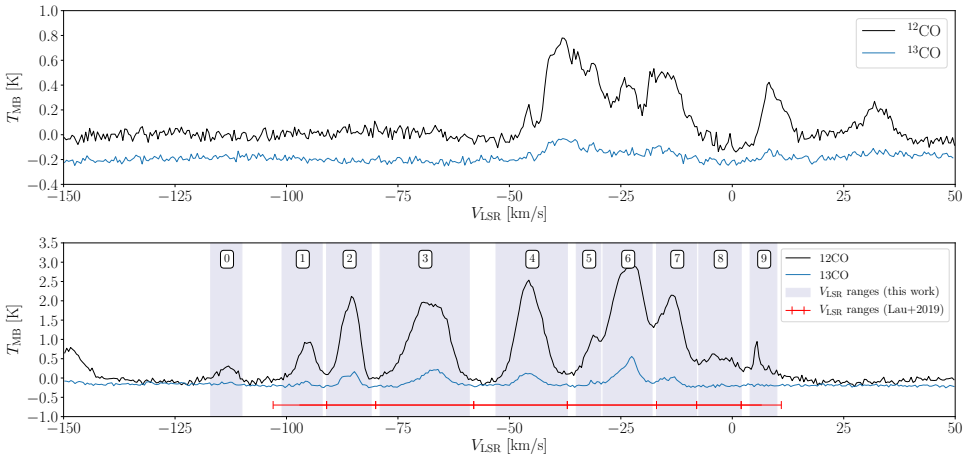

FIGURE 6.1: ^{12}CO and ^{13}CO velocity profiles for the analysis validation (top) and HESS J1702-420A region (bottom). In the bottom panel, the peak integration ranges used in this work (in [181]) are indicated by the blue shaded areas (red bars).

- hydrogen molecules (H_2) are the main constituent of so-called molecular clouds (MCs), that have sizes ranging from tens to hundreds of parsecs, masses from few to millions of solar masses and low temperatures ($\approx 10\,K$). They are the primary sites in which star formation takes place, and are distributed along the Galactic spiral arms. Since the hydrogen molecule is symmetric, its transition lines are extremely weak. For this reason we cannot directly observe the H_2 fraction of molecular clouds, and we have to resort to other tracers such as carbon monoxide (CO, primarily in the form of the ^{12}CO isotope). The latter is the second most abundant molecule in MCs[4] and, unlike H_2, has a permanent dipole moment that allows it to radiate efficiently. The CO($J = 1 \rightarrow 0$) transition, with $\lambda = 26\,$mm (11.53 GHz, 47.69 μeV) spectral line, is a good H_2 tracer[5] because it is triggered by collisions between the CO and H_2 molecules [189]. In practice, this relation is expressed by a direct proportionality between the H_2 column density (N_{H_2}, units of cm^{-2}) and the velocity-integrated CO brightness temperature (W_{CO}):

$$N_{H_2} = X_{CO} \times W_{CO}\ , \tag{6.1}$$

  where X_{CO} the so-called conversion X-factor. In the early 2000s, [190] has performed an extensive ^{12}CO survey of the Milky Way with an angular resolution of 8′. More recently, the Mopra radio telecope in Australia has released[6] a 109-115 GHz survey of multiple CO isotopes (^{12}CO, ^{13}CO, ^{17}CO, ^{18}CO) with better angular (0.6′) and spectral (0.1 km s^{-1}) resolutions [191].

- ionized hydrogen athoms (HII, or H^+) form so-called HII regions, created by the ionising effects of the UV radiation from young and massive stars within giant MCs. They play an important role in star formation, since they typically expand supersonically inside underdense bubbles carved by stars into the ISM, creating a shock which compresses the swept-up material triggering the star formation process.

[4] With about 1 CO molecule per 10^4 hydrogen molecules.
[5] Especially for H_2 densities of $10^2 - 10^3\,$cm^{-3} and temperatures above few K.
[6] At https://doi.org/10.7910/DVN/LH3BDN.

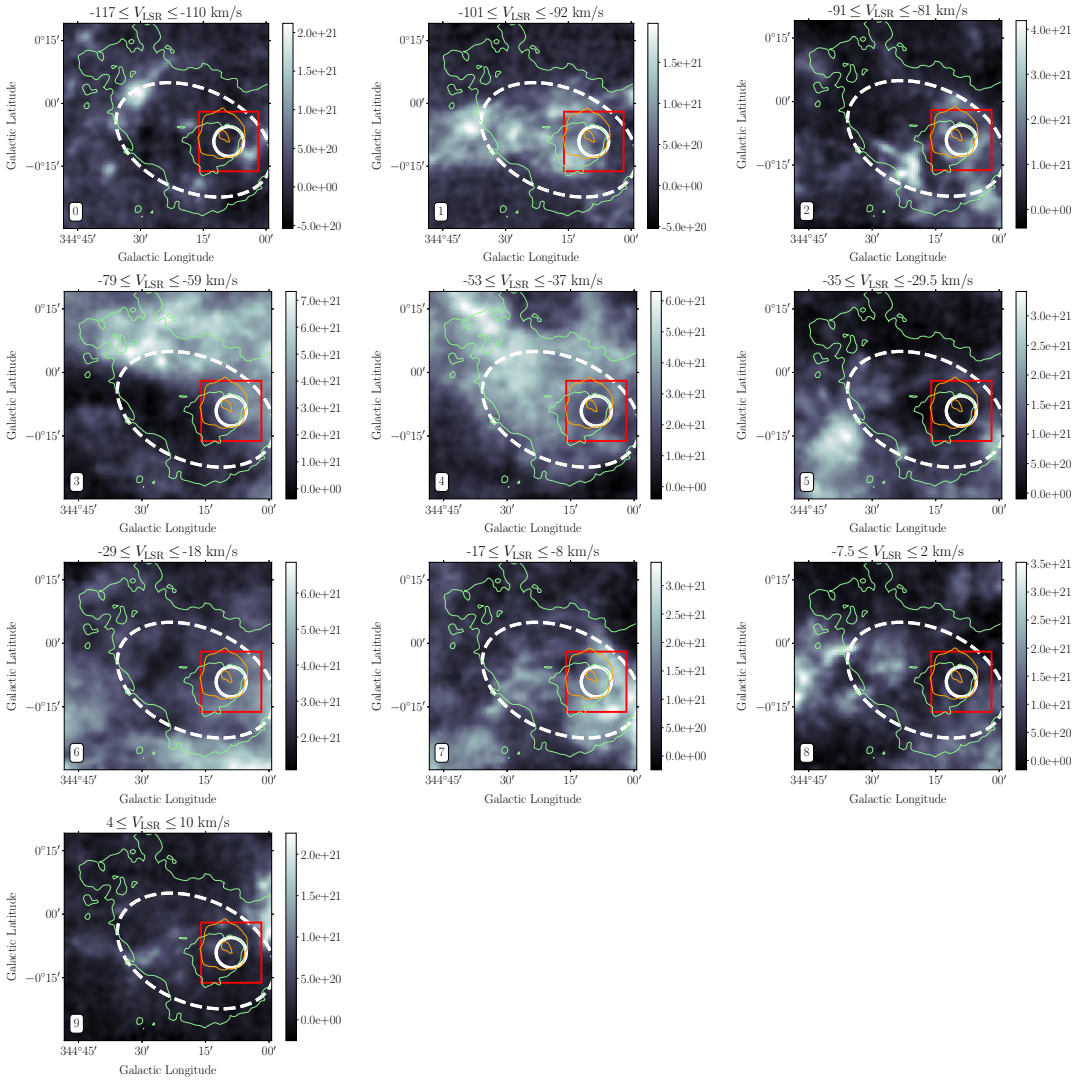

FIGURE 6.2: Column density maps of molecular hydrogen in the direction of HESS J1702-420, obtained by integrating the brightness temperature profile of ^{12}CO($J = 1 \rightarrow 0$) data from the Mopra radio survey within the velocity intervals indicated above each panel (corresponding to the peaks in figure 6.1, bottom panel). The images have been smoothed using a 0.6′ radius Gaussian kernel, corresponding to the angular resolution of Mopra, and the colorbars are in units of cm^{-2}. The green (orange) contours indicate the 5 and 12σ (3 and 5σ) significance levels of the TeV γ-ray flux above 2 TeV (40 TeV). The dashed ellipse and solid circle represent the 1σ morphologies of HESS J1702-420B and HESS J1702-420A, respectively. Finally, the red square, centered at the best-fit position of HESS J1702-420A, indicates the extraction region used to produce the profile reported in figure 6.1.

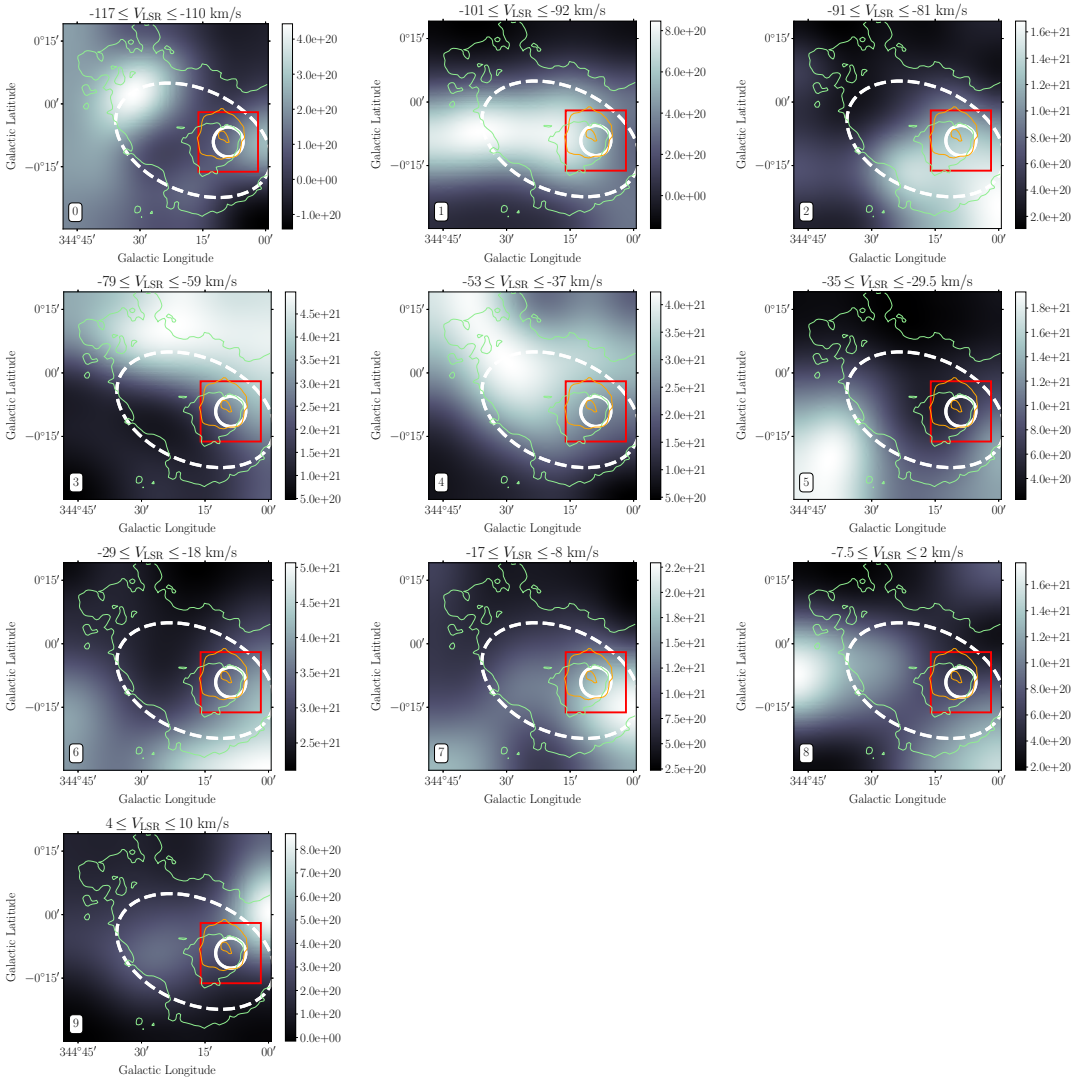

FIGURE 6.3: Same as figure 6.2, but the HI images were smoothed using a 0.1° radius Gaussian kernel corresponding to the angular resolution of H.E.S.S..

In [181], HI data from the SGPS and H_2 data from the Mopra survey were analyzed, to probe the origin of HESS J1702-420 via the characteristics of its surrounding ISM. The gas densities along the line of sight were measured by integrating the velocity peaks within a $0.30^o \times 0.15^o$ ellipse centered at $l = 344.30^o$ and $b = -0.18^o$. This choice of integration region reflected the most up-to-date morphology reported for HESS J1702-420 at that time (from [40]). Based on the updated H.E.S.S. analysis presented in chapter 4 of this thesis, we repeated the ISM analysis, with the same radio data and approach as in [181] but adopting a smaller extraction window to focus directly on HESS J1702-420A.

We validated our CO data analysis pipeline by reproducing a reference picture from the literature (the top panel plot in figure 12 from [191]). To do so, we retrieved the FITS data cubes corresponding to the $300^o \leq l \leq 301^o$ and $|b| < 0.5^o$ region and $-150 \leq V_{\rm LSR} \leq 50\,{\rm km\,s^{-1}}$, where $V_{\rm LSR}$ denotes the relative velocity of the ISM with respect to the local standard reference frame (which comoves with the Sun). We divided the data (in units of antenna temperature, K) by the Mopra beam efficiency $\eta = 0.55$ to convert them to main beam brightness temperature $T_{\rm MB}$ [187, 191]. To produce a $V_{\rm LSR}$-$T_{\rm MB}$ profile plot, we computed the average $T_{\rm MB}$ value for each velocity slice of the cube. The result is shown in the top panel of figure 6.1, which closely matches the reference figure from [191].

After the analysis validation, we focused on the HESS J1702-420A region, to find out whether a MC could be found near its position. We extracted the velocity profile within a square box centered at the best-fit position of HESS J1702-420A and with half-side of 0.12^o corresponding to the 2σ extension of HESS J1702-420A (see figure 6.1, bottom panel). We manually defined the velocity intervals for each peak, which is a less precise but quicker procedure than the multi-gaussian fit implemented in [181]. We then integrated the velocity profile peak-by-peak,

$$W(CO) = \int_{V_{\rm LSR}^{\rm min}}^{V_{\rm LSR}^{\rm max}} T_{MB}\, dV_{\rm LSR}\,, \tag{6.2}$$

and converted the resulting maps (in units of $[{\rm K\,km\,s^{-1}}]$) to H_2 column density maps (units of $[{\rm cm^{-2}}]$) using the X-factor $X_{\rm CO} = 1.5 \times 10^{20}\,{\rm cm^{-2}\,(K\,km\,s^{-1})^{-1}}$ [181, 192]. They are shown, for each peak, in figure 6.2. The images have been smoothed with a Gaussian filter corresponding to the angular resolution of Mopra ($0.6'$), which is one order of magnitude better than the one of H.E.S.S. ($\approx 0.1^o = 6'$). Therefore, to properly investigate possible morphology association, we smoothed the Mopra images down to the level of the H.E.S.S. PSF, obtaining the figure 6.3. Following again [181], we also computed HI column density maps (see figures 6.4 and 6.5) integrating the velocity profile inside the same region centered on HESS J1702-420A and within the velocity ranges obtained from the H_2 distribution (see figure 6.6).

From figures 6.2, 6.3, 6.4 and 6.5 we concluded that any possible correlation between HESS J1702-420 (in particular HESS J1702-420A) and the ISM is, at best, speculative. As an example, by looking at the cloud number 4 in figure 6.2, one may have the impression that the lower energy H.E.S.S. contours (in green, $E > 2\,{\rm TeV}$) follow the "raindrop" profile of the H_2 maps, while the high-energy H.E.S.S. contours (in orange, $E > 40\,{\rm TeV}$) correspond to an under-dense region of the H_2 cloud. If ever confirmed by means of TeV observations with better angular resolution (e.g. from CTA-South), this could suggest that HESS J1702-420A is associated with a powerful object (e.g. s pulsar) which has carved the surrounding ISM with its wind. The large-scale emission

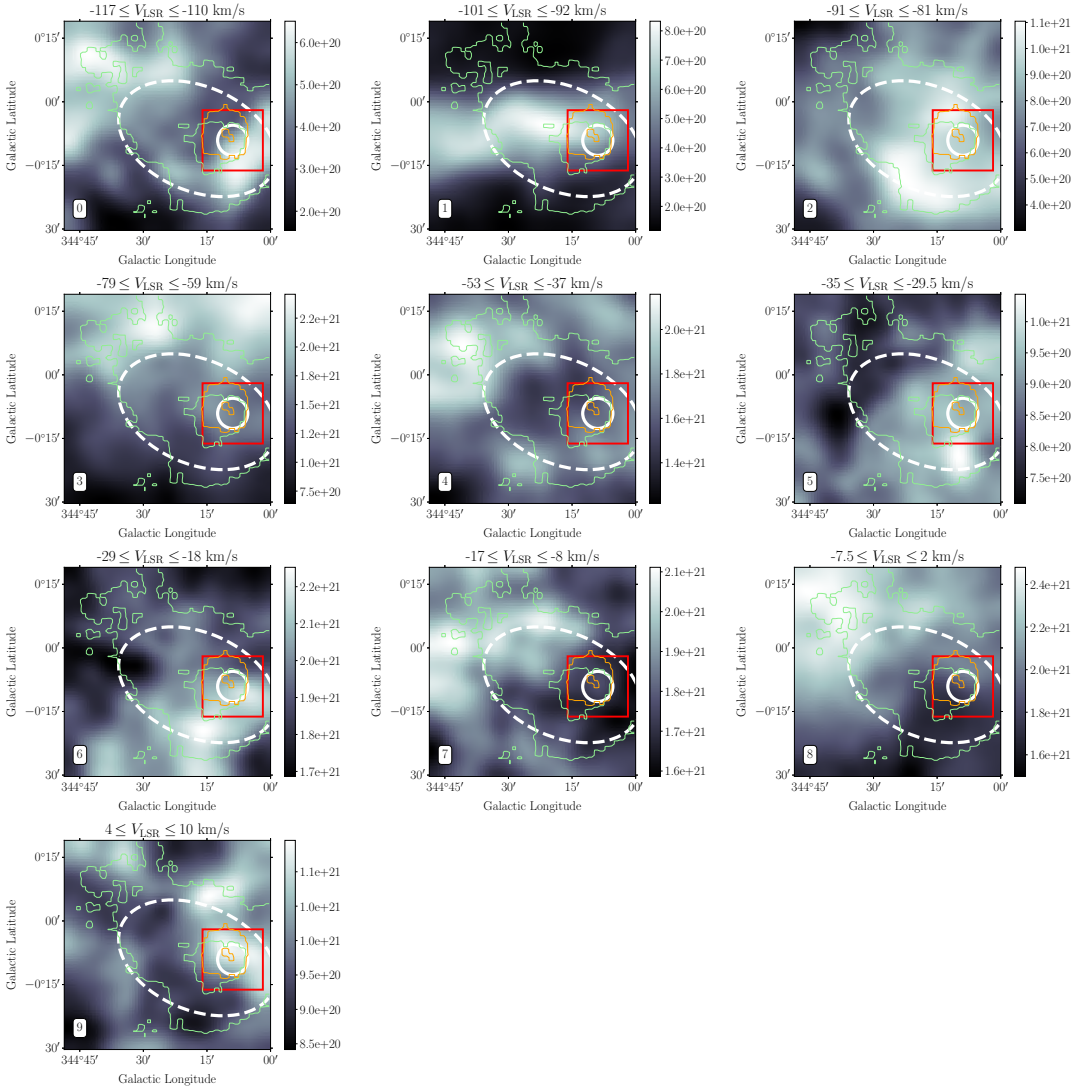

FIGURE 6.4: Column density maps of atomic hydrogen in the direction of HESS J1702-420, obtained by integrating the brightness temperature profile of from the SGPS within the velocity intervals indicated above each panel (corresponding to the peaks in figure 6.1, bottom panel). The images have been smoothed using a 2′ radius Gaussian kernel, corresponding to the angular resolution of the radio survey, and the colorbars are in units of cm^{-2}. The H.E.S.S. contours look more "squared" in these maps than in the Mopra ones (e.g. figure 6.2), due to the coarser pixel size of the SGPS maps. Further details on the colorbar, contours and markers and provided in figure 6.2.

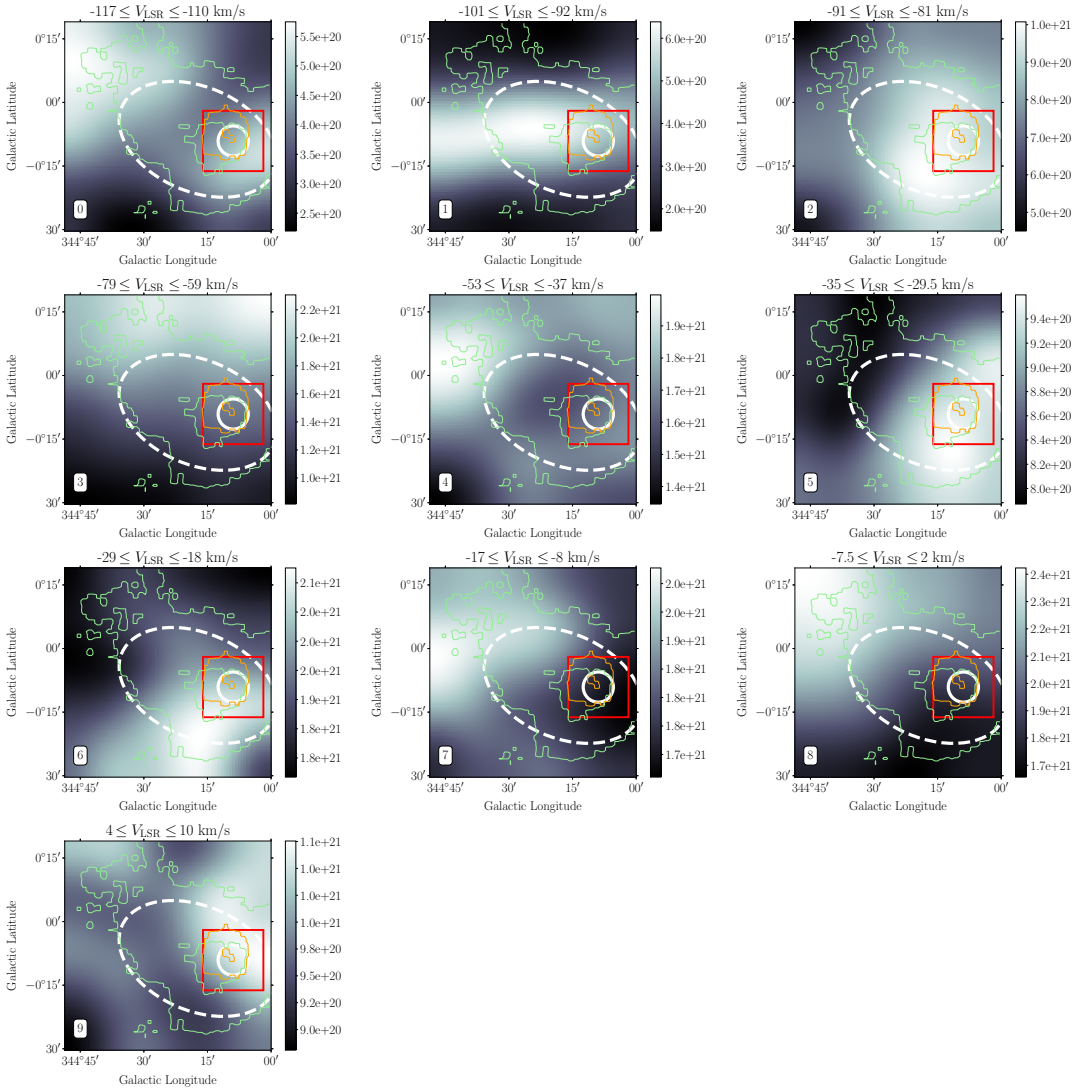

FIGURE 6.5: Same as figure 6.4, but the HI images were smoothed using a 0.1° radius Gaussian kernel corresponding to the angular resolution of H.E.S.S..

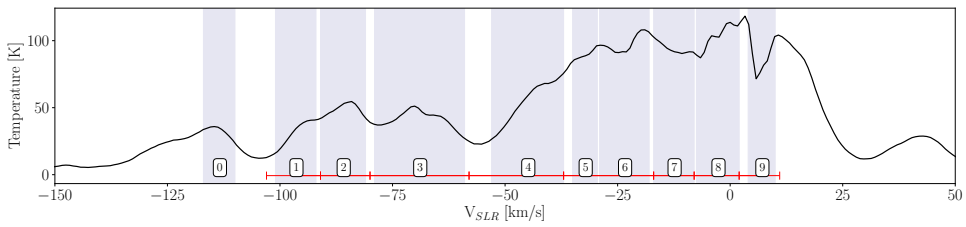

FIGURE 6.6: HI velocity profiles for the HESS J1702-420A region (corresponding to the red box in figure 6.4). The peak integration ranges are the same as in figure 6.1, bottom panel.

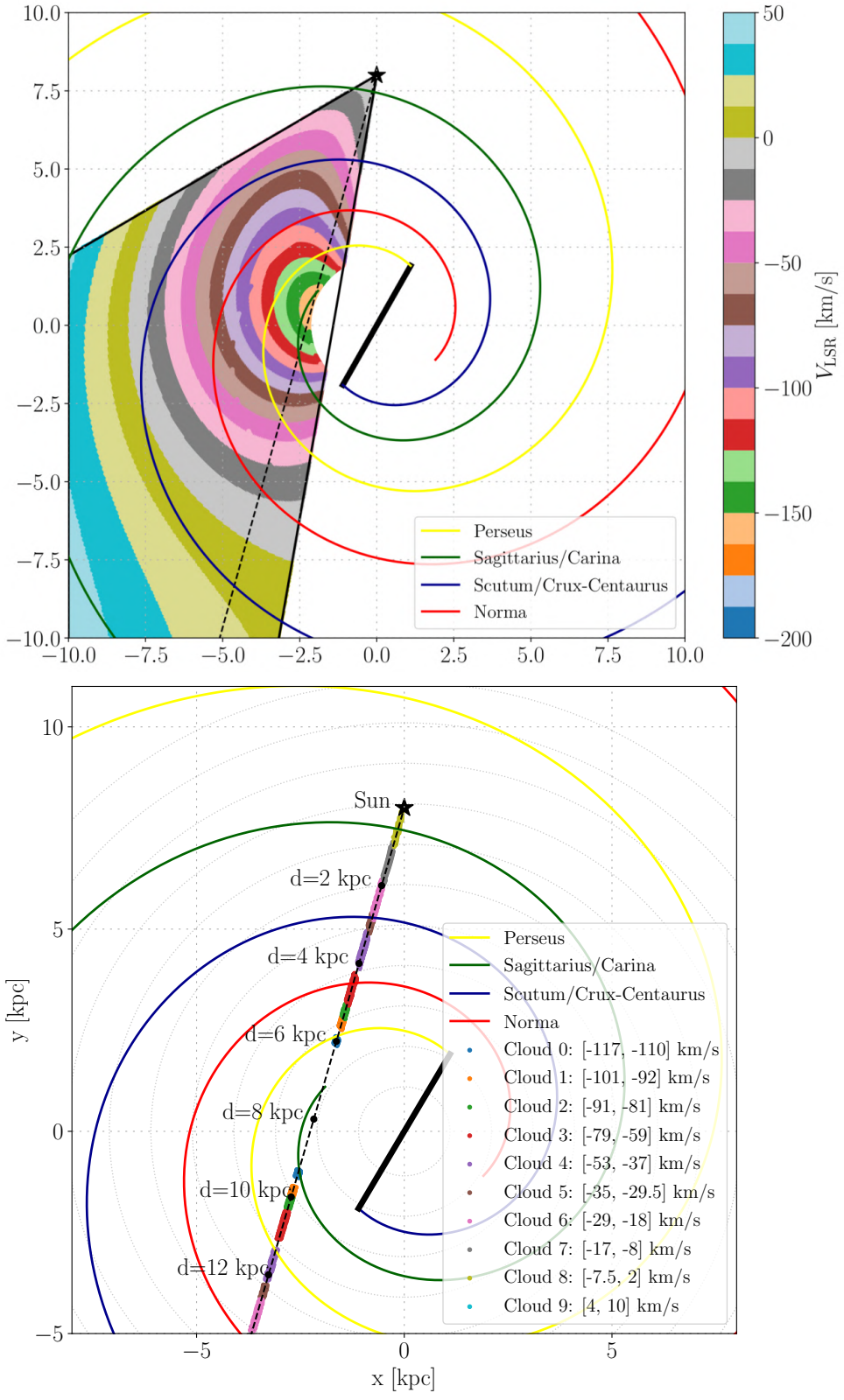

FIGURE 6.7: Top: a view of the Milky Way Galaxy model from [193], with a colour scale displaying the relative kinematic line-of-sight velocity (V_{LSR}) from the reference point of the Sun. Bottom: Estimation of the kinematic distance of the molecular clouds corresponding to the peaks of figure 6.1 (bottom panel). The cloud 9, which corresponds to positive V_{LSR}, is not shown since it lies on the opposite direction of HESS J1702-420 with respect to the Sun's position, which excludes an association.

from HESS J1702-420B could then be the result of the interaction between the wind and the molecular cloud, either hadronic (by proton collisions against the cloud material) or leptonic (in the form of electron acceleration at a termination shock, which stands at the interface between the supersonic pulsar wind and the surrounding MC). The leptonic (PWN) interpretation would be favored in this case, because the anti-correlation between HESS J1702-420A and the gas density would be challenging for hadronic scenarios. This is just one of many possibilities, and for the moment we must agree with [181] in that dense target material, although present at various distances along the line of sight, does not clearly correlate with (any component of) HESS J1702-420. For this reason, we did not go into further detail, for example by estimating the clouds mass. A detailed study can be found in [181], and the results would be very close in our case since we are considering similar velocity ranges (see e.g. figure 6.1).

We finally used a model of the Milky Way to convert the measured V_{LSR} of the clouds into their so-called *kinematic distances*. The model is based on a perfect logarithmic Galaxy spiral [193]:

$$r(\phi) = r_0 e^{\phi/\tan p}\,, \tag{6.3}$$

where ϕ is the angle measured counterclockwise from the positive x axis direction (in the reference frame of figure 6.7), $p = -13.1^{\mathrm{o}}$ is the (constant) pitch angle of the spiral, the Sun's position is $(x, y) = (0, 8\,\mathrm{kpc})$ and the velocity curve is assumed to be flat ($v(r) = 220\,\mathrm{km\,s^{-1}}$). The length of the spiral central bar is assumed to be 2.2 kpc, with an inclination angle from the Sun's position of 30^{o}. By computing the instantaneous velocity of an object which comoves with the Galaxy, subtracting it to the Sun's velocity and projecting the result along the line of sight from the Sun's position, we produced the V_{LSR} map shown in figure 6.7 (top panel). The figure compares well with the figure 7 from [191], in which the same Galaxy model was assumed, which validates our V_{LSR} calculation. We therefore applied the model to estimate the cloud's kinematic distances as visually shown in figure 6.7 (bottom panel). In the latter figure one can notice that for some clouds (e.g. the number 6, 7 and 8) the velocity intervals for the peaks integration are possibly too large, because they result in physical dimensions of the MCs of the order of 1 kpc. However for the remaining clouds the esimated sizes are in the more realistic range of hundreds of parsecs. We estimated the approximate distance for each cloud directly from figure 6.7 (bottom panel), by taking the distance corresponding to the center of the cloud's velocity interval. The resulting (near) cloud's distances, reported in table 6.1, closely correspond to those estimated by [181], as expected since the used Galaxy model and the peak integration ranges are similar. The far distances are not reported, since clouds further away than ≈ 8 kpc are unlikely to be asssociated with HESS J1702-420 given the H.E.S.S. sensitivity [38].

We finally note that the considerable work duplication between this section of the thesis and [181] results from the fact that we had independently started working on this ISM analysis before [181] was published.

6.3 X-ray observations of HESS J1702-420

The extremely hard power-law spectrum of HESS J1702-420A, extending with no sign of curvature up to 100 TeV, makes it a PeVatron candidate. And yet, as reported in the previous section, there is no obvious support to the hadronic hypothesis from

Cloud number	0	1	2	3	4	5	6	7	8	9
$V_{\mathbf{LSR}}^{\mathbf{peak}}$ **[km/s]**	-113.5	-96.5	-86	-69	-45	-32.3	-23.5	-12.5	-2.5	7
Near distance [kpc]	6	5.5	5.1	4.6	3.5	3.1	2.5	1.5	0.5	-

TABLE 6.1: The table reports the distance values for the MCs on the line of sight of HESS J1702-420, estimated from the approximate position of the centers of the intervals shown in figure 6.7 (bottom panel).

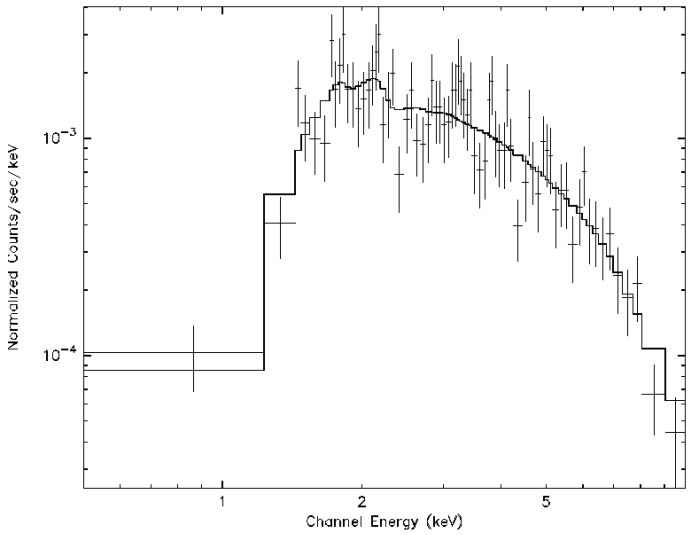

FIGURE 6.8: Simulation (spectral points) and spectral modeling (solid line) of a 60 ks XMM pointing on *Suzaku* src B, based on the assumptions presented in the text. This is just one of the multiple realizations we made to estimate the average errors on the free model parameters obtained from the fit.

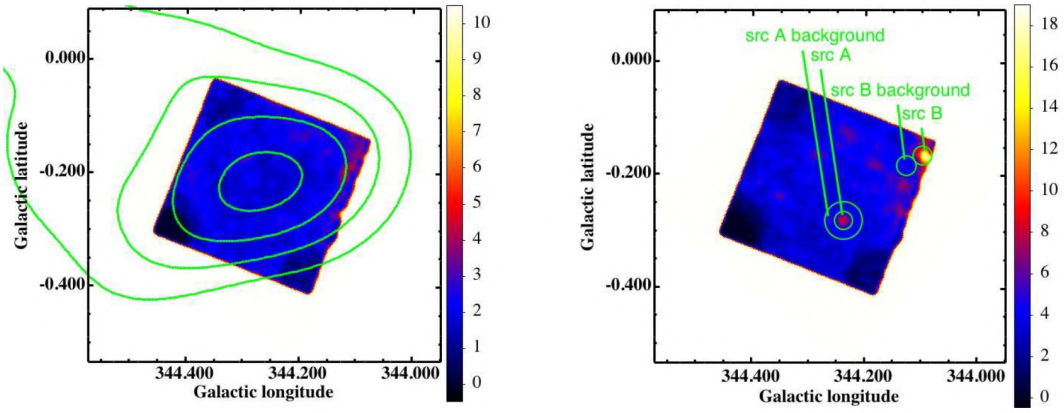

FIGURE 6.9: Suzaku XIS images of HESS J1702-420 field in the 0.5-2 keV (left) and the 2-8 keV band (right), corrected for vignetting after NXB subtraction. Left panel: green contours represent the VHE gamma-ray intensity map (archival data, up to 2008). Right panel: X-ray point sources discovered by *Suzaku*. Image credits: Fujinaga et el. 2011

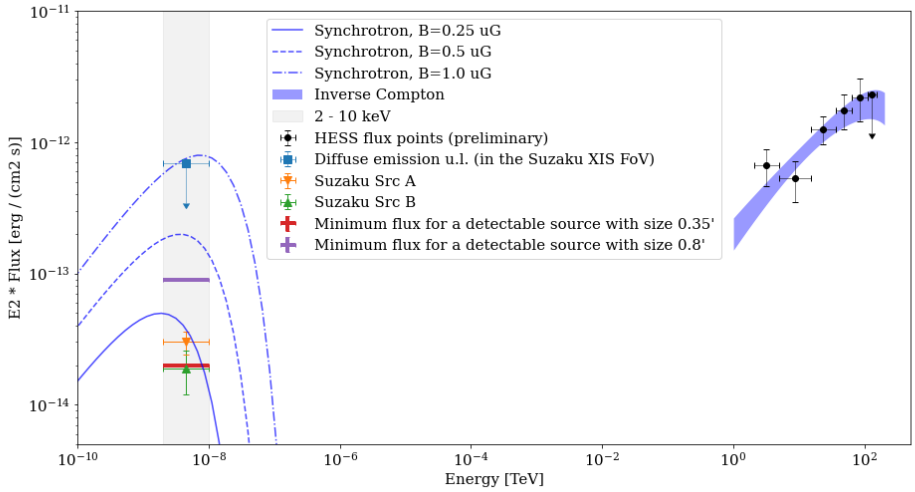

FIGURE 6.10: Spectral modeling of HESS J1702-420A, previously hidden under the bulk emission of HESS J1702-420. The 1σ butterfly is obtained adjusting an inverse Compton model to the flux points of HESS J1702-420A. Horizontal lines (red and violet) represent the minimal fluxes of diffuse sources that can be detected by XMM (60 ks exposure). Blue curves are synchrotron spectra for given magnetic field values. In the X-ray band, the fluxes of src A and B are also indicated, together with the diffuse emission upper limit. More details on the leptonic modeling are provided in chapter 7.

the morphology of the nearby ISM. Also, the overall morphology of HESS J1702-420, showing indications of energy-dependent shrinking toward HESS J1702-420A, may be suggestive of a (leptonic) PWN scenario. In this context, it is interesting to notice the spatial proximity between the new TeV source HESS J1702-420A and one of the unidentified *Suzaku* sources reported by [186], called src B (see figure 4.17), which might point toward the first MW detection of the compact object (e.g. a pulsar) operating as particle accelerator inside HESS J1702-420. Unfortunately, based on the *Suzaku* observation (≈ 200 ks) it was not possible to measure the X-ray spectra of src A and B, due to poor statistics. Assuming instead a spectral index of $\Gamma = 2.1$ and a hydrogen column density $N_H = 1.5 \times 10^{22}\,\mathrm{cm}^{-2}$, the *Suzaku* team estimated an absorbed X-ray flux in the $2-10$ keV band of (3.0 ± 0.6) and $(1.9 \pm 0.7) \times 10^{-14}\,\mathrm{erg\,s^{-1}\,cm^{-2}}$ for src A and src B, respectively. Obviously, these estimates are strongly dependent on the assumed spectral index and N_H, not to mention that src B is barely covered by the *Suzaku* FoV, in a noisy edge region.

This led us to to propose a re-observation of HESS J1702-420 with another X-ray instrument, called XMM-Newton. The basic motivation for the choice of XMM was in its sensitivity[7], which guarantees that in a standard PWN scenario the X-ray synchrotron emission from src B would be clearly detectable (see below). The main objectives of our XMM proposal were:

- providing a full X-ray coverage of the new compact TeV source, HESS J1702-420A, in order to detect the nearby *Suzaky* src B and perform a MW spectral modeling;
- evaluate the level of diffuse X-ray emission in the vicinity of HESS J1702-420A, looking for a weak X-ray nebula supporting a PWN scenario;

[7] The effective area of XMM is roughly 10 times higher than *Suzaku*.

- measure the N_H to obtain a rough estimate of the distance of the src B (by comparison with a cumulative ISM profile obtained as in figure 7 of [181]), crucial to estimate its energy budget.

We estimated that a 60 ks (+ a 20% flare fraction, adding up to 72 ks) observation with both types (MOS and PN) of European photon imaging camera (EPIC) onboard of XMM-Newton, centered at the position of the *Suzaku* src B, would suffice to fulfill the above goals. We used the following arguments:

- the expected X-ray background isotropic count-rate $\tau_{\rm bkg}$ $(2-10\,{\rm keV})$ is about $7\times10^{-7}\,{\rm s}^{-1}\,{\rm arcsec}^{-2}$ for PN and $3\times10^{-7}\,{\rm s}^{-1}\,{\rm arcsec}^{-2}$ for MOS cameras [194]. To take into account the Galactic ridge emission we conservatively doubled these values. Therefore, the number of background counts enclosed by a radius r (for e.g. PN) is $N_{\rm bkg}=\tau_{\rm bkg}\times(60\,{\rm ks})\times\pi r^2\approx950\,(r/{\rm arcmin})^2$, and the level of 3σ background fluctuations is $3\sqrt{N_{\rm bkg}}\approx90\,(r/{\rm arcmin})$. Assuming that a diffuse source is detected when its signal counts exceed the 3σ background fluctuation level, we obtained the minimal number of signal counts (that we converted to X-ray fluxes using `WebPIMMS`) allowing an XMM detection, as a function of the source size r. These fluxes are reported in figure 6.10 as horizontal lines between 2 and 10 keV. The figure shows that a 60 ks observation allows to detect diffuse X-ray emission in the vicinity of the HESS J1702-420A, if present. In other words, if the TeV emission is due to inverse Compton processes from a PWN, its synchrotron X-ray counterpart should be detected;

- using the `Nh` tool and referring to figure 7 of [181], we estimated a conservative value for the total (HI + H_2) column density of $N_H=3\times10^{22}\,{\rm cm}^{-2}$ (which may be even higher if the source distance is $\gtrsim6\,{\rm kpc}$), doubled with respect to [186]. We also revisited the flux of src B by doubling it, because the reported flux from [186] is almost certainly underestimated. This can be seen in figure 6.9, right panel, from which it is clear that the src B was not 100% contained in the Suzaku FoV and the level of diffuse emission around its position appears to be larger than elsewhere in the FoV. Then, assuming for the src B a spectral index of $\Gamma=2.1$ as in [186] (or 1.53 as HESS J1702-420A), the expected XMM-Newton count rate between 2 and 10 keV from `WebPIMMS` is $5.4\,(4.9)\times10^{-3}\,{\rm s}^{-1}$ for PN and $1.9\,(1.7)\times10^{-3}\,{\rm s}^{-1}$ for each MOS camera. A 60 ks observation would therefore yield roughly 300 photons in the PN and 110 in each MOS camera. This way, the total number of background events (roughly 30 for the PN and 11 for each MOS detector) enclosed by the $\approx10''$ PSF of XMM would be low enough to detect the source and measure its spectrum. We confirmed this by performing spectral simulations (using `WebSpec`, see figure 6.8) of a 60 ks observation using all EPIC instruments, and found that on average we could reconstruct the spectral index of src B with a precision better than ±0.3, and the value of N_H with a precision better than 20%.

The proposal was accepted, which means that further updates will be provided in the written and/or oral presentation of this thesis or in a future publication, depending on the progress of the XMM data taking and analysis. These new observations will hopefully allow to constrain the leptonic scenario for the origin of HESS J1702-420.

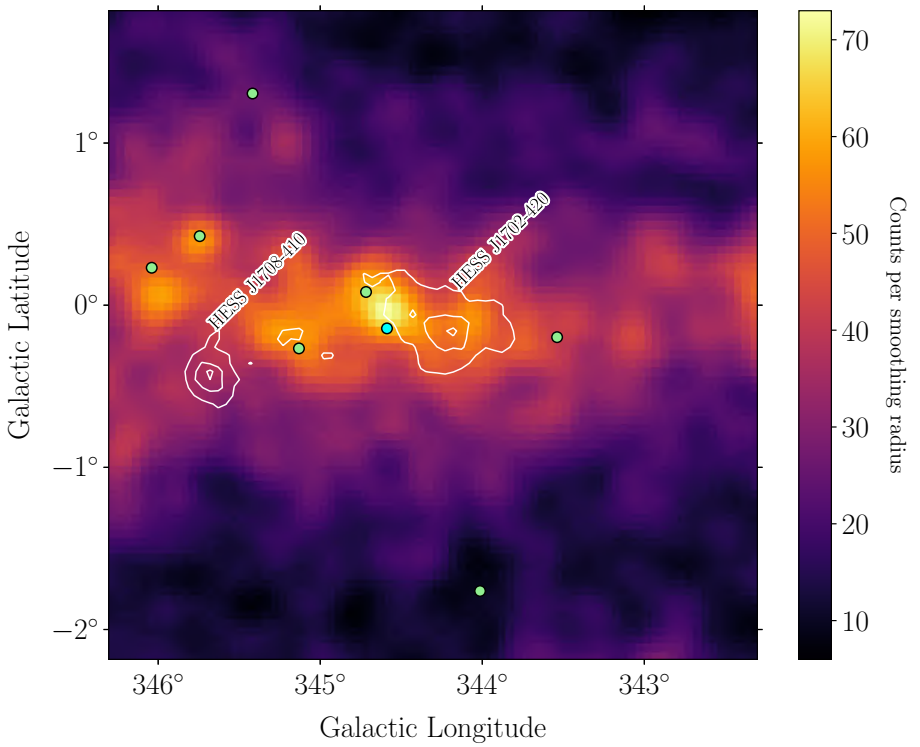

FIGURE 6.11: *Fermi*-LAT γ-ray counts map of the HESS J1702-420 region, correlated with a 0.1°-radius Gaussian filter. The white contours represent the 70, 150 and 200 count levels from the H.E.S.S. maps (above 2 TeV). The positions of nearby 4FGL and 2FHL sources are shown as green and cyan circles, respectively.

Direction (Gal)	**Radius**	**Time range (Gregorian)**	**Energy (GeV)**
$(344.3°, -0.2°)$	21.21°	2008-08-04 — 2020-06-26	1 — 1000

TABLE 6.2: Query details for the *Fermi*-LAT data.

zmax	**evclass**	**evtype**	**Selection filter**
90	120	3	`(DATA_QUAL>0)&&(LAT_CONFIG==1)`

TABLE 6.3: Events selection cuts for the *Fermi*-LAT analysis.

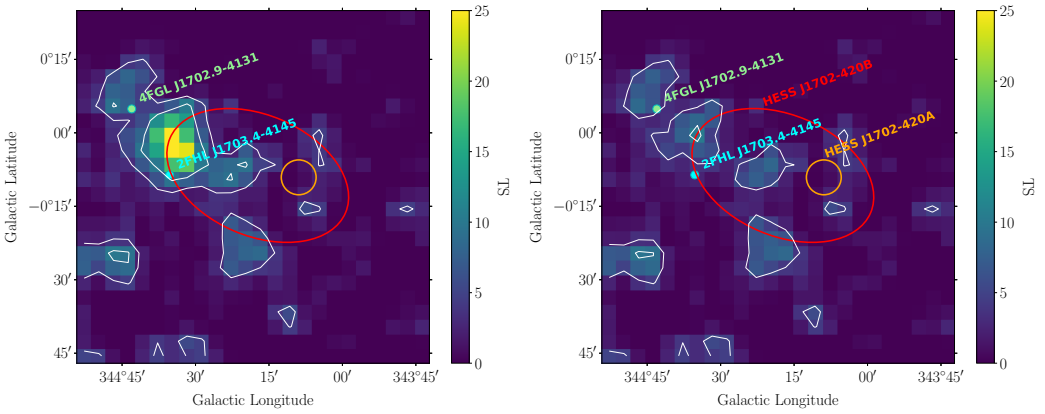

FIGURE 6.12: The left (right) image shows the residuals TS map before (after) source modeling in the FoV (see the main text for details). The white contours represent TS = 4 (2σ) and TS = 9 (3σ) significance levels. The red ellipse (orange circle) correspond to the 1σ shape of HESS J1702-420B (HESS J1702-420A). The positions of nearby 4FGL and 2FHL sources are shown as green and cyan circles, respectively.

6.4 The *Fermi*-LAT view of HESS J1702-420

Launched in 2008, the *Fermi* Large Area Telescope is a pair-conversion instrument sensitive to the HE γ-ray domain [91]. To see whether HESS J1702-420 has any counterpart at GeV energies, we analyzed ≈ 12 yr of events in the $10-900$ GeV band[8]. The data (photon event file and spacecraft file) were retrieved from the LAT data server through a query defined by the parameters in Table 6.2. We adopted the event selection cuts described in Table 6.3. Figure 6.11 shows a *Fermi*-LAT counts map zoomed on HESS J1702-420, including TeV contours and known GeV sources. For the analysis, we defined a square $10^\circ \times 10^\circ$ RoI, fully inscribed within the events selection circle. The events were binned spatially using $0.05^\circ \times 0.05^\circ$ pixels, and spectrally using 8 bins per energy decade. The analysis, performed with `fermipy` [196], made use of Pass 8 IRFs [197].

To build the source model, we selected all sources from the Fourth *Fermi* General Catalog (4FGL; [198]) and second *Fermi*-LAT Catalog of High Energy Sources (2FHL; [199]) within 20° from the RoI center. In the model, we also included recent diffuse γ-ray emission templates, both Galactic (`gll_iem_v07.fits`) and extra-Galactic (`iso_P8R3_SOURCE_V2_v1.txt`). During the maximum likelihood fit, the spectral index and normalization of all sources within 3° from the RoI center and having a TS value higher than 25 were left free to vary. Additionally, the spectral normalization of all sources with TS > 30 within the whole $10^\circ \times 10^\circ$ was also adjusted. The Galactic diffuse emission model was left free to vary, while the extra-Galactic diffuse model was considered fixed to the default one. After the maximum likelihood fit, we produced a TS map to investigate the presence of statistically significant excesses. For each spatial bin, the algorithm compared the maximum log-likelihood obtained by fitting the model, with the addition of a point source ($\Gamma = 2$ frozen, amplitude free) at that position, with that of the starting model alone (null hypothesis). We verified that the TS map did not significantly depend on the spectral index or spatial morphology

[8] Similarly to the Fermi high-energy catalogs [195], we excluded events with reconstructed energy below 10 GeV, because at those energies the diffuse γ-ray background is much stronger and would have complicated the analysis.

chosen for the test source. The TS map displayed in figure 6.12 (right panel) shows that, within the source region, there is no evidence for a significant excess, but some low-significance fluctuations are present. For comparison, the left panel of figure 6.12 shows a TS map computed before removing the contribution from point sources.

We then included an additional model component defined by a power law spectrum and a Gaussian morphology identical to the spatial model of HESS J1702-420B. Its 1σ contour is indicated by the red ellipse in Figure 6.12. We left free to vary the spectral normalization and index of this component, performed a maximum likelihood fit and compared the resulting model likelihood with the null hypothesis (no source) using the likelihood ratio test. We found only marginal significance ($\approx 4\sigma$) for a positive excess corresponding to the chosen Gaussian template, a result that was confirmed also assuming different morphologies[9]. The best-fit value for the spectral index of the additional extended component is ≈ 1.6, which means that (unless the spectral measurement is biased by poor statistics) the difference in spectral index between the GeV and TeV portions of the HESS J1702-420B spectrum is $\Delta\Gamma \approx 1$. This suggests that the underlying particle population likely has spectral break around TeV energies (see section 7.1.2 for further details). In the absence of a clear detection, we estimated the 99% confidence-level upper limit for the HE emission, associated with the HESS J1702-420B template shape, at the level of

$$\left(E^2 \frac{dN}{dE}\right)_{E=E_{\rm ref}} \leq 7.6 \times 10^{-9}\,{\rm GeV cm^{-2} s^{-1}}\,, \tag{6.4}$$

where $E_{\rm ref} \sim 95\,{\rm GeV}$ is the geometric mean of the *Fermi*-LAT energy range. In the future, with more *Fermi*-LAT exposure time, it is possible that HESS J1702-420 will be clearly detected at GeV energies, which will greatly help to constrain the physical scenarios underlying the source emission.

[9] In particular we tested the cases of a symmetric disk or Gaussian template with radius $0.2^{\rm o}$, corresponding to the HGPS extension of HESS J1702-420, with fixed center position but free radius.

Chapter 7

Discussion of the analysis results

7.1 Introduction

The fact that HESS J1702-420 lies within the Galactic plane, together with its considerable flux and significant spatial extension, make it almost certainly a Galactic source. But why is it undetected at lower energies, and what is the origin of its TeV γ-ray emission? In particular, is it powered by hadronic or leptonic processes? The latter question is particulary relevant in the context of the PeVatrons quest, since the Galactic cosmic ray factories are expected to be hadronic.

In this chapter we will try to give possible interpretations based on the available data. To do so, we repeated the 3D analysis of H.E.S.S. data presented in chapter 4 replacing the simple γ-ray spectral models of HESS J1702-420A and HESS J1702-420B with physically-motivated non thermal radiative models from Naima[1] [165]. Owing to the `NaimaSpectralModel` class implemented in Gammapy (see section 3.4.1), we could forward-fold the Naima radiative models directly on the H.E.S.S. 3D data. This way we derived the spectral shape of the parent cosmic ray population, exploring both hadronic and leptonic emission scenarios. We chose to adopt the simplest possible radiative models, based on minimal physical assumptions, leaving more complicated modeling scenarios to future studies. In particular, because of the unclear level of association between HESS J1702-420A and HESS J1702-420B, we decided to model them independently, trying to limit the study to one-zone particle models.

We notice that (as mentioned in section 3.4.1), the effects of energy-dependent electron cooling and escape are not taken into account by Naima. This means that what we measured with the Naima inverse-Compton models are the present-day electron distributions, which are a result of the entire acceleration and cooling history of each source. In the future, a more elaborate time and energy-dependent modeling of HESS J1702-420, using ad hoc softwares such as GAMERA[2] will possibly provide more precise results than our minimal modeling approach.

During the fit, a fiducial distance from Earth of $d = 3.5\,\mathrm{kpc}$ (for both source components) was adopted. This particular choice was motivated by the similarity between the molecular cloud number 4 and the TeV emission described in the previous chapter (section 6.2). This association is admittedly speculative, but we note that it does not influence in any way the modeling results on the spectral shape, since the source distance is completely degenerate with its intrinsic luminosity. Therefore, even if the

[1] https://naima.readthedocs.io/en/latest/
[2] http://libgamera.github.io/GAMERA/docs/documentation.html

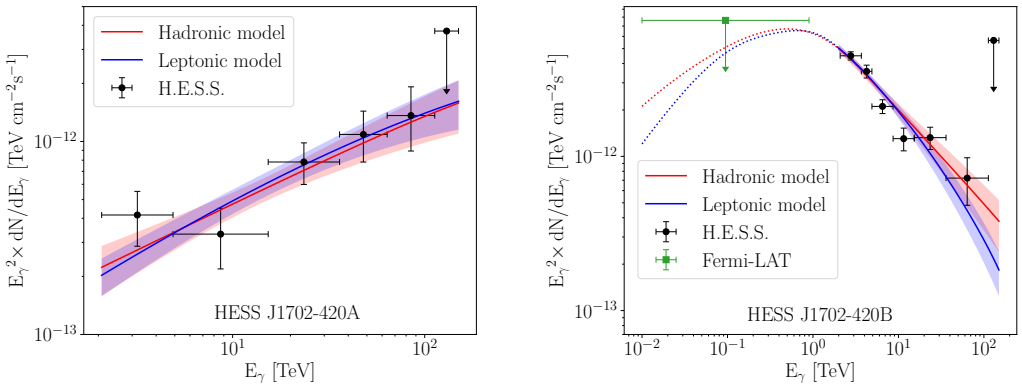

FIGURE 7.1: Models of γ-ray emission based on hadronic (red) and leptonic (blue) one-zone scenarios, for HESS J1702-420A (left panel) and HESS J1702-420B (right panel). The best-fit spectra, under the assumption of simple power law distribution of the underlying particle populations, are shown as solid lines, while the shaded areas and dotted lines represent the 1σ statistical error envelope and extrapolations outside the fit range, respectively. The H.E.S.S. and Fermi-LAT flux points are also shown, for reference purpose. Fit results were obtained with a 3D fit of H.E.S.S. data.

cloud number 4 didn't have anything to do with either of the TeV source components, its (fixed) distance value would not impact the fit conclusions[3].

For the hadronic emission models, based on the analytic parametrization of p-p interaction and subsequent π^0 decay developed in [23] (see section 1.3.1), we assumed a fixed target density $n_{\rm H} = 100\,{\rm cm}^{-3}$. Similarly to the source distance, this parameter is degenerate with the source brightness. In the leptonic scenario, based on the analytic approximation presented in [200], the VHE γ-ray emission was attributed to inverse-Compton up-scattering by electrons of the cosmic microwave background (CMB) and infrared (IR) low-energy photon fields (see section 1.3.2). The uniform CMB field was described as a black-body radiation with energy density of $\epsilon_{\rm CMB} = 0.261\,{\rm eV\,cm}^{-3}$ and temperature of $T_{\rm CMB} = 2.73\,{\rm K}$. The starlight emission in the near IR ($\epsilon_{\rm NIR} = 1\,{\rm eV\,cm}^{-3}$ and $T_{\rm NIR} = 3000\,{\rm K}$) and dust re-emission in the far IR ($\epsilon_{\rm FIR} = 0.5\,{\rm eV\,cm}^{-3}$ and $T_{\rm FIR} = 30\,{\rm K}$) were obtained using the 3D interstellar radiation field (ISRF) model from [26], at the coordinates of HESS J1702-420 and the assumed 3.5 kpc distance. We verified that the level of fluctuations of the ISRF along the line of sight did not significantly impact the modeling conclusions. The results are discussed in Sections 7.1.1 and 7.1.2.

7.1.1 HESS J1702-420A

HESS J1702-420A has one of the hardest γ-ray spectra ever detected in a VHE γ-ray source (compare for example with the figure (14) from [38]). This means that the spectral indices of the underlying particle distributions, responsible for the γ-ray flux via hadronic or leptonic processes, have to be extremely hard themselves. Using Naima, we found that a pure (one-zone) power law distribution of protons (electrons) with slope $\Gamma_p = 1.58 \pm 0.14_{\rm stat}$ ($\Gamma_e = 1.61 \pm 0.15_{\rm stat}$) is well suited to produce the γ-ray

[3] This can be seen for example in equation 7.4, where it is clear how the modeling results can be rescaled a posteriori assuming a different distance value.

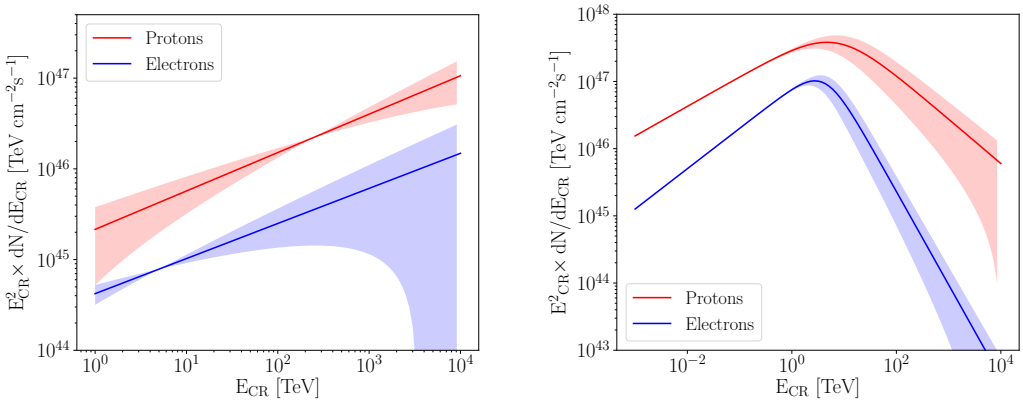

FIGURE 7.2: Cosmic particle distributions responsible for the γ-ray emission of HESS J1702-420A (left) and HESS J1702-420B (right), under the assumption of hadronic (red) and leptonic (blue) one-zone scenarios. The best-fit spectra, under the assumption of simple power law proton and electron distribution of the underlying particle populations, are shown as solid lines, while the shaded areas and dotted lines represent the 1σ statistical error envelope from the fit.

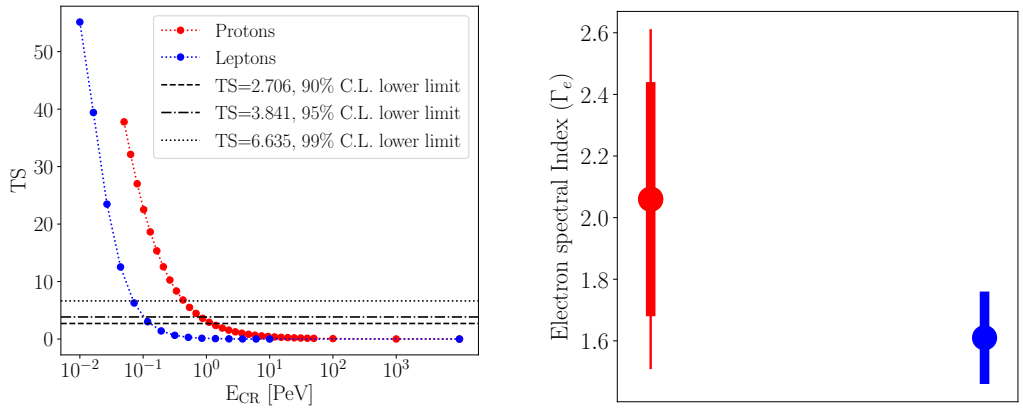

FIGURE 7.3: Left: Likelihood profiles for the proton (red) and electron (blue) energy cutoffs for HESS J1702-420A, together with the horizontal levels (black lines) corresponding to the 90, 95 and 99% confidence level lower limits. More details are provided in the text. Right: Comparison between the electron spectral index powering HESS J1702-420A, obtained from the Naima model fit (blue) and the theoretical expectation (equation 1.29, red). The thick and thin bars indicate the statistical and $\sqrt{\text{statistical}^2 + \text{systematic}^2}$ uncertainties, respectively.

emission of HESS J1702-420A, via hadronic (leptonic) radiative processes. The two γ-ray spectra, with their 1σ butterfly envelopes, are shown in figure 7.1 (left panel), where the H.E.S.S. spectral points (see Table 4.3) are shown for reference purpose only (they were not used for the fit, which was instead performed with the 3D technique). Figure 7.2 instead shows directly the electron and proton distributions responsible for the γ-ray emission from HESS J1702-420A.

Based on the currently available H.E.S.S. data, any attempt of fitting the cutoff energy of the particle spectra as an additional parameter led either to a non-covergence of the fit or to an unphysically high cutoff energy value. This means that a particle cutoff could not be detected, given the available data in the H.E.S.S. energy range. We therefore computed lower limits on the particle cutoff energy, using the following procedure:

i we first defined a logarithmically-spaced array of trial particle cutoff energies $\{E_1^{\rm c}, \ldots, E_N^{\rm c}\}$, ranging from a sufficiently low value (100 TeV for protons and 10 TeV for leptons) to such a high value ($\gtrsim 10^3$ PeV) that the exponential cut-off model likelihood becomes identical to the one of the simple power law model;

ii for each fixed cutoff energy $E_i^{\rm c}$, we adjusted a power-law with exponential cutoff to the H.E.S.S. data, in a full 3D fit. The spectral normalization and index of the particle distribution powering HESS J1702-420A, together with all free nuisance parameters of the source and background models, were left free to vary at each step. For each trial cutoff energy, we stored the (*Cash*) fit statistic value, $\mathcal{C}^{\rm min}_{(E_i^{\rm c})}$;

iii then we computed the profile of

$$\mathrm{TS}(E_i^{\rm c}) = \mathcal{C}^{\rm min}_{(\rm PL)} - \mathcal{C}^{\rm min}_{(E_i^{\rm c})} \,, \tag{7.1}$$

where $\mathcal{C}^{\rm min}_{(\rm PL)}$ refers to the null power law (or equivalently $E^{\rm c}\to\infty$) hypothesis. The resulting array of $\mathrm{TS}(E_i^{\rm c})$ can be treated as a *likelihood profile*, marginalized over the model's nuisance parameters [201]. The profiles are shown in figure 7.3 (left panel);

iv since the exponential cutoff power-law is an extension of the power-law model, with 1 additional degree of freedom, according to Wilk's theorem (see section 3.3.1) the TS in equation 7.1 is distributed ad a χ^2_1. Therefore, following [201], we computed the 90%, 95% and 99% confidence level lower limits on the particle cutoff energy by finding the values where the likelihood profile increases from 0 (which in our case is at infinity) by the amounts $\mathrm{TS}_{(90\%)} = 2.706$, $\mathrm{TS}_{(95\%)} = 3.841$ and $\mathrm{TS}_{(99\%)} = 6.635$ respectively. These values were obtained by computing the right-tail inverse CDF of a χ^2_1 distribution corresponding to the p-values 10%, 5% and 1% respectively. Since the right edge of the confidence intervals estimated this way is at infinity (meaning that the cutoff is not detected), this procedure naturally yields lower limits. More elaborate and statistically accurate approaches (based for example on [202]) may be considered for future studies.

Additionally, to estimate the lower limits, we had to tackle the issue of nuisance parameters exiting from their physically meaningful value range. In particular, we observed that when testing very low trial cutoff energies the fitted particle spectral index of HESS J1702-420A floated toward nonphysical regions, such as very small ($\Gamma_{e/p} \lesssim 1$) or even negative values. This is mainly due to the reduced lever arm for this spectral modeling, and is a natural consequence of the fact that model "tries" to compensate for a low cutoff energy with an unrealistically hard particle spectrum.

To prevent this, we manually modified the (*Cash*) fit statistic value as

$$\mathcal{C} \rightarrow \mathcal{C} + (-2 \ln \mathcal{G}) \,, \tag{7.2}$$

where $\mathcal{G}$ is a prior probability distribution with Gaussian shape, for the particle spectral index of HESS J1702-420A. In the case of the hadronic model, we assumed as a prior a Gaussian distribution centered at $\Gamma_p = 2$ and with $\sigma = 0.5$, based on standard diffusive shock acceleration theory[4]. We estimated the impact of this prior choice by varying the Gaussian central values to $\Gamma_p = 1.7$ and $\Gamma_p = 2.3$. We found that for a prior centered at $\Gamma_p = 2$ (1.7, 2.3) the 95% confidence-level lower limit on the proton cutoff energy is 0.82 (0.55, 1.16) PeV. The fact that, independenly of the chosen prior, the cutoff energy lower limit is found at $E_p > 0.5\,\mathrm{PeV}$ means that in a hadronic scenario the source likely harbors PeV cosmic rays. In the leptonic case, we tested three different Gaussian priors, all having width $\sigma = 0.5$. Based on [69] and [203], we chose a prior centered at $\Gamma_e = 1.5$ to probe shock-driven magnetic reconnection in conditions of moderate wind magnetization, $\Gamma_e = 2.5$ to account for Fermi-like acceleration at the termination shock in conditions of low upstream magnetization, and finally $\Gamma_e = 2.0$ as an intermediate scenario. Our results showed that assuming $\Gamma_e = 2.0$ (1.5, 2.5) the 95% confidence-level lower limit on the electron cutoff energy is 106 (64, 152) TeV.

The energy contents in protons and electrons, necessary to sustain the γ-ray emission of HESS J1702-420A, were computed integrating the particle spectra above 1 TeV[5]:

$$W_{p/e}(E_{p/e} > 1\,\mathrm{TeV}) = \int_{1\,\mathrm{TeV}}^{\infty} E_{p/e} \frac{dN}{dE_{p/e}} \, dE_{p/e} \,. \tag{7.3}$$

Given the best-fit proton and electron distributions found for HESS J1702-420A, with power law indices $\Gamma_{p/e} \approx 1.6$, equation 7.3 would diverge unless the presence of a high energy cutoff is assumed[6]. We therefore adopted the 95% confidence level lower limits on the cutoff energies, thus obtaining a finite integration which corresponds to a lower limit on the integrated particle energetics. We verified that the results are not strongly influenced by the choice of spectral index prior. They are:

$$W_p(E_p > 1\,\mathrm{TeV}) \gtrsim 1.8 \times 10^{47} \left(\frac{d}{3.5\,\mathrm{kpc}} \right)^2 \left(\frac{n_\mathrm{H}}{100\,\mathrm{cm}^{-3}} \right)^{-1} \mathrm{erg} \tag{7.4}$$

$$W_e(E_e > 1\,\mathrm{TeV}) \gtrsim 8.1 \times 10^{45} \left(\frac{d}{3.5\,\mathrm{kpc}} \right)^2 \mathrm{erg} \,. \tag{7.5}$$

Leptonic scenarios

In a leptonic scenario, HESS J1702-420A would be powered by an electron population with unusually hard spectral index, $\Gamma_e = 1.61 \pm 0.15_\mathrm{stat}$ (obtained from the

[4] We note that the prior choice has to be based on theoretical expectations, and cannot be based on the spectral index obtained from the γ-ray power-law fit. Indeed, the latter would have assumed a different value if it was obtained imposing a prior. For this reason, to obtain the likelihood profile for each prior choice, we also repeated the simple power-law fit adding the same prior on the spectral index of HESS J1702-420A.

[5] The particle distribution $dN/dE_{p/e}$ in equation 7.3 has units of [1/Energy].

[6] To be precise, equation 7.3 converges for $\Gamma_{p/e} > 2$, while it has a logarithmic (power-law) divergence for $\Gamma_{p/e} = 2$ ($\Gamma_{p/e} < 2$).

3D analysis). The expected electron index from inverse Compton in the Thomson regime, based on the measured γ-ray index $\Gamma = 1.53 \pm 0.19_{\rm stat} \pm 0.20_{\rm sys}$ and the relation $\Gamma = (\Gamma_e + 1)/2$ (see equation 1.29), would be $\Gamma_e = 2.06 \pm 0.38_{\rm stat} \pm 0.40_{\rm sys}$, steeper than the measured one. This is likely explained by the large statistical and systematic uncertainties which make the measured and expected Γ_e values compatible within the errors (see the right panel of figure 7.3). Alternatively, it could mean that we are measuring an inverse Compton spectrum from electrons that are not in the Thomson regime, for which the relation 1.29 does not hold.

We estimated the magnetic field value in the vicinity of HESS J1702-420A, by supposing that the TeV source is a PWN associated with the *Suzaku* src B (see section 6.3). As shown in figure 6.10, we made use of our simple static one-zone leptonic model to match the synchrotron emission of HESS J1702-420A with the measured X-ray flux of src B (solid blue curve). Even doubling the src B flux, likely underestimated due to systematics in the *Suzaku* measurements (see section 6.3), the magnetic field value associated with the putative PWN turns out to be unrealistically low: $B \lesssim 0.3\,\mu G$. This poses the question of how a region with such a low magnetic pressure could be in equilibrium with the surrounding ISM. This problem renders an association between HESS J1702-420A and *Suzaku* src B (and with it a simple pulsar-PWN model) premature, but it also cannot be ruled out due to the uncertainties on the X-ray measurement and the fact that we tested only a very minimal one-zone leptonic model. This matter will be further addressed in the future, by means of more precise X-ray measurements with e.g. XMM-Newton or eROSITA.

We note that an alternative interpretation is possible, in which the observed γ-ray emission is due to inverse Compton from electrons that are accelerated by magnetic reconnection in the current sheets of a pulsar striped wind. There the magnetic field value is expected to be faint, and hard electron spectral indices ($\Gamma_e \approx 1.2 - 1.5$) can arise [69, 203, 204]. If true, this would be the first time that a TeV measurement probes the reconnection spectrum of a pulsar striped wind, thanks to the 3D analysis technique which allowed us to disentangle the reconnection (HESS J1702-420A) and Fermi-like (HESS J1702-420B) emission zones of a pulsar-PWN complex. However, the lack of a clear multi-wavelength detection of the compact object providing the necessary electron population challenges for the moment this hypothesis.

In conclusion, we could not find consistent evidence in favor of a simple one-zone leptonic scenario or for a reconnection-based hypothesis for HESS J1702-420A. However we cannot exclude that in the future more elaborate leptonic models (possibly based on new X-ray measurements) may successfully explain the γ-ray emission from HESS J1702-420A.

Hadronic scenarios

In a hadronic scenario, VHE γ-ray emission is attributed to the interaction of energetic protons with target material within a source or a nearby molecular cloud. In this case, the 100 TeV γ-ray emission from HESS J1702-420A, together with its proton cutoff energy lower limit at $0.55 - 1.16$ PeV, would make it a compelling candidate site for the presence of PeV cosmic ray protons. Therefore HESS J1702-420A becomes one of the most interesting PeVatron candidates detected in H.E.S.S. data, also based on the modest value of the total energy in protons that is necessary to power its γ-ray emission (see equation 7.4) and the excellent agreement of a simple proton power law spectrum with the data.

However, we notice that a proton spectrum with a slope of $\Gamma_p = 1.58 \pm 0.14_{\rm stat}$ (similar to the γ-ray slope, as expected) over two energy decades is hard to achieve in a standard DSA framework, in which the expected proton slope is (slightly steeper than) 2 [205]. This fact may suggest that HESS J1702-420A, instead of being a PeVatron, is in fact a gas cloud that, being illuminated by cosmic rays transported from elsewhere, acts as a passive γ-ray emitter. In that case, the hard measured proton spectrum could result from the energy-dependent particle escape from a nearby proton PeVatron, from which only the highest-energy particles have reached the target gas [206]. Alternatively, the γ-ray emission from HESS J1702-420A might be interpreted as the hard high energy end of a concave spectrum arising from nonlinear DSA effects [17], originate from the interaction of SNR shock waves with a young stellar cluster wind [80] or cosmic ray interactions with turbulent plasma near OB Associations [207].

The absence of a clear spatial correlation between the ISM and the TeV emission (see section 6.2) prevents a confirmation of the hadronic emission scenario, unless an extremely powerful hidden PeVatron is present. In the latter case, since the hadronic γ-ray flux is proportional not only to the amount of gas but also of cosmic rays in the emission region (see equation 1.16), even a modest gas density would suffice to produce the measured γ-ray emission of HESS J1702-420A, explaining the observed nonlinearity between the ISM and TeV maps. This hypothesis is however challenged by the absence of any MW signature of the presence of such powerful hidden PeVatron.

7.1.2 HESS J1702-420B

The simplest possible baseline proton and electron spectra, used to model the γ-ray emission of HESS J1702-420B, are broken power laws of the form

$$\frac{dN}{dE} \propto \begin{cases} (E/E_0)^{-\alpha_1} & ,\text{if } E < \tilde{E} \\ (\tilde{E}/E_0)^{\alpha_2-\alpha_1}(E/E_0)^{-\alpha_2} & ,\text{if } E > \tilde{E} \end{cases} \tag{7.6}$$

where $\tilde{E}$ and E_0 are the energy of the spectral break and the reference energy, respectively. The introduction of a spectral break was necessary, because a simple power law extrapolation from the VHE to the HE γ-ray range would have led to unrealistic energy budgets and an overshoot of the *Fermi*-LAT upper limit (section 6.4). The first power law index, α_1, was adjusted manually with respect to the *Fermi*-LAT upper limit. Its value is therefore not to be interpreted as a fit result, but rather as a working assumption. The presence of a spectral break in the electron spectrum might be either due to the presence of two different particle population, or to the energy-dependent escape of particles from a single population. In the hadronic (leptonic) scenario, the best-fit proton (electron) spectrum corresponds to a broken power-law with slopes $\alpha_1 = 1.6$ (1.4) and $\alpha_2 = 2.66 \pm 0.11_{\rm stat}$ ($3.39 \pm 0.11_{\rm stat}$), and with break energy of $\tilde{E} = (6.77 \pm 3.64_{\rm stat})$ TeV ($(4.19 \pm 1.25_{\rm stat})$ TeV). The best-fit radiative models and particle spectra are shown in figures 7.1 and 7.2, respectively. Even if the VHE spectrum of HESS J1702-420B is rather steep, limiting the interest of an exponential cutoff measurement, we applied the same procedure described in the HESS J1702-420A section (this time without using priors) to derive the 95% confidence-level lower limit on the proton (electron) cutoff energy, which turn out to be 550 (140) TeV. The values of proton and electron energetics, necessary to power the γ-ray emission of HESS J1702-420B, were computed integrating the broken power

law particle spectra above 1 GeV. They are:

$$W_p(E_p > 1\,\mathrm{GeV}) \approx 2.8 \times 10^{48} \left(\frac{d}{3.5\,\mathrm{kpc}}\right)^2 \left(\frac{n_\mathrm{H}}{100\,\mathrm{cm}^{-3}}\right)^{-1} \mathrm{erg} \tag{7.7}$$

$$W_e(E_e > 1\,\mathrm{GeV}) \approx 4.5 \times 10^{47} \left(\frac{d}{3.5\,\mathrm{kpc}}\right)^2 \mathrm{erg}\,. \tag{7.8}$$

Leptonic scenarios

In a emission leptonic scenario, HESS J1702-420A and HESS J1702-420B could be seen as different zones belonging to the same (likely evolved [73]) PWN complex. However, this interpretation appears problematic for several reasons. First of all, a leptonic scenario for HESS J1702-420A is not obvious, by the arguments presented in section 7.1.1. But perhaps the biggest problem is that the only known nearby pulsar is PSR J1702-4128, that to power the whole TeV source would require an extremely high conversion efficiency (ϵ) of its spin-down luminosity into $1-10$ TeV γ-rays. Using the new H.E.S.S. data, we updated the [183] estimation of $\epsilon \approx 11\%$ to:

$$\epsilon = \frac{L_{1-10\,\mathrm{TeV}}}{\dot{E}} \approx 19\%\,, \tag{7.9}$$

where $L_{1-10\,\mathrm{TeV}}$ was obtained considering both components HESS J1702-420A and HESS J1702-420B, and using the pulsar's distance from Earth $d = 5.2$ kpc [182]. The result of equation 7.9 is well above the efficiency of all other PWNe identified by H.E.S.S. in the same energy range [184].

Another argument against a PWN interpretation is that several PWNe detected by H.E.S.S. are characterized by an energy-dependent morphology with spectral softening away from the pulsar position (e.g., [43, 44]), which seems not to be the case for HESS J1702-420 (see chapter 5). However, we point out that this argument is not very decisive, since we might be biased by insufficient statistics or spatial resolution to detect such spectral and spatial variations, and besides not all TeV-bright PWNe detected by H.E.S.S. have an energy-dependent morphology (see e.g. the case of the Crab nebula [208]).

In conclusion, leptonic scenarios for HESS J1702-420 cannot be definitively ruled out. In particular, as discussed in [183], the PSR J1702-4128 might power only part of the TeV emission from HESS J1702-420B, and in fact we argue that this is likely to be the case. Indeed, by looking at figure 4.17 (upper right panel), it appears that significant (5σ) VHE γ-ray emission is detected by H.E.S.S. around the pulsar's position.

Hadronic scenarios

In a hadronic scenario, HESS J1702-420B might be interpreted as a proton accelerator, whose spectral break around $E_p \approx 7$ TeV is due to energy-dependent cosmic ray escape from the source. As argued in section 7.1.1, the hard γ-ray spectrum of HESS J1702-420A could then be the signature of delayed emission from the highest energy runaway protons, hitting target material in the ISM. In this case, the PeVatron in the region would be HESS J1702-420B, and not HESS J1702-420A. This scenario

is challenged however by the absence of a clear TeV$-n_{\rm H}$ correlation at the location of HESS J1702-420A (see section 6.2).

It remains also possible that the only known nearby (potential) hadronic accelerator, SNR G344.7-0.1, contributes to at least a small part of the TeV emission from HESS J1702-420B, but an association with HESS J1702-420A (which has been suggested by [180]) appears extremely unlikely, given the large SNR distance ($\gtrsim 8\,$kpc) and the absence of molecular clouds correlating with HESS J1702-420A.

7.1.3 Distance from Earth and environmental parameters

An unequivocal interpretation of HESS J1702-420 remains elusive, mostly due to the uncertain relationship between HESS J1702-420A and HESS J1702-420B and the absence of clear MW associations. Nevertheless, the new H.E.S.S. observations allowed us to constrain the source distance from Earth d and the values of the most relevant environmental parameters in a hadronic or leptonic emission scenario, which are respectively the gas density $n_{\rm H}$ and magnetic field strength B. As a working hypothesis, in this section we assume that the two TeV source components are associated. This means considering that their distance from Earth is roughly the same, and their TeV emissions are connected.

We found the constraints shown in Figure 7.4. The top panel focuses on hadronic scenarios:

- molecular clouds on the line of sight are indicated by red circles, with size proportional to (the logarithm of) the proton energy necessary to power the γ-ray emission of the whole HESS J1702-420 in each case. The energy has been computed using equations 7.4 (whose contribution is negligible) and 7.7, by computing $W_p^{\rm cloud} = W_p(d^{\rm cloud}, n_{\rm H}^{\rm cloud})$ for each cloud. The cloud density and distance estimates have been taken from [181] (see table 7.1 for more details). For all clouds, the nearer kinematic distance was assumed;
- the blue exclusion region in the figure was obtained requiring that the total HESS J1702-420 proton energy above 1 GeV (again from equations 7.4 and 7.7) does not exceed $10^{50}\,$erg, which is the amount of kinetic energy transferred to cosmic rays by a typical SNR event:

$$W_p(d, n_{\rm H}) \leq 10^{50}\,{\rm erg} \tag{7.10}$$

- the gray shaded exclusion areas are obtained by imposing that protons fill the whole HESS J1702-420 before being cooled down by inelastic p-p collisions:

$$\tau_{\rm diff} > \tau_{pp}\,. \tag{7.11}$$

This equation correspond to a relation between $n_{\rm H}$ (via τ_{pp}, equation 1.23) and d (via $\tau_{\rm diff}$). The diffusion time-scale $\tau_{\rm diff}$ was estimated as in [25]:

$$\tau_{\rm diff} \approx \frac{[R_{\rm source}(d)]^2}{6D(E,B)}\,, \tag{7.12}$$

where

$$D(E,B) = \chi D_0 \left(\frac{E}{\rm GeV}\right)^{\delta} \left(\frac{B}{3\,\mu G}\right)^{-\delta} \tag{7.13}$$

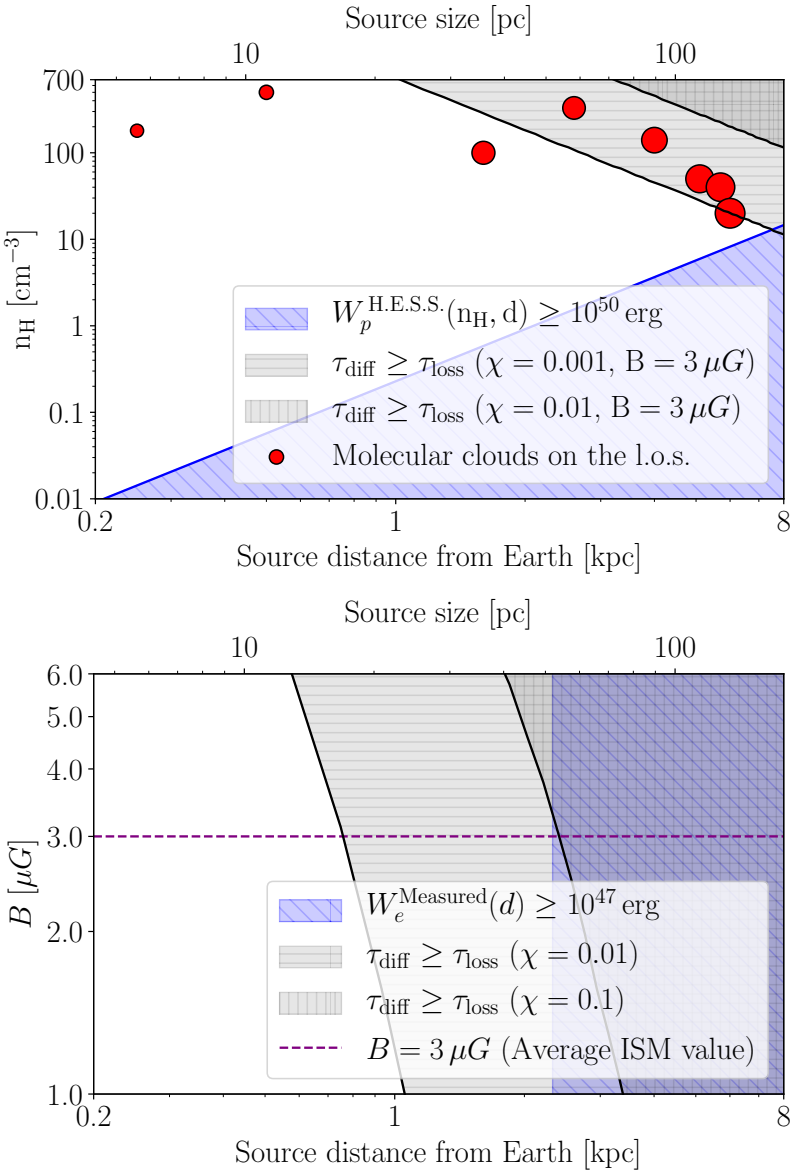

FIGURE 7.4: Possible constraints on the gas density, magnetic field and distance of HESS J1702-420, based on multi-wavelegth observations, under the assumption of simple one-zone hadronic (left panel) or leptonic (right panel) scenarios. More details are given in the main text.

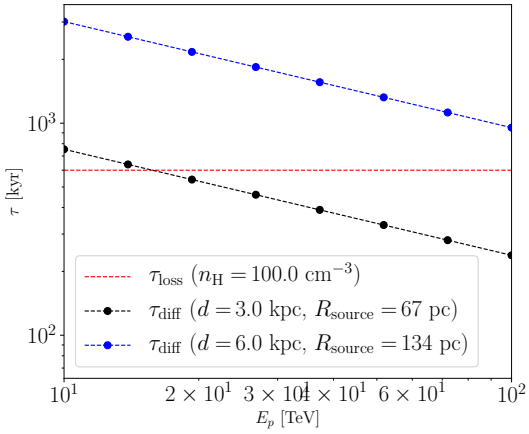

FIGURE 7.5: Comparison of the energy-dependent diffusion and cooling time-scales for protons, under the assumptions that p-p interactions are powering HESS J1702-420. For these example plots we assumed $\chi = 0.001$. More details are given in the main text.

is the diffusion coefficient for protons of energy E propagating in the cloud magnetic field B (we assumed $B = 3\,\mu G$). We adopted the typical Galactic values $D_0 = 3 \times 10^{27}\,\mathrm{cm^2\,s^{-1}}$ and $\delta = 0.5$, but tested several values of the normalization factor χ which accounts for possible suppressions of the diffusion coefficient due to the proton propagation into turbulent and partly ionized media. The source physical size $R_{\rm source}$ in equation 7.12 depends directly on the distance from Earth d and the measured angular size of the source $\theta_{\rm source}$, as $R_{\rm source} = d \times \tan(\theta_{\rm source})$. Here, we assumed $\theta_{\rm source} = 1.28^{\rm o}$, which corresponds to the major 2σ diameter of HESS J1702-420B. For each possible choice of $n_{\rm H}$ and d, the condition 7.11 can be imposed as shown in figure 7.5. In particular, excluded all combinations of $n_{\rm H}$ and d for which protons with energy in the range 10–100 TeV are cooled down before having time to diffuse across the whole (distance-dependent) source size (see e.g. the black line in figure 7.5), testing different values for the normalization factor of the diffusion coefficient χ.

Near distance [kpc]	$\mathbf{n_H}$ $[\times \mathbf{100\,cm^{-3}}]$	$\mathbf{W_p(E > 1\,GeV)}$ **[erg]**
0.25	1.8	$7.9\,10^{45}$
0.5	5	$1.1\,10^{46}$
1.6	1	$5.8\,10^{47}$
2.6	3.3	$4.7\,10^{47}$
4	1.4	$2.6\,10^{48}$
5.1	0.5	$1.2\,10^{49}$
5.7	0.4	$1.9\,10^{49}$
6	0.2	$4.1\,10^{49}$

TABLE 7.1: For each one of the molecular clouds on the line of sight of HESS J1702-420, we report the distance and density from [181], and the proton energetics that would be necessary to power the observed VHE emission of HESS J1702-420B in each case.

From figure 7.4 (top panel) it appears that, under hadronic scenarios and if the source lies in the diluted ISM where $n_{\rm H} \lesssim 1\,\mathrm{cm^{-3}}$, it has to be relatively close ($d \lesssim 2\,$kpc)

unless its proton energy budget exceeds 10^{50} erg. If the normalization of the diffusion coefficient is low ($\chi \lesssim 0.001$), only the three nearest molecular clouds would be apt to harbor the source, whose distance would again be $d \lesssim 2\,\mathrm{kpc}$.

In the bottom panel of figure 7.4, which focuses on leptonic scenarios, we imposed similar conditions on the total electron energy (blue area). There, the the gray exclusion areas correspond to portions of the parameter space in which the electrons with energy $E_e \geq 1\,\mathrm{TeV}$ are cooled down before filling the whole source. From the figure, it is clear that if the normalization of the diffusion coefficient is low ($\chi \lesssim 0.01$), then the source has to be relatively close, less than $\approx 3\,\mathrm{kpc}$ away, for realistic values of B field. These informations will hopefully be useful in the future, to build a coherent MW description of HESS J1702-420.

7.2 Future perspectives

In the future, improved facilities such as CTA-South and SWGO (see chapter 2) will observe the Southern VHE and UHE γ-ray sky. If HESS J1702-420 is of the same type as the new unidentified LHAASO objects [47], then its γ-ray spectrum might extend up to hundreds of TeV. This is in fact an argument in favor of the construction of SWGO, along with the fact that the Southern γ-ray sky is expected to host many more UHE sources than the Northern one, where LHAASO has already detected 12 sources in less than 1 year of operations and with an half-finished array. On the other hand, the improved angular resolution of the CTA-South array will help constraining the source morphology in the VHE range, complementing the SWGO observations and possibly closing the debate on the source nature. Observations in the X-ray band will also be important, to search for a multiwavelength counterpart of the TeV source, estimate the value of the magnetic field in the region and clarify the relationship between HESS J1702-420A and the unidentified *Suzaku* src B. In the context of this thesis, XMM-Newton observations have been proposed, that will potentially lead to a future publication on the subject.

Part III

Toward a high-energy catalog of H.E.S.S. sources: A legacy for CTA

Chapter 8

A high-energy survey of the Galactic plane with H.E.S.S.

8.1 Introduction

The field of VHE γ-ray astronomy is developing rapidly, thanks to the combined contribution of IACTs and WCTs. In the Northern hemisphere, the HAWC experiment has reported the detection of 9 γ-ray sources (in the eHWC catalog [209]) with significant emission above 56 TeV, 3 of which still persist above 100 TeV. Of these sources, 6 are found at $45^{\circ} \leq l \leq 5^{\circ}$, a region that is also visible by Southern instruments such as H.E.S.S., although at high zenith angle. More recently, LHAASO has reported the breaktrough discovery of 12 Galactic γ-ray sources up to several hundred TeV, demonstrating the feasibility and scientific interest of UHE γ-ray astronomy [47]. Of these sources, 6 are located in the Galactic plane at $l \lesssim 60^{\circ}$, and 5 of them correspond to sources from the eHWC catalog. The LHAASO result was obtained with just one year of operations and a half-completed array, strongly suggesting that the Southern γ-ray sky, with the higher density region of the Galactic center, should be even more crowded with powerful UHE γ-ray sources. Below $l \approx 5^{\circ}$, however, the Galactic plane remains mostly unexplored at energies exceeding few tens of TeV, with few exceptions such as the Galactic center region, already detected up to tens of TeV by multiple IACTs [74, 75, 77, 78], and HESS J1702-420 (see the part II of this thesis). In the next decade(s), new observatories such as CTA-South and SWGO will be deployed, likely leading to the discovery of tens of UHE γ-ray sources and bringing us toward the conclusion of a century-old quest for the Galactic cosmic ray factories.

In this context, present-day experiments such as H.E.S.S. have the opportunity to say their final word on the most promising PeVatron candidates in the Southern γ-ray sky. This will become a valuable legacy for future small-FoV experiments such as CTA: a reduced list of targets to be observed with high priority, helping to efficiently allocate the limited amount of time dedicated to the PeVatron key science project. In this scope, we have recently developed an analysis pipeline for a new H.E.S.S. high-Energy Galactic Plane Survey (HEGPS) catalog. This work is based on the HAP-Fr *he* H.E.S.S. analysis configuration (see chapter 2), expressely developed for PeVatron studies, which already led us to evidence of 100 TeV γ-ray emission from HESS J1702-420 (see part II of this thesis). The survey analysis is improved, with respect to the past H.E.S.S. history, by the use of Gammapy (v0.18.2 [210]), whose first prototype was in fact developed in the context of the HGPS catalog [38]. The structure of this study, presented in the same order in the chapter, is the following:

1. first, we performed a full data reduction using events selected with the HAP-Fr *he* configuration (referred to as the main analysis, or MA), for the same spatial region as the HGPS (see section 8.2.1);
2. we then produced pre-trial significance maps for the whole HGPS region above 2, 20 and 50 TeV (see section 8.2.2);
3. we corrected for the trial factors introduced by the survey analysis, and determined a list of detected source seeds ($> 5\sigma$ post trial) and hotspots ($> 2\sigma$ post trial) above 20 TeV (see section 8.2.3);
4. we performed a crosscheck analysis (CA) using again the HAP-Hd *std_zeta* configuration data, as in chapter 5. This is not yet a full analysis crosscheck, but more a minimal set of tests that we made to quickly verify the MA results. In particular, we used a simulation-based approach to understand the differences in the catalogs obtained from the MA and CA (section 8.2.5);
5. finally, we discussed the HEGPS implications by focusing on the single sources, comparing with HAWC and LHAASO and correlating the source positions with the list of known powerful Galactic pulsars (see section 8.3).

The analysis and results contained in this chapter have been presented at private H.E.S.S. Collaboration meetings, but have not been refereed and approved for publication yet. Therefore they should be regarded as preliminary studies, whose conclusions are not expected to substantially change but with details that may be re-tuned in the future. In order to simplify the description of the procedure, most of the crosscheck material has been moved to Appendix A.

8.2 The HEGPS

The objective of this study is to pinpoint the most promising PeVatron candidates in the H.E.S.S. γ-ray sky, by finding the sources of significant emission at $E > 20$ TeV. In the following sections, the MA and CA are presented in parallel, from the data reduction steps up to the discussion of the results.

8.2.1 Data reduction

We performed a full 3D data reduction along the lines of the one presented in sections 4.4.1 and 4.4.2 for the case of HESS J1702-420, with some minor modifications.

We selected all H.E.S.S. observations with pointing direction within the HGPS region, corresponding to $|b| \leq 5^\circ$, $0^\circ \leq l \leq 70^\circ$ and $250^\circ \leq l \leq 360^\circ$. By integrating over the whole H.E.S.S. history, this led us to select 8196 runs in the MA (10309 in the CA). The distribution of observation IDs, which are unique identifier numbering the H.E.S.S. runs, is shown in figure 8.1. The two runlists are roughly consistent, with the larger number of observations in the CA due to different data quality cuts (that are looser in the CA). We then defined the reconstructed and true energy axes, the safe energy threshold and FoV background adjustment method similar to what described in sections 4.4.1 and 4.4.2. However, we used a coarser pixel size of $0.05^\circ \times 0.05^\circ$, due to the much larger analysis region (1800 deg^2, compared to the 16 deg^2 of the HESS J1702-420 analysis) which demands a significant amount of computation power.

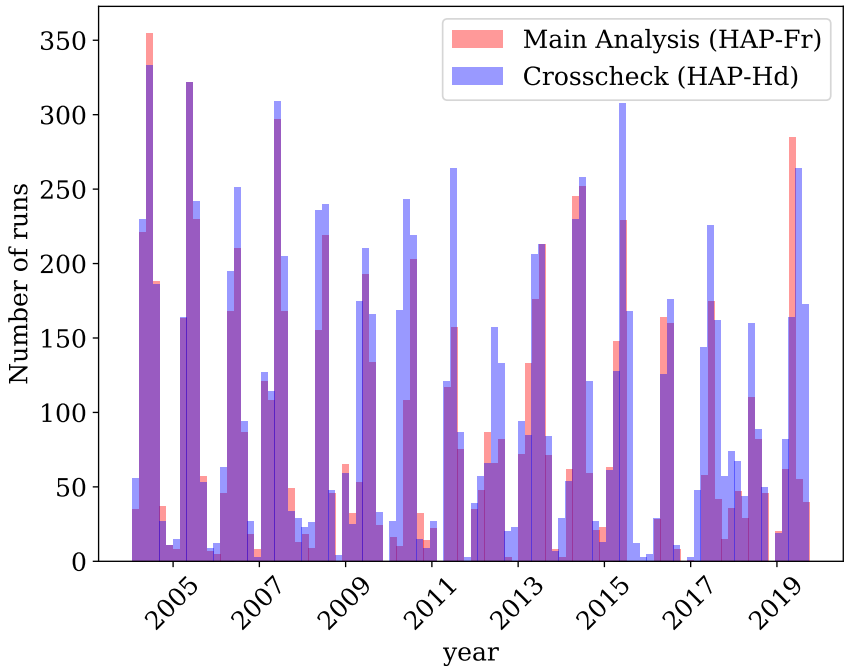

FIGURE 8.1: Number of observations per year, for the MA (red) and CA (blue).

The FoV background modeling was performed above 2 TeV instead of 20 TeV, to achieve an accurate background normalization thanks to the higher number of low-energy counts. As an improvement with respect to the HESS J1702-420 study, we imposed additional cuts on the background modeling quality, to reject runs with poor background estimation due to an insufficient number of OFF counts (i.e. counts outside the exclusion regions) or systematics in the background model. In particular, we accepted only runs for which:

- the background model fit converged successfully;
- the relative error on the background `norm` parameter was at most 25%[1];
- the absolute error on the background `tilt` parameter was less than 0.2[2].

For the FoV background normalization an exclusion mask is needed, which was determined iteratively. We started from a first-guess mask, the one shipped with the HGPS catalog, and iteratively enlarged it by excluding significant emission regions. In particular, we used a histeresis threshold method which excluded all pixels with significance higher than 4σ or higher than 3σ but neighbouring a 4σ pixel[3]. We applied this double-threshold agorithm on the correlated significance maps above 2 TeV. To exclude both small and large-scale emission regions, we conservatively multiplied the masks obtained with a 0.1° and 0.4° correlation radii. Figure 8.3 shows a comparison

[1] This condition supposes that the fitted `norm` value is non-zero. We relaxed this requirement to 40% for the CA, which has less exposure above 2 TeV leading to less OFF counts and bigger uncertainties on the background normalization.

[2] Relaxed to 0.4 in the CA, which provides lower exposure at $E > 2$ TeV and is therefore affected by larger statistical uncertainties than the MA.

[3] This is the same procedure described in section 4.5. Here we chose slightly higher significance cuts, because in this case we were dealing with *Cash* statistics which is always a bit overestimated compared to *wstat*, due to the assumption of a perfectly known background model without fluctuations.

of the HGPS exclusion mask (in black) with the final HEGPS one (orange), for the MA (*top* panel) and CA (*bottom* panel). For both analyses, three iterations sufficed to obtain a stable exclusion mask with correctly distributed significance outside of the exclusion regions (they are shown in figures A.1 and A.2). After each iteration, the enlargement of the exclusion regions resulted in fewer counts available for the background modeling, which in turn implied larger errors on the fitted background parameters leading to the rejection of more runs. At the end of the process, the final MA (CA) analysis runlist contained 7047 (6940) runs. Figure 8.2, shows the final distribution of the best-fit values and errors of the `norm` and `tilt` parameters (defined in equation 3.29), in the MA (red) and CA (blue), at the end of the iterations. The `norm` distributions (upper left panel) are similar, centered on 1 as expected but with a larger spread than the one estimated for example by [153], most likely due to the higher energy threshold used in our analysis. The upper left and both lower panels show instead significant differences between the MA and CA, which can be seen as a signature of the presence of different background model systematics. In particular, the `tilt` distribution in the MA is not centered at zero, which is in line with what already found for the HESS J1702-420 analysis (see figure 4.11), and the error distributions are much larger in the CA than the MA, which is a direct consequence of the lower exposure above 2 TeV for the CA.

Figures 8.4, A.3 and 8.5 show the spatial distribution of the exposure[4] for the MA and CA, integrated above 20 TeV and considering only the runs belonging to the final analysis runlists. The exposure provided by the MA configuration is systematically higher than for the CA, due to the high-energy optimization (> 1 TeV) of the MA cuts. The only region where the CA exposure exceeds the MA one is around $l \approx 305°$, where a group of runs with background model issues were manually removed from the MA runlist.

After the data reduction, the complete H.E.S.S. view of the Galactic plane was stored in a `Dataset` object measuring only ≈ 350 MB. We then used Gammapy to compile a catalog of high-energy sources, as explained in the following section.

[4] Defined as the product between the effective area of the array in the used analysis chain and the observation livetime.

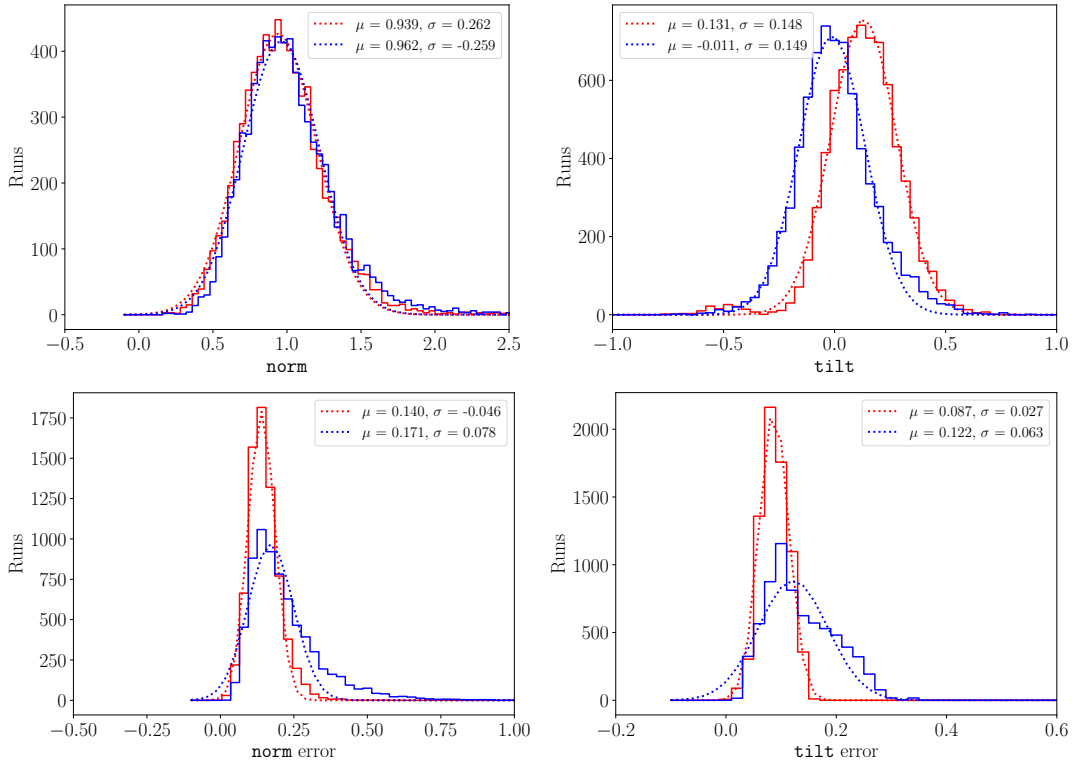

FIGURE 8.2: Distribution of best-fit values and errors for the background model *norm* and *tilt* parameters, for the MA (red) and CA (blue).

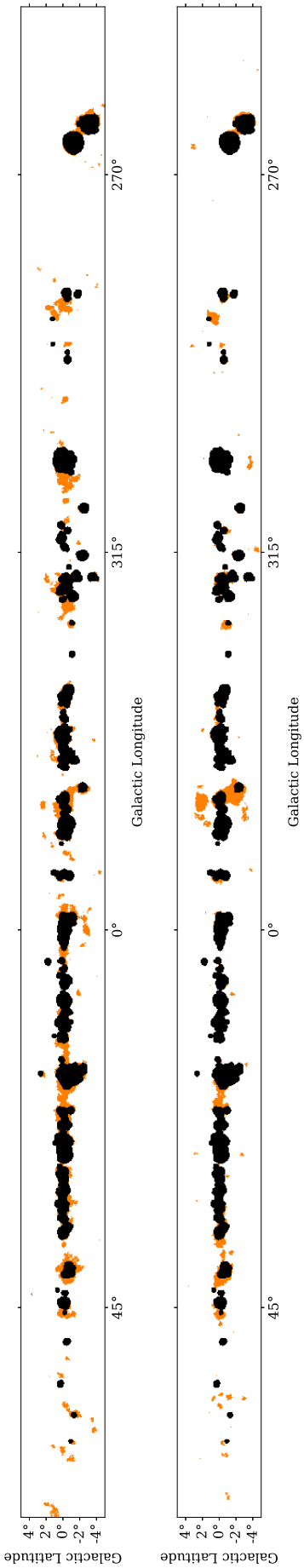

FIGURE 8.3: Exclusion masks for the HEGPS, obtained from the iterative procedure described in the main text. The top (bottom) panel refers to the MA (CA), the black exclusion regions correspond to the first-guess mask (from the HGPS) and the orange regions indicate the extensions of the original exclusion mask in the HEGPS.

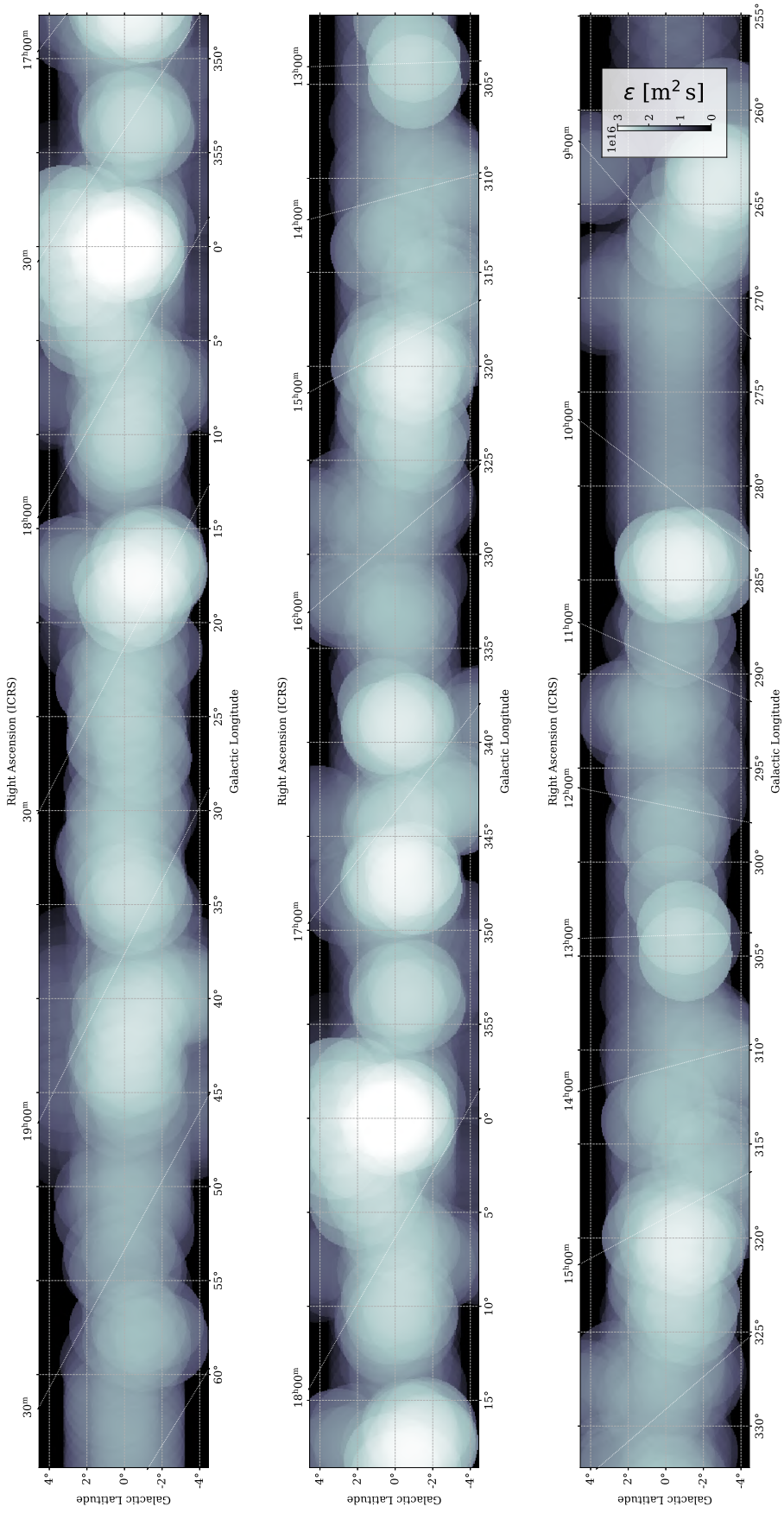

FIGURE 8.4: Exposure map for the MA, converted to reconstructed energy assuming a power-law spectral index of 2 and integrated above $E_{\mathrm{reco}} = 20\,\mathrm{TeV}$. The colorbar is in units of $\mathrm{m}^2\,\mathrm{s}$ per 0.3°-radius smoothing area, and is shown in log scale to enhance features.

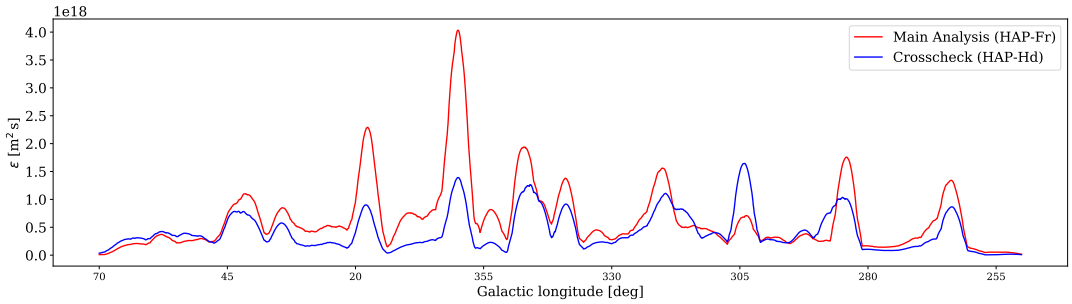

FIGURE 8.5: One-dimensional exposure profiles, obtained integrating the figures 8.4 (MA, red) and A.3 (CA, blue) over the Galactic latitude axis ($|b| \leq 5^{o}$).

8.2.2 The H.E.S.S. multi-TeV view of the Galactic plane

We computed[5] correlated significance maps of the whole Galactic plane region, above 2, 20 and 50 TeV. Due to the use of the 3D background model, assumed to be perfectly known and without Poisson fluctuations, the significance computation corresponds to the *Cash* definition (equation 3.24). In addition to the $E > 20\,\text{TeV}$ significance map, used to compile the HEGPS catalog, we also produced lower energy maps at $E > 2\,\text{TeV}$ to check the consistency of this study with the HGPS survey and higher energy maps, $E > 50\,\text{TeV}$, to identify potential PeVatrons. To produce the significance maps, we used a top-hat correlation kernel with radius increasing with energy, thus compensating for the decrease in the available photon statistics. In particular, we used a 0.1^{o} radius at 2 TeV, a 0.3^{o} at 20 TeV and 0.5^{o} at 50 TeV. The resulting maps, for the MA, are shown in figures 8.6– 8.8, while the corresponding CA images are A.4– A.6.

We note the overall consistency between the CA and MA plots. In all panels, and especially at the highest energies ($> 50\,\text{TeV}$), the MA provides a slightly enhanced significance with respect to the CA, as expected due to its higher exposure. The maps corresponding to the 2 TeV threshold can be directly compared with the HGPS [38], which share most of the features (although they were obtained using a higher energy threshold). Above 20 TeV there is instead only a lower number of sources which are still visible in the MA and CA, among which the brightest (by eye) include HESS J1825-137, HESS J0835-455 (Vela X) and HESS J1702-420. Their emission still persists in the highest energy range, $> 50\,\text{TeV}$, at least in the MA. The CA does not show evidence of source emission above 50 TeV, apart from few isolated photons corresponding to HESS J1702-420; this is most likely due to the smaller effective area of the CA at the highest energies, and can be seen as an argument in favor of the use of dedicated optimization schemes for high-energy event selection in the case of PeVatron studies. Since the significance maps are biased by the different exposure level, the best way to crosscheck the data reduction results is to compare γ-ray flux maps. They can be found in Appendix A, for the same energy ranges of the significance maps. An inspection of the flux maps confirms the consistency of the MA and CA.

[5] Using the `ExcessMapEstimator` implemented in Gammapy.

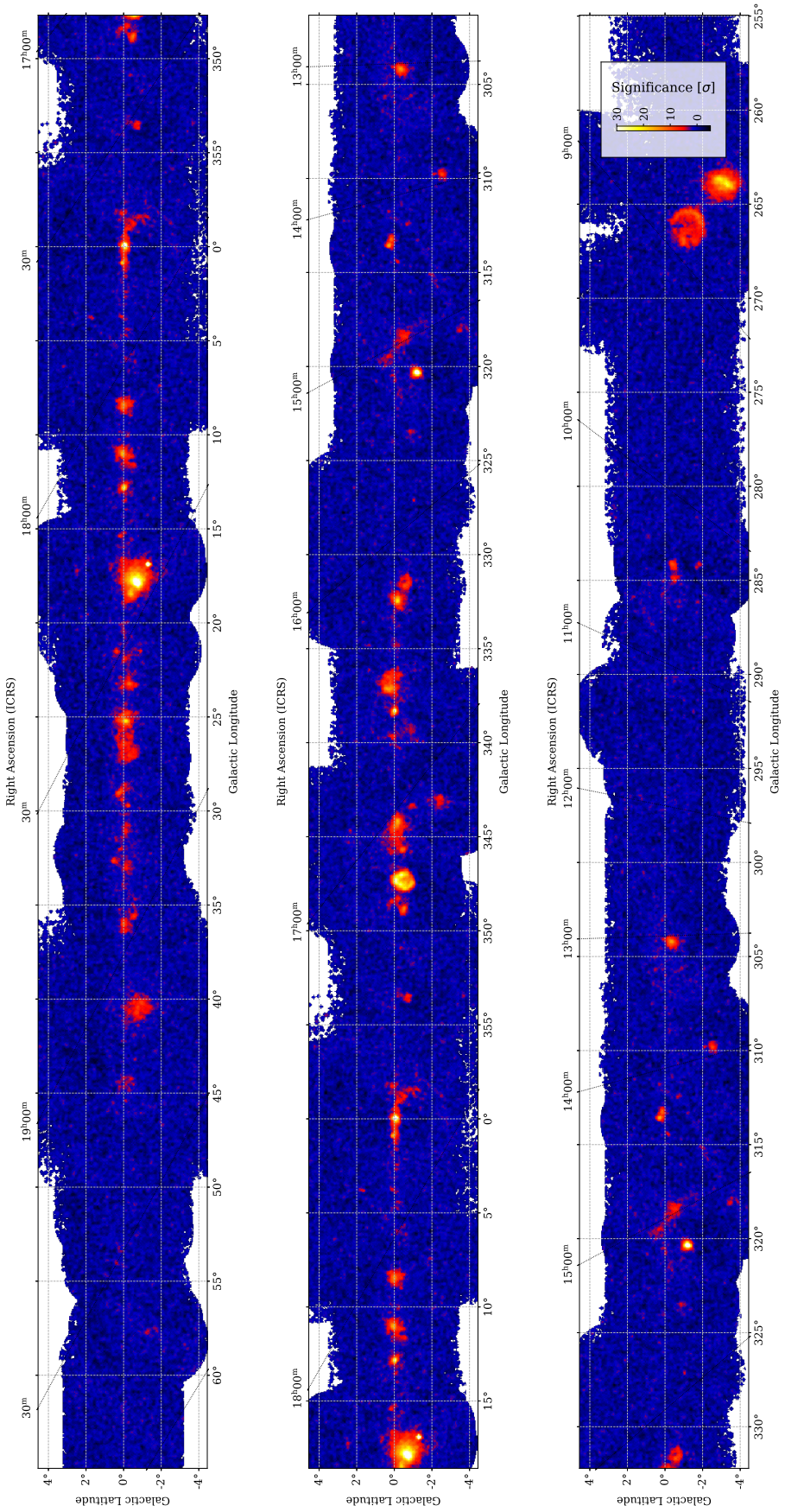

FIGURE 8.6: Map of *Cash* pre-trial significance for the MA, for the energy threshold of 2 TeV and a 0.1° correlation radius.

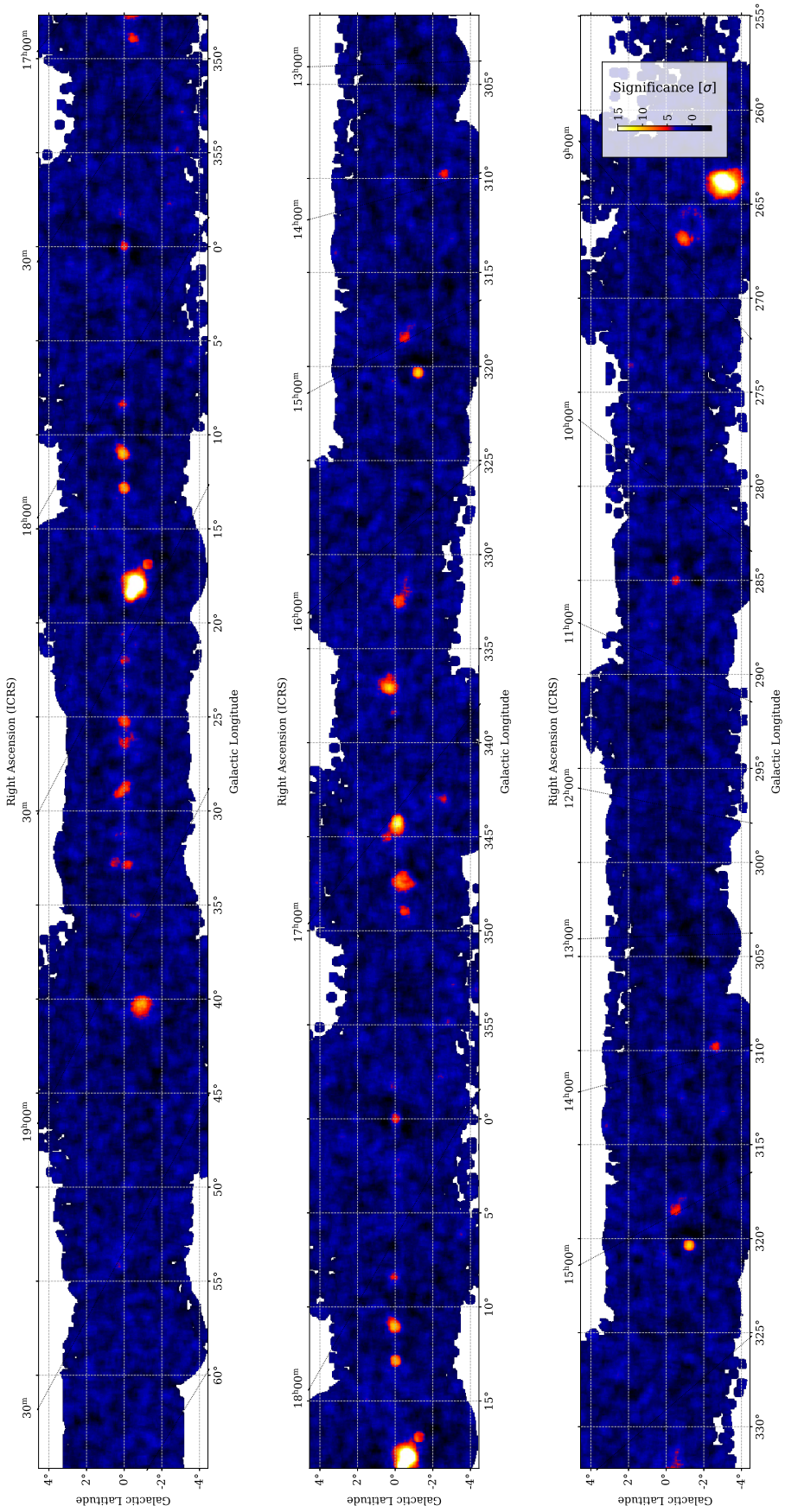

FIGURE 8.7: Map of *Cash* pre-trial significance for the MA, for the energy threshold of 20 TeV and a 0.3° correlation radius.

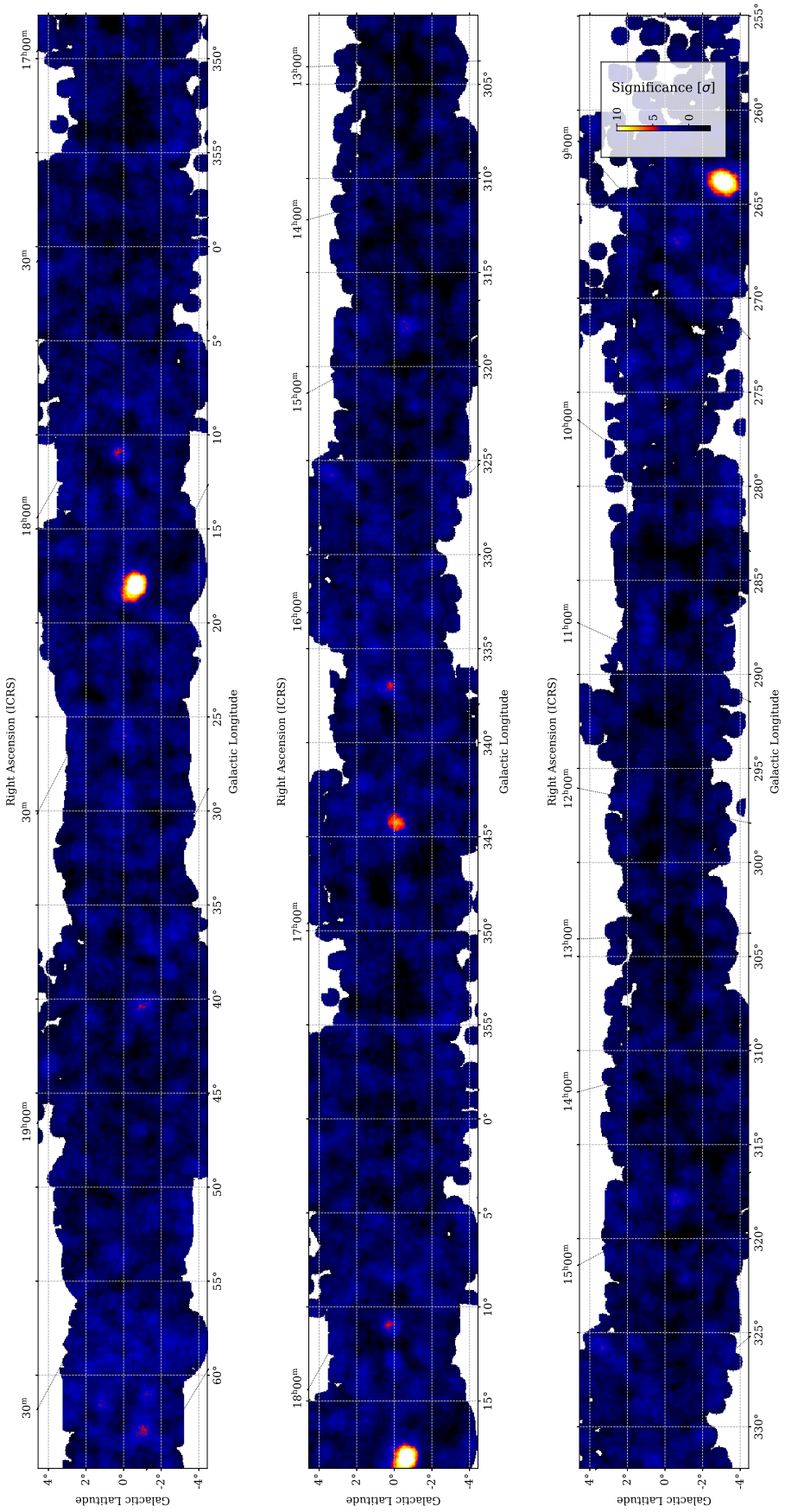

FIGURE 8.8: Map of *Cash* pre-trial significance for the MA, for the energy threshold of 50 TeV and a 0.5° correlation radius.

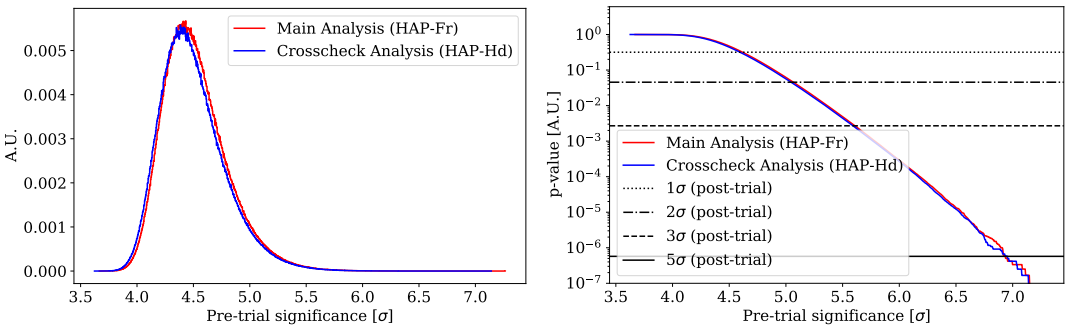

FIGURE 8.9: Left: Normalized distribution of the maximum pre-trial significance values in each of the 12 million simulations of the Galactic plane (with a background-only model), for the MA (red) and CA (blue). Right: p-values for each pre-trial significance value from the ditribution in the left panel, compared with the two-tail p-values of a standard normal Gaussian corresponding to 1, 2, 3, and 5σ post-trial significance.

8.2.3 Correcting for trials

The significance computation performed in the previous section did not take into account the inevitable presence of positive background fluctations in the large region covered by the survey. Indeed, when doing a blind source search, the larger the spatial RoI of the survey, the higher the probability that high-significance background fluctuations are observed. This means that the actual significance value of all features in the maps 8.6– A.6 should be scaled down for the purposes of a blind source detection. More precisely, they correspond to maps of *pre-trial* γ-ray signal significance, that need to be corrected to *post-trial*. To do so, we used a simulation-based approach.

We simulated 12×10^6 realizations of the Galactic plane ($E > 20\,\mathrm{TeV}$), by Poisson-fluctuating the background model[6] of the MA and CA stacked datasets, without adding any source component. We used the same spatial and energy binning specified in section 8.2.1. For each simulation, we computed a pre-trial significance map in the same way as explained in section 8.2.2, then we extracted and stored the maximum pixel significance value. The ensemble of the peak significances extracted from all simulations, after being normalized, is a probability distribution (shown figure 8.9, left panel) with a precise meaning: for each pre-trial significance value $\hat{S}$ on the x-axis, the integral of the distribution from $\hat{S}$ to ∞ (i.e. the right-tail p-value of the distribution) corresponds to the probability of observing by chance at least one background fluctuation $\geq \hat{S}$. We computed the p-value $1 - \mathrm{CDF}$ of this distribution for each value on the x-axis and compared it with the two-tail p-value of a standard normal Gaussian, thus obtaining an estimation for the pre-to-post significance relation (see figure 8.9, right panel). We found that, as shown in the figure, a $\approx 7\sigma$ (5.7σ, 5.2σ, 4.8σ) pre-trial significance has to be corrected to 5σ (3σ, 2σ, 1σ) post-trial significance, for blind source searches with both the MA and CA.

[6] This means sampling cunts in each spatial and spectral bin according to a Poisson distribution with expected value corresponding to the background model in the bin.

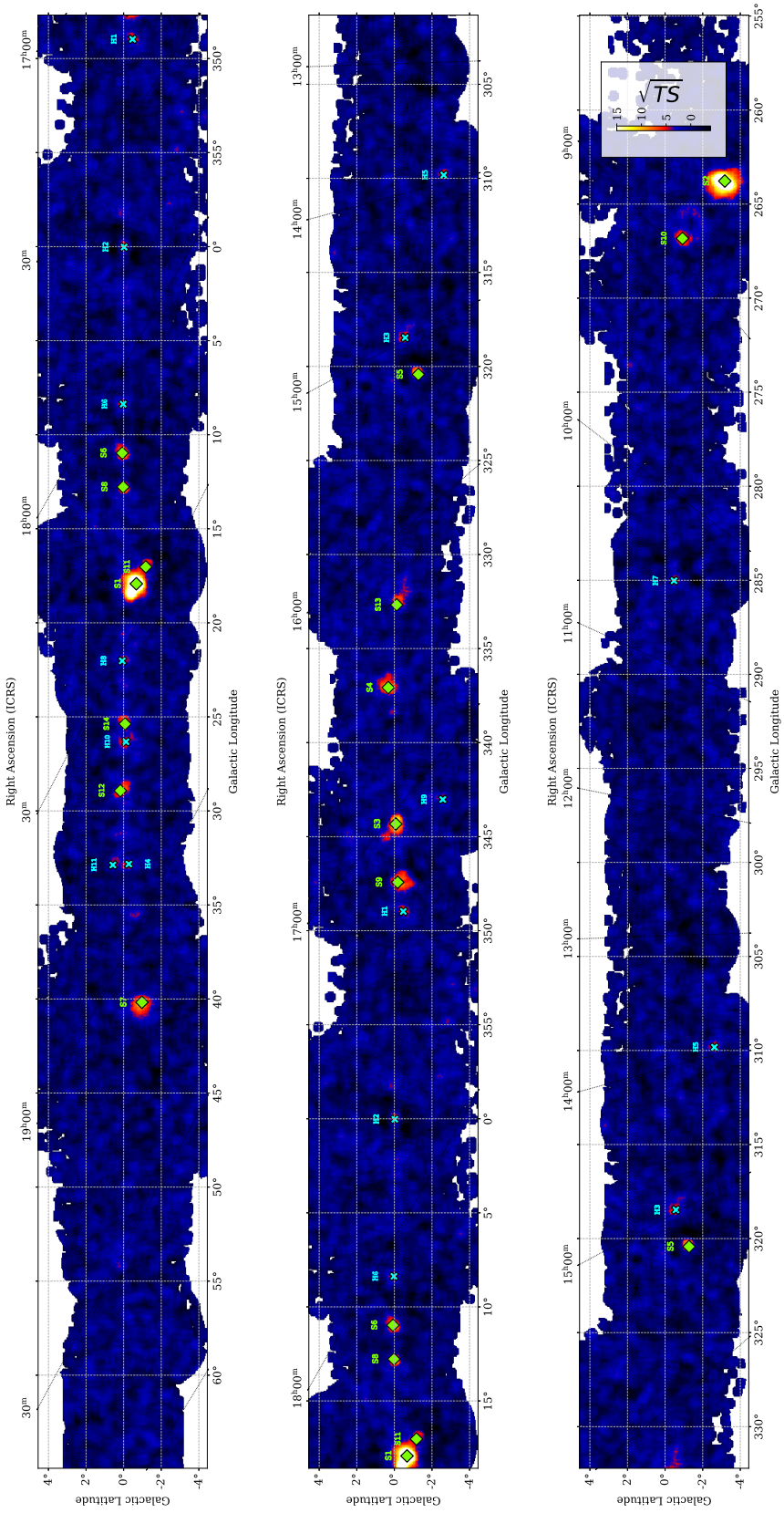

FIGURE 8.10: Same as figure 8.7 with markers indicating the positions of the detected sources (green diamonds) and hotspots (cyan crosses) listed in tables 8.1 and 8.2

8.2.4 Results

We used the pre-to-post trial significance relation derived in the previous section to look for source candidates in the $E > 20\,\mathrm{TeV}$ Galactic plane survey. We conservatively defined a significance threshold for source detection of 5σ post-trial, and a second lower threshold (2σ post-trial) to produce a list of high-energy "hotspots"[7]. To determine the sources and hotspot locations, we ran a simple blind-search algorithm[8] which finds local image peaks above a given threshold, with the requirement that they must be separated by a given minimum distance (we assumed $\sqrt{(PSF)^2 + R_{\mathrm{corr}}^2}$). We note that the significance peaks do not necessarily correspond to the exact object positions, due to exposure bias. However, we have verified a posteriori (see section 8.3) that each seed corresponds also to a peak in the exposure-corrected flux maps.

This approach resulted for the MA (CA) in a list of 14 (4) significantly detected sources and 11 (8) hotspots at $E > 20\,\mathrm{TeV}$. They can be seen in figures 8.10 and A.13, where they are respectively indicated as green diamonds and cyan crosses. The detected sources (hotspots) have are as S# (H#), where S (H) stands for *Source* (*Hotspot*) and # is a number standing for the significance ranking, ordered from the highest to the lowest value. We note that, despite the choice of the name *Source* for the significantly detected objects, it is not excluded a priori that some of them are actually part of the diffuse γ-ray emission (a mixture of unresolved sources and truly diffuse photons).

Table 8.1 reports the positions, pre-trial significance and most likely HGPS association of all detected sources in the HEGPS, for the MA. The hotspots list is presented later in the chapter. The source types listed in the last column of table 8.1 are based on the latest available information found on the TeVCat catalog. The source association is purely based on spatial proximity, and was manually achieved by plotting a zoomed flux map ($E > 20\,\mathrm{TeV}$) centered on each detected source (figure A.14) and hotspot (figure A.15) together with the HGPS catalog sources. The corresponding source table and plots for the CA can also be found in Appendix A. It is interesting to see that the three most significant sources (S1—3) are the same in both the MA and CA, although with different order. They are HESS J1825-137, HESS J0835-455 (Vela X) and HESS J1702-420, which are also the only three sources whose emission persists above 50 TeV (see figure 8.8). HESS J1514-501-137 (S5) is also detected in the CA, while two other sources from the MA (S9 and S10) are down-ranked to hotspots in the CA. The other 8 sources were detected only in the MA. From this comparison, the advantage of the MA configuration in the context of PeVatron studies becomes evident.

8.2.5 3D analysis of the detected sources

We selected and studied five sources from the MA list, being the most straightforward to analyze due to their simple morphology (at $E > 20\,\mathrm{TeV}$) and lack of nearby companions. They are HESS J1702-420, HESS J1514-591, HESS J0852-463, HESS J1843-033 and HESS J1616-508. For each of them, we performed a 3D analysis above 20 TeV using the MA IRFs. The high analysis energy threshold allowed us to

[7] We note that these definitions are very conservative, because they are based on the probability that there is just one such random background fluctuation if the full survey. In the final work, looser criteria may be adopted.

[8] Implemented in Gammapy, and called `find_peaks`.

Name	$\sqrt{TS}$ [σ]	Galactic l, b	HGPS association	CA	Common name	Type
S1	30.82	$17.93^o, -0.68^o$	HESS J1825-137	S3	–	PWN (?)
S2	22.84	$263.77^o, -3.17^o$	HESS J0835-455	S1	Vela X	PWN
S3	14.15	$344.32^o, -0.08^o$	HESS J1702-420	S2	–	UNID
S4	11.35	$337.07^o, 0.32^o$	HESS J1634-472	–	–	UNID
S5	11.05	$320.43^o, -1.27^o$	HESS J1514-591	S4	MSH 15-52	PWN
S6	10.64	$10.97^o, 0.07^o$	HESS J1809-193	–	–	UNID
S7	10.11	$40.17^o, -0.98^o$	HESS J1908+063	–	MGRO 1908+063	UNID
S8	9.87	$12.78^o, 0.03^o$	HESS J1813-178	–	–	COMP
S9	9.35	$347.43^o, -0.17^o$	HESS J1713-397	H3	RX J1713-3946	SNR
S10	8.67	$266.82^o, -0.93^o$	HESS J0852-463	H4	Vela Jr	PWN*
S11	8.22	$17.02^o, -1.18^o$	HESS J1826-148	–	LS 5039	BINARY
S12	8.05	$28.93^o, 0.17^o$	HESS J1843-033	–	–	UNID
S13	7.57	$332.68^o, -0.13^o$	HESS J1616-508	–	–	PWN (?)
S14	7.50	$25.38^o, -0.07^o$	HESS J1837-069	–	–	PWN

* Vela Jr is an SNR, but the emission > 20 TeV is due to a PWN on the same line of sight. (see section 8.3.10)

TABLE 8.1: Peak significance (pre-trial), position, most likely HGPS association, CA ranking, other names and source type for each of the detected sources at $E > 20$ TeV, for the MA. The "?" symbol in the last column indicates that the association is likely, but not certain (based on the TeVCat catalog information). Further details are provided in the main text.

avoid all contaminations from multiple sources (both resolved and diffuse) at lower energies. We implemented an automatic fit routine to test both point-like and extended (symmetric Gaussian) morphologies, preferring the latter in case of TS ≥ 9. Due to the limited lever arm of the high-energy fit, we assumed simple power-law spectra. The fit results for these sources are preliminary, and analysis will be extended to the other detected sources in the future.

For the five analyzed source, the best-fit spatial residuals and spectra are shown in figures 8.11 and 8.12, respectively. The best-fit values for the spectral and spatial parameters of each source are reported in appendix (table A.3). The fit results show that a simple 3D modeling above 20 TeV is possible, and leads to results that are generally compatible with the high-energy extrapolation of the HGPS spectra. We note that this is a first-time achievement, which proves that, at least in case of the simple analyzed sources, the 3D analysis systematics are still under control even with a fit energy threshold as high as 20 TeV. The case of HESS J052-463 (Vela Jr) is a bit peculiar, since the high-energy spectrum is much harder than the one reported in the HGPS (see figure 8.12). This is however understood, because our modeling refers not to the SNR shell but to a PWN superimposed on the same line of sight (see also section 8.3.10). All sources were spatially modeled as point-like or single Gaussians above 20 TeV, with the exception of HESS J1843-033. The latter required a more complicated modeling, with the presence of two Gaussians sharing the same spectral model, similarly to the HGPS description of the source.

After obtaining a 3D model for each source, we used it to investigate the origin of the differences in the MA and CA detected source lists, to confirm that they are only due to the different exposure (and therefore sensitivity) levels of the two configurations. For each source we Poisson-fluctuated the background model together with the best-fit 3D source models for 100 times, and for each realization we applied the same

source finding algorithm that was used to produce the HEGPS source list. With this, we evaluated the probability of detecting the sources ($> 5\sigma$ post-trial) with the MA and CA IRFs. The result is shown in figure 8.13, for the MA (red) and CA (blue). The error bars were obtained by manually up and down-scaling the source fluxes by 20%, to account for possible systematics in the 3D model fit. The figure shows that the detection probabilities are in line with the expectations from the HEGPS source list (table 8.1). For example, the sources HESS J1702-420 and HESS J1514-591, with a high detection probability in both the MA and CA, were indeed detected in both cases. HESS J0852-463, with a $\approx 70\%$ and $\approx 50\%$ detection probability respectively in the MA and CA, was significantly detected in the MA and identified as a hotspot in the CA. Finally, the sources HESS J1843-033 and HESS J1616-508, with a detection probability close to 0 in the CA, were detected only in the MA. This confirms that the difference in the detection sensitivity is, at least for the simple analyzed sources, at the origin of the differences between the MA and CA source lists.

8.3 Discussion

Most of the sources detected by H.E.S.S. above 20 TeV (table 8.1) are either associated with PWNe (6) or unidentified (5), with a small minority of SNRs (1), plerions (1) and binary systems (1). The high number of PWNe indicates that most of the extreme particle accelerators observed by H.E.S.S. are of leptonic nature, unless models of PWNe are incomplete and they also efficiently accelerate cosmic rays. The presence of a significant fraction of unidentified objects also leaves room for hadronic accelatarors. This will be further discussed in section 8.4. In the rest of this section we will instead focus individually on each of the detected sources (from the MA), by dedicating a short paragraph to their associated TeV publications and nearby astrophysical objects.

8.3.1 S1 (HESS J1825-137)

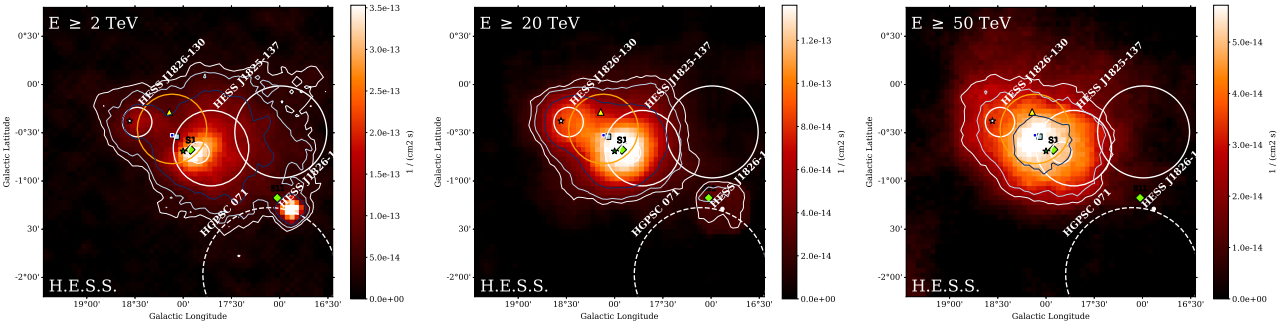

FIGURE 8.14: Flux maps integrated above 2 TeV (left, $R_{\rm corr} = 0.1°$), 20 TeV (center, $R_{\rm corr} = 0.3°$) and 50 TeV (right, $R_{\rm corr} = 0.5°$) centered on the S1 source. The HGPS sources are indicated in white, while the HAWC and eHWC sources in blue and orange respectively. The contours represent the 5, 7 and 12σ pre-trial significance levels. The green star, white star, yellow triangle and light blue square respectively indicate PSR J1826-1334, PSR J1826-1256, the star cluster [BDS2003] 8 and LHAASO J1825-1326.

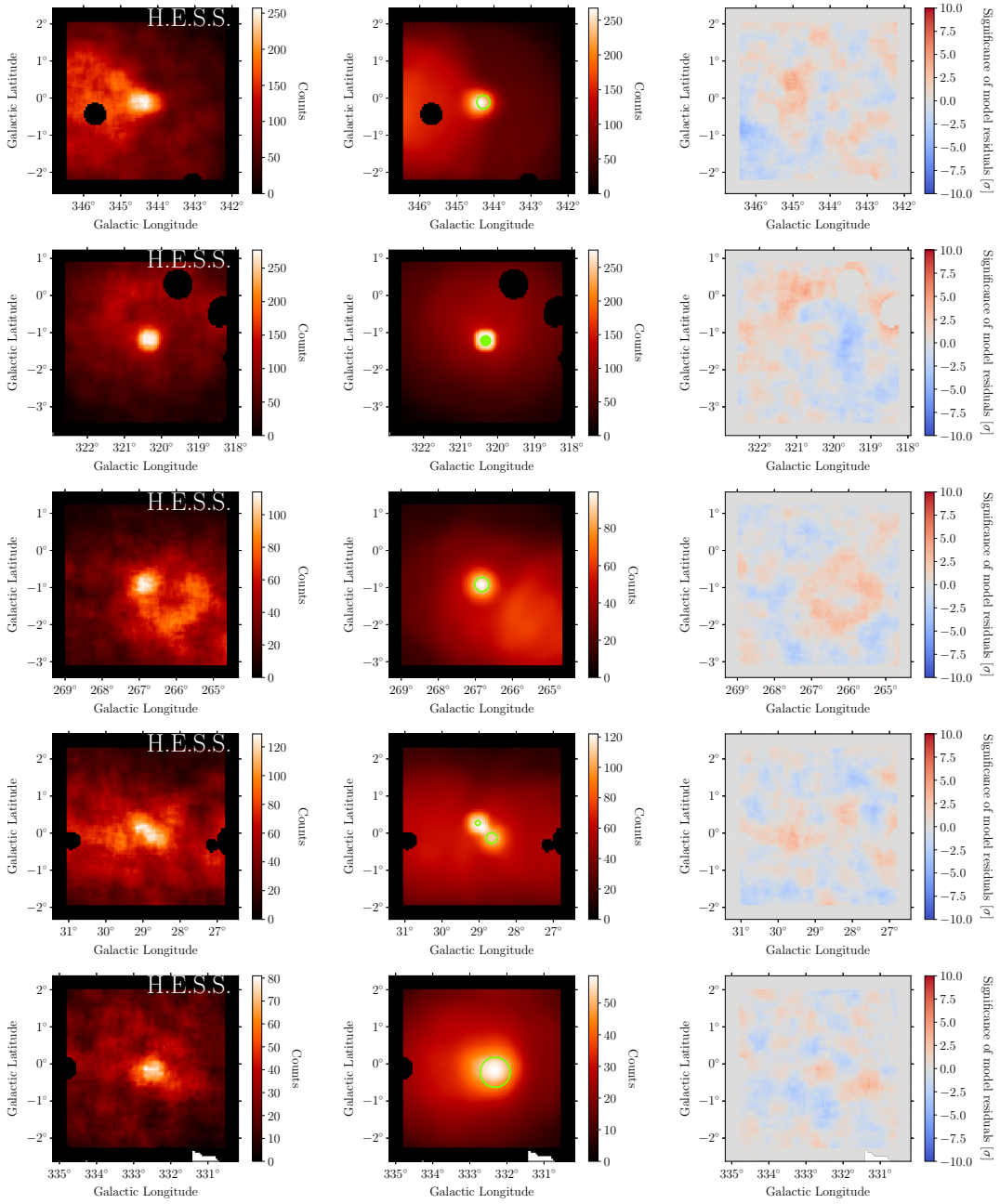

FIGURE 8.11: Left column: counts map ($E > 20\,\mathrm{TeV}$) from the MA configuration, centered on the five selected sources for the 3D analysis. Central column: map of model-predicted counts, assuming the best-fit 3D model for each source. Right column: significance of model residuals. All maps were correlated with a 0.3°-radius top-hat kernel. The figure rows, in order, refer to: HESS J1702-420, HESS J1514-591, HESS J0852-463, HESS J1843-033 and HESS J1616-508.

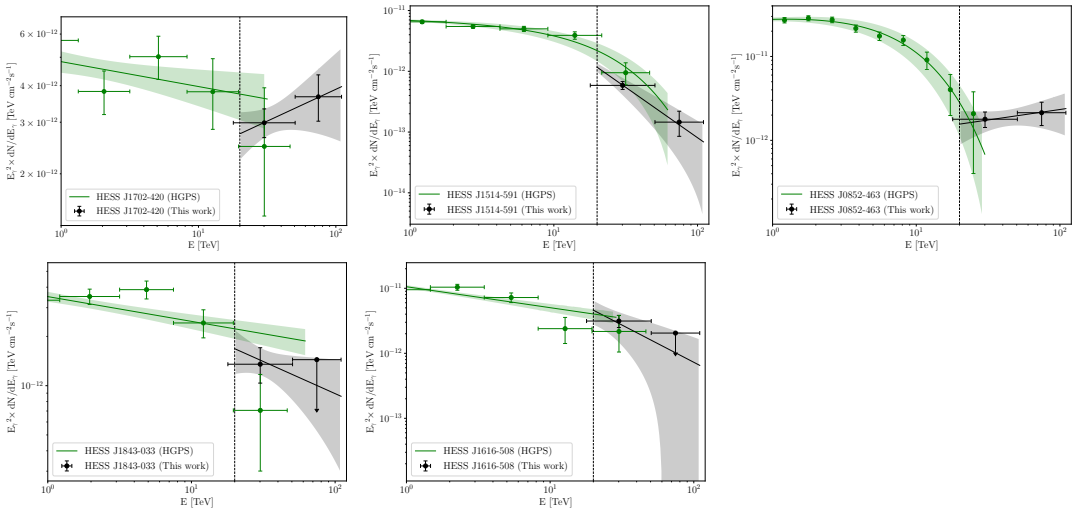

FIGURE 8.12: Best-fit spectra from the 3D analysis with the MA IRFs (black), compared with the HGPS spectra (green).

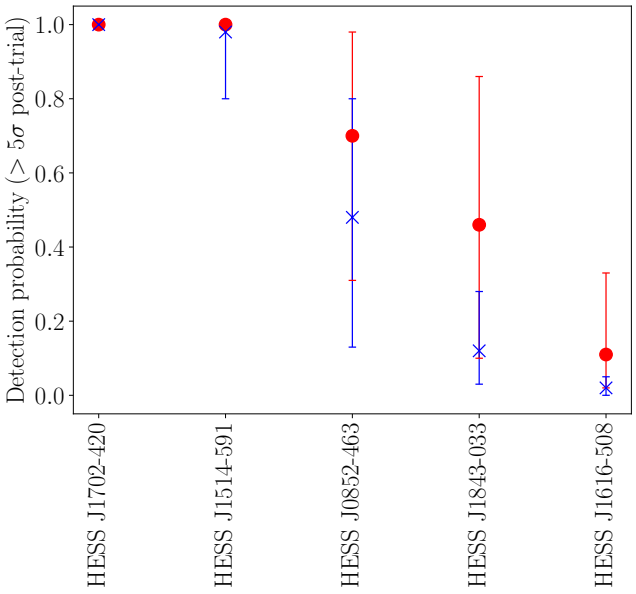

FIGURE 8.13: Source detection probability ($> 5\sigma$) post-trial for the MA (red) and CA (blue) configurations, assuming the best-fit source models from the 3D analysis of the MA data. More details are provided in the text.

HESS J1825-137 is one of the brightest known TeV PWNe (see e.g. [184], figure 7), for which H.E.S.S. has measured a strongly energy-dependent morphology[9] and a spectral softening away from the position of PSR J1826-1334 [44]. This pulsar, with a spin-down age $\tau \approx 2.14 \times 10^4\,\mathrm{yr}$ and power $\dot{E} \approx 3 \times 10^{36}\,\mathrm{erg\,s^{-1}}$, is most likely the (leptonic) particle accelerator powering the TeV source. HESS J1825-137 is also one of the only three sources for which the eHWC catalog has reported a significant emission at energies $> 100\,\mathrm{TeV}$ [209]. As visible in figure 8.14, the HAWC source position (from both the eHWC and 2HWC catalogs) is slightly shifted toward the middle point between HESS J1825-137 and HESS J1826-130. This is likely due to the known systematic shift in the position of sources reported by HAWC and IACTs (see [211], figure 11), but we also notice that the peak of the emission seen by H.E.S.S. above 50 TeV appears to shift toward the position of the HAWC association (see 8.14, third panel).

Recently, HAWC has reported a spectral measurement of this UHE source up to 200 TeV, without evidence of a break or cutoff, and found it to be positionally coincident with a dense ($n_\mathrm{H} = 700\,\mathrm{cm^{-3}}$) giant molecular cloud and a young massive star cluster called [BDS2003] 8 [212]. The region of HESS J1825-137 has also been detected by LHAASO at 16σ significance above 100 TeV, with the highest-energy γ-ray reaching the energy of 420 TeV [47]. It seems therefore possible that the VHE (H.E.S.S.) and UHE (HAWC/LHAASO) sources have different origins, the VHE one being associated with the leptonic accelerator PSR B1823-13 and the UHE one that might originate from hadronic interactions of the highest energy protons escaping from the star cluster and illuminating the molecular cloud. In such scenario, given that the proton cutoff energy lower limit is 1.3 PeV at 95% confidence level [212], the star cluster [BDS2003] 8 would be a proton PeVatron. However, an association of the UHE source with the pulsar PSR J1826-1334 cannot not be ruled out at this stage.

8.3.2 S2 (HESS J1835-455, Vela X)

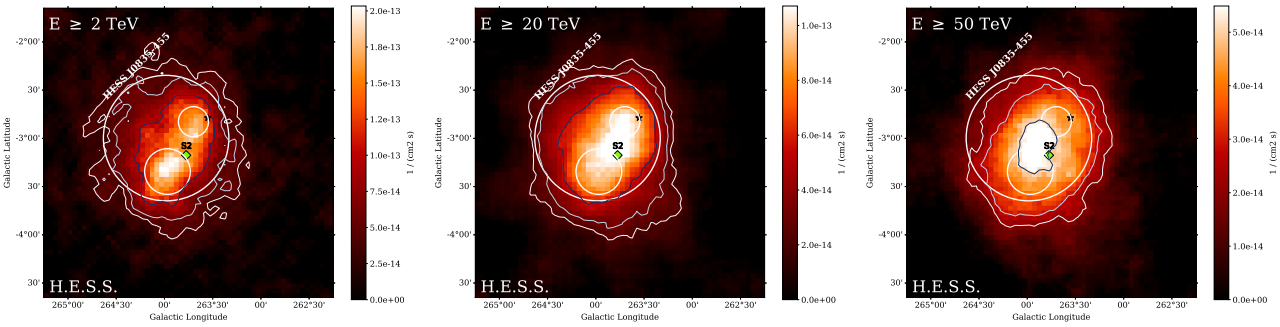

FIGURE 8.15: Same as figure 8.14, but for the S2 source. Here the black star indicates PSR J0834-4511.

Vela X is a nearby ($d \approx 287\,\mathrm{pc}$) PWN, powered by the powerful pulsar PSR J0834-4511 (also known as the Vela pular, $\tau \approx 1.1 \times 10^4\,\mathrm{yr}$ and $\dot{E} \approx 7 \times 10^{36}\,\mathrm{erg\,s^{-1}}$). Its complex morphology was modeled in the HGPS by a 3-Gaussian model, while a more recent combined H.E.S.S. and *Suzaku* study, based on previous H.E.S.S. and ROSAT observations, has focused on the elongated structure of the multiwavelenth source emission, called the Vela X *cocoon* [213]. The cocoon extends for about 4 pc from the position of

[9] Rendered in the HGPS as a superposition of 3 Gaussians, as visible in figure 8.14.

the Vela pulsar, and its TeV emission is due to inverse Compton either from electron diffusing beyond the termination shock or advected by a highly asymmetric reverse shock [213]. In [213], a slightly lower significance for the presence of a γ-ray spectral cutoff was found nearby the pulsar with respect to the rest of the cocoon. This is in agreement with our measurement, in which the peak position shifts toward the pulsar from the $E > 2\,\mathrm{TeV}$ and $E > 20\,\mathrm{TeV}$ images (see figure 8.15, and figure A.16 for the CA).

8.3.3 S3 (HESS J1702-420)

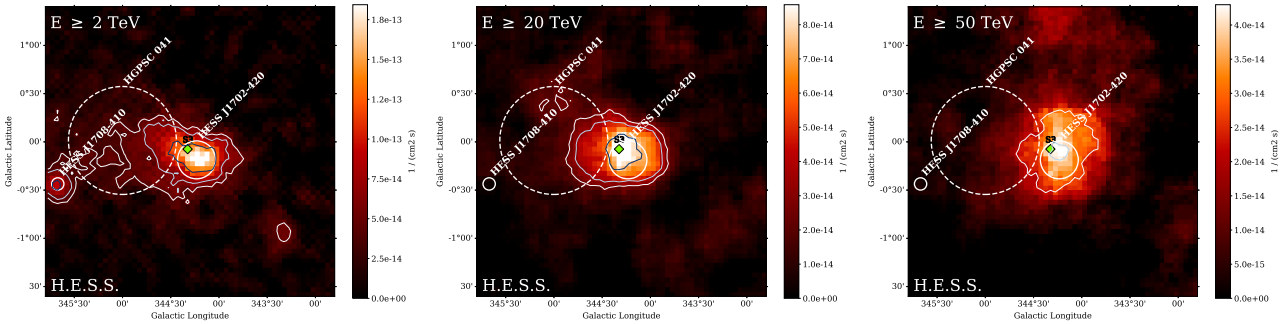

FIGURE 8.16: Same as figure 8.14, but for the S3 source.

HESS J1702-420 has been covered in detail in part II of this thesis. Here we merely observe, as a further crosscheck, the overall consistency between the flux maps resulting from the HEGPS analysis (figure 8.16) and those produced during the dedicated source study. Also, the hard spectrum measured in the 3D analysis above 20 TeV (see figure 8.12) is consistent with the presence of the new source component HESS J1702-420A, discussed in the part II of this thesis.

8.3.4 S4 (HESS J1634-472)

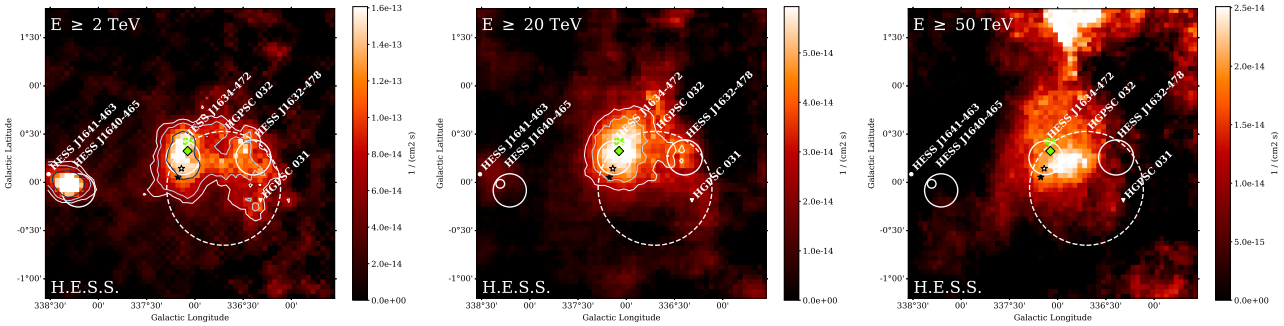

FIGURE 8.17: Same as figure 8.14, but for the S4 source. Here the black and white stars indicate respectively the center of SNR G337.2+0.1 and the *Fermi*-LAT source 3FGL J1636.2-4709c. The bright spot at $b \approx 1.5^{\circ}$, not present in the significance maps, is likely due to a background fluctuation in a low exposure region at the borders of the map.

HESS J1634-472 is an unidentified source, for which the most likely counterpart appears to be the closeby SNR G337.2+0.1 (indicated by a black star in figure 8.17). The latter is a radio and X-ray bright composite SNR (or plerion), i.e. an SNR with inside a PWN powered by a (yet undetected) pulsar [214, 215]. The *Fermi*-LAT source 3FGL J1636.2-4709c is located between the plerion and HESS J1634-472 (see the white star in figure 8.17), and its GeV spectrum is well connected to the VHE one [216]. Possible origins for the multi-TeV γ-ray emission from HESS J1634-472 are either hadronic interactions between runaway protons from the SNR and a MC, or inverse-compton from energetic electrons diffusing or advected away from the pulsar's termination shock.

8.3.5 S5 (HESS J1514-591, MSH 15-52)

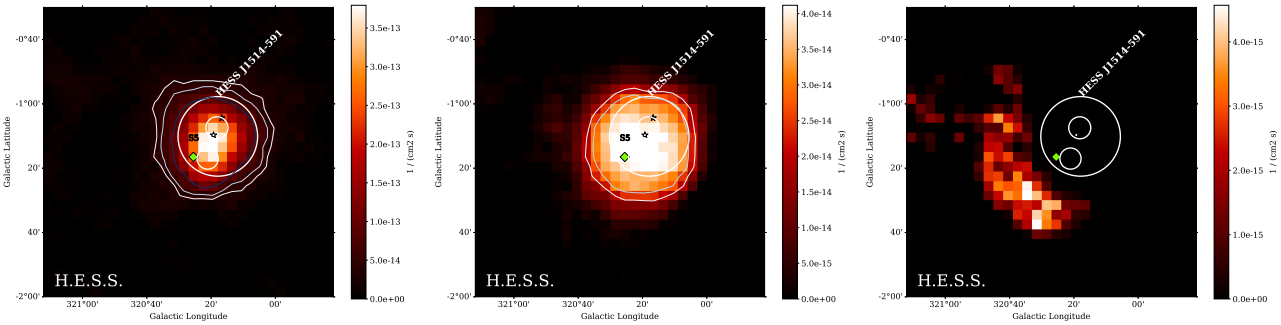

FIGURE 8.18: Same as figure 8.14, but for the S5 source. Here the black and white stars indicate respectively the center of SNR G320.4-1.2 and the *Fermi*-LAT source 3FGL J1513.9-5908.

MSH 15-52 is a composite SNR, with a radio-bright shell surrounding the bright X-ray PWN of PSR B1509-58. The γ-ray emission detected by *Fermi*-LAT, as well as the VHE source, are generally associated with the PWN [216, 217]. This source has been detected, as a hotspot, also in the CA above 20 TeV, but it disappears at $E > 50$ TeV (see figure 8.18). This may be due to the presence of a high-energy spectral cutoff, compatible with the HGPS specrum of MSH 15-52 (see figure 8.12, upper center panel), or a lack of sensitivity at the highest energies. For this source, the spectrum obtained from a 3D analysis above 20 TeV is completely compatible with the high-energy extrapolation of the HGPS one (see figure 8.12, upper center panel).

8.3.6 S6 (HESS J1809-193)

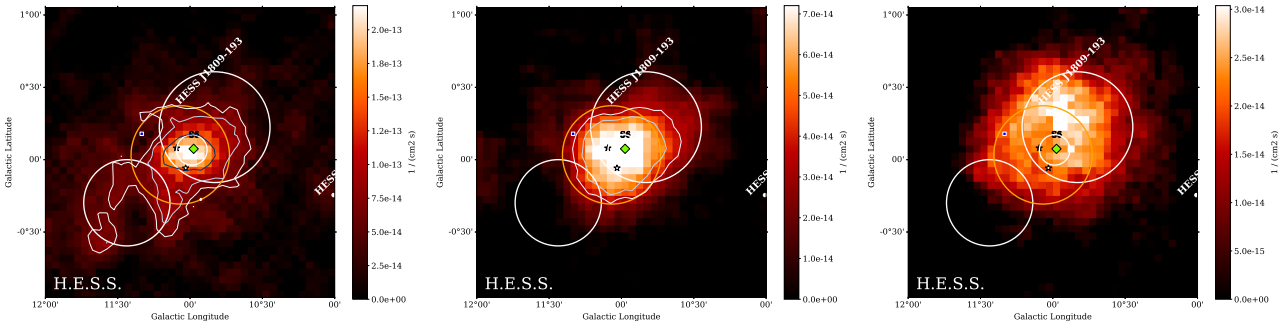

FIGURE 8.19: Same as figure 8.14, but for the S6 source. Here the black and white stars indicate respectively PSR J1809-1917 and the center of SNR G011.0-0.0. The 2HWC and eHWC associations are indicated by the blue square (point-like source) and orange circle (extended source), respectively.

The multi-wavelength picture of the HESS J1809-193 region is complicated. In the beginning it was thought that the VHE source was powered by the PWN associated with PSR J1809-1917 [218]. However, no evidence supporting this scenario was found by subsequent radio observations, which instead pointed toward an association with the SNR G011.0-0.0 and a nearby molecular cloud [219]. Today the origin of this source remains elusive. As visible in figure 8.19, the TeV emission detected by H.E.S.S. at $E > 20\,\text{TeV}$ (with also a hint of emission above 50 TeV) is in excellent positional agreement with the HAWC association ($E > 56\,\text{TeV}$), called eHWC J1809-193 [209].

8.3.7 S7 (HESS J1908+063)

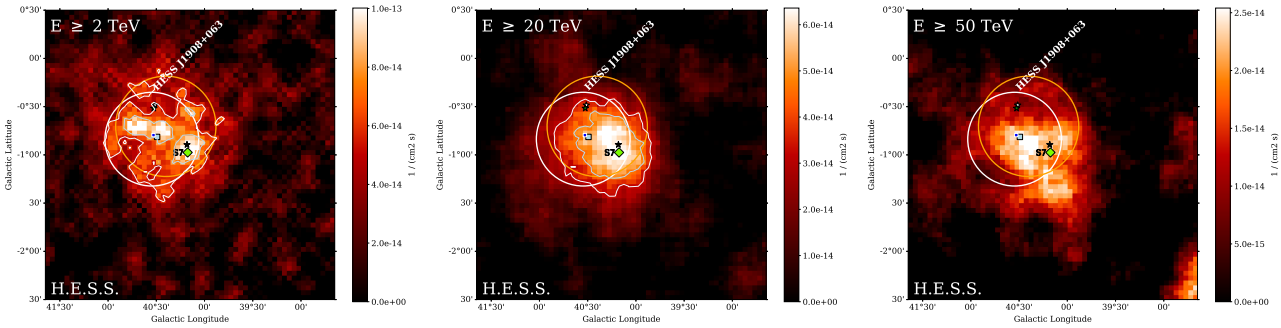

FIGURE 8.20: Same as figure 8.14, but for the S7 source. Here the black, white and green stars indicate respectively PSR J1907+0602, PSR J1907+0631 and the center of SNR G40.5-0.5, while the lightblue square denotes the position of LHAASO J1908+0621. The 2HWC and eHWC associations are indicated by the blue square (point-like source) and orange circle (extended source), respectively.

Discovered by Milagro in 2007 and subsequently observed by H.E.S.S., VERITAS, ARGO-YBJ, HAWC and LHAASO, HESS J1908+063 is an unidentified source with many possible counterparts (see figure 8.20). It is one of the three sources detected by HAWC above 100 TeV [209], and more recently up to $\approx 200\,\text{TeV}$ [220]. LHAASO has

also reported a 17.2σ significance source detection above 100 TeV, with the highest-energy photon reaching 440 TeV [47]. Historically its emission has been associated with the powerful pulsar PSR J1907+0602 ($\dot{E} \approx 2.8 \times 10^{36}\,\mathrm{erg\,s^{-1}}$), that is the nearest object to the position of the source S7, but other objects such as the SNR G40.5-0.5 and a giant molecular cloud also contribute. Indeed, given the abundance of potential powerful accelerators on the line of sight of HESS J1908+063, it seems plausible that its emission comes from a mixture of hadronic and leptonic processes [220].

8.3.8 S8 (HESS J1813-178)

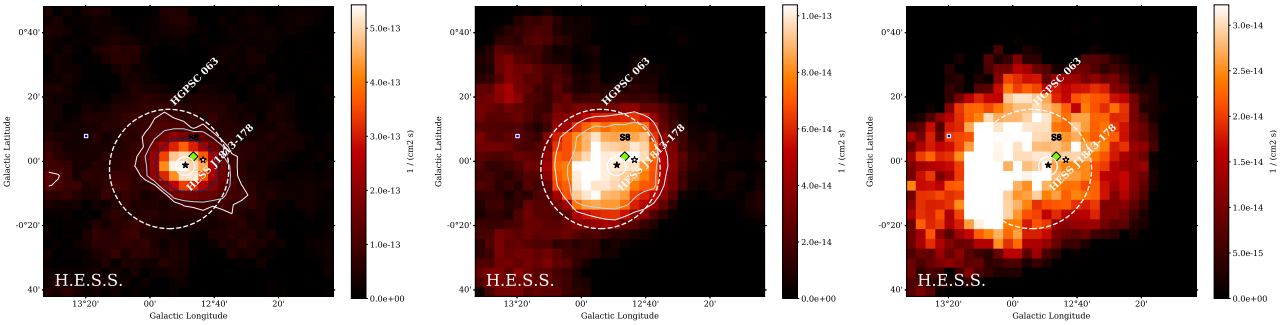

FIGURE 8.21: Same as figure 8.14, but for the S8 source. Here the black and white stars indicate respectively PSR J1813-1749 and the center of SNR G12.7-0.0.

HESS J1813-178 is associated with a plerion, whose γ-ray emission might originate either from leptonic processes in the PWN powered by the pulsar PSR J1813-1749 or hadronic interactions from protons accelerated by the SNR G12.7-0.0 [221]. Remarkably, PSR J1813-1749 is the second known Galactic pulsar in terms of spin-down luminosity ($\dot{E} \approx 5.6 \times 10^{37}\,\mathrm{ergs/s}$), about one order of magnitude higher than all the other pulsars powering PWNe detected by H.E.S.S. [184]. This source has been detected by HAWC, but is not part of the eHWC catalog, although looking at figure 1 from [209] one can actually notice a hint of emission above 56 TeV.

8.3.9 S9 (HESS J1713-397, RX J1713.7-3946)

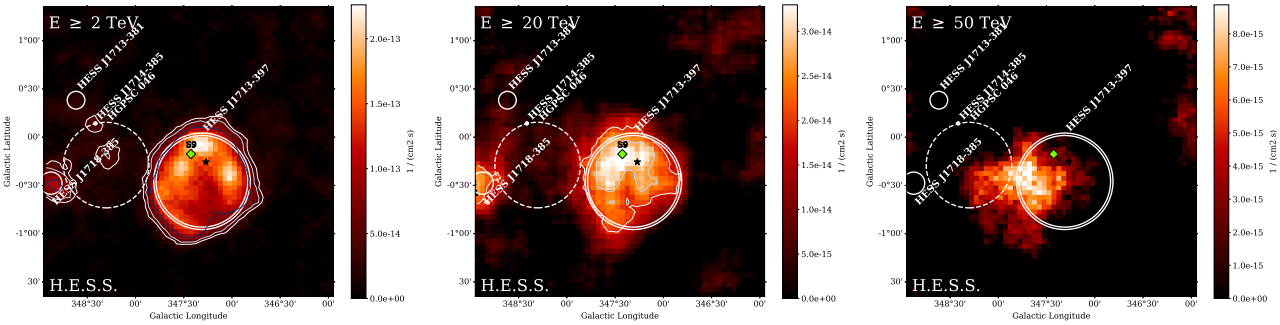

FIGURE 8.22: Same as figure 8.14, but for the S9 source. Here the black star indicates the position of SNR G347.3-0.5, from the TeVCat catalog. The SNR shell, taken from the HGPS [38], is indicated by the two concentric white circles.

HESS J1713-397 is firmly identified with the shell-type remnant SNR G347.3-0.5, for which the ratio between the hadronic and leptonic components of the TeV emission is however not yet determined [222, 223]. The γ-ray emission detected by H.E.S.S. above 20 TeV appears to localize in the Northern part of the shell (see figure 8.22), but the poor angular resolution of the image and the fact that the hotspot detected in the CA is located more toward the eastern part of the shell (see figure A.17) prevent us from drawing more detailed conclusions. Still, it seems clear that the morphology evolves significantly from the TeV to the multi-TeV range, suggestive of different physical conditions along the SNR shock.

8.3.10 S10 (HESS J0852-463, Vela Jr)

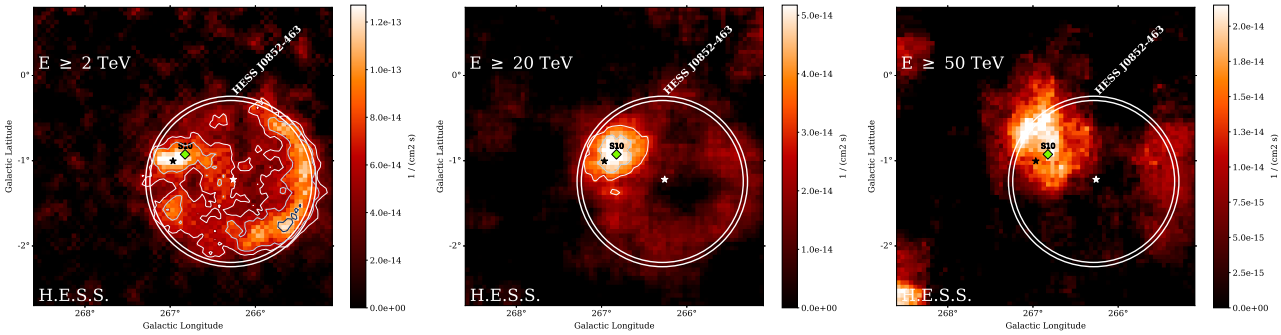

FIGURE 8.23: Same as figure 8.14, but for the S10 source. Here the black and white stars indicate respectively PSR J0855-4644 and the center of RX J0852.0-4622. The SNR shell, taken from the HGPS [38], is indicated by the two concentric white circles.

Vela Jr is arguably one of the most interesting sources detected in the HEGPS. The TeV source HESS J0852-463 is generally considered a firmly established shell-type SNR, whose TeV emission traces the profile of the remnant RX J0852.0-4622 (see figure 8.23, left panel). However, at higher energies (> 20 TeV) there is a clear transition, with the shell fading away apart from a significantly detected γ-ray cluster most likely associated with the PWN powered by the pulsar PSR J0855-4644 (see figure 8.23, center panel). The latter is a powerful pulsar ($\dot{E} \approx 1.1 \times 10^{36}\,\mathrm{erg\,s^{-1}}$) located less than 1 kpc away, at a similar distance as the SNR but not associated with it [224].

This is the first time that the γ-ray emission from the X-ray bright PWN powered by PSR J0855-4644 is clearly separated from the Vela Jr shell. Given the overlap of the two sources, this complex region represents a textbook case for the 3D analysis technique, in which the spectra and morphologies of the SNR and PWN can be disentangled by means of a maximum likelihood model fit. For the moment, we modeled the source emission above 20 TeV using just a Gaussian model accounting for the PWN (see figures 8.12 and 8.11), but a full 3D analysis study of this source above 2 TeV, with a Gaussian source superimposed on a shell-shaped model, is currently in preparation. The spectral index that we obtained from our preliminary analysis is extremely hard ($\Gamma = 1.75 \pm 0.5$), in line with the spectrum of HESS J1702-420A (see chapter 4) and the one of the pulsed emission from the Vela pulsar (with a paper in praparation by the H.E.S.S. Collaboration). This might be seen as evidence that the three objects are of the same class, although for the case of Vela the hard TeV

emission is phase-resolved. Further studies and more rigorous 3D modeling of the Vela Jr region will be necessary to further discuss this possibility.

8.3.11 S11 (HESS J1826-148, LS 5039)

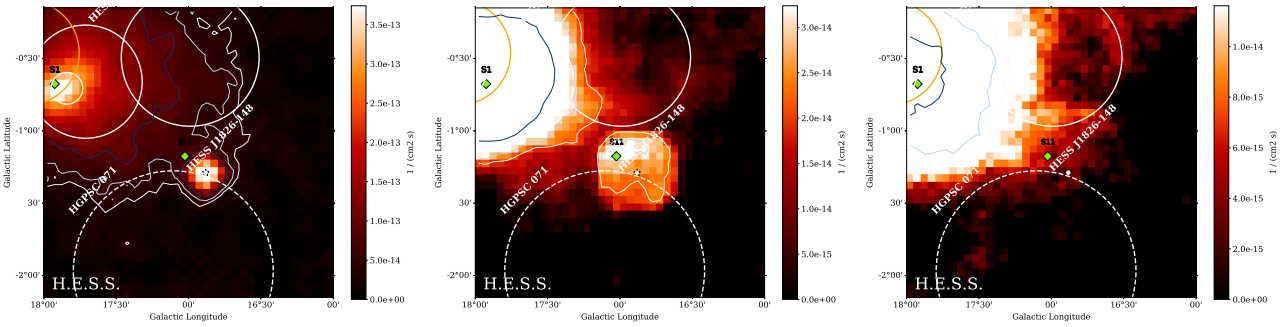

FIGURE 8.24: Same as figure 8.14, but for the S11 source. Here the black star indicates the position of LS 5039.

LS 5039 is a high-mass γ-ray binary system discovered more than 20 years ago [225], comprising a hot and massive O or B type star orbiting a yet unidentified compact object, either a neutron star or a black hole. Here, since we are integrating over the whole H.E.S.S. observation history, the emission detected from the binary system is averaged over the orbital phase. The γ-ray production mechanism of such systems is unclear, the most plausible possibilities being the emission from the jets of an accretion-powered microquasar or inverse Compton scattring of starlight from the massive star by relativistic electrons from the pulsar wind. LS 5039 has been previously detected up to $\lesssim 20\,\mathrm{TeV}$ by H.E.S.S. [37], but HAWC reported only upper limits above 10 TeV [36], likely due to the small angular size of this source. Therefore, this is the first time that LS 5039 is detected above 20 TeV.

8.3.12 S12 (HESS J1843-033)

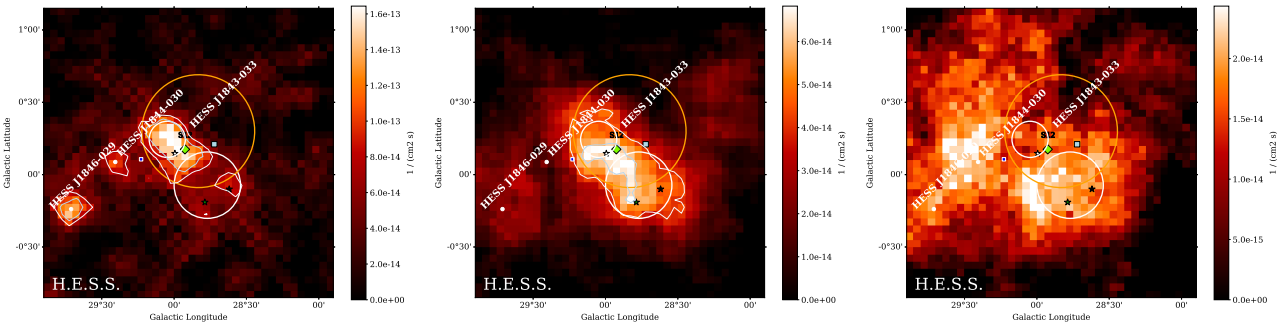

FIGURE 8.25: Same as figure 8.14, but for the S12 source. Here the black, white and green stars indicate respectively the center of SNR G28.6-0.1, 3FGL J1843.7-0322 and 3FGL J1844.3-0344, while the lightblue square denotes the position of LHAASO J1843-0338. The 2HWC and eHWC associations are indicated by the blue square (point-like source) and orange circle (extended source), respectively.

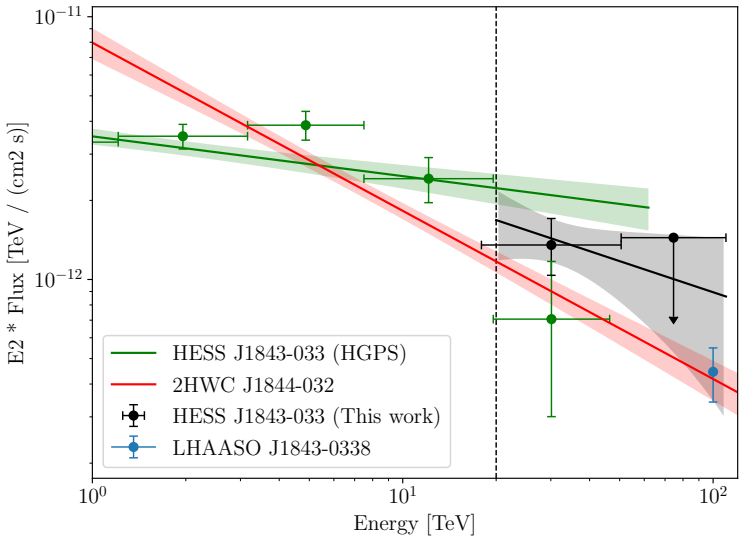

FIGURE 8.26: Best-fit spectrum obtained from a 3D analysis above 20 TeV for the source HESS J1843-033 (black), together with the reference spectra from the HGPS (green) and 2HWC (red) catalogs. The blue flux point is the LHAASO spectral measurement at 100 TeV (the full spectrum is not yet published), from [47].

HESS J1843-033 is an unidentified source, whose morphology was described in the HGPS by two Gaussian component separated by approximately 0.2° (see figure 8.25). The only known possible counterparts appear to be the remnant SNR G28.6-0.1, although there are also two unidentified *Fermi*-LAT objects overlapping with the TeV emission. The source has been detected above 56 TeV by HAWC [209] and, more recently, by LHAASO up to 260 TeV [47]. If HESS J1843-033, with a γ-ray spectrum detected up to hundreds of TeV, is associated via hadronic interactions with the SNR G28.6-0.1, the latter is likely a proton PeVatron.

The new spectral measurement provided by our work (the same of figure 8.12, with details in table A.3) is shown in figure 8.26, together with the HGPS, HAWC and LHAASO spectra. The updated H.E.S.S. spectrum above 20 TeV is consistent with the other multi-instrument measurements. This confirms once again that even with such a high energy threshold the systematics of the 3D analysis are under control, and that H.E.S.S. is capable of extending its analysis energy range up to 100 TeV.

8.3.13 S13 (HESS J1616-508)

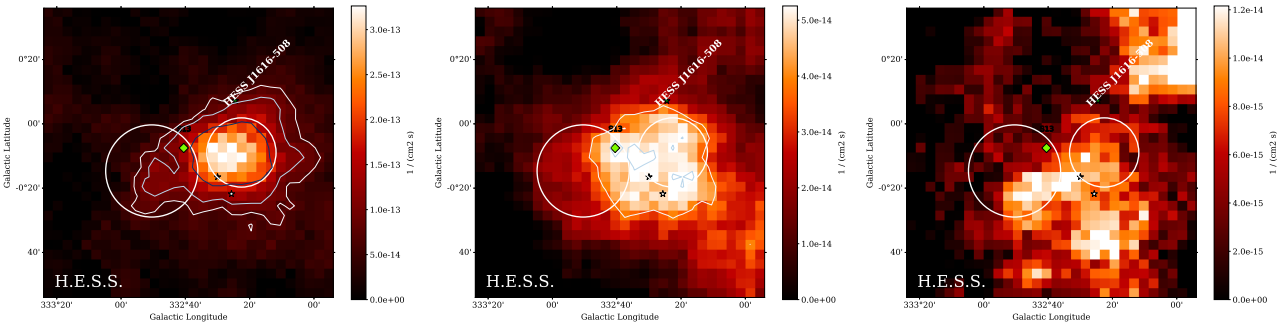

FIGURE 8.27: Same as figure 8.14, but for the S13 source. Here the black, white and green stars indicate respectively PSR J1617-5055, the center of SNR G332.4-0.4 and that of SNR G332.4+0.1.

HESS J1616-508 is an unidentified source, described in the HGPS by two Gaussian components and with multiple SNRs and pulsars possibly (but not clearly) associated with the TeV emission [226]. The bright emission from the North-Western corner of the $E > 50\,\mathrm{TeV}$ map likely corresponds to a positive background fluctuation in a low exposure region. The spectrum that we obtained with a 3D analysis above 20 TeV is compatible with the high-energy extrapolation of the HGPS one (see figure 8.12).

8.3.14 S14 (HESS J1837-069)

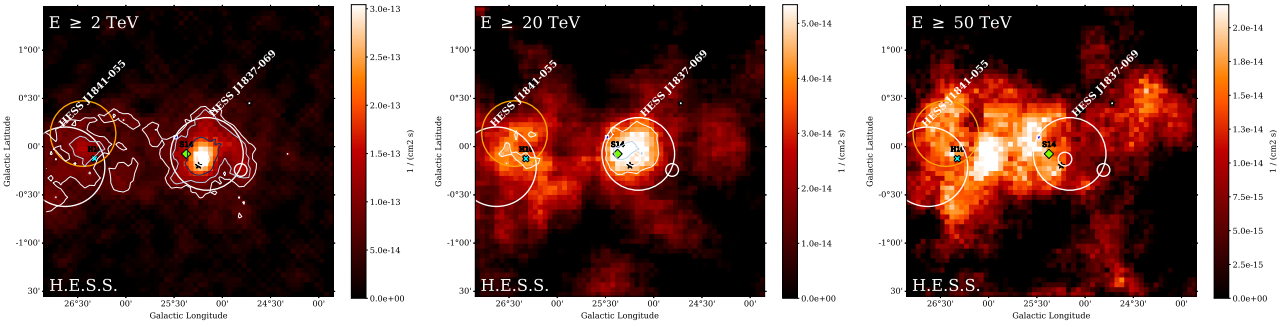

FIGURE 8.28: Same as figure 8.14, but for the S14 source. Here the black and white stars indicate respectively PSR J1838-0655 and the center of SNR G24.7+0.6. The 2HWC and eHWC associations are indicated by the blue square (point-like source) and orange circle (extended source), respectively.

HESS J1837-069 is considered in the HGPS as a firmly identified PWN, associated with the pulsar PSR J1838-0655 and detected by *Fermi*, MAGIC [227] and HAWC (2HWC J1837-069). Our measurement shows that the emission above 50 TeV is shifted toward the middle point between HESS J1837-069 and HESS J1841-055 (see the right panel of figure 8.28), but its low significance prevents us from speculating on its possible association with the nearby 2HWC and eHWC UHE sources.

Name	$\sqrt{TS}$ [σ]	Galactic l, b	HGPS association	CA	Common name	Type
H1	6.73	$348.98°, -0.47°$	HESS J1718-385	–	–	PWN (?)
H2	6.41	$0.02°, -0.02°$	HESS J1745-290	–	Sgr A*	UNID
H3	6.39	$318.48°, -0.57°$	HESS J1457-593	H2	–	SNR (?)
H4	6.26	$32.83°, -0.28°$	HESS J1852-000	–	–	UNID
H5	6.13	$309.82°, -2.62°$	HESS J1356-645	–	—	PWN
H6	5.93	$8.38°, 0.02°$	HESS J1804-216	–	–	UNID
H7	5.89	$285.02°, -0.48°$	HESS J1026-582	–	–	PWN (?)
H8	5.81	$22.02°, 0.07°$	HGPSC 072	–	–	UNID
H9	5.59	$343.02°, -2.58°$	HESS J1708-443	–	–	PWN (?)
H10	5.54	$26.32°, -0.12°$	HESS J1841-055	–	–	UNID
H11	5.47	$32.88°, 0.57°$	HESS J1849-000	–	IGR J18490-0000	PWN

TABLE 8.2: Peak significance (pre-trial), position, most likely HGPS association, CA ranking, other names and source type for each of the hotspots at $E > 20$ TeV, for the MA. The "?" symbol in the last column indicates that the association is likely, but not certain (based on the TeVCat catalog information). Further details are provided in the main text.

8.3.15 The hostpots list

Apart from the significantly detected sources, several objects corresponding to $\gtrsim 2\sigma$ (post-trial) hotspots above 20 TeV were found. They are listed in table 8.2 for the MA, and table A.2 for the CA. They are mostly unidentified sources or PWN candidates, with interesting exceptions such as HESS J1745-290 (H2), likely associated with the diffuse emission surrounding the Galactic center region. Its low significance above 20 TeV is at odds with the recent Veritas measurement of a straight power law up to 40 TeV [77], but appears to be consistent with the indication of a spectral softening beyond 20 TeV reported by H.E.S.S. and MAGIC [75, 78]. Other interesting objects are the candidate SNR called HESS J1457-593 (H3) and the PWN HESS J1849-000 (H9), detected by HAWC above 56 TeV and by LHAASO up to 350 TeV [47, 209]. We note that we did not find evidence for high-energy emission from the young massive stellar cluster HESS J1646-458 (Westerlund 1), located at $(l, b) = (339.55°, -0.35°)$, which has been proposed as a PeVatron candidate in [59]. This might be due to the very large angular scale of the source, whose emission is much larger than the correlation radius used to produce the significance maps (0.3°), or to the rejection of many runs as a result of the strict background quality cuts.

Interestingly, there are 5 hotspots that have been detected in the CA and not in the MA (see table A.2). Some of them, such as HESS J1303-631 (H1), HESS J1302-638 (H6) and also the PWN HESS J1420-607 (Kookaburra, H7) have been found in regions of enhanced exposure for the CA with respect to the MA, due to the manual rejection of runs with background model problems in the MA (see figure 8.5). For this reason they might be considered as additional hotspots to monitor at high energies with future observatories, even if they were not detected in the MA. The other hotspots with no MA counterpart, H6 and H9, don't correspond to any known VHE source. Therefore they are most likely explained by background model imperfections, even if a possible presence of real γ-ray emission cannot be excluded.

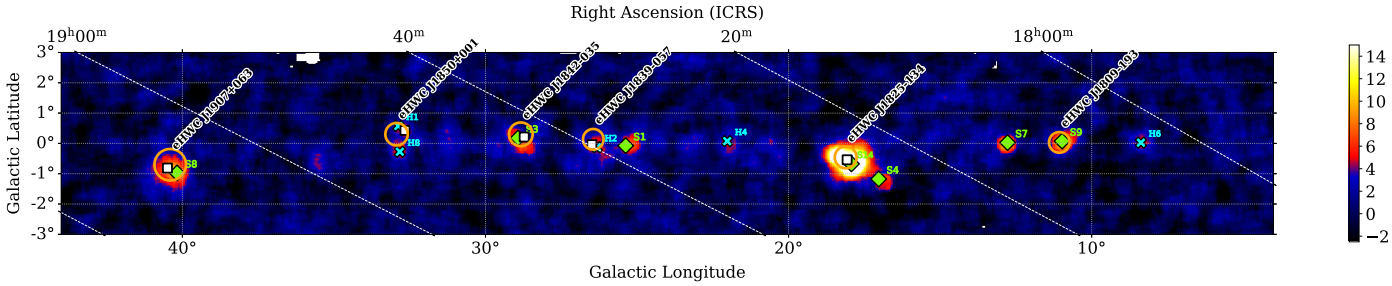

FIGURE 8.29: H.E.S.S. significance map (in units of Gaussian σ per 0.3° correlation radius) above 20 TeV in the $l = 4^\circ$ to 44° range, which is visible also by HAWC and LHAASO. The MA sources (hotspots) are indicated by green diamonds (cyan crosses), while the eHWC and LHAASO sources correspond to the orange circles and white squares, respectively.

8.3.16 Comparison with HAWC and LHAASO

It is interesting to compare the HEGPS source list with the latest available UHE source catalogs from WCTs such as HAWC [209] and LHAASO [47]. Figure 8.29 shows the portion of Galactic plane visible to both HAWC and H.E.S.S., from $l = 4^\circ$ to 44°, corresponding to the same region of the figure 1 from [47]. The figure clearly shows that each of the sources detected by HAWC ($E > 56$ TeV) and LHAASO ($E > 100$ TeV) at UHE energies is also seen by H.E.S.S. above 20 TeV, although in some cases just as a low-significance hotspot. There are also few H.E.S.S. sources and hotspots that do not have a UHE counterpart, either because their angular size is too small to be detected by the WCTs of because they have steep or cutoff γ-ray spectra. Figure 8.29 shows that, in this particular sky region, about half of the H.E.S.S. sources and hotspots ($E > 20$ TeV) still persist at ultra-high γ-ray energies. If this proportion holds for the whole HEGPS region, in which the total number of detected sources and hotspots is 25 (MA), this means that a future Southern WCT should be able to detect at least a dozen of UHE sources. We note that this is a very conservative estimate, since the crowded Galactic center region in the Southern sky likely hosts a much larger fraction of UHE sources than the North.

8.4 Powerful pulsars in the HEGPS

Recently, HAWC has reported observational evidence favoring a spatial correlation between the distribution of UHE sources and the most powerful Galactic pulsars [228]. In particular, motivated by the detection (> 56 TeV) of 8 UHE γ-ray sources located less than 0.5°[10] away from powerful pulsars ($\dot{E} \geq 1 \times 10^{36}\,\mathrm{erg\,s^{-1}}$), they made a joint-likelihood analysis of data from the vicinity of 24 powerful pulsar, some of which are inconspicuous at UHE. This study resulted in a 3σ evidence for the fact that UHE γ-ray emission is a "universal feature" near powerful pulsars. To follow up on this study, we can now try to evaluate the level of correlation between the position of the HEGPS sources and hotspots with the most powerful known Galactic pulsars. This is shown in figure 8.30, where we overlaid the positions of pulsars from the ATNF

[10] Which is the size of the HAWC PSF.

catalog [229][11] having $\dot{E} \geq 1 \times 10^{36}\,\mathrm{erg\,s^{-1}}$ (white circles) and $\dot{E} \geq 1 \times 10^{37}\,\mathrm{erg\,s^{-1}}$ (orange circles) on the HEGPS significance map (corresponding to figure 8.10). Clearly there are several sources and hotspots whose position is extremely close to a powerful pulsar. Table 8.3 reports the detailed information on the powerful pulsars with the smallest angular separation from the HEGPS sources and hotspots.

Out of 25 TeV objects, 16 have a powerful pulsar nearby ($< 0.5^{\circ}$ offset). This does not necessarily imply that all of them have leptonic origin (see e.g. the case of HESS J1745-290, which might be associated with a PWN, Sgr A* or the diffuse emission around the Galactic center), but supports the evidence that powerful pulsars are extremely efficient particle accelerators, and most of the γ-ray emission detected in the UHE band could have leptonic origin.

The TeV objects that do not have a powerful pulsar within 0.5°, that in our sample are 9, are less likely than the others to have leptonic origin, thus naturally becoming a list of hadronic PeVatron candidates to be observed with priority by the next-generation experiments such as CTA and SWGO. They are, in order of decreasing detection significance above 20 TeV:

Sources

HESS J1702-420 (UNID)
HESS J1634-472 (UNID)
HESS J1713-397 (SNR)
HESS J1826-148 (BINARY)
HESS J1843-033 (UNID)

and

Hotspots

HESS J1457-593 (SNR?)
HESS J1852-000 (UNID)
HESS J1026-582 (PWN?)
HESS J1841-055 (UNID)

We note that the sources HESS J1826-148 and HESS J1026-582, included in the above lists for the sake of completeness, are be retained as PeVatron candidates with less observational priority than the others. The first is a γ-ray binary, a class of sources that are not generally believed to be efficient hadronic accelerators, and the second is positionally near (and potentially associated with) the pulsar PSR J1028-5819, whose spin-down luminosity of $\dot{E} = 8.3 \times 10^{35}\,\mathrm{erg\,s^{-1}}$ [232] was only slightly below the threshold of $10^{36}\,\mathrm{erg\,s^{-1}}$ that we set for the search of powerful pulsars. HESS J1702-420 appears in the list with the highest significance value, which confirms its top observervation priority by future VHE and UHE experiments. In the future, a more rigorous priority ranking strategy, based on the exposure-corrected flux and spectral characteristics of each PeVatron candidate, will allow to efficiently allocate observation time with H.E.S.S. and other experiments such as CTA South and SWGO. We finally note that the list of PeVatron candidates presented above must be completed with the other sources that, despite having a powerful pulsar nearby, might still be associated with hadronic emission processes. We refer in particular (based on the source-by-source discussions of section 8.3) to HESS J1825-137 (PWN?), HESS J1809-193 (UNID),

[11] With the exception of the PSR J1849-0001 nearby HESS J1849-000, for which the position and characteristics were taken from [230, 231].

HESS J1908+063 (UNID), HESS J1813-178 (COMP), HESS J1616-508 (PWN?) and HESS J1745-290 (UNID).

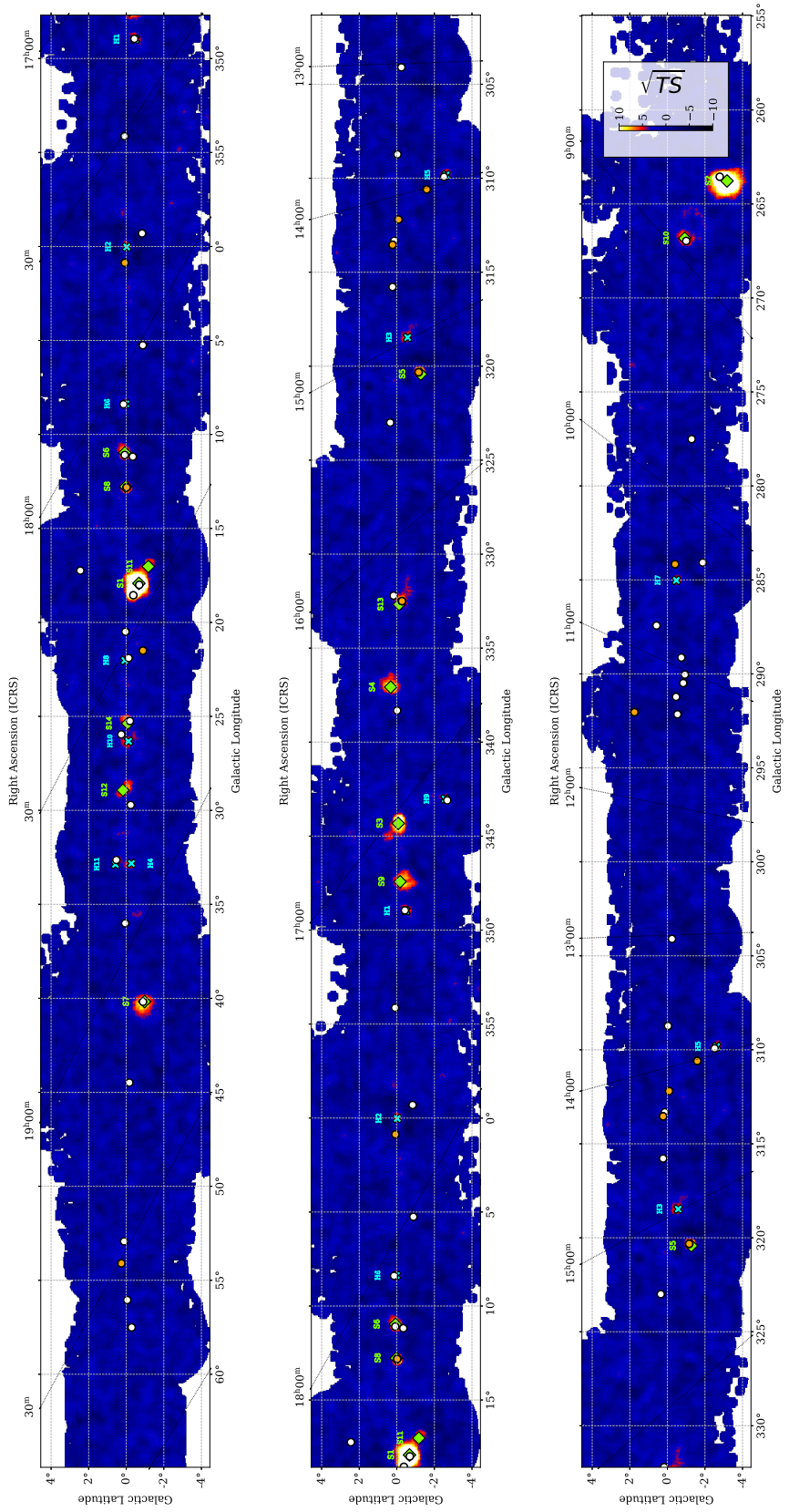

FIGURE 8.30: Same as figure 8.10 with overlaid the positions of the $\dot{E} \geq 1 \times 10^{36}\,\mathrm{erg\,s^{-1}}$ (white circles) and $\dot{E} \geq 1 \times 10^{37}\,\mathrm{erg\,s^{-1}}$ pulsars (orange circles) from the ATNF catalog [229].

Name	HGPS association	Nearest PSR	Offset	$\dot{E}$	$\dot{E}/d^2$	d	τ (P/2$\dot{P}$)	P	$\dot{P}$
			[deg]	[$\times 10^{36}$ erg/s]	[$\times 10^{34}$ erg/(kpc^2 s)]	[kpc]	[kyr]	[s]	[s/s]
S1	HESS J1825-137	PSR J1826-1334	0.08	2.8	21.9	3.6	21.4	0.101	7.53×10^{-14}
S2	HESS J0835-455	PSR J0835-4510	0.45	6.9	8831.0	0.3	11.3	0.089	1.25×10^{-13}
S3	HESS J1702-420	–	$> 0.5^o$	–	–	–	–	–	–
S4	HESS J1634-472	–	$> 0.5^o$	–	–	–	–	–	–
S5	HESS J1514-591	PSR J1513-5908	0.15	17.3	89.5	4.4	1.6	0.152	1.53×10^{-12}
S6	HESS J1809-193	PSR J1809-1917	0.12	1.8	16.7	3.3	51.4	0.083	2.55×10^{-14}
S7	HESS J1908+063	PSR J1907+0602	0.08	2.8	50.3	2.4	19.5	0.107	8.68×10^{-14}
S8	HESS J1813-178	PSR J1813-1749	0.06	55.9	253.2	4.7	5.6	0.045	1.27×10^{-13}
S9	HESS J1713-397	–	$> 0.5^o$	–	–	–	–	–	–
S10	HESS J0852-463	PSR J0855-4644	0.16	1.1	3.3	5.6	141.1	0.065	7.26×10^{-15}
S11	HESS J1826-148	–	$> 0.5^o$	–	–	–	–	–	–
S12	HESS J1843-033	–	$> 0.5^o$	–	–	–	–	–	–
S13	HESS J1616-508	PSR J1617-5055	0.23	16.0	71.1	4.7	8.1	0.069	1.35×10^{-13}
S14	HESS J1837-069	PSR J1838-0655	0.18	5.5	12.7	6.6	22.7	0.070	4.92×10^{-14}
H1	HESS J1718-385	PSR J1718-3825	0.05	1.3	10.3	3.5	89.5	0.075	1.32×10^{-14}
H2	HESS J1745-290	PSR J0359+5414	0.04	1.3	–	–	75.2	0.079	1.67×10^{-14}
H3	HESS J1457-593	–	$> 0.5^o$	–	–	–	–	–	–
H4	HESS J1852-000	–	$> 0.5^o$	–	–	–	–	–	–
H5	HESS J1356-645	PSR J1357-6429	0.15	3.1	32.3	3.1	7.3	0.166	3.60×10^{-13}
H6	HESS J1804-216	PSR J1803-2137	0.12	2.2	11.5	4.4	15.8	0.134	1.34×10^{-13}
H7	HESS J1026-582	–	$> 0.5^o$	–	–	–	–	–	–
H8	HGPSC 072	PSR J1831-0952	0.24	1.1	8.0	3.7	128.0	0.067	8.32×10^{-15}
H9	HESS J1708-443	PSR J1709-4429	0.13	3.4	50.5	2.6	17.5	0.102	9.30×10^{-14}
H10	HESS J1841-055	–	$> 0.5^o$	–	–	–	–	–	–
H11	HESS J1849-000	PSR J1849-0001*	0.03	9	18.4	7	42.9	0.039	1.42×10^{-14}

TABLE 8.3: Detected sources and hotspots from the MA, with their nearest powerful pulsar.

Chapter 9

Perspectives and conclusions

9.1 Introduction

The Cherenkov Telescope Array (CTA), introduced in chapter 2, will be the major VHE γ-ray detector of the near future. In particular, its Chilean site will observe for the first time the Southern γ-ray sky with nearly $10\times$ better sensitivity and angular resolution up to $\approx 100\,\mathrm{TeV}$ compared to H.E.S.S.. Waiting for the array to be deployed, it is useful to evaluate its potential in matter of detection and identification of the Galactic PeVatrons. A CTA Consortium paper dedicated to this topic is currently in preparation. I have contributed by supporting the set up of a simulation and analysis pipeline with Gammapy that allows one to evaluate the detection and modeling capabilities of the future CTA array. In this final chapter, some of the elements and first results of this pipeline will be described (see section 9.2).

All results presented in this chapter are preliminary, and are based on a simulated version of the CTA IRFs (called `prod3b-v2`, available on the CTA webpage) that does not precisely reflect the performance of the future array. The main reason why this IRF release is considered outdated is that the planned array has been reduced in size with respect to the original project, on which the IRF simulations were based (see section 2.4). In particular, the number of SSTs that will be deployed at the Southern CTA site has been halved with respect to the initial plan (37 vs. 70), mainly for reasons of cost. Since the SSTs are responsible for the γ-ray detection at the highest energies, this will inevitably have a negative impact on the CTA PeVatron studies. Therefore the performance plots presented in section 9.2 are to be considered optimistic. Also, the real CTA IRFs will be distributed on a run-by-run basis, with a response adapted (via interpolation) to the observation conditions, while at the moment they were simulated only for a small set of zenith angles. With these caveats, it can still be interesting to look at the methodologies applied in this study, that may be updated once a new version of the CTA IRFs will be distributed.

Finally, we end the chapter with a section dedicated to the general summary, remarks and conclusions of the thesis (section 9.3).

9.2 The CTA potential in the search for PeVatrons

In this section we describe a series of predictions that can be made, using Gammapy[1], on the ability of CTA to detect and correctly model Galactic PeVatrons. The starting

[1] The results presented in section 9.2.1 (9.2.2) were obtained using Gammapy 0.15 (0.18.2).

point is the simulation of CTA data, based on the assumption of a γ-ray spectral shape and spatial morphology. The simulated data cube can be modeled to estimate the source detection potential and the accuracy of the model parameters reconstruction. The results are strongly dependent on the characteristics of the simulated source, and for this reason the study has to be iterated across a multi-dimensional parameter space defined by the degrees of freedom of the simulated model. An example of the products of such pipeline are the *spectral cutoff detection maps* described in section 9.2.1. They provide an insight on the spectral reconstruction accuracy by CTA at the highest energies, which is a crucial point for PeVatron studies. A similar method can be applied, as discussed in section 9.2.2, to get an idea of the kind of predictions that CTA will be able to make on the detectability of UHE sources by facilities such as SWGO and LHAASO.

9.2.1 Spectral cutoff detection maps

Estimating the detection probablity of high-energy spectral cutoffs with CTA is an important point in the search for Galactic PeVatrons. In principle, all non-thermal spectra are cut off at a sufficiently high energy, associated with the maximum particle energy of the parent cosmic ray distribution. A non-detection of the γ-ray spectral cutoff is therefore due to a limited sensitivity at the highest energies. Instead, for the cases in which the cutoff can be detected, its measurement well below (above) 100 TeV can be seen as an argument against (in favor of) the PeVatron hypothesis for a given source[2]. Throughout this section, the γ-ray spectral shape is always assumed to be a power law with exponential cutoff, of the form

$$\frac{dN}{dE}(E) = \Phi_0 \left(\frac{E}{E_0}\right)^{-\Gamma} e^{-E/E_{\rm cut}} \,. \tag{9.1}$$

In Gammapy $E_{\rm cut}$ is parametrized as $1/\lambda$, where λ has units of TeV^{-1}. This simplifies, from a computational point of view, the $E_{\rm cut} \to +\infty$ case to $\lambda \to 0^+$.

There are a few practical questions that we can try to tackle with our Gammapy simulation pipeline. For example, under which conditions would CTA be capable of detecting an $E_{\rm cut} < 100\,\mathrm{TeV}$, thus constraining the PeVatron nature of a source? Or, for a source with $E_{\rm cut} > 100\,\mathrm{TeV}$, would the CTA high-energy sensitivity be enough to detect the cutoff, thus providing an accurate spectral measurement up to the UHE range, or a simple power law would always be preferred? To answer these questions, we defined a discrete simulation parameter space based on the degrees of freedom of the function 9.1, with $E_0 = 1\,\mathrm{TeV}$. In particular we chose $\Phi_0 \in [5, 50]\,\mathrm{mCrab}$[3], $\Gamma \in [1.7, 2.3]$ and $E_{\rm cut} = 50, 100,$ and $200\,\mathrm{TeV}$. We then assumed a point-like source morphology and used the background model from the CTA IRFs, to perform 10^3 simulations at each node of the three-dimensional $(\Phi_0, \Gamma, E_{\rm cut})$ grid. For each simulation we computed the maximum likelihood values obtained from a fit of the fake data using a power law with and without an exponential cutoff, and compared them using the likelihood ratio test, i.e. computing the TS defined in equation 3.8. As a criterion for the cutoff detection we used $\mathrm{TS} \geq 9$, which is equivalent to a $\geq 3\sigma$ confidence level detection. By computing the fraction of simulations for which the presence of

[2] Even if, as discussed in the previous chapter, also leptonic particle accelerator such as PWNe emit γ-rays $E \gtrsim 100\,\mathrm{TeV}$.

[3] Throughout section 9.2.1 1 Crab Unit is defined as $3.8 \times 10^{-11}\,\mathrm{TeV}^{-1}\,\mathrm{cm}^{-2}\,\mathrm{s}^{-1}$, which corresponds to the differential Crab nebula flux at 1 TeV (from [233]).

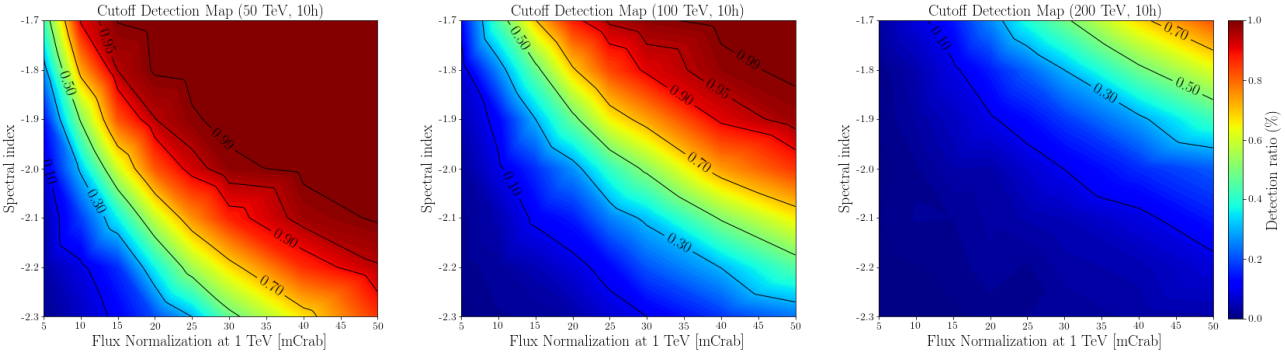

FIGURE 9.1: Spectral cutoff detection probability assuming a 10 h CTA South pointing, as a function of the spectral index and brightness of the simulated source, for an injected cutoff at 50 TeV (left), 100 TeV (center) and 200 TeV (right). More detailed informations are provided in the main text.

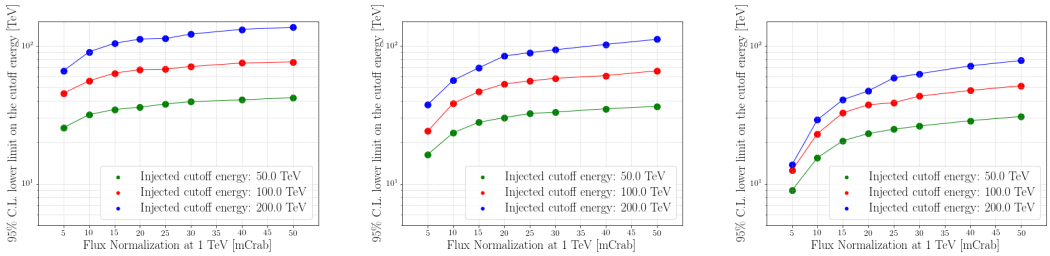

FIGURE 9.2: 95% confidence level lower limits on the spectral cutoff for the cases of non-detection of the cutoff. The left (center, right) panel correspond to a simulated spectral index $\Gamma = 1.7$ (2, 2.3).

an exponential cutoff was preferred over a simple power law hypothesis, we then obtained the cutoff detection probability at each node of the grid. After interpolating the grid we finally produced the cutoff detection maps shown in figure 9.1, which were computed assuming a 10 h observation time with the CTA South array and for a 20° zenith angle pointing. Each panel of the figure corresponds to a different cutoff value for the simulated source. The color bar encodes the spectral cutoff detection probability as a function of the simulated model parameters.

The maps in figure 9.1 show that for bright sources with hard spectra and relatively low cutoff energies the latter can be easily detected. In particular, the PeVatron nature of a source with $E_{\rm cut} = 50\,\text{TeV}$, $\Phi_0 \gtrsim 20\,\text{mCrab}$ and $\Gamma \lesssim 2.0$ would be easily excluded, since the cutoff detection probability is over 90%. Instead for sources that are faint, have soft spectra and cutoff at $\gtrsim 100\,\text{TeV}$, the latter is unlikely to be detected. In such cases it can be interesting to estimate a cutoff energy lower limit, $E_{\rm cut}^{\rm low}$, and compare it with the value of the simulated cutoff. Figure 9.2 shows the variations of the average $E_{\rm cut}^{\rm low}$ values (corresponding to a 95% confidence level), as a function of the spectral normalization, cutoff and index of the simulated source. The figure shows that the most constraining (i.e. closest to the injected value) $E_{\rm cut}^{\rm low}$ estimates are obtained for a hard and bright source (left panel, green curve), while the $E_{\rm cut}^{\rm low}$ prediction becomes more and more conservative (i.e. lower than the simulated value) for sources with steeper and fainter spectra.

Other more detailed studies are possible using the same analysis pipeline. For example, one can evaluate the cutoff detection probability as a function of the simulated source size. This is shown in figure 9.3 for two different choices of simulated spectral parameters, i.e. $(\Gamma, \Phi_0/\text{mCrab}, E_{\text{cut}}/\text{TeV}) = (2, 20, 100)$ in red and $(1.7, 50, 200)$ in blue. For each source size and set of source parameters, we performed 10^3 simulations, assuming a source offset from the pointing position of 0.7^{o}. The figure additionally compares the performance obtained from the 1D (square markers) and 3D (round markers) analysis techniques (described in sections 3.4.2 and 3.4.4), used in both cases to measure and fit the simulated source spectrum. The 1D analysis was in this case performed using an OFF background measurement extracted from the FoV background model, leading (as for the 3D analysis) to *Cash* statistic. One can see from the left panel of the figure that the cutoff detection probability decreases significantly with the source size, as expected due to the spread of the source flux over a larger area (which worsens the signal to background ratio). The right panel shows instead that for the cases in which the cutoff is not detected the lower limit becomes more and more conservative with the increase of the source size (although in a slower way than the cutoff detection probability). In all cases, the 3D analysis approach provides better performance than the 1D one, likely due to the lack of sufficient photon statistics at high energies to compute a reliable background estimate. This holds even more in a real life scenario, where other effects such as the contamination between different sources will further limit the potential of the 1D analysis technique.

Another possible improvement toward a realistic analysis scenario consists in the use of physically motivated radiative models, instead of simple γ-ray power law spectra, to simulate and fit the source emission from PeVatron candidates. This is an important point, because the typical γ-ray spectra from hadronic interactions are not necessarily expected to be power laws with exponential cutoffs. For example, it is known that an exponential cutoff power law distribution of protons produces, via hadronic interactions, a γ-ray spectrum with a sub-exponential cutoff (see section 1.3.1). Therefore, to avoid spectral modeling biases at the highest energies, either an additional degree of freedom controlling the cutoff shape should be added to the γ-ray spectral models, or the simulation and modeling should be performed directly in the proton parameter space with the `NaimaSpectralModel`. Finally, all these studies should take into account the presence of the diffuse γ-ray emission field, which complicates the source modeling and further disfavors the use of the 1D analysis technique against the 3D one. All of this is currently being developed by the main authors of the dedicated CTA Consortium paper.

9.2.2 CTA observations of UHE sources

Thanks to the recent LHAASO detection of 12 UHE sources [47], a real breaktrough in the field, we now have an idea of the kind of γ-ray flux levels and spectral shapes that are expected to be observed up to $\approx 100\,\text{TeV}$ by CTA. In particular, LHAASO has measured and published the γ-ray spectra of three sources, LHAASO J2226+6057, LHAASO J1908+0621 and LHAASO J1825-1326, from ≈ 10 to $\approx 600\,\text{TeV}$. All three spectra are characterized by a significant spectral curvature, which is better described by a *log-parabola* model than a simple power law. The log-parabola is defined as

$$\frac{dN}{dE}(E) = \Phi_0 \left(\frac{E}{E_0}\right)^{-\alpha-\beta\log_{10}(E/E_0)}, \tag{9.2}$$

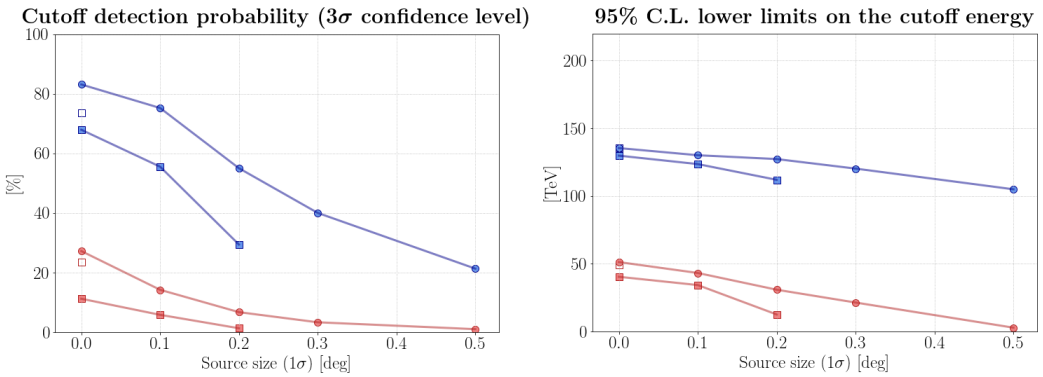

FIGURE 9.3: Spectral cutoff detection probability (left) and lower limit (right) as a function of the simulated source size, for two particular choices of simulated source parameters: $(\Gamma, \Phi_0/\text{mCrab}, E_{\text{cut}}/\text{TeV}) = (2, 20, 100)$, in red, and $(1.7, 50, 200)$ in blue. The round (square) markers refer to the 3D (1D) analysis results. The 1D analysis results for an extended source (filled square markers) were obtained in full containment, which means adopting a sufficiently large integration region to enclose the whole source flux. Instead the 1D analysis for a point-like source (conventionally indicated by a source size of 0.0°) was performed both in full containment (for coherence with the extended source analysis) and with the more traditional point-like approach (i.e. assuming as containment region the 68% containment of the PSF and correcting for leakage). The latter is shown by the unfilled square markers.

where $E_0 = 10\,\text{TeV}$ is the reference energy, $\Phi_0 = dN/dE(E_0)$ is the spectral normalization at E_0, α is the spectral index and β measures the curvature of the spectrum. Using this kind of function as an input for the CTA simulations, one can directly get an idea of the future CTA view of UHE sources that are similar to the LHAASO ones.

As an example, here we adopted a spectral index $\alpha = 2.27$ and curvature $\beta = 0.46$, corresponding to the ones measured by LHAASO for the source LHAASO J1908+0621 (associated with the H.E.S.S. source HESS J1908+063). This choice was dictated by the fact that, among the 3 sources with a published spectrum, LHAASO J1908+0621 is the one with the smallest error bars at high energy (this can be seen in figure 1 of [47]). Following again the LHAASO paper, we assumed as 2D Gaussian spatial morphology with a 0.58° radius. We then defined an array of trial spectral normalizations at 100 TeV, $\Phi_{100} \in [0.3, 3]\,\text{C.U.}$ [4], and evaluated the possibility of source detection at the highest energies with CTA as a function of the observation livetime for each value of Φ_{100}. In the future, full multi-dimensional matrices may be produced, by also varying the other spectral and spatial parameters. The left panel (right panel) of figure 9.4 shows the variation of *Cash* significance for the source detection above 50 TeV (100 TeV) with CTA, as a function of the observation livetime. The blue (yellow) significance distributions refer to a source with a flux of 0.3 (3) C.U. at 100 TeV, which is faint (bright) compared to LHAASO J1908+0621 (1.36 C.U.). The bright source can be easily detected at $E > 50\,\text{TeV}$, and also reaches 5σ significance above 100 TeV with a 100 h observation time. Instead, the faint source is only marginally detected ($\approx 3\sigma$) above 50 TeV and it remains undetectable above 100 TeV

[4] Throughout the section 9.2.2, the C.U. is defined as the differential γ-ray flux from the Crab nebula at 100 TeV, $\text{C.U.} = 6.1 \times 10^{-17}\,\text{TeV}^{-1}\text{cm}^{-2}\text{s}^{-1}$, from [47].

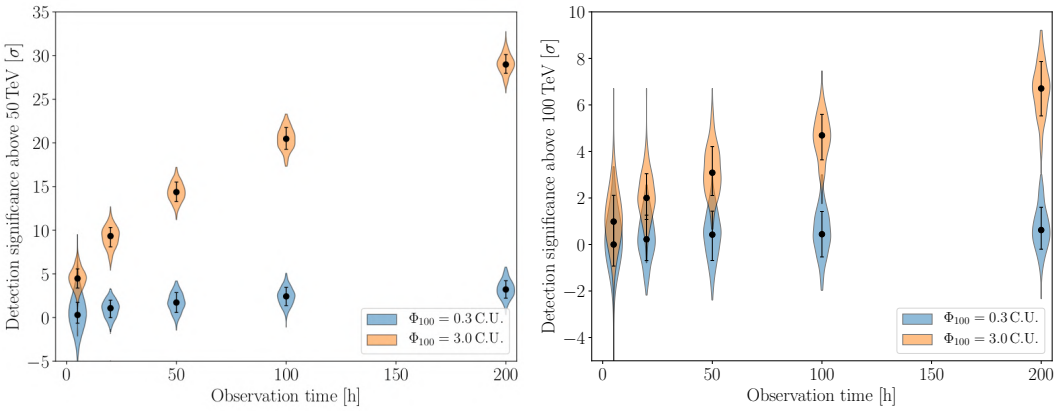

FIGURE 9.4: Source detection significance above 50 TeV (left) and 100 TeV (right) as a function of the CTA observation livetime, obtained assuming the spectral shape of the source LHAASO J1908+0621 ($R_{\text{source}} = 0.58^{\circ}$) and re-scaling its flux to make the cases of a faint and bright source at 100 TeV, respectively shown by the blue and yellow significance distributions. The error bars indicate the 1σ statistical confidence interval of the distributions.

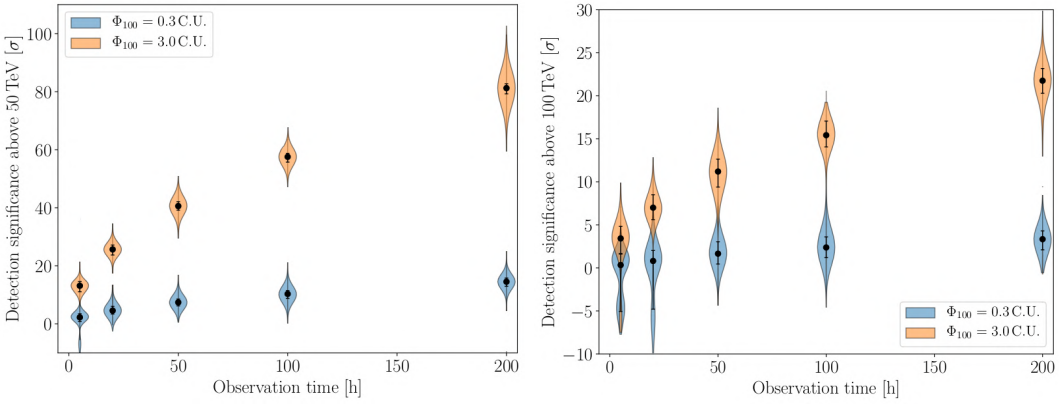

FIGURE 9.5: Same as figure 9.4, but for a source with the spectral parameters of LHAASO J1908+0621 and a 0.1° spatial Gaussian radius.

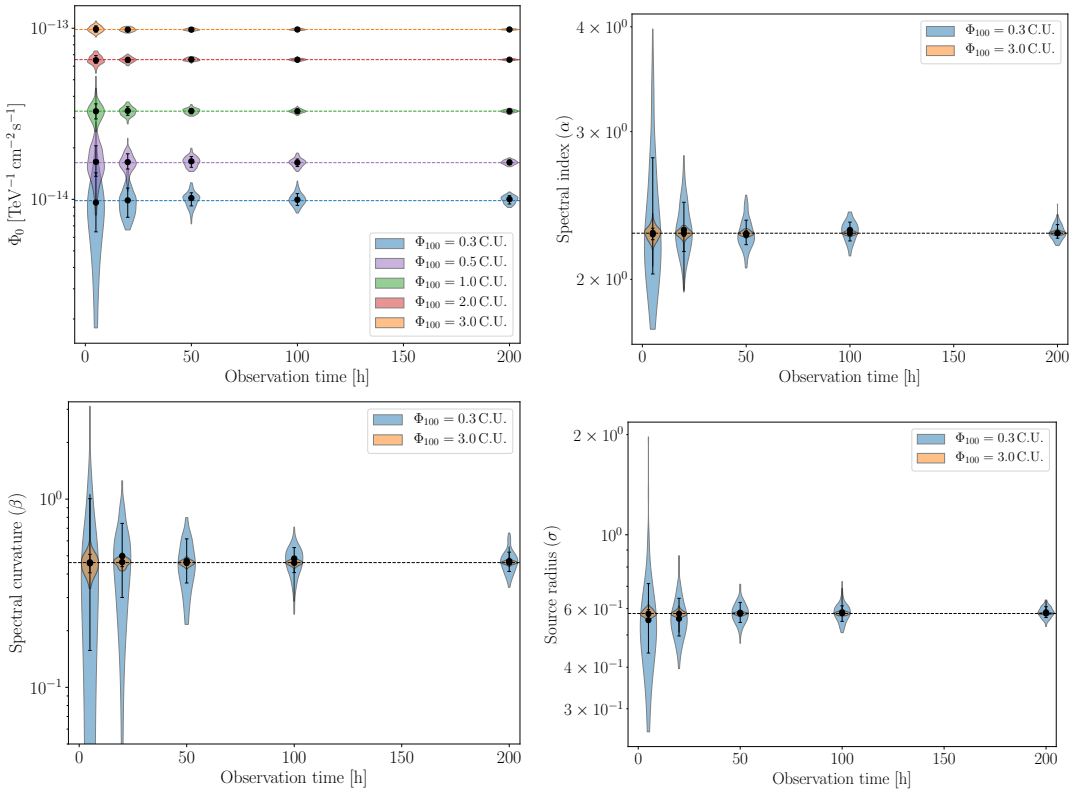

FIGURE 9.6: Distributions of the best-fit parameter values obtained by fitting the simulated emission from a source with a spectral shape similar to LHAASO J1908+0621 ($R_{\text{source}} = 0.58^{\circ}$), as a function of the CTA observation livetime. Here we used 500 simulations per point. The parameter names, indicated in the y-axis labels of all panels, correspond to the conventions of equation 9.2. The simulated parameter values are shown by the dashed horizontal lines. As visible in the upper left panel, we have repeated the study for an array of source fluxes, ranging from a faint source at 100 TeV (in blue) to a fairly bright one (yellow). In the other panels, to simplify the visualization of the results, only the two extreme cases are shown. In all panels, the error bars indicate the 1σ statistical confidence intervals of the distributions.

even with a 200 h pointing. For sources with smaller size than LHAASO J1908+0621, with a better signal to background ratio, the high-energy detection would be easier. This is visible in figure 9.5, where the time-evolution of the detection significance of a 0.1°-radius source (again with the spectrum of LHAASO J1908+0621) is shown. The 5σ detection time is significantly reduced with respect to the 0.58° radius case, meaning that the source size may prove to be an important element of detection bias for CTA, with only the smaller-scale sources detected up to the highest energies.

We additionally looked at the accuracy in the model parameters reconstruction, obtained from a fit in the whole CTA energy range, as a function of the observation livetime. The figure 9.6 shows that, as expected for a case in which the statistical uncertainties dominate over the systematic ones, the spread of the best-fit parameter value distributions decreases with increasing Φ_{100} and observation livetime. But in all cases, the average fitted parameter values are always correctly distributed around the simulated ones (indicated by the dashed horizontal lines). This is in line with the expectation, in case the statistical uncertainties dominate over the systematic ones.

Looking back to figure 9.4, one may conclude that CTA will be able to significantly detect γ-ray emission above 100 TeV only from extremely bright sources, if they are as extended as LHAASO J1802+0621 ($R_{\rm source} = 0.58^{\circ}$). Since the figure 9.4 was produced assuming an optimistic IRF version, we notice that even such sources might need an extremely long exposure (hundreds of hours) in order to be detected above 100 TeV. Instead, for typical γ-ray sources, unless their spatial extension is close to the CTA PSF, the significant detection will likely be limited to $E \lesssim 100$ TeV. However, as demonstrated by figure 9.6, even in such cases the spectral modeling of CTA data below 100 TeV is statistically accurate. Therefore CTA may play an important role for the PeVatron studies even in those cases in which the detection is limited to $E \lesssim 100$ TeV, by extrapolating its measured spectra up to the UHE range and making predictions on the source detectability by other facilities such as SWGO and LHAASO.

To get an idea of the conditions under which this would be possible, we extrapolated at 200 TeV the source spectrum resulting from each simulation and fit of a source having the same morphology and spectral shape as LHAASO J1908+0621, for a range of spectral normalizations. We then compared the extrapolated fluxes with the source detection sensitivities of SWGO and LHAASO. By computing the fraction of realizations for which the source flux is higher than the sensitivities, we then obtained the CTA prediction on the source detection probability at 200 TeV by SWGO and LHAASO, as a function of the source spectral normalization and observation live-time. This way we also estimated the impact of the statistical mis-reconstruction of the spectral model parameters from the CTA simulations. The result is shown in figure 9.7, for SWGO (left panel) and LHAASO (right panel). For a faint source ($\Phi_{100} \lesssim 1$ C.U.), CTA predicts that the source is not detectable by SWGO at 200 TeV. The estimated detection probability decreases with the observation time in this case, because the increasing quality in the model parameters reconstruction brings the prediction closer to the expected non-detectability outcome (see figure 9.8). Instead for LHAASO, which has a better sensitivity around 200 TeV, the detection probability better than 60% already for $\Phi_{100} \gtrsim 0.5$ C.U.. In this study, the strongest assumptions that are made are on the spatial shape of the simulated source, assumed to be constant over the whole CTA energy range, and on the estimated SWGO and LHAASO detection sensitivities for extended sources. The latter were obtained from the reference plots in the webpage https://www.cta-observatory.org/science/ctao-performance/#1472563157332-1ef9e83d-426c, and linearly re-scaled to correct for the point-source assumption.

Despite all the caveats, this study allows us to conclude that CTA will likely be able to pinpoint the most promising PeVatron candidates to be observed in the UHE range by WCTs such as SWGO and LHAASO, especially if they are less extended than LHAASO J1908+0621. Their measured UHE spectra will then provide a complement to the lower-energy CTA observations, hopefully allowing to firmly identify their emission mechanisms and close the debate on their possible PeVatron nature.

9.3 Summary and conclusions

In this thesis we described the search for the Galactic cosmic ray factories, called PeVatrons, using data from H.E.S.S., a VHE γ-ray telescope array located in Namibia. For the first time in the history of H.E.S.S. the 3D analysis technique was used to

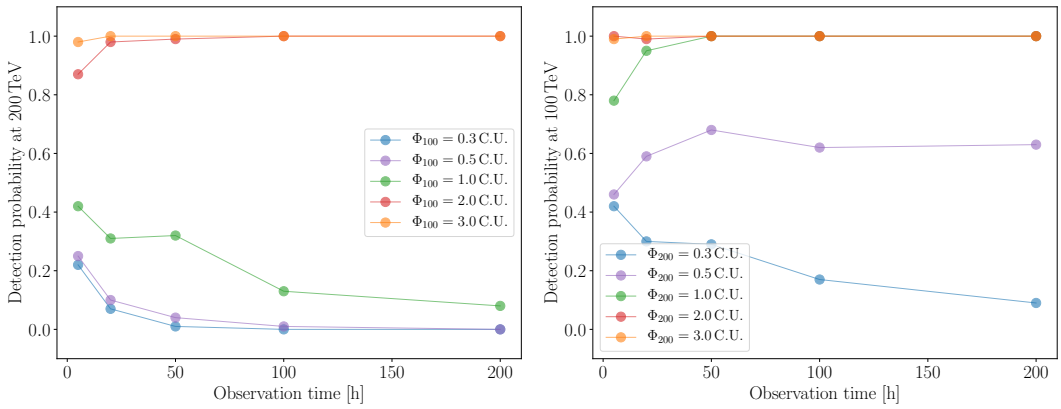

FIGURE 9.7: Detection probability at 200 TeV predicted by CTA for a source with the spectral index and curvature of LHAASO J1908+0621 ($R_{\rm source} = 0.58^{\rm o}$), by SWGO (left) and LHAASO (right). The probability is computed as a function of the CTA observation livetime and the source flux normalization at 100 TeV. More details are provided in the main text.

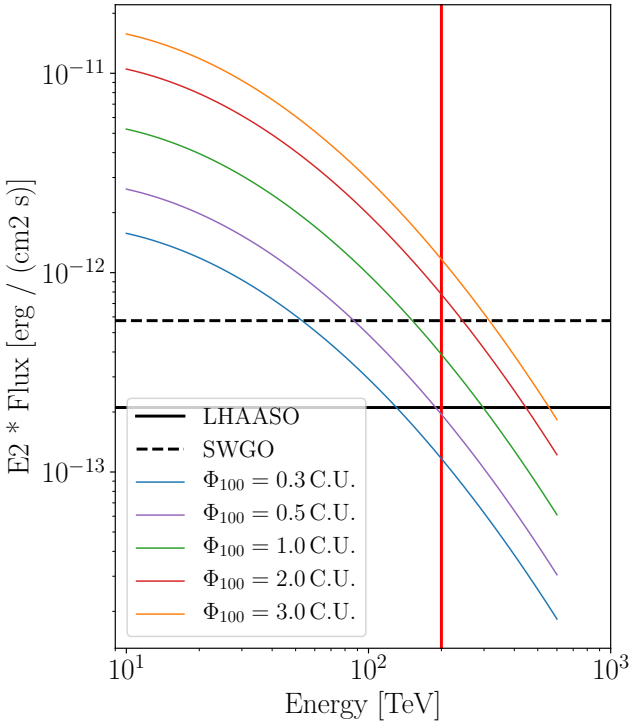

FIGURE 9.8: The γ-ray spectrum of LHAASO J1908+0621, from [47], whose spectrum has been re-scaled in a range of 1 order of magnitude in flux. The vertical red line indicates the energy of 200 TeV, while the horizontal solid (dashed) lines show the estimate of the extended source detection sensitivity of LHAASO (SWGO) that we used to produce figure 9.7.

derive information on the physical properties of Galactic objects using spatial and spectral parametric templates. We also contributed to the development of Gammapy, the official software tool of the Cherenkov Telescope Array (CTA) Observatory. Using Gammapy, we created an analysis pipeline that allowed us to pinpoint promising PeVatron candidates in the Southern γ-ray sky, to be observed with priority by future-generation instruments such as CTA and SWGO.

We first focused on a particular source called HESS J1702-420 (see the part II). The 3D analysis allowed us to separate from the bulk of HESS J1702-420 a new small-size source component, called HESS J1702-420A, for which we found evidence of γ-ray emission up to 100 TeV. HESS J1702-420A has a symmetric shape, with spatial extension of $(0.06 \pm 0.02_{\rm stat} \pm 0.03_{\rm sys})^{\rm o}$, and a remarkably hard γ-ray spectral index of $\Gamma = 1.53 \pm 0.19_{\rm stat} \pm 0.20_{\rm sys}$. Based on the available data, it was not possible to establish whether this new object is independent from the rest of HESS J1702-420, or if it is just a high-energy emission zone in a source with complex morphology. In either case, our study allowed us to conclude that, if powered by hadronic processes, the γ-ray emission from HESS J1702-420A is likely associated with the presence of PeV protons. This scenario however could not be confirmed due to the lack of a clear correlation between the HESS J1702-420A morphology and gas distribution images, which leave a leptonic interpretation for this new γ-ray source still possible. The nature of HESS J1702-420, and in particular of HESS J1702-420A, remains elusive, but our analysis allowed us to identify it as a PeVatron candidate and a high-priority target for future VHE and UHE γ-ray facilities.

After such a detailed study dedicated to HESS J1702-420, the logical step forward was the application of a similar analysis approach to a larger set of sources. We therefore adopted the same basic ingredients (Gammapy, high-energy optimized IRFs and 3D modeling) to set up a full survey analysis pipeline. This effort has led us to the production of the preliminary version of a H.E.S.S. high-Energy Galactic Plane Survey (HEGPS) catalog (see chapter 8). This is a collection of 14 sources significantly detected by H.E.S.S. above 20 TeV, in the $|b| \leq 5^{\rm o}$, $0^{\rm o} \leq l \leq 70^{\rm o}$ and $250^{\rm o} \leq l \leq 360^{\rm o}$ region. The three of them with the highest detection significance are HESS J1825-137, HESS J0835-455 (Vela X) and HESS J1702-420. Remarkably, the same three source have been confirmed as the brightest ones above 20 TeV by crosscheck analysis, and they are also the only three objects for which H.E.S.S. detected significant γ-ray emission above 50 TeV. Therefore they become high-priority targets for future VHE and UHE telescopes.

For the first time, the 3D analysis technique allowed us to separate the γ-ray emission above 20 TeV associated with the PWN of PSR J0855-4644 from the shell of the Vela Jr SNR, which is inconspicuous at such high energies. The spectral index of the PWN, ≈ 1.75, is extremely hard and remarkably similar to the one of HESS J1702-420A, which might point toward a common emission mechanism. Another achievement was the detection of γ-ray emission above 20 TeV from the binary system LS 5039, for which all existing measurements stop below 20 TeV.

We compared the HEGPS with the most recent HAWC and LHAASO catalogs, in the overlapping observation region. We found that all of the UHE sources detected by WCTs have VHE (H.E.S.S.) counterparts above 20 TeV, wherheas only half of the H.E.S.S. objects persist in the UHE range. We also compared the spatial distribution of the HEGPS sources with that of the known powerful Galactic pulsars. Out of 25 H.E.S.S. objects, 16 have a high $\dot{E}$ pulsar nearby ($< 0.5^{\rm o}$ offset). The remaining 9 sources (plus 6 others which have powerful but not clearly associated pulsars nearby)

naturally constitute a H.E.S.S. legacy list of hadronic PeVatron candidates. In the future, the HEGPS work will be fully cross-checked using an alternative analysis configuration. This will allow us to validate the analysis results, export the DL4 (datasets) and DL5 (catalog) products to FITS format and release them in the spirit of the open source science approach.

In this last chapter we discussed the PeVatron identification prospects for the future CTA array. All results are preliminary, since the IRFs of the final array are not yet available, and should be intended more as a proof of concept than a real estimation of the CTA potential. Still, it is interesting to see that, based on the currently available version of the CTA IRFs, the future array will be able to detect and correctly model at least the brightest or smaller-scale sources up to 100 TeV, and to make predictions on the source detectability by UHE facilities such as SWGO and LHAASO. This kind of interplay between UHE water Cherenkov telescopes, with their good sensitivity but poor angular resolution above 100 TeV, and CTA, with its excellent sensitivity and PSF up to 100 TeV, will be one of the most important new elements of the field in the coming years. In these exciting times, we may be close to the long awaited identification of the powerful factories of cosmic rays in the Galaxy.

Appendix A

Additional HEGPS material

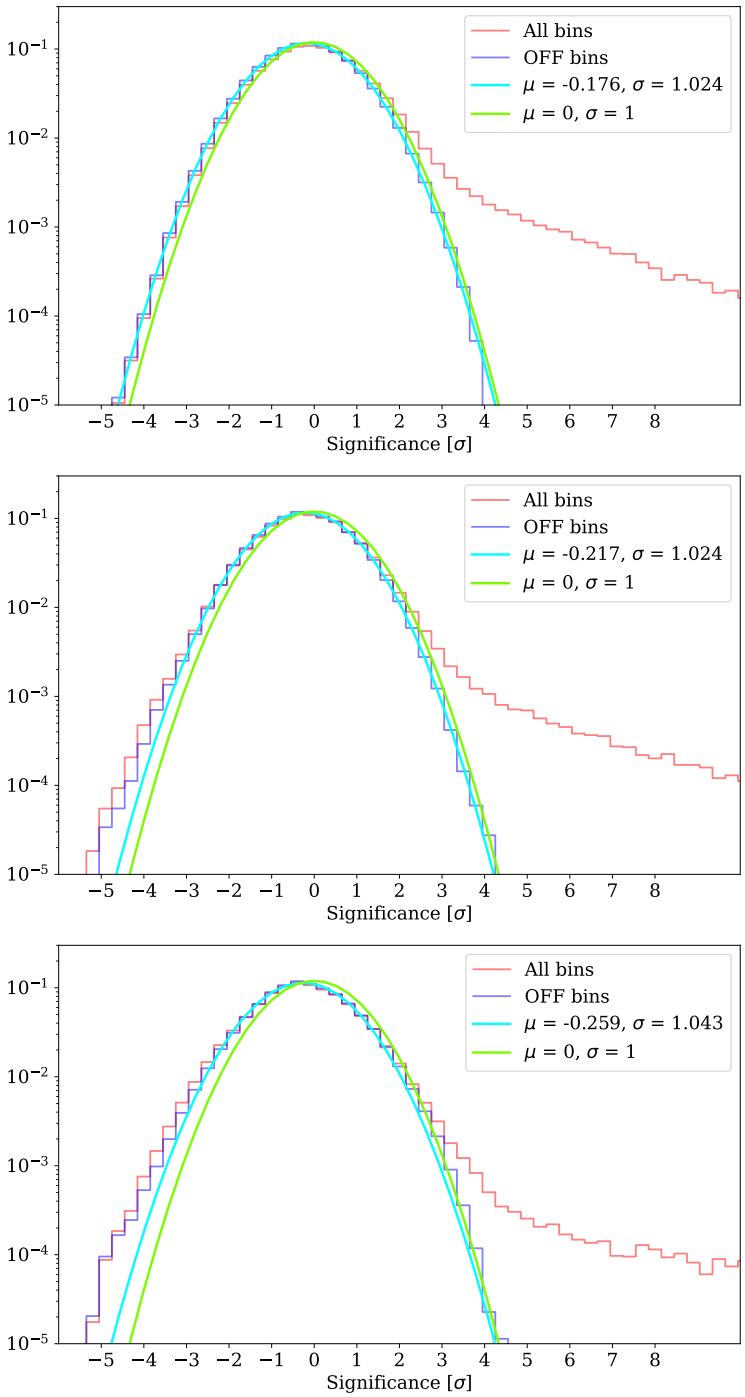

FIGURE A.1: One-dimensional distribution of significance entries from the figures 8.6 (top), 8.7 (center) and 8.8 (bottom).

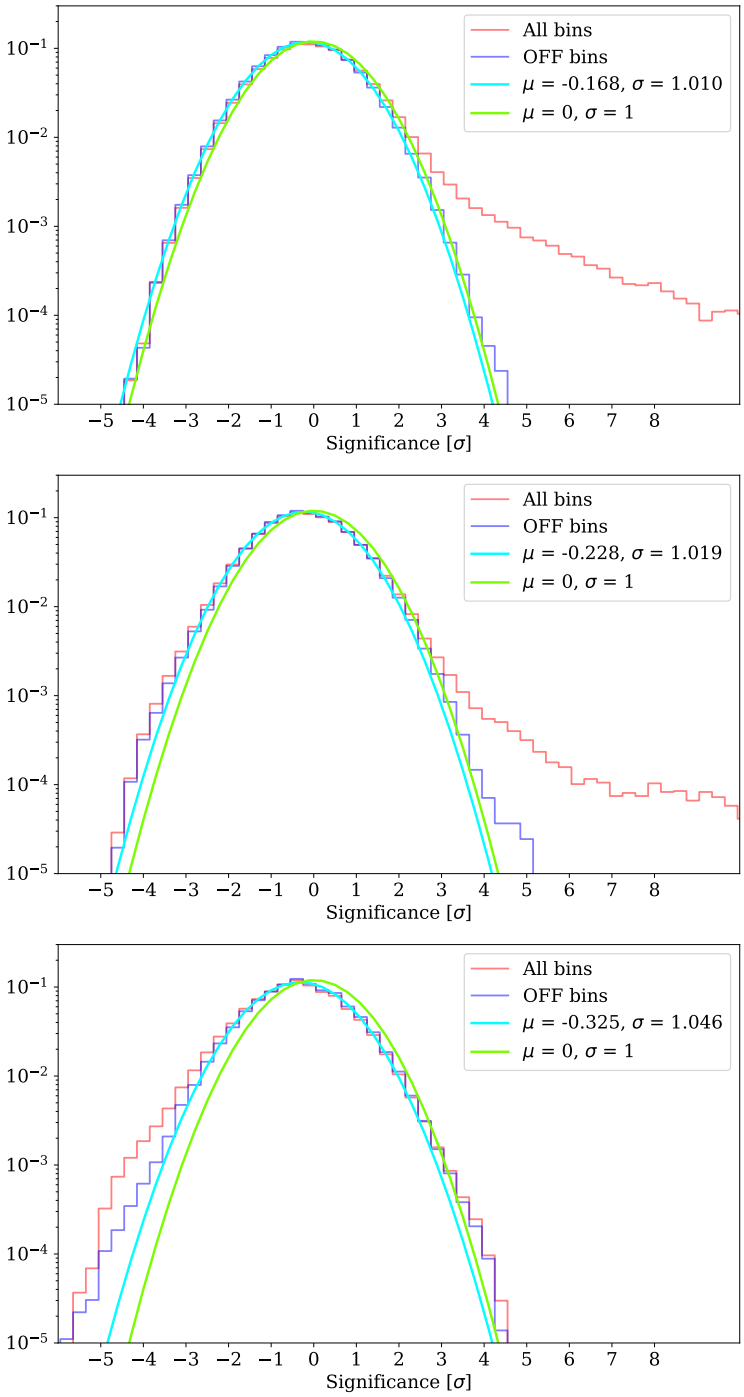

FIGURE A.2: One-dimensional distribution of significance entries from the figures A.4 (top), A.5 (center) and A.6 (bottom).

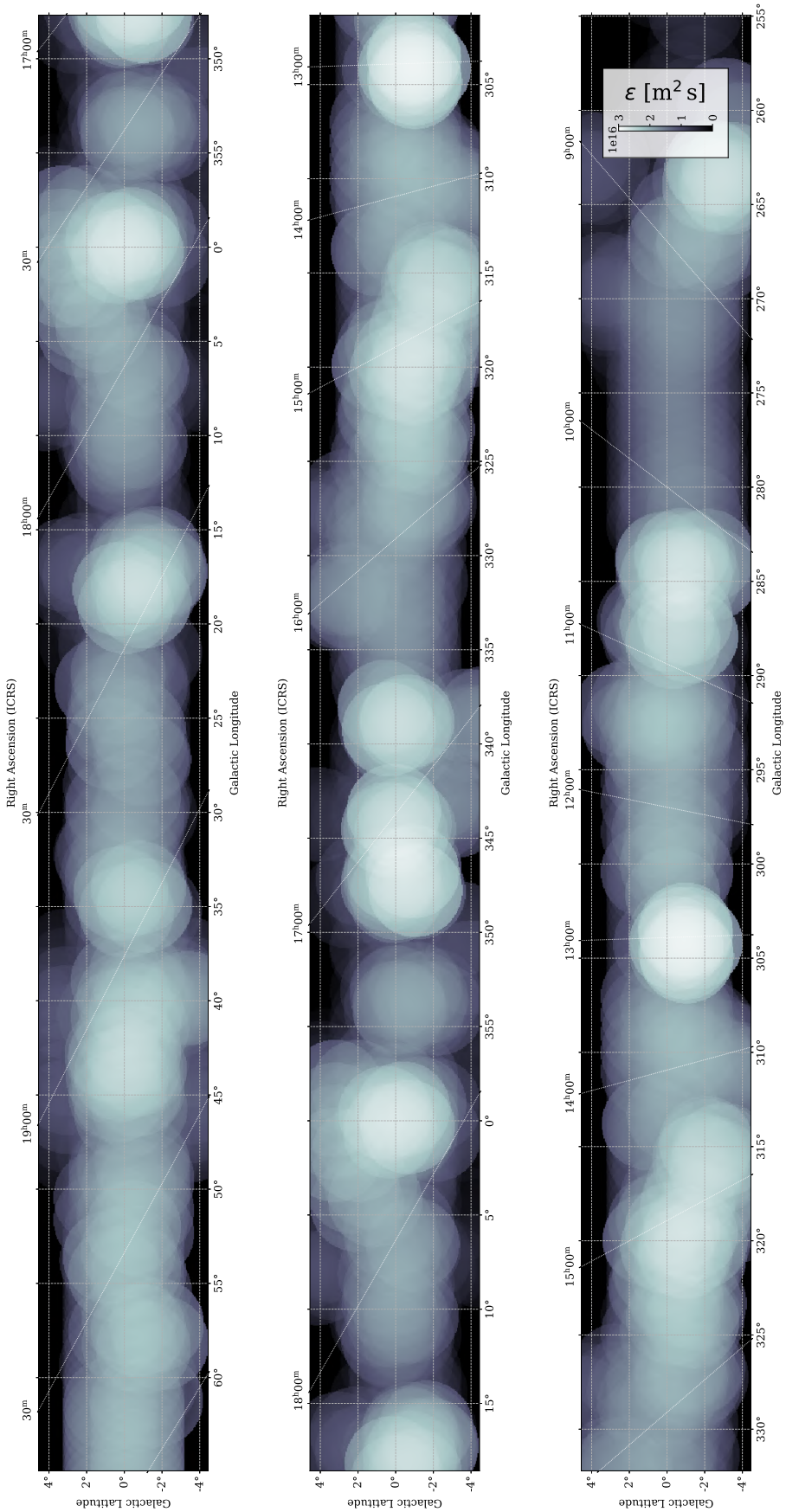

FIGURE A.3: Same as figure 8.4 but for the CA.

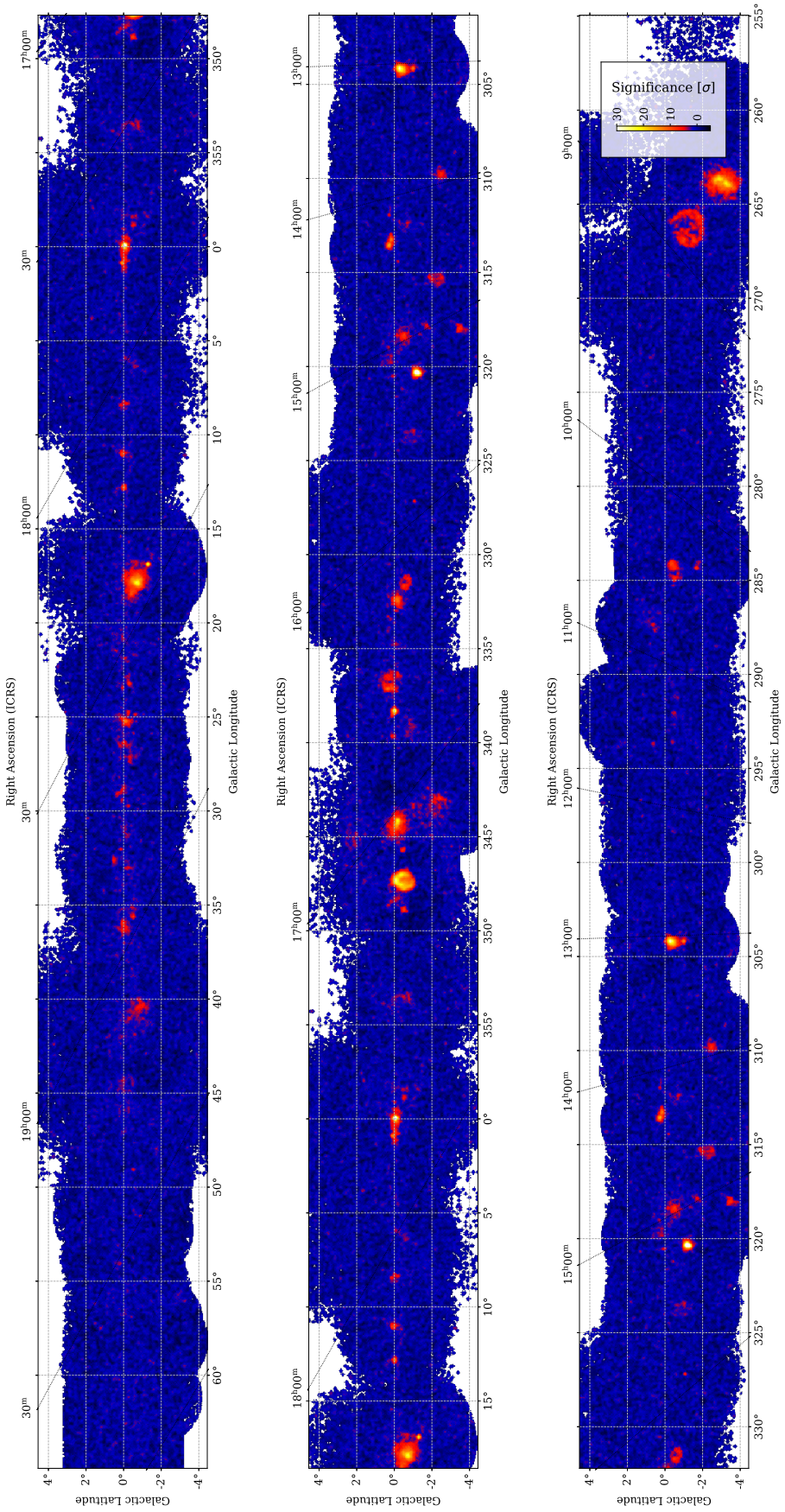

FIGURE A.4: Map of *Cash* pre-trial significance for the CA, for the energy threshold of 2 TeV and a 0.1° correlation radius.

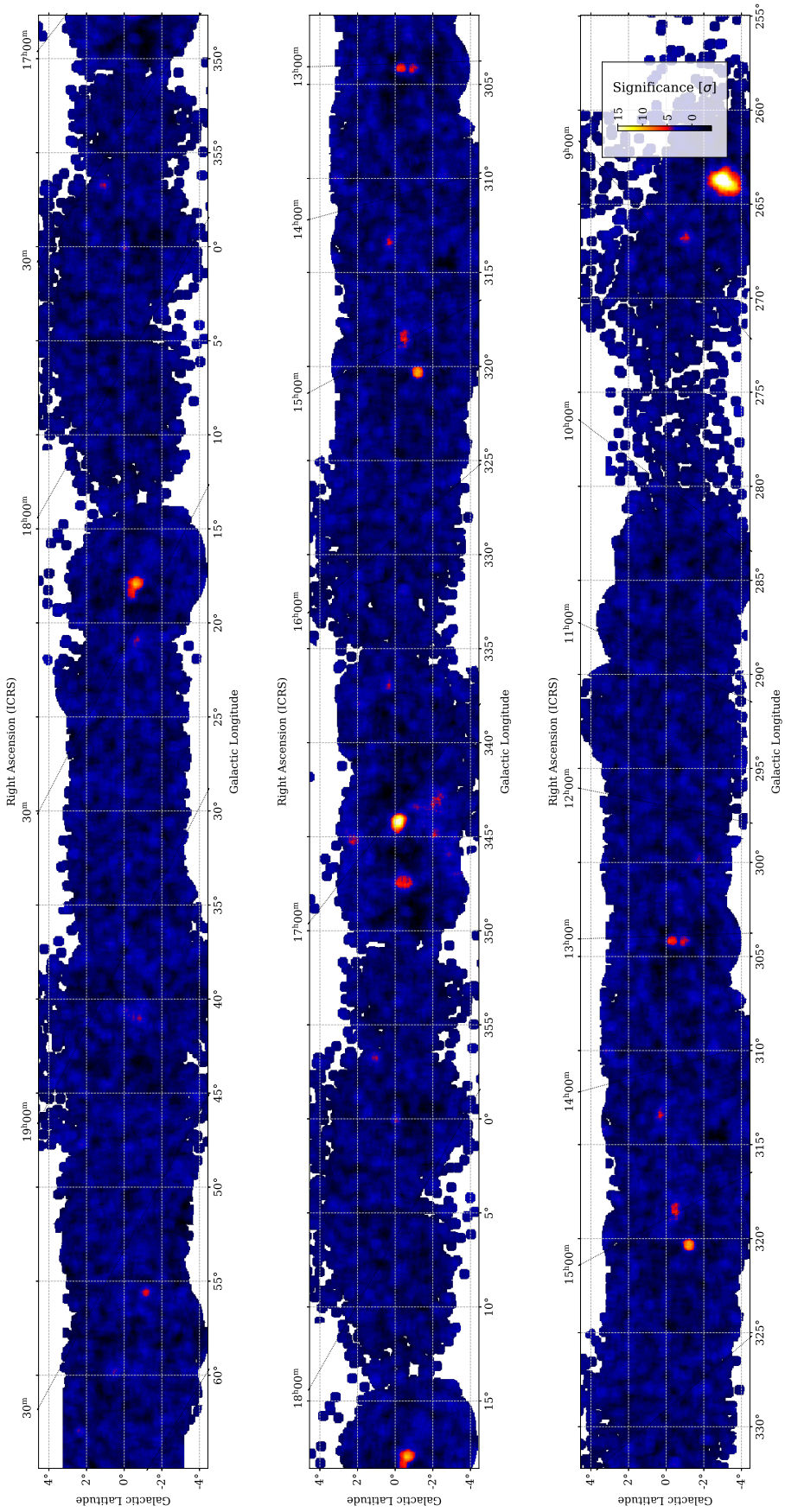

FIGURE A.5: Map of *Cash* pre-trial significance for the CA, for the energy threshold of 20 TeV and a 0.3° correlation radius.

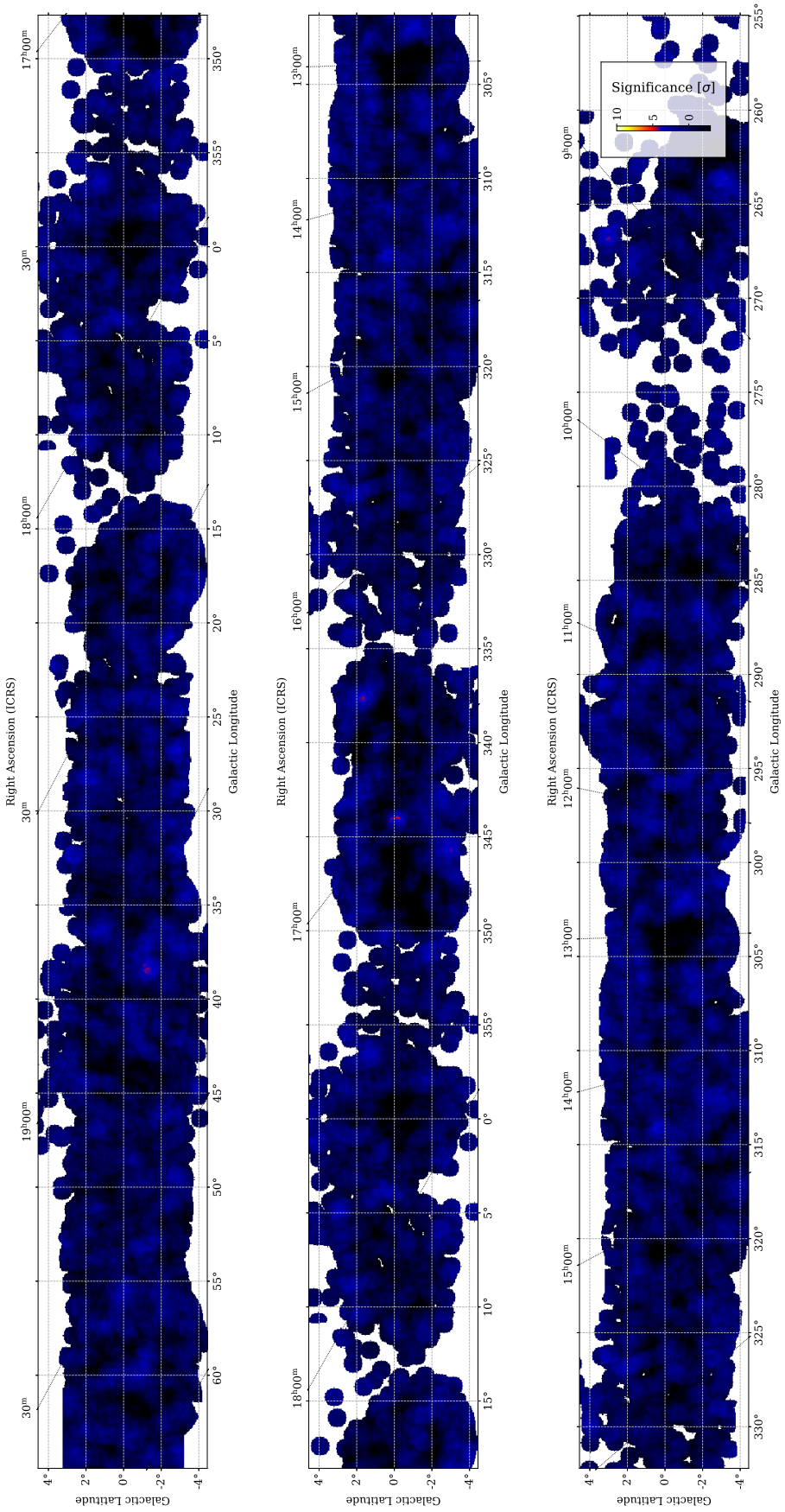

FIGURE A.6: Map of *Cash* pre-trial significance for the CA, for the energy threshold of 50 TeV and a 0.5° correlation radius.

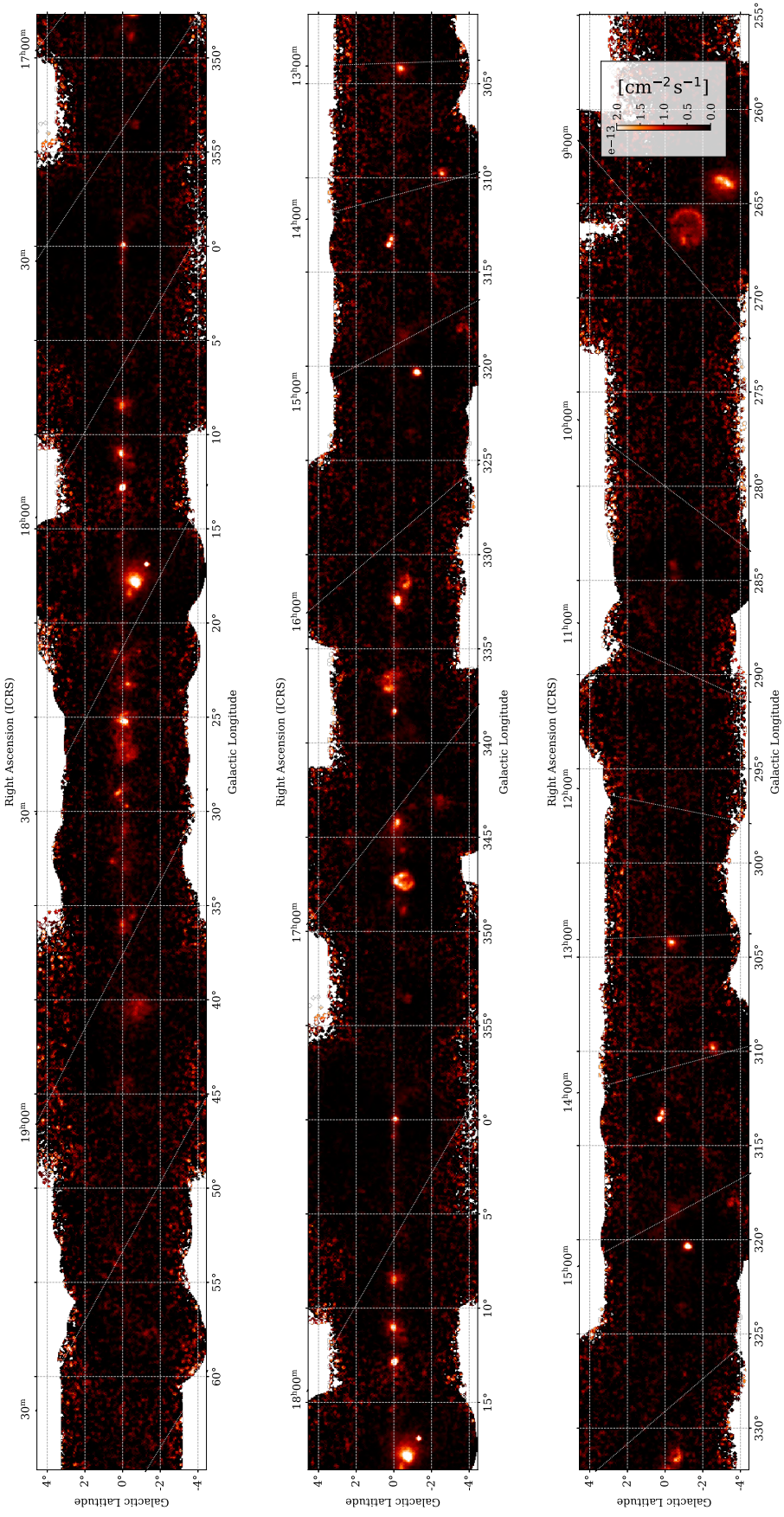

FIGURE A.7: Map of γ-ray flux for the MA, for the energy threshold of 2 TeV and a 0.1° correlation radius, assuming a spectral index $\Gamma = 2$.

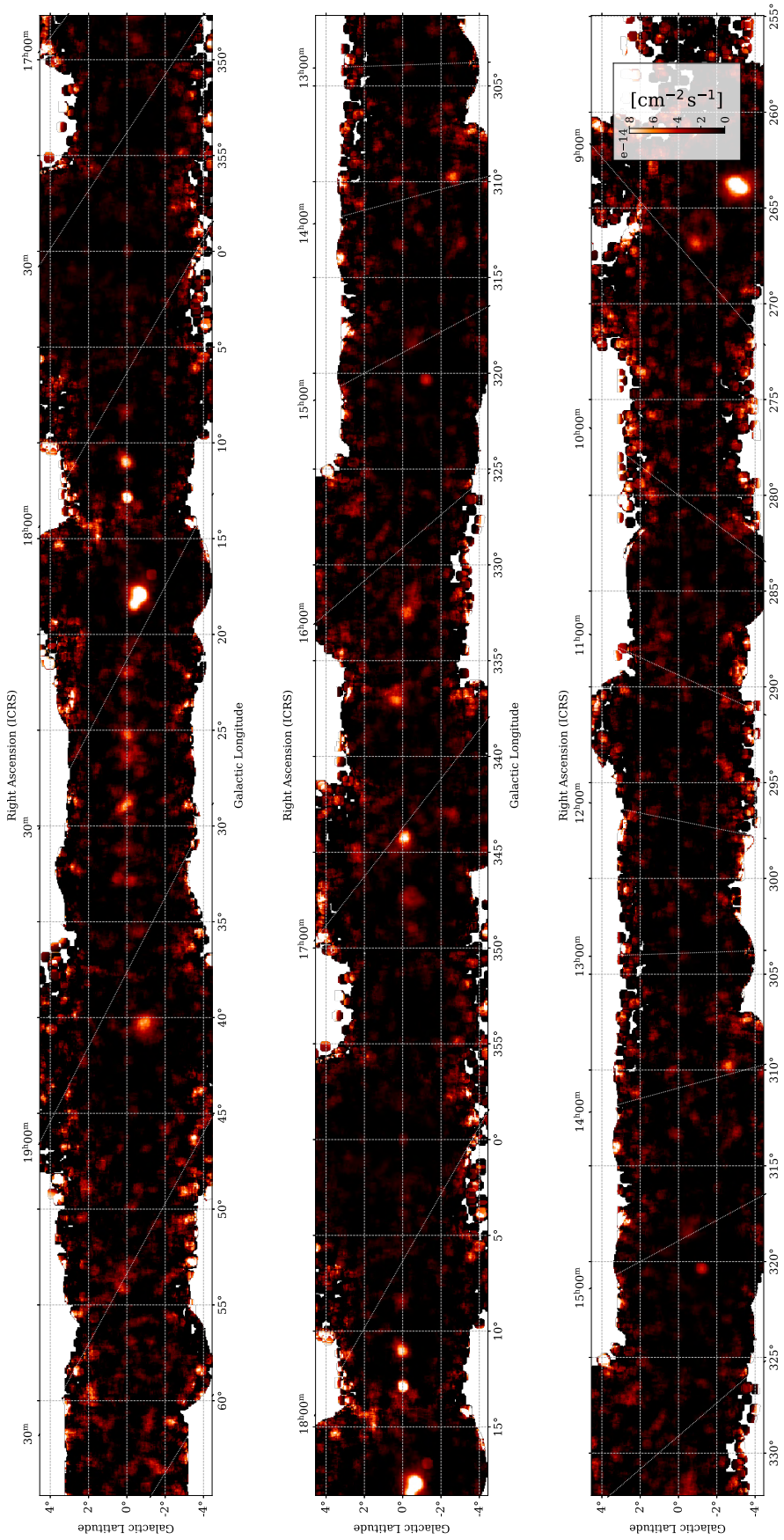

FIGURE A.8: Map of γ-ray flux for the MA, for the energy threshold of 20 TeV and a 0.3° correlation radius, assuming a spectral index $\Gamma = 2$.

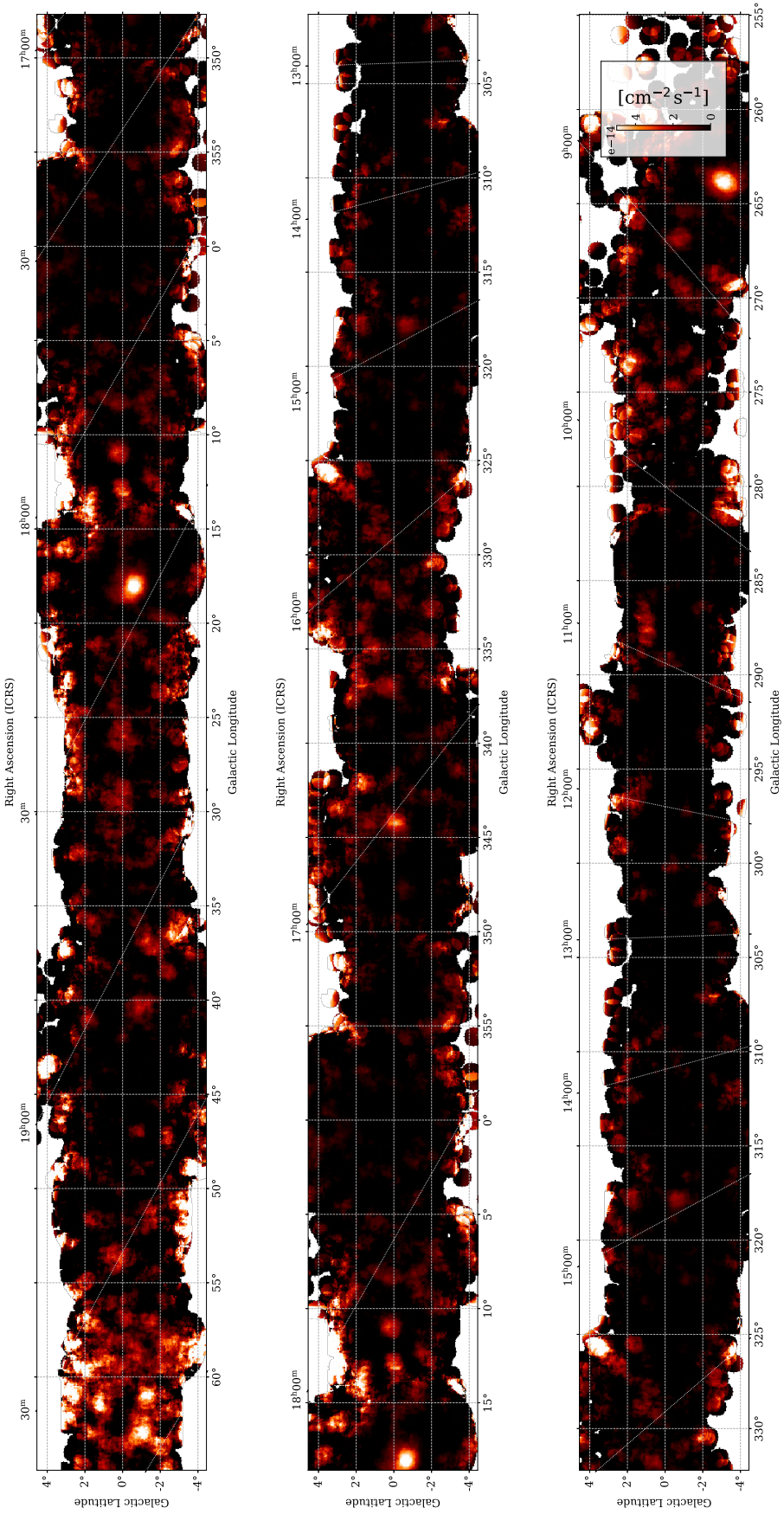

FIGURE A.9: Map of γ-ray flux for the MA, for the energy threshold of 50 TeV and a 0.5° correlation radius, assuming a spectral index $\Gamma = 2$.

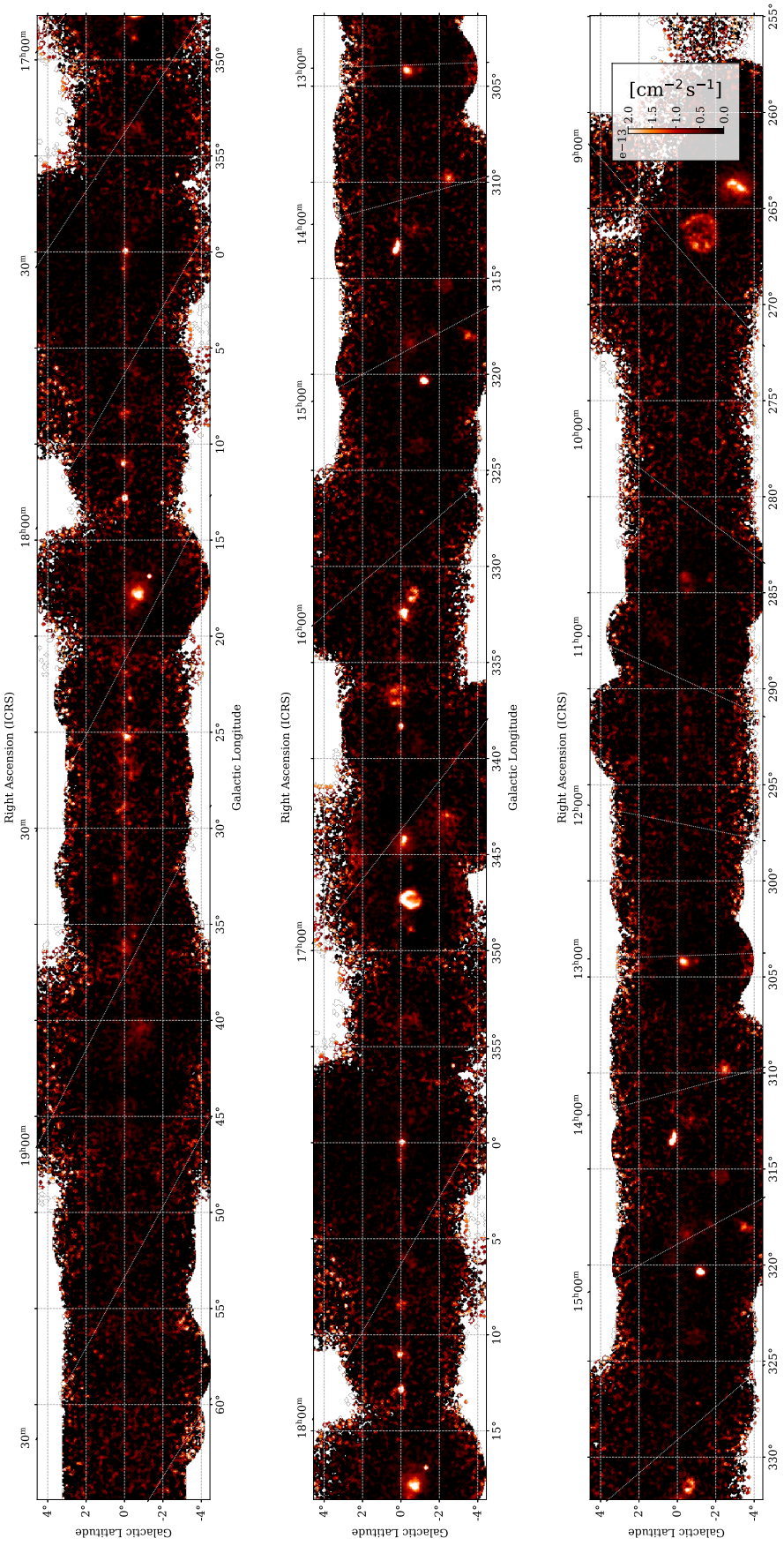

FIGURE A.10: Map of γ-ray flux for the CA, for the energy threshold of 2 TeV and a 0.1 ° correlation radius, assuming a spectral index $\Gamma = 2$.

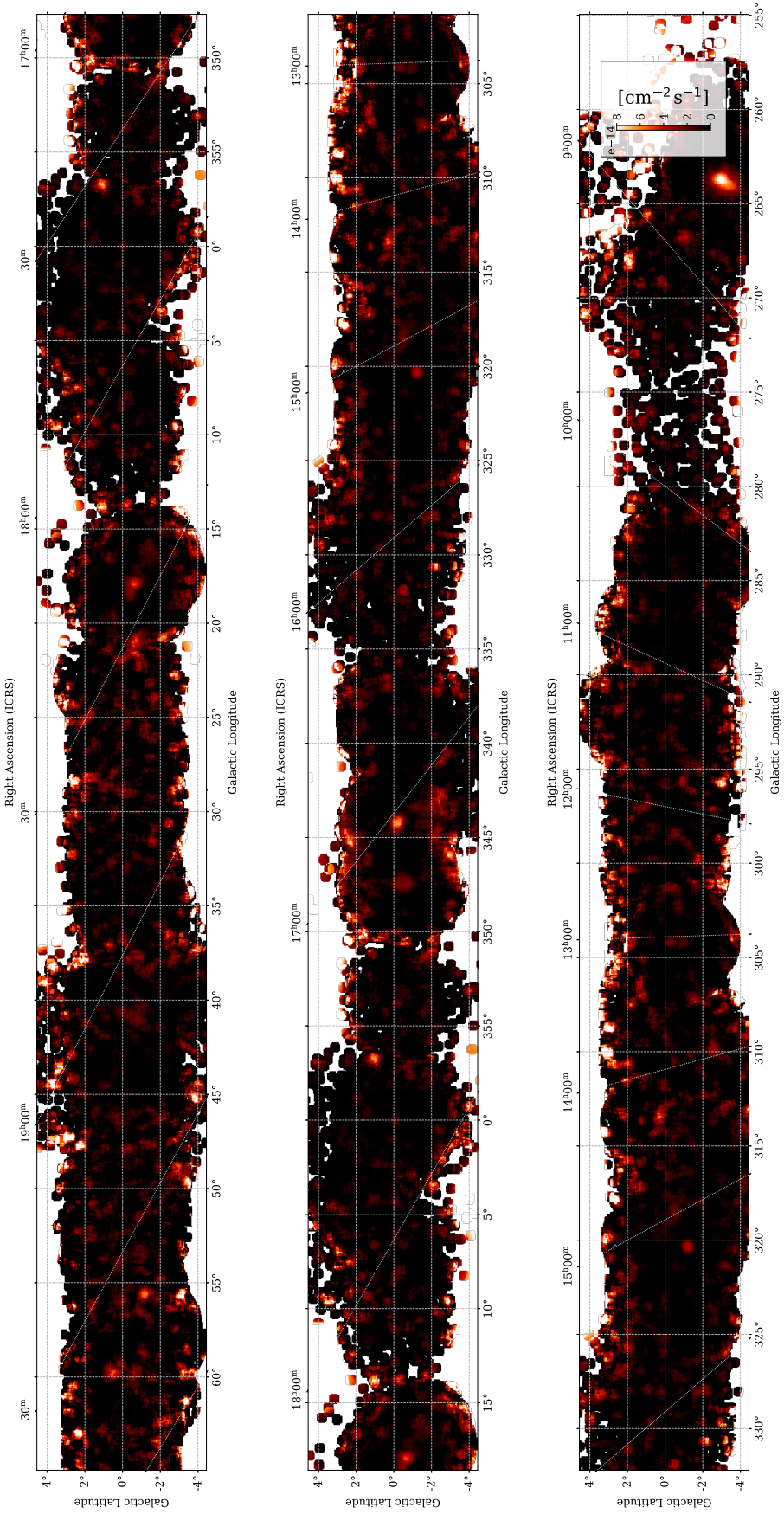

FIGURE A.11: Map of γ-ray flux for the CA, for the energy threshold of 20 TeV and a 0.3° correlation radius, assuming a spectral index $\Gamma = 2$.

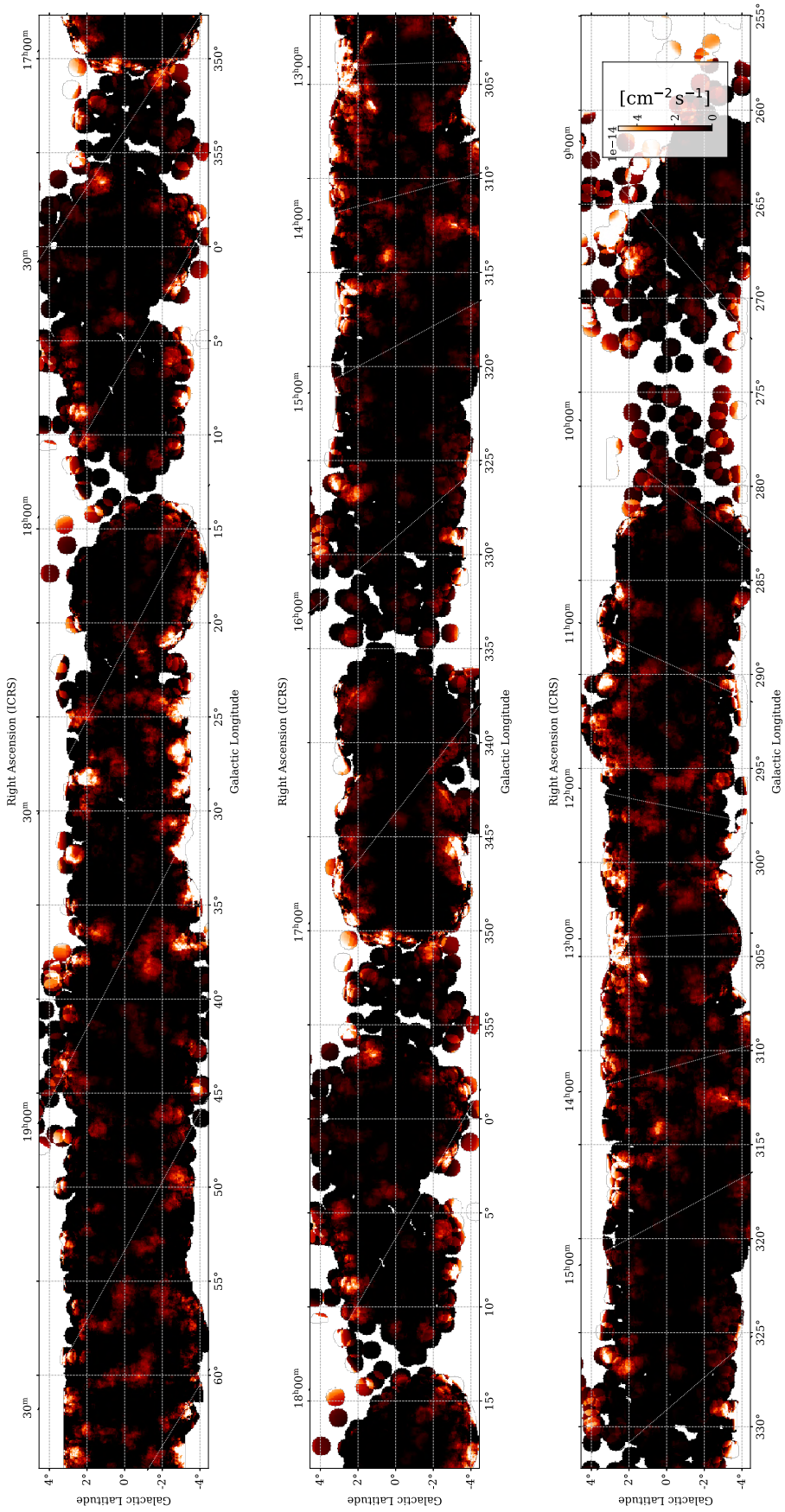

FIGURE A.12: Map of γ-ray flux for the CA, for the energy threshold of 50 TeV and a 0.5° correlation radius, assuming a spectral index $\Gamma = 2$.

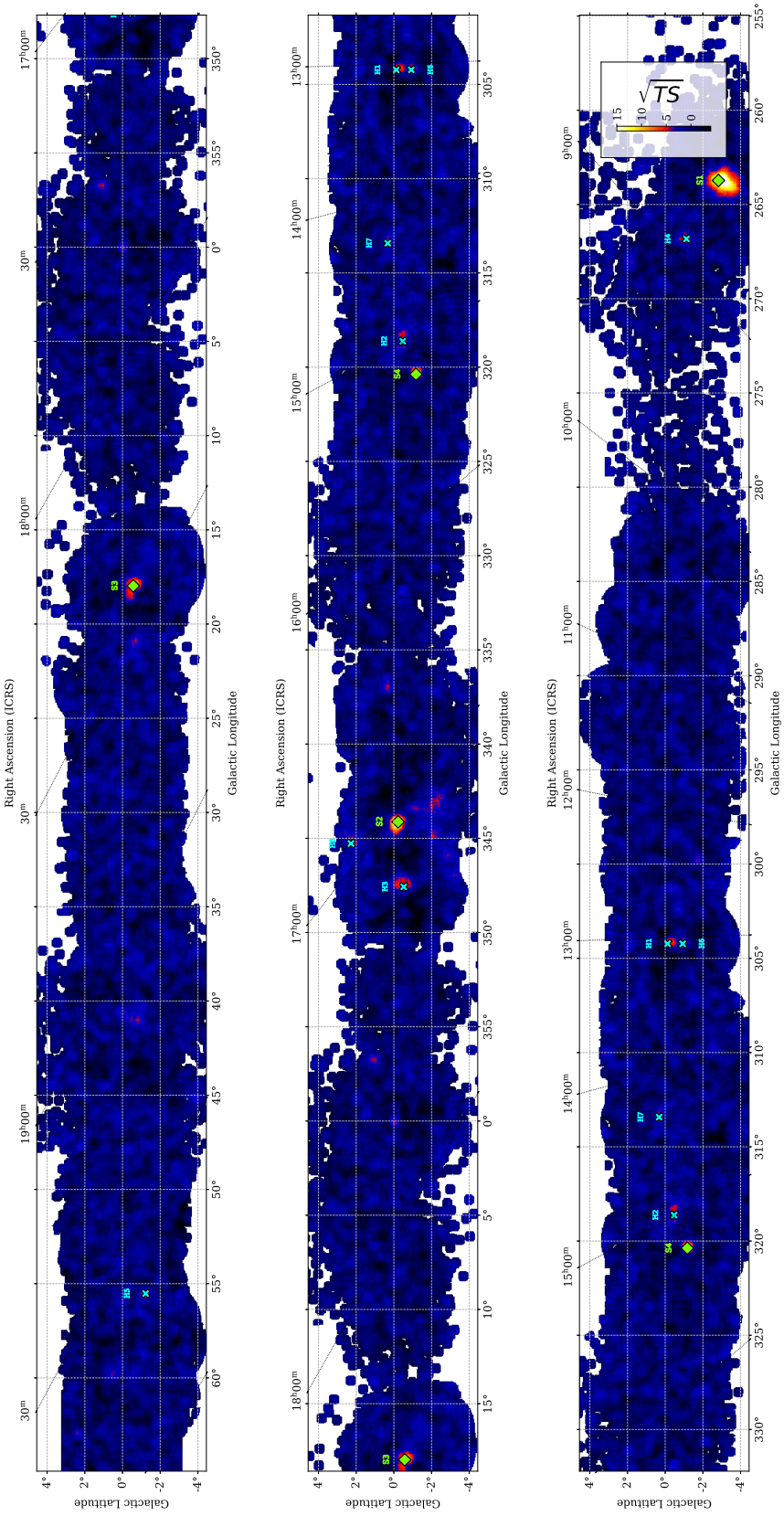

FIGURE A.13: Same as figure 8.10 for the CA.

Name	$\sqrt{TS}$ [σ]	Galactic l, b	HGPS association	MA	Common name	Type
S1	19.59	$263.73^o, -2.83^o$	HESS J0835-455	S2	Vela X	PWN
S2	14.93	$344.12^o, -0.22^o$	HESS J1702-420	S3	–	UNID
S3	10.71	$17.98^o, -0.57^o$	HESS J1825-137	S1	–	PWN
S4	9.76	$320.38^o, -1.18^o$	HESS J1514-591	S5	MSH 15-52	PWN

TABLE A.1: Same as table 8.1, for the CA.

Name	$\sqrt{TS}$ [σ]	Galactic l, b	HGPS association	MA	Common name	Type
H1	6.67	$304.23^o, -0.12^o$	HESS J1303-631	–	–	PWN
H2	6.39	$318.62^o, -0.47^o$	HESS J1457-593	H3	–	SNR
H3	6.22	$347.57^o, -0.53^o$	HESS J1713-397	S9	RX J1713-3946	SNR
H4	5.57	$266.82^o, -1.12^o$	HESS J0852-463	S10	Vela Jr	PWN
H5	5.43	$55.52^o, -1.23^o$	–	–	–	–
H6	5.42	$304.23^o, -0.93^o$	HESS J1302-638	–	LS 2883	BINARY
H7	5.38	$313.43^o, 0.32^o$	HESS J1420-607	–	Kookaburra	PWN
H8	5.37	$345.27^o, 2.27^o$	HGPSC 039	–	–	–

TABLE A.2: Same as table 8.2, for the CA.

Name	H.E.S.S. association	Galactic longitude [deg]	Galactic latitude [deg]	Radius [deg]
S3	HESS J1702-420	344.28 ± 0.03	-0.11 ± 0.02	0.18 ± 0.02
S5	HESS J1514-591	320.33 ± 0.01	-1.22 ± 0.01	—
S10	HESS J0852-463	266.83 ± 0.05	-0.92 ± 0.05	0.19 ± 0.04
S12	HESS J1843-033 (A)	29.04 ± 0.03	0.27 ± 0.03	0.06 ± 0.03
S12	HESS J1843-033 (B)	28.66 ± 0.08	-0.13 ± 0.05	0.14 ± 0.04
S13	HESS J1616-508	332.32 ± 0.22	-0.23 ± 0.13	0.40 ± 0.15

(A) Best-fit morphology parameters. The rotation angle is measured counterclockwise starting from the $l = 0$, $b > 0$ axis.

Name	H.E.S.S. association	Spectral index	Decorrelation energy [TeV]	$\mathbf{dN/dE(E = E_{decorr})}$ $[\mathbf{TeV^{-1}\,cm^{-2}\,s^{-1}}]$
S3	HESS J1702-420	1.78 ± 0.28	33.72	$(2.70 \pm 0.29) \times 10^{-15}$
S5	HESS J1514-591	3.66 ± 0.50	17.32	$(4.94 \pm 0.70) \times 10^{-15}$
S10	HESS J0852-463	1.75 ± 0.50	42.26	$(1.05 \pm 0.23) \times 10^{-15}$
S12	HESS J1843-033	2.39 ± 0.51	31.64	$(1.40 \pm 0.26) \times 10^{-15}$
S13	HESS J1616-508	3.15 ± 0.90	21.08	$(9.75 \pm 3.85) \times 10^{-15}$

(B) Best-fit spectral parameters.

TABLE A.3: Modeling results obtained with a 3D maximum-likelihood analysis of H.E.S.S. data above 20 TeV, using the MA configuration. The quoted errors correspond to the 1σ statistical uncertainties.

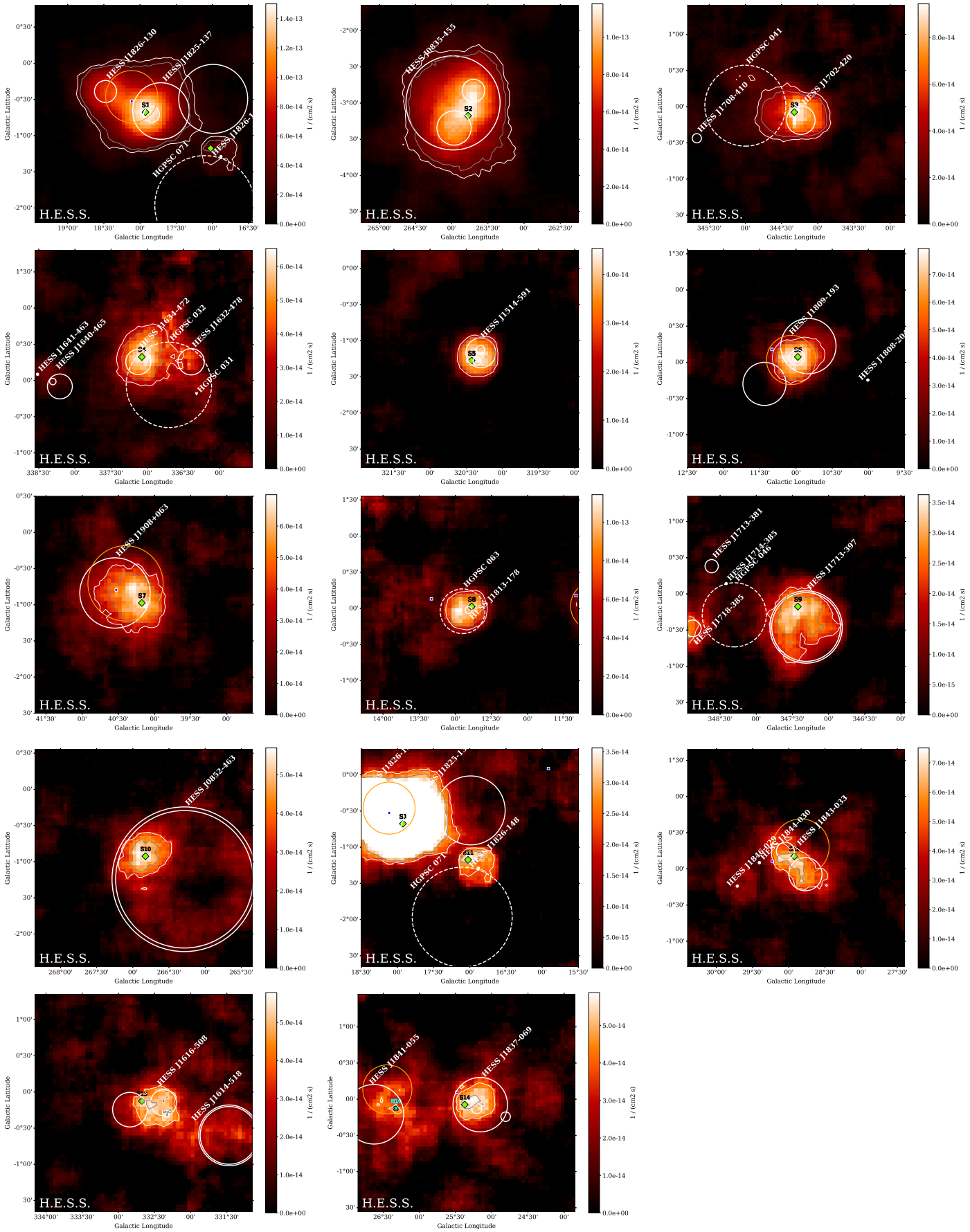

FIGURE A.14: Flux maps centered on the detected sources found in the MA > 20 TeV, computed assuming a spectral index $\Gamma = 2$. The HGPS sources, non-confirmed large and small-scale objects are indicated by white solid lines, dashed circles and triangles, respectively. The 2σ (5σ) post-trial significance contours are shown in white (grey). Sources from the 2HWC (eHWC) catalog are indicated by blue dots (orange circles).

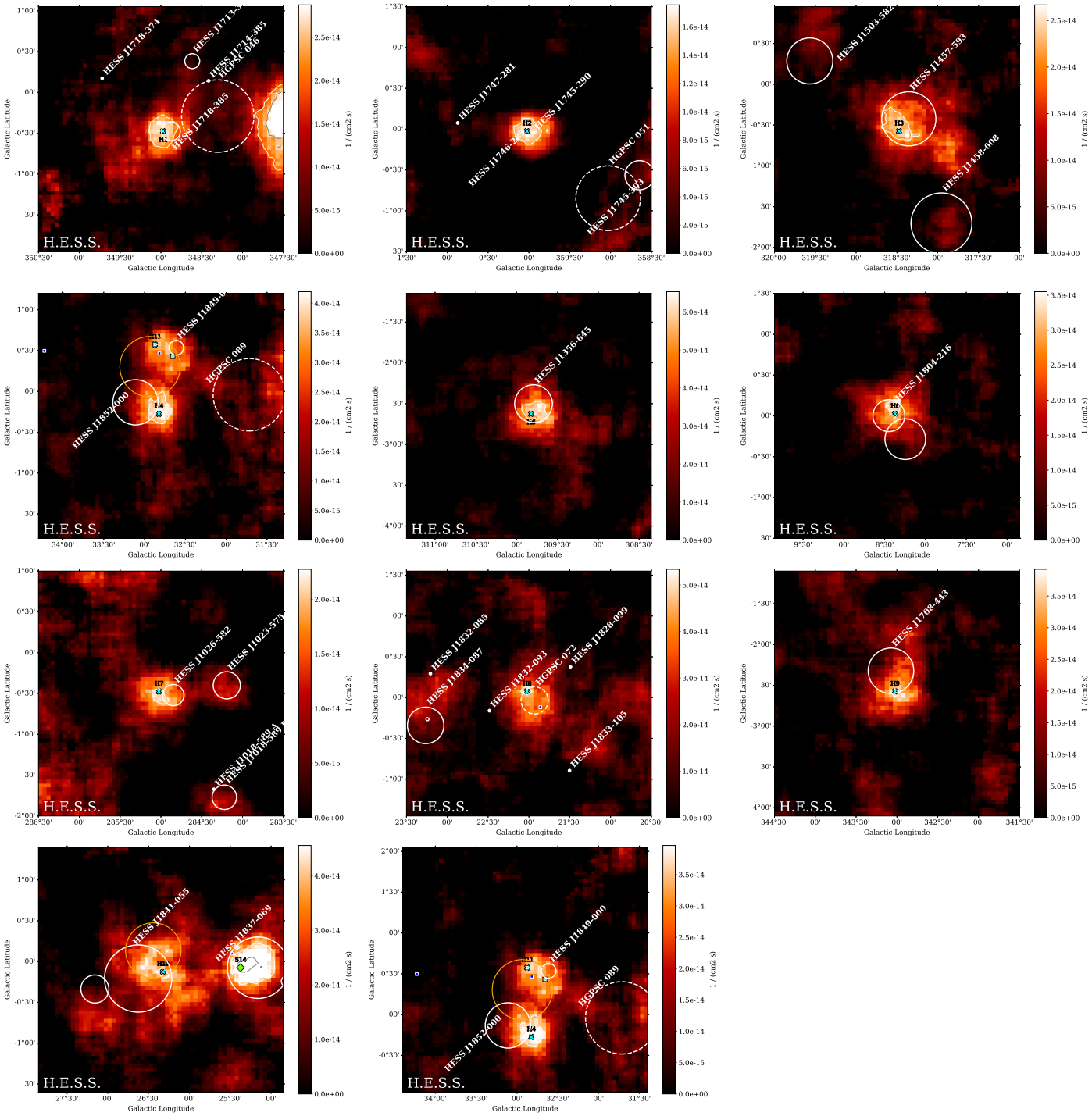

FIGURE A.15: Flux maps centered on the hotspots found in the MA $> 20\,\mathrm{TeV}$, computed assuming a spectral index $\Gamma = 2$. The HGPS sources, non-confirmed large and small-scale objects are indicated by white solid lines, dashed circles and triangles, respectively. The 2σ (5σ) post-trial significance contours are shown in white (grey). Sources from the 2HWC (eHWC) catalog are indicated by blue dots (orange circles).

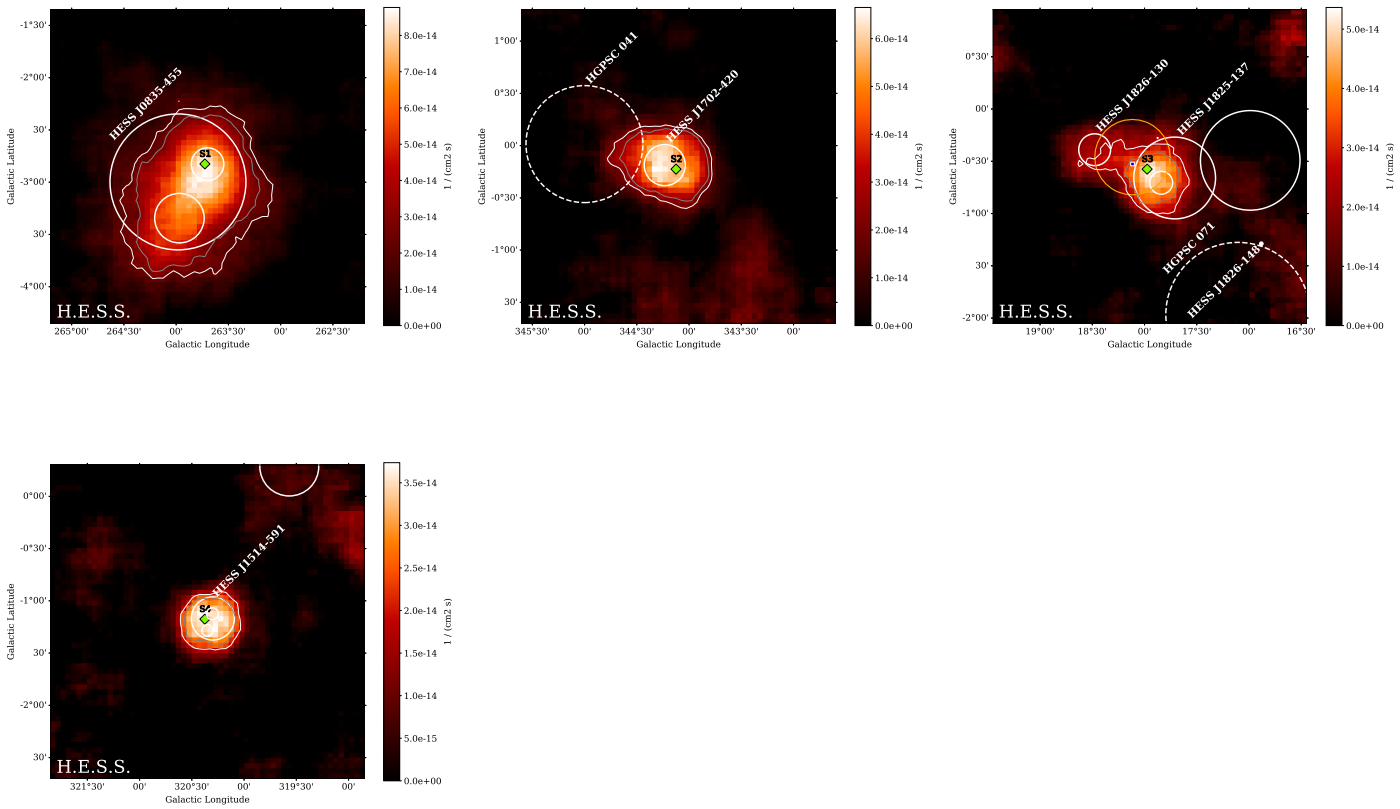

FIGURE A.16: Same as figure A.14, but for the CA.

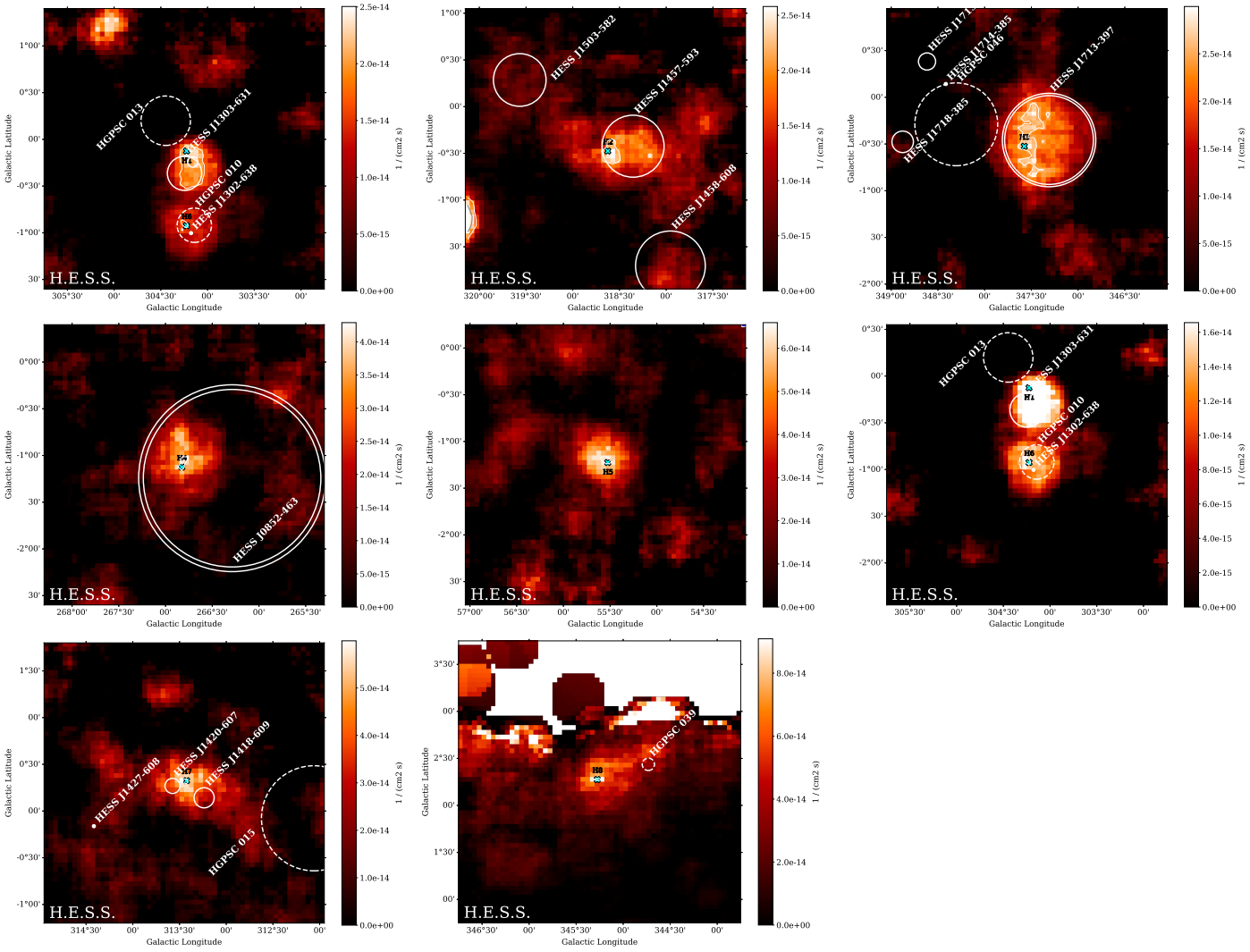

FIGURE A.17: Same as figure A.15, but for the CA.

Acknowledgements

Bibliography

[1] Victor F. Hess. "Über Beobachtungen der durchdringenden Strahlung bei sieben Freiballonfahrten". In: *Phys. Z.* 13 (1912), pp. 1084–1091.

[2] Malcolm S. Longair. *High Energy Astrophysics*. 2011.

[3] T. Antoni et al. "KASCADE measurements of energy spectra for elemental groups of cosmic rays: Results and open problems". In: *Astroparticle Physics* 24.1-2 (Sept. 2005), pp. 1–25. DOI: 10.1016/j.astropartphys.2005.04.001. arXiv: astro-ph/0505413 [astro-ph].

[4] O. Adriani et al. "PAMELA Measurements of Cosmic-Ray Proton and Helium Spectra". In: *Science* 332.6025 (Apr. 2011), p. 69. DOI: 10.1126/science.1199172. arXiv: 1103.4055 [astro-ph.HE].

[5] The KASCADE-Grande Collaboration et al. "KASCADE-Grande measurements of energy spectra for elemental groups of cosmic rays". In: *arXiv e-prints*, arXiv:1306.6283 (June 2013), arXiv:1306.6283. arXiv: 1306.6283 [astro-ph.HE].

[6] B. Bartoli et al. "Knee of the cosmic hydrogen and helium spectrum below 1 PeV measured by ARGO-YBJ and a Cherenkov telescope of LHAASO". In: *Physical Review D* 92.9, 092005 (Nov. 2015), p. 092005. DOI: 10.1103/PhysRevD.92.092005. arXiv: 1502.03164 [astro-ph.HE].

[7] T. K. Gaisser. "The cosmic-ray spectrum: From the knee to the ankle". In: *J. Phys. Conf. Ser.* 47 (2006), pp. 15–20. DOI: 10.1088/1742-6596/47/1/002.

[8] J org R. H orandel. "Cosmic rays at the highest energies". In: *Progress in Particle and Nuclear Physics* 64.2 (2010). Neutrinos in Cosmology, in Astro, Particle and Nuclear Physics, pp. 351–359. ISSN: 0146-6410. DOI: https://doi.org/10.1016/j.ppnp.2009.12.047. URL: https://www.sciencedirect.com/science/article/pii/S0146641009001252.

[9] G. Giacinti, M. Kachelrieß, and D. V. Semikoz. "Explaining the Spectra of Cosmic Ray Groups above the Knee by Escape from the Galaxy". In: *Phys. Rev. D* 90.4 (2014), p. 041302. DOI: 10.1103/PhysRevD.90.041302. arXiv: 1403.3380 [astro-ph.HE].

[10] G. Giacinti, M. Kachelrieß, and D. V. Semikoz. "Escape model for Galactic cosmic rays and an early extragalactic transition". In: *Phys. Rev. D* 91.8 (2015), p. 083009. DOI: 10.1103/PhysRevD.91.083009. arXiv: 1502.01608 [astro-ph.HE].

[11] Stefano Gabici. "Cosmic Rays and Molecular Clouds". In: *Astrophysics and Space Science Proceedings* (2013), pp. 221–247. ISSN: 1570-6605. DOI: 10.1007/978-3-642-35410-6_16. URL: http://dx.doi.org/10.1007/978-3-642-35410-6_16.

[12] A. W. Strong et al. "Global cosmic-ray related luminosity and energy budget of the Milky Way". In: *The Astrophysical Journal* 722.1 (2010), pp. L58–L63. DOI: 10.1088/2041-8205/722/1/l58. URL: https://doi.org/10.1088/2041-8205/722/1/158.

[13] Thomas K. Gaisser, Ralph Engel, and Elisa Resconi. *Cosmic Rays and Particle Physics*. 2nd ed. Cambridge University Press, 2016. DOI: 10.1017/CBO9781139192194.

[14] Felix A. Aharonian. *Very high energy cosmic gamma radiation : a crucial window on the extreme Universe*. 2004. DOI: 10.1142/4657.

[15] Enrico Fermi. "On the Origin of the Cosmic Radiation". In: *Phys. Rev.* 75 (8 1949), pp. 1169–1174. DOI: 10.1103/PhysRev.75.1169. URL: https://link.aps.org/doi/10.1103/PhysRev.75.1169.

[16] A. R. Bell. "The Acceleration of cosmic rays in shock fronts. I". In: *Mon. Not. Roy. Astron. Soc.* 182 (1978), pp. 147–156.

[17] Hyesung Kang, Dongsu Ryu, and T. W. Jones. "Self-Similar Evolution of Cosmic-Ray Modified Shocks: The Cosmic-Ray Spectrum". In: *The Astrophysical Journal* 695.2 (Apr. 2009), pp. 1273–1288. DOI: 10.1088/0004-637X/695/2/1273. arXiv: 0901.1702 [astro-ph.HE].

[18] R. G. Giovanelli. "A Theory of Chromospheric Flares". In: *NATURE* 158.4003 (July 1946), pp. 81–82. DOI: 10.1038/158081a0.

[19] J. W. Dungey. "Interplanetary Magnetic Field and the Auroral Zones". In: *Phys. Rev. Lett.* 6 (2 1961), pp. 47–48. DOI: 10.1103/PhysRevLett.6.47. URL: https://link.aps.org/doi/10.1103/PhysRevLett.6.47.

[20] A. Iyono et al. "The Cosmic Ray Anisotropy Observed by the Large Area Air Shower Experiments". In: *29th International Cosmic Ray Conference (ICRC29), Volume 6*. Vol. 6. International Cosmic Ray Conference. Jan. 2005, p. 181.

[21] Particle Data Group et al. "Review of Particle Physics". In: *Progress of Theoretical and Experimental Physics* 2020.8 (Aug. 2020). 083C01. ISSN: 2050-3911. DOI: 10.1093/ptep/ptaa104. eprint: https://academic.oup.com/ptep/article-pdf/2020/8/083C01/34673722/ptaa104.pdf. URL: https://doi.org/10.1093/ptep/ptaa104.

[22] Floyd William Stecker. *Cosmic gamma rays*. Vol. 249. 1971.

[23] Ervin Kafexhiu et al. "Parametrization of gamma-ray production cross sections for p p interactions in a broad proton energy range from the kinematic threshold to PeV energies". In: *Physical Review D* 90.12, 123014 (Dec. 2014), p. 123014. DOI: 10.1103/PhysRevD.90.123014. arXiv: 1406.7369 [astro-ph.HE].

[24] S. R. Kelner and F. A. Aharonian. "Energy spectra of gamma rays, electrons, and neutrinos produced at interactions of relativistic protons with low energy radiation". In: *Physical Review D* 78.3, 034013 (Aug. 2008), p. 034013. DOI: 10.1103/PhysRevD.78.034013. arXiv: 0803.0688 [astro-ph].

[25] Stefano Gabici, Felix A. Aharonian, and Pasquale Blasi. "Gamma rays from molecular clouds". In: *Astrophysics and Space Science* 309.1-4 (June 2007), pp. 365–371. DOI: 10.1007/s10509-007-9427-6. arXiv: astro-ph/0610032 [astro-ph].

[26] Troy Porter, Gudlaugur Johannesson, and Igor Moskalenko. "The Interstellar Radiation Field of the Milky Way in Three Spatial Dimensions". In: *PoS* ICRC2017 (2018), p. 737. DOI: 10.22323/1.301.0737.

[27] Guðlaugur Jóhannesson, Troy A. Porter, and Igor V. Moskalenko. "The Three-Dimensional Spatial Distribution of Interstellar Gas in the Milky Way: Implications for Cosmic Rays and High-Energy Gamma-Ray Emissions". In: *Astrophys. J.* 856.1 (2018), p. 45. DOI: 10.3847/1538-4357/aab26e. arXiv: 1802.08646 [astro-ph.HE].

[28] M. Breuhaus et al. "Ultra-high Energy Inverse Compton Emission from Galactic Electron Accelerators". In: *The Astrophysical Journal Letters* 908.2, L49

(Feb. 2021), p. L49. DOI: 10.3847/2041-8213/abe41a. arXiv: 2010.13960 [astro-ph.HE].

[29] Alice K. Harding and Robert Preece. "Quantized Synchrotron Radiation in Strong Magnetic Fields". In: *The Astrophysical Journal* 319 (Aug. 1987), p. 939. DOI: 10.1086/165510.

[30] Valenti Bosch-Ramon and Dmitry Khangulyan. "Understanding the very-high energy emission from microquasars". In: *International Journal of Modern Physics D* 18.03 (2009), pp. 347–387. ISSN: 1793-6594. DOI: 10.1142/s0218271809014601. URL: http://dx.doi.org/10.1142/S0218271809014601.

[31] GEORGE R. BLUMENTHAL and ROBERT J. GOULD. "Bremsstrahlung, Synchrotron Radiation, and Compton Scattering of High-Energy Electrons Traversing Dilute Gases". In: *Rev. Mod. Phys.* 42 (2 1970), pp. 237–270. DOI: 10.1103/RevModPhys.42.237. URL: https://link.aps.org/doi/10.1103/RevModPhys.42.237.

[32] Rafal Moderski et al. "Klein-Nishina effects in the spectra of non-thermal sources immersed in external radiation fields". In: *Monthly Notices of the Royal Astronomical Society* 363.3 (Nov. 2005), pp. 954–966. ISSN: 0035-8711. DOI: 10.1111/j.1365-2966.2005.09494.x. eprint: https://academic.oup.com/mnras/article-pdf/363/3/954/3954953/363-3-954.pdf. URL: https://doi.org/10.1111/j.1365-2966.2005.09494.x.

[33] Rafal Moderksi et al. "Klein-Nishina effects in the spectra of non-thermal sources immersed in external radiation fields". In: *Mon. Not. Roy. Astron. Soc.* 363.3 (2005). [Erratum: Mon.Not.Roy.Astron.Soc. 364, 1488 (2005)], pp. 954–966. DOI: 10.1111/j.1365-2966.2005.09814.x. arXiv: astro-ph/0504388.

[34] E. Aliu et al. "Long-term TeV and X-Ray Observations of the Gamma-Ray Binary HESS J0632+057". In: *The Astrophysical Journal* 780.2, 168 (Jan. 2014), p. 168. DOI: 10.1088/0004-637X/780/2/168. arXiv: 1311.6083 [astro-ph.HE].

[35] H. E. S. S. Collaboration et al. "Detection of very-high-energy γ-ray emission from the colliding wind binary η Car with H.E.S.S." In: *Astronomy & Astrophysics* 635, A167 (Mar. 2020), A167. DOI: 10.1051/0004-6361/201936761. arXiv: 2002.02336 [astro-ph.HE].

[36] A. Albert et al. "HAWC Search for High-Mass Microquasars". In: *Astrophys. J. Lett.* 912.1 (2021), p. L4. DOI: 10.3847/2041-8213/abf35a. arXiv: 2101.08945 [astro-ph.HE].

[37] C. Mariaud et al. "VHE observations of the gamma-ray binary system LS 5039 with H.E.S.S". In: *PoS* ICRC2015 (2016), p. 885. DOI: 10.22323/1.236.0885. arXiv: 1509.05791 [astro-ph.HE].

[38] H.E.S.S. Collaboration et al. "The H.E.S.S. Galactic plane survey". In: *Astronomy & Astrophysics* 612, A1 (Apr. 2018), A1. DOI: 10.1051/0004-6361/201732098. arXiv: 1804.02432 [astro-ph.HE].

[39] F. Aharonian et al. "A New population of very high energy gamma-ray sources in the Milky Way". In: *Science* 307 (2005), pp. 1938–1942. DOI: 10.1126/science.1108643. arXiv: astro-ph/0504380.

[40] F. Aharonian. "HESS VHE Gamma-Ray Sources Without Identified Counterparts". In: *Astron. Astrophys.* 477 (2008), pp. 353–363. DOI: 10.1051/0004-6361:20078516. arXiv: 0712.1173 [astro-ph].

[41] F. Aharonian et al. "Serendipitous discovery of the unidentified extended TeV γ-ray source HESS J1303-631". In: *Astronomy & Astrophysics* 439.3 (Sept. 2005), pp. 1013–1021. DOI: 10.1051/0004-6361:20053195. arXiv: astro-ph/0505219 [astro-ph].

[42] F. Aharonian et al. “The H.E.S.S. survey of the inner galaxy in very high-energy gamma-rays”. In: *Astrophys. J.* 636 (2006), pp. 777–797. DOI: 10.1086/498013. arXiv: astro-ph/0510397.

[43] H.E.S.S. Collaboration et al. “Identification of HESS J1303-631 as a pulsar wind nebula through γ-ray, X-ray, and radio observations”. In: *Astronomy & Astrophysics* 548, A46 (Dec. 2012), A46. DOI: 10.1051/0004-6361/201219814. arXiv: 1210.6513 [astro-ph.HE].

[44] H.E.S.S. Collaboration et al. “Particle transport within the pulsar wind nebula HESS J1825-137”. In: *Astronomy & Astrophysics* 621, A116 (Jan. 2019), A116. DOI: 10.1051/0004-6361/201834335. arXiv: 1810.12676 [astro-ph.HE].

[45] Pierre Cristofari et al. “On the search for Galactic supernova remnant PeVatrons with current TeV instruments”. In: *Mon. Not. Roy. Astron. Soc.* 479.3 (2018), pp. 3415–3421. DOI: 10.1093/mnras/sty1589. arXiv: 1803.09728 [astro-ph.HE].

[46] A. Albert et al. “Evidence that Ultra-high-energy Gamma Rays Are a Universal Feature near Powerful Pulsars”. In: *Astrophys. J. Lett.* 911.2 (2021), p. L27. DOI: 10.3847/2041-8213/abf4dc. arXiv: 2101.07895 [astro-ph.HE].

[47] Aharonian F.A. An Q. et al. Cao Z. “Ultrahigh-energy photons up to 1.4 petaelectronvolts from 12 γ-ray Galactic sources”. In: *Nature* (2021). DOI: https://doi.org/10.1038/s41586-021-03498-z.

[48] W. Baade and F. Zwicky. “On Super-novae”. In: *Proceedings of the National Academy of Science* 20.5 (May 1934), pp. 254–259. DOI: 10.1073/pnas.20.5.254.

[49] W. Baade and F. Zwicky. “Cosmic Rays from Super-Novae”. In: *Proceedings of the National Academy of Sciences* 20.5 (1934), pp. 259–263. ISSN: 0027-8424. DOI: 10.1073/pnas.20.5.259. eprint: https://www.pnas.org/content/20/5/259.full.pdf. URL: https://www.pnas.org/content/20/5/259.

[50] Jacco Vink. “X-Ray Emission Properties of Supernova Remnants”. In: *Handbook of Supernovae*. Ed. by Athem W. Alsabti and Paul Murdin. 2017, p. 2063. DOI: 10.1007/978-3-319-21846-5_92.

[51] A M Hillas. “Can diffusive shock acceleration in supernova remnants account for high-energy galactic cosmic rays?” In: *Journal of Physics G: Nuclear and Particle Physics* 31.5 (2005), R95–R131. DOI: 10.1088/0954-3899/31/5/r02. URL: https://doi.org/10.1088/0954-3899/31/5/r02.

[52] Pasquale Blasi. “Origin of Galactic Cosmic Rays”. In: *Nuclear Physics B Proceedings Supplements* 239 (June 2013), pp. 140–147. DOI: 10.1016/j.nuclphysbps.2013.05.023. arXiv: 1211.4799 [astro-ph.HE].

[53] A. R. Bell et al. “Cosmic-ray acceleration and escape from supernova remnants”. In: *Monthly Notices of the Royal Astronomical Society* 431.1 (Feb. 2013), pp. 415–429. ISSN: 0035-8711. DOI: 10.1093/mnras/stt179. eprint: https://academic.oup.com/mnras/article-pdf/431/1/415/18243010/stt179.pdf. URL: https://doi.org/10.1093/mnras/stt179.

[54] E. G. Berezhko, L. T. Ksenofontov, and H. J. Voelk. “Confirmation of strong magnetic field amplification and nuclear cosmic ray acceleration in sn 1006”. In: *Astron. Astrophys.* 412 (2003), pp. L11–L14. DOI: 10.1051/0004-6361:20031667. arXiv: astro-ph/0310862.

[55] M. Pohl, H. Yan, and A. Lazarian. “Magnetically Limited X-Ray Filaments in Young Supernova Remnants”. In: *The Astrophysical Journal* 626.2 (2005), pp. L101–L104. DOI: 10.1086/431902. URL: https://doi.org/10.1086/431902.

[56] Y. Uchiyama et al. "Extremely fast acceleration of cosmic rays in a supernova remnant". In: *Nature* 449 (2007), pp. 576–578. DOI: 10.1038/nature06210.

[57] Yousaf Butt et al. "X-ray Hotspot Flares and Implications for Cosmic Ray Acceleration and Magnetic Field amplification in Supernova Remnants". In: *Mon. Not. Roy. Astron. Soc.* 386 (2008), p. 20. DOI: 10.1111/j.1745-3933.2008.00452.x. arXiv: 0801.4954 [astro-ph].

[58] H. Abdalla et al. "H.E.S.S. observations of RX J1713.7−3946 with improved angular and spectral resolution: Evidence for gamma-ray emission extending beyond the X-ray emitting shell". In: *Astron. Astrophys.* 612 (2018), A6. DOI: 10.1051/0004-6361/201629790. arXiv: 1609.08671 [astro-ph.HE].

[59] Felix Aharonian, Ruizhi Yang, and Emma de Oña Wilhelmi. "Massive Stars as Major Factories of Galactic Cosmic Rays". In: *Nature Astron.* 3.6 (2019), pp. 561–567. DOI: 10.1038/s41550-019-0724-0. arXiv: 1804.02331 [astro-ph.HE].

[60] Pierre Cristofari, Pasquale Blasi, and Elena Amato. "The low rate of Galactic pevatrons". In: *Astroparticle Physics* 123, 102492 (Dec. 2020), p. 102492. DOI: 10.1016/j.astropartphys.2020.102492. arXiv: 2007.04294 [astro-ph.HE].

[61] Iwona Mochol. "Pulsar striped winds". In: *Astrophys. Space Sci. Libr.* 446 (2017). Ed. by Diego F. Torres, pp. 135–159. DOI: 10.1007/978-3-319-63031-1_7. arXiv: 1702.00720 [astro-ph.HE].

[62] F. Curtis Michel. "Rotating Magnetosphere: a Simple Relativistic Model". In: *The Astrophysical Journal* 180 (Feb. 1973), pp. 207–226. DOI: 10.1086/151956.

[63] S. V. Bogovalov. "On the physics of cold mhd winds from oblique rotators". In: *Astron. Astrophys.* 349 (1999), pp. 1017–1026. arXiv: astro-ph/9907051.

[64] Y. E. Lyubarsky. "The termination shock in a striped pulsar wind". In: *Monthly Notices of the Royal Astronomical Society* 345.1 (Oct. 2003), pp. 153–160. ISSN: 0035-8711. DOI: 10.1046/j.1365-8711.2003.06927.x. eprint: https://academic.oup.com/mnras/article-pdf/345/1/153/3068277/345-1-153.pdf. URL: https://doi.org/10.1046/j.1365-8711.2003.06927.x.

[65] Takahiro Sudoh, Tim Linden, and John F. Beacom. "TeV Halos are Everywhere: Prospects for New Discoveries". In: *Phys. Rev. D* 100.4 (2019), p. 043016. DOI: 10.1103/PhysRevD.100.043016. arXiv: 1902.08203 [astro-ph.HE].

[66] Benoît Cerutti, Alexander A. Philippov, and Anatoly Spitkovsky. "Modelling high-energy pulsar light curves from first principles". In: *Monthly Notices of the Royal Astronomical Society* 457.3 (Feb. 2016), pp. 2401–2414. ISSN: 0035-8711. DOI: 10.1093/mnras/stw124. eprint: https://academic.oup.com/mnras/article-pdf/457/3/2401/8000820/stw124.pdf. URL: https://doi.org/10.1093/mnras/stw124.

[67] S. Ansoldi et al. "Teraelectronvolt pulsed emission from the Crab Pulsar detected by MAGIC". In: *Astronomy & Astrophysics* 585 (2016), A133. ISSN: 1432-0746. DOI: 10.1051/0004-6361/201526853. URL: http://dx.doi.org/10.1051/0004-6361/201526853.

[68] H. Abdalla et al. "First Ground-based Measurement of Sub-20 GeV to 100 GeV γ-rays from the Vela Pulsar with H.E.S.S. II". In: *Astron. Astrophys.* 620 (2018), A66. DOI: 10.1051/0004-6361/201732153. arXiv: 1807.01302 [astro-ph.HE].

[69] Lorenzo Sironi and Anatoly Spitkovsky. "Acceleration of particles at the termination shock of a relativistic striped wind". In: *The Astrophysical Journal* 741.1 (2011), p. 39. DOI: 10.1088/0004-637x/741/1/39. URL: https://doi.org/10.1088%2F0004-637x%2F741%2F1%2F39.

[70] G. R. Werner et al. "The extent of power-law energy spectra in collisionless relativistic magnetic reconnection in pair plasmas". In: *Astrophys. J. Lett.* 816.1 (2016), p. L8. DOI: 10.3847/2041-8205/816/1/L8. arXiv: 1409.8262 [astro-ph.HE].

[71] Claire Guépin, Benoît Cerutti, and Kumiko Kotera. "Proton acceleration in pulsar magnetospheres". In: *Astron. Astrophys.* 635 (2020), A138. DOI: 10.1051/0004-6361/201936816. arXiv: 1910.11387 [astro-ph.HE].

[72] Claire Guépin et al. "Pevatron at the Galactic Center: Multi-Wavelength Signatures from Millisecond Pulsars". In: *JCAP* 07 (2018), p. 042. DOI: 10.1088/1475-7516/2018/07/042. arXiv: 1806.03307 [astro-ph.HE].

[73] Fabio Acero. "Pulsar Wind Nebulae Viewed Through the Gamma-Ray Eye". In: *Astrophys. Space Sci. Libr.* 446 (2017). Ed. by Diego F. Torres, pp. 47–59. DOI: 10.1007/978-3-319-63031-1_3.

[74] H.E.S.S. Collaboration et al. "Acceleration of petaelectronvolt protons in the Galactic Centre". In: *Nature* 531.7595 (Mar. 2016), pp. 476–479. DOI: 10.1038/nature17147. arXiv: 1603.07730 [astro-ph.HE].

[75] H. E. S. S. Collaboration et al. "Characterising the VHE diffuse emission in the central 200 parsecs of our Galaxy with H.E.S.S." In: *Astronomy & Astrophysics* 612, A9 (Apr. 2018), A9. DOI: 10.1051/0004-6361/201730824. arXiv: 1706.04535 [astro-ph.HE].

[76] J. A. Hinton and F. A. Aharonian. "Inverse Compton Scenarios for the TeV Gamma-Ray Emission of the Galactic Center". In: *The Astrophysical Journal* 657.1 (2007), pp. 302–307. ISSN: 1538-4357. DOI: 10.1086/510283. URL: http://dx.doi.org/10.1086/510283.

[77] C. B. Adams et al. "VERITAS Observations of the Galactic Center Region at Multi-TeV Gamma-Ray Energies". In: *Astrophys. J.* 913.2 (2021), p. 115. DOI: 10.3847/1538-4357/abf926. arXiv: 2104.12735 [astro-ph.HE].

[78] MAGIC Collaboration et al. "MAGIC observations of the diffuse γ-ray emission in the vicinity of the Galactic center". In: *Astronomy & Astrophysics* 642, A190 (Oct. 2020), A190. DOI: 10.1051/0004-6361/201936896. arXiv: 2006.00623 [astro-ph.HE].

[79] A. M. Bykov, P. E. Gladilin, and S. M. Osipov. "Non-linear model of particle acceleration at colliding shock flows". In: *Monthly Notices of the Royal Astronomical Society* 429.3 (Jan. 2013), pp. 2755–2762. ISSN: 0035-8711. DOI: 10.1093/mnras/sts553. eprint: https://academic.oup.com/mnras/article-pdf/429/3/2755/3302100/sts553.pdf. URL: https://doi.org/10.1093/mnras/sts553.

[80] A. M. Bykov et al. "Ultrahard spectra of PeV neutrinos from supernovae in compact star clusters". In: *Monthly Notices of the Royal Astronomical Society* 453.1 (Aug. 2015), pp. 113–121. ISSN: 0035-8711. DOI: 10.1093/mnras/stv1606. eprint: https://academic.oup.com/mnras/article-pdf/453/1/113/4920892/stv1606.pdf. URL: https://doi.org/10.1093/mnras/stv1606.

[81] T Vieu, S Gabici, and V Tatischeff. "Particle acceleration at colliding shock waves". In: *Monthly Notices of the Royal Astronomical Society* 494.3 (Apr. 2020), pp. 3166–3176. ISSN: 0035-8711. DOI: 10.1093/mnras/staa799. eprint: https://academic.oup.com/mnras/article-pdf/494/3/3166/33137514/staa799.pdf. URL: https://doi.org/10.1093/mnras/staa799.

[82] M. Ackermann et al. "A Cocoon of Freshly Accelerated Cosmic Rays Detected by Fermi in the Cygnus Superbubble". In: *Science* 334.6059 (2011), pp. 1103–1107. ISSN: 0036-8075. DOI: 10.1126/science.1210311. eprint: https://

science.sciencemag.org/content/334/6059/1103.full.pdf. URL: https://science.sciencemag.org/content/334/6059/1103.

[83] Felix Aharonian, Ruizhi Yang, and Emma de Oña Wilhelmi. "Massive stars as major factories of Galactic cosmic rays". In: *Nature Astronomy* 3 (Mar. 2019), pp. 561–567. DOI: 10.1038/s41550-019-0724-0. arXiv: 1804.02331 [astro-ph.HE].

[84] A. U. Abeysekara et al. "HAWC observations of the acceleration of very-high-energy cosmic rays in the Cygnus Cocoon". In: *Nature Astron.* 5.5 (2021), pp. 465–471. DOI: 10.1038/s41550-021-01318-y. arXiv: 2103.06820 [astro-ph.HE].

[85] M. Amenomori et al. "Gamma-ray Observation of the Cygnus Region in the 100 TeV Energy Region". In: (July 2021). arXiv: 2107.01064 [astro-ph.HE].

[86] M. Amenomori et al. "First Detection of sub-PeV Diffuse Gamma Rays from the Galactic Disk: Evidence for Ubiquitous Galactic Cosmic Rays beyond PeV Energies". In: *Phys. Rev. Lett.* 126.14 (2021), p. 141101. DOI: 10.1103/PhysRevLett.126.141101. arXiv: 2104.05181 [astro-ph.HE].

[87] M. Bouyahiaoui, M. Kachelriess, and D.V. Semikoz. "Vela as the Source of Galactic Cosmic Rays above 100 TeV". In: *JCAP* 01 (2019), p. 046. DOI: 10.1088/1475-7516/2019/01/046. arXiv: 1812.03522 [astro-ph.HE].

[88] A. Albert et al. "HAWC J2227+610 and its association with G106.3+2.7, a new potential Galactic PeVatron". In: *Astrophys. J. Lett.* 896 (2020), p. L29. DOI: 10.3847/2041-8213/ab96cc. arXiv: 2005.13699 [astro-ph.HE].

[89] M. Amenomori et al. "Potential PeVatron supernova remnant G106.3+2.7 seen in the highest-energy gamma rays". In: *Nature Astron.* 5.5 (2021), pp. 460–464. DOI: 10.1038/s41550-020-01294-9.

[90] Victor A. Acciari et al. "Resolving the origin of very-high-energy gamma-ray emission from the PeVatron candidate SNR G106.3+2.7 using MAGIC telescopes". In: *PoS* ICRC2021 (2021), p. 796. DOI: 10.22323/1.395.0796.

[91] W. B. Atwood et al. "The Large Area Telescope on the Fermi Gamma-Ray Space Telescope Mission". In: *The Astrophysical Journal* 697.2 (June 2009), pp. 1071–1102. DOI: 10.1088/0004-637X/697/2/1071. arXiv: 0902.1089 [astro-ph.IM].

[92] Jamie Holder. "Atmospheric Cherenkov Gamma-ray Telescopes". In: *arXiv e-prints*, arXiv:1510.05675 (Oct. 2015), arXiv:1510.05675. arXiv: 1510.05675 [astro-ph.IM].

[93] Mathieu de Naurois and Daniel Mazin. "Ground-based detectors in very-high-energy gamma-ray astronomy". In: *Comptes Rendus Physique* 16 (2015), pp. 610–627. DOI: 10.1016/j.crhy.2015.08.011. arXiv: 1511.00463 [astro-ph.IM].

[94] Jürgen Knödlseder. "The future of gamma-ray astronomy". In: *Comptes Rendus Physique* 17 (2016), pp. 663–678. DOI: 10.1016/j.crhy.2016.04.008. arXiv: 1602.02728 [astro-ph.IM].

[95] Pierre Auger et al. "Extensive Cosmic-Ray Showers". In: *Rev. Mod. Phys.* 11 (3-4 1939), pp. 288–291. DOI: 10.1103/RevModPhys.11.288. URL: https://link.aps.org/doi/10.1103/RevModPhys.11.288.

[96] W. Galbraith and J. V. Jelley. "Light Pulses from the Night Sky associated with Cosmic Rays". In: *Nature* 171.4347 (Feb. 1953), pp. 349–350. DOI: 10.1038/171349a0.

[97] T. C. Weekes and K. E. Turver. "Gamma-Ray Astronomy from 10-100 GeV: a New Approach". In: *Recent Advances in Gamma-Ray Astronomy*. Ed. by

R. D. Wills and B. Battrick. Vol. 124. ESA Special Publication. July 1977, p. 279.

[98] T. C. Weekes et al. "Observation of TeV Gamma Rays from the Crab Nebula Using the Atmospheric Cerenkov Imaging Technique". In: *The Astrophysical Journal* 342 (July 1989), p. 379. DOI: 10.1086/167599.

[99] M. S. Schubnell et al. "Very High Energy Gamma-Ray Emission from the Blazar Markarian 421". In: *The Astrophysical Journal* 460 (Apr. 1996), p. 644. DOI: 10.1086/176998. arXiv: astro-ph/9602068 [astro-ph].

[100] P. Fleury and G. Vacanti, eds. *Towards a major atmospheric Cherenkov detector for TeV astroparticle physics. Proceedings, 1st Palaiseau Workshop, Palaiseau, France, June 11-12, 1992*. 1992.

[101] A. Barrau et al. "The CAT imaging telescope for very high-energy gamma-ray astronomy". In: *Nucl. Instrum. Meth. A* 416 (1998), pp. 278–292. DOI: 10.1016/S0168-9002(98)00749-9. arXiv: astro-ph/9804046.

[102] A. Kohnle et al. "Stereoscopic imaging of air showers with the first two HEGRA Cherenkov telescopes". In: *Astropart. Phys.* 5 (1996), pp. 119–131. DOI: 10.1016/0927-6505(96)00011-4.

[103] F. A. Aharonian et al. "Observations of MKN 421 during 1997 and 1998 in the energy range above 500 GeV with the HEGRA stereoscopic Cherenkov telescope system". In: *Astronomy & Astrophysics* 350 (Oct. 1999), pp. 757–764. arXiv: astro-ph/9905032 [astro-ph].

[104] J. Aleksić et al. "Performance of the MAGIC stereo system obtained with Crab Nebula data". In: *Astroparticle Physics* 35.7 (Feb. 2012), pp. 435–448. DOI: 10.1016/j.astropartphys.2011.11.007. arXiv: 1108.1477 [astro-ph.IM].

[105] Dave B. Kieda. "The Gamma Ray Detection sensitivity of the upgraded VERITAS Observatory". In: *33rd International Cosmic Ray Conference*. Aug. 2013. arXiv: 1308.4849 [astro-ph.IM].

[106] Douglas M. Gingrich et al. "The STACEE ground-based gamma-ray detector". In: *IEEE Trans. Nucl. Sci.* 52 (2005), pp. 2977–2985. DOI: 10.1109/TNS.2005.855705. arXiv: astro-ph/0506613.

[107] P. Goret et al. "Observations of TeV gamma rays from the Crab Nebula." In: *Astronomy & Astrophysics* 270 (Mar. 1993), pp. 401–406.

[108] P. Baillon et al. "Gamma-ray spectrum of the Crab Nebula in the multiTeV region". In: *Astropart. Phys.* 1 (1993). [Erratum: Astropart.Phys. 5, 79 (1996)], pp. 341–356. DOI: 10.1016/0927-6505(93)90001-T.

[109] M. de Naurois et al. "Measurement of the Crab Flux above 60 GeV with the CELESTE Cerenkov Telescope". In: *The Astrophysical Journal* 566.1 (2002), 343âĂŞ357. ISSN: 1538-4357. DOI: 10.1086/337991. URL: http://dx.doi.org/10.1086/337991.

[110] R. Atkins et al. "TeV gamma-ray survey of the northern hemisphere sky using the Milagro Observatory". In: *Astrophys. J.* 608 (2004), pp. 680–685. DOI: 10.1086/420880.

[111] A. U. Abeysekara et al. "Sensitivity of the High Altitude Water Cherenkov Detector to Sources of Multi-TeV Gamma Rays". In: *Astropart. Phys.* 50-52 (2013), pp. 26–32. DOI: 10.1016/j.astropartphys.2013.08.002. arXiv: 1306.5800 [astro-ph.HE].

[112] X. A. Huo et al. "Tibet-AS γ Experiment". In: *International Cosmic Ray Conference*. Vol. 2. International Cosmic Ray Conference. Jan. 1990, p. 427.

[113] Masato Takita et al. "The Tibet AS+MD Project; status report 2017". In: *PoS* ICRC2017 (2018), p. 831. DOI: 10.22323/1.301.0831.

[114] M. Amenomori et al. "First Detection of Photons with Energy Beyond 100 TeV from an Astrophysical Source". In: *Phys. Rev. Lett.* 123.5 (2019), p. 051101. DOI: 10.1103/PhysRevLett.123.051101. arXiv: 1906.05521 [astro-ph.HE].

[115] F. Aharonian et al. "Observations of the Crab Nebula with H.E.S.S". In: *Astron. Astrophys.* 457 (2006), pp. 899–915. DOI: 10.1051/0004-6361:20065351. arXiv: astro-ph/0607333.

[116] A. Balzer et al. "The H.E.S.S. central data acquisition system". In: *Astroparticle Physics* 54 (Feb. 2014), pp. 67–80. DOI: 10.1016/j.astropartphys.2013.11.007. arXiv: 1311.3486 [astro-ph.IM].

[117] John M. Davies and Eugene S. Cotton. "Design of the quartermaster solar furnace". In: *Solar Energy* 1.2-3 (Apr. 1957), pp. 16–22. DOI: 10.1016/0038-092X(57)90116-0.

[118] François Hénault et al. "Design of light concentrators for Cherenkov telescope observatories". In: *Nonimaging Optics: Efficient Design for Illumination and Solar Concentration X*. Ed. by Roland Winston and Jeffrey Gordon. Vol. 8834. Society of Photo-Optical Instrumentation Engineers (SPIE) Conference Series. Sept. 2013, p. 883405. DOI: 10.1117/12.2024049. arXiv: 1309.4252 [astro-ph.IM].

[119] T. Ashton et al. "A NECTAr-based upgrade for the Cherenkov cameras of the H.E.S.S. 12-meter telescopes". In: *Astroparticle Physics* 118 (2020), p. 102425. ISSN: 0927-6505. DOI: https://doi.org/10.1016/j.astropartphys.2019.102425. URL: https://www.sciencedirect.com/science/article/pii/S0927650519302282.

[120] G. Lamanna et al. *Cherenkov Telescope Array Data Management*. 2015. arXiv: 1509.01012 [astro-ph.IM].

[121] F. Aharonian et al. "Calibration of cameras of the H.E.S.S. detector". In: *Astropart. Phys.* 22 (2004), pp. 109–125. DOI: 10.1016/j.astropartphys.2004.06.006. arXiv: astro-ph/0406658.

[122] A. M. Hillas. "Cerenkov Light Images of EAS Produced by Primary Gamma Rays and by Nuclei". In: *19th International Cosmic Ray Conference (ICRC19), Volume 3*. Vol. 3. International Cosmic Ray Conference. Aug. 1985, p. 445.

[123] M. Lemoine-Goumard, B. Degrange, and M. Tluczykont. "Selection and 3D-Reconstruction of Gamma-Ray-induced Air Showers with a Stereoscopic System of Atmospheric Cherenkov Telescopes". In: *Astropart. Phys.* 25 (2006), pp. 195–211. DOI: 10.1016/j.astropartphys.2006.01.005. arXiv: astro-ph/0601373.

[124] Mathieu de Naurois and Loïc Rolland. "A high performance likelihood reconstruction of γ-rays for imaging atmospheric Cherenkov telescopes". In: *Astroparticle Physics* 32.5 (Dec. 2009), pp. 231–252. DOI: 10.1016/j.astropartphys.2009.09.001. arXiv: 0907.2610 [astro-ph.IM].

[125] R. D. Parsons and J. A. Hinton. "A Monte Carlo Template based analysis for Air-Cherenkov Arrays". In: *Astropart. Phys.* 56 (2014), pp. 26–34. DOI: 10.1016/j.astropartphys.2014.03.002. arXiv: 1403.2993 [astro-ph.IM].

[126] L. Breiman et al. *Classification and Regression Trees*. Monterey, CA: Wadsworth and Brooks, 1984.

[127] Yoav Freund and Robert E. Schapire. "Experiments with a New Boosting Algorithm". In: *Proceedings of the Thirteenth International Conference on International Conference on Machine Learning*. ICML'96. Bari, Italy: Morgan Kaufmann Publishers Inc., 1996, pp. 148–156. ISBN: 1558604197.

[128] A. Hoecker et al. "TMVA - Toolkit for Multivariate Data Analysis". In: *arXiv e-prints*, physics/0703039 (Mar. 2007), physics/0703039. arXiv: physics/0703039 [physics.data-an].

[129] Y. Becherini et al. "A new analysis strategy for detection of faint γ-ray sources with Imaging Atmospheric Cherenkov Telescopes". In: *Astroparticle Physics* 34.12 (July 2011), pp. 858–870. DOI: 10.1016/j.astropartphys.2011.03.005. arXiv: 1104.5359 [astro-ph.HE].

[130] Y. Becherini, M. Punch, and H.E.S.S. Collaboration. "Performance of HESS-II in multi-telescope mode with a multi-variate analysis". In: *High Energy Gamma-Ray Astronomy: 5th International Meeting on High Energy Gamma-Ray Astronomy*. Ed. by Felix A. Aharonian, Werner Hofmann, and Frank M. Rieger. Vol. 1505. American Institute of Physics Conference Series. Dec. 2012, pp. 741–744. DOI: 10.1063/1.4772366.

[131] Bruno Khelifi et al. "HAP-Fr, a pipeline of data analysis for the HESS-II experiment". In: *PoS* ICRC2015 (2016), p. 837. DOI: 10.22323/1.236.0837.

[132] Julien Lefaucheur. "Astronomie gamma depuis le sol et l'espace : premières analyses du réseau hybride HESS-II et recherche de candidats blazars parmi les sources non identifiées du Fermi-LAT". Thèse de doctorat dirigée par Pita, Santiago Physique de l'univers Sorbonne Paris Cité 2015. PhD thesis. 2015, 1 vol. (X–262 p.) URL: http://www.theses.fr/2015USPCC093.

[133] S. Ohm, C. van Eldik, and K. Egberts. "γ/hadron separation in very-high-energy γ-ray astronomy using a multivariate analysis method". In: *Astroparticle Physics* 31.5 (June 2009), pp. 383–391. DOI: 10.1016/j.astropartphys.2009.04.001. arXiv: 0904.1136 [astro-ph.IM].

[134] A. Balzer et al. "The H.E.S.S. data acquisition system". In: *J. Phys. Conf. Ser.* 513 (2014). Ed. by D. L. Groep and D. Bonacorsi, p. 012003. DOI: 10.1088/1742-6596/513/1/012003.

[135] M. P. Kertzman and G. H. Sembroski. "Computer simulation methods for investigating the detection characteristics of TeV air Cherenkov telescopes". In: *Nucl. Instrum. Meth. A* 343 (1994), pp. 629–643. DOI: 10.1016/0168-9002(94)90247-X.

[136] Julien Guy. "Premiers résultats de l'expérience HESS et étude du potentiel de détection de matière noire supersymétrique". Theses. Université Pierre et Marie Curie - Paris VI, May 2003. URL: https://tel.archives-ouvertes.fr/tel-00003488.

[137] Konrad Bernlöhr. "Impact of atmospheric parameters on the atmospheric Cherenkov technique*". In: *Astroparticle Physics* 12.4 (Jan. 2000), pp. 255–268. DOI: 10.1016/S0927-6505(99)00093-6. arXiv: astro-ph/9908093 [astro-ph].

[138] Yoshiki Ohtani et al. "Cross-calibration and combined analysis of the CTA-LST prototype and the MAGIC telescopes". In: *PoS* ICRC2021 (2021), p. 724. DOI: 10.22323/1.395.0724.

[139] Hyuga Abe et al. "Status and results of the prototype LST of CTA". In: *PoS* ICRC2021 (2021), p. 872. DOI: 10.22323/1.395.0872.

[140] Yukiho Kobayashi et al. "Camera Calibration of the CTA-LST prototype". In: *PoS* ICRC2021 (2021), p. 720. DOI: 10.22323/1.395.0720.

[141] Hyuga Abe et al. "Physics Performance of the Large Size Telescope prototype of the Cherenkov Telescope Array". In: *PoS* ICRC2021 (2021), p. 806. DOI: 10.22323/1.395.0806.

[142] Juan Cortina. "Status of the Large Size Telescopes of the Cherenkov Telescope Array". In: *PoS* ICRC2019 (2021), p. 653. DOI: 10.22323/1.358.0653. arXiv: 1907.10146 [astro-ph.IM].

[143] J. F. Glicenstein and M. Shayduk. "NectarCAM, a camera for the medium sized telescopes of the Cherenkov telescope array". In: *6th International Symposium on High Energy Gamma-Ray Astronomy*. Vol. 1792. American Institute of Physics Conference Series. Jan. 2017, p. 080009. DOI: 10.1063/1.4969030. arXiv: 1610.04173 [astro-ph.IM].

[144] Iryna Lypova et al. "A Major Upgrade of the H.E.S.S. Cherenkov Cameras". In: *EPJ Web Conf.* 136 (2017). Ed. by A. Morselli, A. Capone, and G. Rodriguez Fernandez, p. 03002. DOI: 10.1051/epjconf/201713603002.

[145] G. Pühlhofer et al. "FlashCam: A fully digital camera for CTA telescopes". In: *High Energy Gamma-Ray Astronomy: 5th International Meeting on High Energy Gamma-Ray Astronomy*. Ed. by Felix A. Aharonian, Werner Hofmann, and Frank M. Rieger. Vol. 1505. American Institute of Physics Conference Series. Dec. 2012, pp. 777–780. DOI: 10.1063/1.4772375. arXiv: 1211.3684 [astro-ph.IM].

[146] Victor Barbosa Martins and Markus Garczarczyk. "The structure monitoring of the MST prototype of CTA". In: *Society of Photo-Optical Instrumentation Engineers (SPIE) Conference Series*. Vol. 11445. Society of Photo-Optical Instrumentation Engineers (SPIE) Conference Series. Dec. 2020, 114456E. DOI: 10.1117/12.2560930. arXiv: 2012.08995 [astro-ph.IM].

[147] Salvatore Scuderi. "The ASTRI Program". In: *European Physical Journal Web of Conferences*. Vol. 209. European Physical Journal Web of Conferences. Sept. 2019, p. 01001. DOI: 10.1051/epjconf/201920901001.

[148] Richard White and Harm Schoorlemmer. "A Compact High Energy Camera (CHEC) for the Gamma-ray Cherenkov Telescope of the Cherenkov Telescope Array". In: *PoS* ICRC2017 (2018), p. 817. DOI: 10.22323/1.301.0817. arXiv: 1709.05799 [astro-ph.IM].

[149] J. Knödlseder et al. "GammaLib and ctools: A software framework for the analysis of astronomical gamma-ray data". In: *Astron. Astrophys.* 593 (2016), A1. DOI: 10.1051/0004-6361/201628822. arXiv: 1606.00393 [astro-ph.IM].

[150] W. D. Pence et al. "Definition of the Flexible Image Transport System (FITS), version 3.0". In: *Astronomy & Astrophysics* 524, A42 (Dec. 2010), A42. DOI: 10.1051/0004-6361/201015362.

[151] D. Berge, S. Funk, and J. Hinton. "Background modelling in very-high-energy γ-ray astronomy". In: *Astronomy & Astrophysics* 466.3 (May 2007), pp. 1219–1229. DOI: 10.1051/0004-6361:20066674. arXiv: astro-ph/0610959 [astro-ph].

[152] S. P. Wakely and D. Horan. "TeVCat: An online catalog for Very High Energy Gamma-Ray Astronomy". In: *International Cosmic Ray Conference* 3 (2008), pp. 1341–1344.

[153] L. Mohrmann et al. "Validation of open-source science tools and background model construction in γ-ray astronomy". In: *Astronomy & Astrophysics* 632, A72 (Dec. 2019), A72. DOI: 10.1051/0004-6361/201936452. arXiv: 1910.08088 [astro-ph.IM].

[154] Christoph Deil et al. "Open high-level data formats and software for gamma-ray astronomy". In: *6th International Symposium on High Energy Gamma-Ray Astronomy*. Vol. 1792. American Institute of Physics Conference Series. Jan. 2017, p. 070006. DOI: 10.1063/1.4969003. arXiv: 1610.01884 [astro-ph.IM].

[155] Christoph Deil et al. *Data formats for gamma-ray astronomy - version 0.2*. The formats described in this v0.2 are mostly what was used for the 2017 first CTA data challenge, and what will be used for the upcoming H.E.S.S. data release and the joint Crab paper. We expect that the format will change significantly over the next year or two as the CTA formats are being defined. Sept. 2018. DOI: 10.5281/zenodo.1409831. URL: https://doi.org/10.5281/zenodo.1409831.

[156] H. Abdalla et al. "H.E.S.S. first public test data release". In: (Oct. 2018). DOI: 10.5281/zenodo.1421098. arXiv: 1810.04516 [astro-ph.HE].

[157] C. Nigro et al. "Towards open and reproducible multi-instrument analysis in gamma-ray astronomy". In: *Astronomy & Astrophysics* 625, A10 (May 2019), A10. DOI: 10.1051/0004-6361/201834938. arXiv: 1903.06621 [astro-ph.HE].

[158] H. Abdalla et al. "Evidence of 100 TeV gamma-ray emission from HESS J1702-420: a new PeVatron candidate". In: *Astronomy & Astrophysics* (2021). ISSN: 1432-0746. DOI: 10.1051/0004-6361/202140962. URL: http://dx.doi.org/10.1051/0004-6361/202140962.

[159] S. S. Wilks. "The Large-Sample Distribution of the Likelihood Ratio for Testing Composite Hypotheses". In: *Ann. Math. Statist.* 9.1 (Mar. 1938), pp. 60–62. DOI: 10.1214/aoms/1177732360. URL: https://doi.org/10.1214/aoms/1177732360.

[160] T. P. Li and Y. Q. Ma. "Analysis methods for results in gamma-ray astronomy." In: *The Astrophysical Journal* 272 (Sept. 1983), pp. 317–324. DOI: 10.1086/161295.

[161] W. Cash. "Parameter estimation in astronomy through application of the likelihood ratio." In: *The Astrophysical Journal* 228 (Mar. 1979), pp. 939–947. DOI: 10.1086/156922.

[162] C. Deil et al. "Gammapy - A prototype for the CTA science tools". In: *35th International Cosmic Ray Conference (ICRC2017)*. Vol. 301. International Cosmic Ray Conference. Jan. 2017, p. 766. arXiv: 1709.01751 [astro-ph.IM].

[163] Christoph Deil et al. *gammapy/gammapy: v0.17*. Version v0.17. Apr. 2020. DOI: 10.5281/zenodo.4701492. URL: https://doi.org/10.5281/zenodo.4701492.

[164] Hans Dembinski and Piti Ongmongkolkul et al. "scikit-hep/iminuit". In: (2020). DOI: 10.5281/zenodo.4310361. URL: https://doi.org/10.5281/zenodo.4310361.

[165] V. Zabalza. "naima: a Python package for inference of relativistic particle energy distributions from observed nonthermal spectra". In: *Proc. of International Cosmic Ray Conference 2015* (2015), p. 922. eprint: 1509.03319.

[166] A. Daum et al. "First results on the performance of the HEGRA IACT array". In: *Astroparticle Physics* 8.1-2 (Dec. 1997), pp. 1–11. DOI: 10.1016/S0927-6505(97)00031-5.

[167] Quentin Remy et al. "Survey of the Galactic Plane with the Cherenkov Telescope Array". In: July 2021, p. 886. DOI: 10.22323/1.395.0886.

[168] F. Piron et al. "Temporal and spectral gamma-ray properties of Mkn 421 above 250 GeV from CAT observations between 1996 and 2000". In: *Astronomy and Astrophysics - A&A* 374 (2001), pp. 895–906. URL: http://hal.in2p3.fr/in2p3-00010964.

[169] S. Carrigan et al. "Charting the TeV Milky Way: H.E.S.S. Galactic plane survey maps, catalog and source populations". In: *arXiv e-prints*, arXiv:1307.4868 (July 2013), arXiv:1307.4868. arXiv: 1307.4868 [astro-ph.HE].

[170] J. R. Mattox et al. “The Likelihood Analysis of EGRET Data”. In: *The Astrophysical Journal* 461 (Apr. 1996), p. 396. DOI: 10.1086/177068.

[171] A. A. Abdo et al. “Fermi/Large Area Telescope Bright Gamma-Ray Source List”. In: *The Astrophysical Journal* 183.1 (July 2009), pp. 46–66. DOI: 10.1088/0067-0049/183/1/46. arXiv: 0902.1340 [astro-ph.HE].

[172] A. Donath et al. “Gammapy: An open-source Python package for gamma-ray astronomy”. In: *34th International Cosmic Ray Conference (ICRC2015)*. Vol. 34. International Cosmic Ray Conference. July 2015, p. 789. arXiv: 1509.07408 [astro-ph.IM].

[173] Ulisses Barres de Almeida. “The Southern Wide Field Gamma ray Observatory”. In: *Astronomische Nachrichten* 342.431 (Jan. 2021), pp. 431–437. DOI: 10.1002/asna.202113946. arXiv: 2012.13740 [astro-ph.IM].

[174] T. P. Li and Y. Q. Ma. “Analysis methods for results in gamma-ray astronomy.” In: *The Astrophysical Journal* 272 (Sept. 1983), pp. 317–324. DOI: 10.1086/161295.

[175] E. Giacani et al. “A new study of the supernova remnant G344.7-0.1 located in the vicinity of the unidentified TeV source HESS J1702-420”. In: *Astronomy & Astrophysics* 531, A138 (July 2011), A138. DOI: 10.1051/0004-6361/201116768.

[176] G. M. Dubner et al. “Very Large Array Observations at 1465MHz of Galactic Supernova Remnants”. In: *The Astronomical Journal* 105 (June 1993), p. 2251. DOI: 10.1086/116603.

[177] J. B. Z. Whiteoak and A. J. Green. “The MOST supernova remnant catalogue (MSC).” In: *Astronomy & Astrophysics Supplementary Series* 118 (Aug. 1996), pp. 329–380.

[178] H. Yamaguchi et al. “ELEMENTAL ABUNDANCES IN THE POSSIBLE TYPE Ia SUPERNOVA REMNANT G344.7-0.1”. In: *The Astrophysical Journal* 749.2 (2012), p. 137. DOI: 10.1088/0004-637x/749/2/137. URL: https://doi.org/10.1088%2F0004-637x%2F749%2F2%2F137.

[179] J. A. Combi et al. “An X-ray study of the SNR G344.7-0.1 and the central object CXOU J170357.8-414302”. In: *Astronomy & Astrophysics* 522, A50 (Nov. 2010), A50. DOI: 10.1051/0004-6361/200913735. arXiv: 1007.5146 [astro-ph.HE].

[180] J. Eagle et al. “Gamma-ray emission revealed at the western edge of SNR G344.7-0.1”. In: *arXiv e-prints*, arXiv:2006.08757 (June 2020), arXiv:2006.08757. arXiv: 2006.08757 [astro-ph.HE].

[181] J C Lau et al. “Probing the origin of the unidentified TeV Îş-ray source HESSâĂŁJ1702-420 via the surrounding interstellar medium”. In: *Monthly Notices of the Royal Astronomical Society* 483.3 (Dec. 2018), pp. 3659–3672. ISSN: 0035-8711. DOI: 10.1093/mnras/sty3326. eprint: https://academic.oup.com/mnras/article-pdf/483/3/3659/27299894/sty3326.pdf. URL: https://doi.org/10.1093/mnras/sty3326.

[182] M. Kramer et al. “The Parkes Multibeam Pulsar Survey - III. Young pulsars and the discovery and timing of 200 pulsars”. In: *Monthly Notices of the Royal Astronomical Society* 342.4 (July 2003), pp. 1299–1324. ISSN: 0035-8711. DOI: 10.1046/j.1365-8711.2003.06637.x. eprint: https://academic.oup.com/mnras/article-pdf/342/4/1299/2827770/342-4-1299.pdf. URL: https://doi.org/10.1046/j.1365-8711.2003.06637.x.

[183] Yves A. Gallant. “Associations of very high energy gamma-ray sources discovered by H.E.S.S. with pulsar wind nebulae”. In: *Astrophysics and Space Science*

309.1-4 (June 2007), pp. 197–202. DOI: 10.1007/s10509-007-9430-y. arXiv: astro-ph/0611720 [astro-ph].

[184] H.E.S.S. Collaboration et al. "The population of TeV pulsar wind nebulae in the H.E.S.S. Galactic Plane Survey". In: *Astronomy & Astrophysics* 612, A2 (Apr. 2018), A2. DOI: 10.1051/0004-6361/201629377. arXiv: 1702.08280 [astro-ph.HE].

[185] Chulhoon Chang, Alexander Konopelko, and Wei Cui. "Search for Pulsar Wind Nebula Associations of Unidentified TeV Gamma-Ray Sources". In: *Astrophys. J.* 682 (2008), p. 1177. DOI: 10.1086/589225. arXiv: 0709.3614 [astro-ph].

[186] Takahisa Fujinaga et al. "Suzaku Observation of the Unidentified Very High Energy Gamma-Ray Source HESS J1702-420". In: *Publications of the Astronomical Society of Japan* 63.sp3 (Nov. 2011), S857–S864. ISSN: 0004-6264. DOI: 10.1093/pasj/63.sp3.S857. eprint: https://academic.oup.com/pasj/article-pdf/63/sp3/S857/17443961/pasj63-0S857.pdf. URL: https://doi.org/10.1093/pasj/63.sp3.S857.

[187] N. M. McClure-Griffiths et al. "The Southern Galactic Plane Survey: H I Observations and Analysis". In: *The Astrophysical Journal* 158.2 (June 2005), pp. 178–187. DOI: 10.1086/430114. arXiv: astro-ph/0503134 [astro-ph].

[188] Chulhoon Chang, Alexander Konopelko, and Wei Cui. "Search for Pulsar Wind Nebula Associations of Unidentified TeV Gamma-Ray Sources". In: *Astrophys. J.* 682 (2008), p. 1177. DOI: 10.1086/589225. arXiv: 0709.3614 [astro-ph].

[189] F. Acero et al. "Development of the Model of Galactic Interstellar Emission for Standard Point-Source Analysis of Fermi Large Area Telescope Data". In: *Astrophys. J. Suppl.* 223.2 (2016), p. 26. DOI: 10.3847/0067-0049/223/2/26. arXiv: 1602.07246 [astro-ph.HE].

[190] T. M. Dame, Dap Hartmann, and P. Thaddeus. "The Milky Way in molecular clouds: A New complete CO survey". In: *Astrophys. J.* 547 (2001), pp. 792–813. DOI: 10.1086/318388. arXiv: astro-ph/0009217.

[191] Catherine Braiding et al. "The Mopra Southern Galactic Plane CO Survey—Data Release 3". In: *Publications of the Astronomical Society of Australia* 35, e029 (Aug. 2018), e029. DOI: 10.1017/pasa.2018.18. arXiv: 1902.04249 [astro-ph.GA].

[192] A. W. Strong et al. "The distribution of cosmic-ray sources in the galaxy, gamma-rays, and the gradient in the co-to-h2 relation". In: *Astron. Astrophys.* 422 (2004), pp. L47–L50. DOI: 10.1051/0004-6361:20040172. arXiv: astro-ph/0405275.

[193] Jacques P. Vallée. "The Start of the Sagittarius Spiral Arm (Sagittarius Origin) and the Start of the Norma Spiral Arm (Norma Origin): Model-computed and Observed Arm Tangents at Galactic Longitudes -20 deg $<$ l $<$ +23 deg". In: *The Astronomical Journal* 151.3, 55 (Mar. 2016), p. 55. DOI: 10.3847/0004-6256/151/3/55. arXiv: 1602.02183 [astro-ph.GA].

[194] Read, A. M. and Ponman, T. J. "The XMM-Newton EPIC background: Production of background maps and event files*". In: *A&A* 409.1 (2003), pp. 395–410. DOI: 10.1051/0004-6361:20031099. URL: https://doi.org/10.1051/0004-6361:20031099.

[195] M. Ajello et al. "3FHL: The Third Catalog of Hard Fermi-LAT Sources". In: *Astrophys. J. Suppl.* 232.2 (2017), p. 18. DOI: 10.3847/1538-4365/aa8221. arXiv: 1702.00664 [astro-ph.HE].

[196] M. Wood et al. "Fermipy: An open-source Python package for analysis of Fermi-LAT Data". In: *35th International Cosmic Ray Conference (ICRC2017)*. Vol. 301. International Cosmic Ray Conference. Jan. 2017, p. 824. arXiv: 1707.09551 [astro-ph.IM].

[197] W. Atwood et al. "Pass 8: Toward the Full Realization of the Fermi-LAT Scientific Potential". In: *arXiv e-prints*, arXiv:1303.3514 (Mar. 2013), arXiv:1303.3514. arXiv: 1303.3514 [astro-ph.IM].

[198] David John Thompson. "The Fourth Fermi LAT Source Catalog (4FGL)". In: *AAS/High Energy Astrophysics Division*. Vol. 17. AAS/High Energy Astrophysics Division. Mar. 2019, p. 109.33.

[199] M. Ackermann et al. "2FHL: The Second Catalog of Hard Fermi-LAT Sources". In: *The Astrophysical Journal* 222.1, 5 (Jan. 2016), p. 5. DOI: 10.3847/0067-0049/222/1/5. arXiv: 1508.04449 [astro-ph.HE].

[200] D. Khangulyan, F. A. Aharonian, and S. R. Kelner. "Simple Analytical Approximations for Treatment of Inverse Compton Scattering of Relativistic Electrons in the Blackbody Radiation Field". In: *The Astrophysical Journal* 783.2, 100 (Mar. 2014), p. 100. DOI: 10.1088/0004-637X/783/2/100. arXiv: 1310.7971 [astro-ph.HE].

[201] Wolfgang A. Rolke, Angel M. López, and Jan Conrad. "Limits and confidence intervals in the presence of nuisance parameters". In: *Nuclear Instruments and Methods in Physics Research A* 551.2-3 (Oct. 2005), pp. 493–503. DOI: 10.1016/j.nima.2005.05.068. arXiv: physics/0403059 [physics.data-an].

[202] Gary J. Feldman and Robert D. Cousins. "A Unified approach to the classical statistical analysis of small signals". In: *Phys. Rev. D* 57 (1998), pp. 3873–3889. DOI: 10.1103/PhysRevD.57.3873. arXiv: physics/9711021.

[203] G. R. Werner et al. "The extent of power-law energy spectra in collisionless relativistic magnetic reconnection in pair plasmas". In: *The Astrophysical Journal* 816.1 (2015), p. L8. DOI: 10.3847/2041-8205/816/1/l8. URL: https://doi.org/10.3847%2F2041-8205%2F816%2F1%2Fl8.

[204] Fan Guo et al. "Particle Acceleration and Plasma Dynamics during Magnetic Reconnection in the Magnetically-dominated Regime". In: *The Astrophysical Journal* 806.2 (2015), p. 167. DOI: 10.1088/0004-637x/806/2/167. URL: https://doi.org/10.1088%2F0004-637x%2F806%2F2%2F167.

[205] A. R. Bell. "The Acceleration of cosmic rays in shock fronts. I". In: *Mon. Not. Roy. Astron. Soc.* 182 (1978), pp. 147–156.

[206] S. Gabici, F. A. Aharonian, and S. Casanova. "Broad-band non-thermal emission from molecular clouds illuminated by cosmic rays from nearby supernova remnants". In: *MNRAS* 396.3 (July 2009), pp. 1629–1639. DOI: 10.1111/j.1365-2966.2009.14832.x. arXiv: 0901.4549 [astro-ph.HE].

[207] A. M. Bykov and I. N. Toptygin. "A Model of Particle Acceleration to High Energies by Multiple Supernova Explosions in OB Associations". In: *Astronomy Letters* 27.10 (Oct. 2001), pp. 625–633. DOI: 10.1134/1.1404456.

[208] H. E. S. S. Collaboration. "Resolving the Crab pulsar wind nebula at teraelectronvolt energies". In: *Nature Astronomy* 4 (Feb. 2020), pp. 167–173. DOI: 10.1038/s41550-019-0910-0. arXiv: 1909.09494 [astro-ph.HE].

[209] A. U. Abeysekara et al. "Multiple Galactic Sources with Emission Above 56 TeV Detected by HAWC". In: *Phys. Rev. Lett.* 124.2 (2020), p. 021102. DOI: 10.1103/PhysRevLett.124.021102. arXiv: 1909.08609 [astro-ph.HE].

[210] Christoph Deil et al. *gammapy/gammapy: v.0.18.2*. Version v0.18.2. Nov. 2020. DOI: 10.5281/zenodo.4701500. URL: https://doi.org/10.5281/zenodo.4701500.

[211] A. Albert et al. "3HWC: The Third HAWC Catalog of Very-High-Energy Gamma-ray Sources". In: *Astrophys. J.* 905.1 (2020), p. 76. DOI: 10.3847/1538-4357/abc2d8. arXiv: 2007.08582 [astro-ph.HE].

[212] A. Albert et al. "Evidence of 200 TeV photons from HAWC J1825-134". In: *Astrophys. J. Lett.* 907.2 (2021), p. L30. DOI: 10.3847/2041-8213/abd77b. arXiv: 2012.15275 [astro-ph.HE].

[213] H. E. S. S. Collaboration et al. "H.E.S.S. and Suzaku observations of the Vela X pulsar wind nebula". In: *Astronomy & Astrophysics* 627, A100 (July 2019), A100. DOI: 10.1051/0004-6361/201935458. arXiv: 1905.07975 [astro-ph.HE].

[214] Jorge Ariel Combi et al. "G337.2+0.1: A New x-ray supernova remnant?" In: *Astron. Astrophys.* 431 (2005), p. L9. DOI: 10.1051/0004-6361:200400136. arXiv: astro-ph/0501051.

[215] Jorge A. Combi et al. "XMM observation of the SNR G337.2+0.1". In: *Astrophys. J. Lett.* 653 (2006), pp. L41–L44. DOI: 10.1086/510329. arXiv: astro-ph/0610708.

[216] F. Acero et al. "Constraints on the Galactic Population of TeV Pulsar Wind Nebulae Using Fermi Large Area Telescope Observations". In: *The Astrophysical Journal* 773.1, 77 (Aug. 2013), p. 77. DOI: 10.1088/0004-637X/773/1/77. arXiv: 1306.5735 [astro-ph.HE].

[217] Michelle Tsirou et al. "VHE gamma-ray study of the composite SNR MSH 15-52 with H.E.S.S". In: *PoS* ICRC2017 (2018), p. 681. DOI: 10.22323/1.301.0681. arXiv: 1709.01422 [astro-ph.HE].

[218] F. Aharonian et al. "Discovery of two candidate pulsar wind nebulae in very-high-energy gamma rays". In: *Astronomy & Astrophysics* 472.2 (Sept. 2007), pp. 489–495. DOI: 10.1051/0004-6361:20077280. arXiv: 0705.1605 [astro-ph].

[219] G. Castelletti, E. Giacani, and A. Petriella. "Unveiling the origin of HESS J1809-193". In: *Astronomy & Astrophysics* 587, A71 (Mar. 2016), A71. DOI: 10.1051/0004-6361/201527578. arXiv: 1601.04962 [astro-ph.HE].

[220] Kelly Malone. "The Ultra-High-Energy Source MGRO J1908+06". In: July 2021. arXiv: 2107.14364 [astro-ph.HE].

[221] S. Funk et al. "XMM-Newton observations of HESS J1813-178 reveal a composite Supernova remnant". In: *Astronomy & Astrophysics* 470.1 (July 2007), pp. 249–257. DOI: 10.1051/0004-6361:20066779. arXiv: astro-ph/0611646 [astro-ph].

[222] H. Abdalla et al. "H.E.S.S. observations of RX J1713.7−3946 with improved angular and spectral resolution: Evidence for gamma-ray emission extending beyond the X-ray emitting shell". In: *Astron. Astrophys.* 612 (2018), A6. DOI: 10.1051/0004-6361/201629790. arXiv: 1609.08671 [astro-ph.HE].

[223] Yasuo Fukui et al. "Pursuing the Origin of the Gamma Rays in RX J1713.7-3946 Quantifying the Hadronic and Leptonic Components". In: *The Astrophysical Journal* 915.2, 84 (July 2021), p. 84. DOI: 10.3847/1538-4357/abff4a. arXiv: 2105.02734 [astro-ph.HE].

[224] F. Acero et al. "A new nearby pulsar wind nebula overlapping the RX J0852.0-4622 supernova remnant". In: *Astronomy & Astrophysics* 551, A7 (Mar. 2013), A7. DOI: 10.1051/0004-6361/201220799. arXiv: 1212.4156 [astro-ph.HE].

[225] J. Marti, J. M. Paredes, and M. Ribo. "The system LS 5039: a new massive radio emitting X-ray binary". In: *Astronomy & Astrophysics* 338 (Oct. 1998), pp. L71–L74.

[226] J. C. Lau et al. "A Study of the Interstellar Medium Towards the Unidentified Dark TeV γ-Ray Sources HESS J1614-518 and HESS J1616-508". In: *Publications of the Astronomical Society of Australia* 34, e064 (Dec. 2017), e064. DOI: 10.1017/pasa.2017.59. arXiv: 1711.01687 [astro-ph.HE].

[227] MAGIC Collaboration et al. "Discovery of TeV γ-ray emission from the neighbourhood of the supernova remnant G24.7+0.6 by MAGIC". In: *MNRAS* 483.4 (Mar. 2019), pp. 4578–4585. DOI: 10.1093/mnras/sty3387. arXiv: 1812.04854 [astro-ph.HE].

[228] A. Albert et al. "Evidence that Ultra-high-energy Gamma Rays Are a Universal Feature near Powerful Pulsars". In: *Astrophys. J. Lett.* 911.2 (2021), p. L27. DOI: 10.3847/2041-8213/abf4dc. arXiv: 2101.07895 [astro-ph.HE].

[229] R. N. Manchester et al. "The Australia Telescope National Facility Pulsar Catalogue". In: *The Astronomical Journal* 129.4 (Apr. 2005), pp. 1993–2006. DOI: 10.1086/428488. arXiv: astro-ph/0412641 [astro-ph].

[230] R. Terrier et al. "Discovery of a pulsar wind nebula associated with IGR J18490-0000". In: *American Institute of Physics Conference Series*. Ed. by Felix A. Aharonian, Werner Hofmann, and Frank Rieger. Vol. 1085. American Institute of Physics Conference Series. Dec. 2008, pp. 312–315. DOI: 10.1063/1.3076669.

[231] E. V. Gotthelf et al. "Discovery of an Energetic 38.5 ms Pulsar Powering the Gamma-ray Source IGR J18490-0000/HESS J1849-000". In: *The Astrophysical Journal Letters* 729.2, L16 (Mar. 2011), p. L16. DOI: 10.1088/2041-8205/729/2/L16. arXiv: 1012.2121 [astro-ph.HE].

[232] R. P. Mignani et al. "VLT and Suzaku observations of the Fermi pulsar PSR J1028-5819". In: *Astronomy & Astrophysics* 543, A130 (July 2012), A130. DOI: 10.1051/0004-6361/201218869. arXiv: 1205.1905 [astro-ph.HE].

[233] H. E. S. S. Collaboration et al. "H.E.S.S. observations of the Crab during its March 2013 GeV gamma-ray flare". In: *Astronomy & Astrophysics* 562, L4 (Feb. 2014), p. L4. DOI: 10.1051/0004-6361/201323013. arXiv: 1311.3187 [astro-ph.HE].